Numerical Investigation of Catalyst Structure for Steam Reforming Process

A thesis submitted to the Faculty of Computing, Engineering and the Built Environment (CEBE), in partial fulfilment for the degree of

Doctor of Philosophy

by

Muhammad Abdullah Arslan

Faculty of Computing, Engineering and the Built Environment (CEBE)

Birmingham City University

July 2021

Declaration

Muhammad Abdullah Arslan asserts his right to be identified as the author of this work in accordance with the Copyright, Designs and Patents Act 1988.

Acknowledgement

First praise is to Allah, the Almighty, the beneficent and the most merciful. Then, I am eternally grateful to my supervisors, Dr. Reaz Hasan and Dr. Dominic Flynn, for their guidance and encouragement throughout this research work. Their experience and enthusiasm for my studies helped me to better plan my research activities.

I would like to thank external examiner Dr. Pak Sing (Ken) Leung of Northumbria University Newcastle and independent internal examiner Dr. Noel Perera of Birmingham City University for conducting my viva and providing valuable feedback to finalize my thesis. I also would like to acknowledge Dr. Abdelhakim Settar[1] for his help with my queries regarding his research papers.

A bundle of thanks goes to CEBE staff members and the IT help desk for timely assistance regarding my various queries and problems during this study period. I would also like to thank Birmingham City University for providing the license for ICEM and CFX 18.1.

Lastly, I express my sincere gratitude to my grandparents, parents and family members for their continuous support to this day. Their unconditional love has eased off my burden during this journey. Without them, I would have never made it this far, so I am eternally thankful. Also, I thank my colleagues who made my stay delightful at the university.

---

[1] Dr Abdelhakim Settar is an associate professor assigned to the PRISME Laboratory of INSA Centre Val de Loire - Campus de Bourges in France

Abstract

Internal combustion engines substantially lose fuel energy in the form of heat without contributing to the vehicle's propulsion. About a third of this waste energy gets released from the exhaust pipeline. Catalysts recover this unused heat for their essential function to curb emissions; however, a fuel reformer catalyst can take it further. An onboard fuel reformer makes hydrogen and carbon monoxide, known as syngas. The syngas and primary fuel increases fuel heating value and modify combustion characteristics towards low emissions.

This study numerically investigates catalyst design impacts on its efficiency. The primary goal of this research is to achieve a higher hydrogen yield without altering the catalyst dimensions. Structural changes such as cell height, catalyst segmentation, and passive passages remarkably affect catalyst efficiency. Meanwhile, key catalyst characteristics such as flow uniformity, pressure drop, light-off, and residence time remain under consideration during these variations.

For this purpose, after verifying the simulation against an experimental study, a successful channel height reduction is achieved by employing metal foam as a support structure (protrusion). Usually, the catalyst cell wall contains a reacting material layer. Putting this layer on the protrusion and elevating it to the middle of the cell height increases the hydrogen mass fraction (H_2 mf) by more than fifty per cent. The nearby fluid temperature for this pattern is 60 K higher than the conventional design, which is the primary reason for the higher yield. This modification also enables channel height variation without changing the cell height or shape.

The channel is then divided into inert and catalytic portions. This segmentation allows the reactants to regain heat after passing over these inactive isothermal parts. Thus, fluid mixing and higher temperature increase the reaction rate before reactants reach the next catalyst section. The length of these patterns is carefully kept equal to the reference design. As a result of these modifications, the hydrogen mf increases 11% further.

Transverse flow channels permit inter-channel heat and mass transfer. The location and number of these passive passages need further investigation. Metal foam existence at these paths can direct fluid flow by varying the foam properties. Directional porosity and permeability mainly affect the flow pattern. In addition, metal foam presence at these perforations enhances the neighbouring gas temperature by 20 K and the hydrogen production by 15%.

Overall, numerical calculations show that compared to the conventional structure, cell height and segmentation can increase H_2 mf by 50-80%, whereas passive passages increase it by 15%.

Nomenclature

Symbols

A	Pre-exponential factor, Area
a	Temperature-dependent Seebeck coefficient
CO_2	Carbon dioxide
cc	Cubic centimetre
CH_4	Methane
CH4P	Methane partial pressure
cpsi	Cells per square inch
C_p	Specific heat capacity
CO	Carbon monoxide
D	Diffusion coefficient, Down
D	Binary diffusion coefficient
d	Diameter
D_c	Darcy coefficient
E	Activation energy
eta	Porosity
f	Contraction/expansion factor
F1	Cumulative factor of variables at local conditions
H_2	Hydrogen
h	Protuberance height
H	Channel height, enthalpy
H	Hole, High
H2OP	Water partial pressure
ht	Heat transfer coefficient

iad	Interfacial area density
I	Iso
K_1 and K_2	Linear and quadratic combined constants
L	Length
loss	Resistance loss coefficient
M	Molar mass
Mod	Modified
$\dot{m}$	Mass flow rate
Ni	Nickel
NO_x	Nitrous oxides
P	Pressure
perm	Permeability
P_D	Pressure drop
ppmC	Parts per million carbon percentage
ppm	Parts per million
Pt	Platinum
R	Resistance, region
Rh	Rhodium
rate	Volumetric reaction rate
Rate	Surface reaction rate
Re	Reynolds number
SO_2	Sulphur dioxide
S/C	Steam to carbon ratio
SS	Steady-state
T	Temperature
T	Transient

U	Up
V	Voltage
u *and* v	Horizontal and vertical components of velocity
w	Mass fraction
W	Wall, Watt
x and y	Horizontal and vertical axes
Z	Figure of merit

Abbreviations

ATR	Autothermal reforming
CCC	Close-coupled catalyst
CHP	Combined heat and power
CI	Compression ignition
CPHE	Catalytic plate type heat exchanger
DPF	Diesel particulate filter
DOC	Diesel oxidation catalyst
EGR	Exhaust gas recirculation
EU	European Union
FC	Fuel cell
FR	Fuel reformer
GHG	Greenhouse gas
GSA	Geometric surface area
HC	Hydrocarbon
IC	Internal combustion
LNT	Lean NO$_x$ trap
MF	Metal foam
mf	Mass fraction

NEDC	New European Driving Cycle
NPL	Non-patent literature
OFA	Open frontal area
OPEC	The Organization of the Petroleum Exporting Countries
ORC	Organic Rankine cycle
PAHs	Polycyclic aromatic hydrocarbons
PM	Particulate matter
POX	Partial oxidation
RC	Rankine cycle
REGR	Reformate exhaust gas recirculation
RG	Reformer gas or syngas
SC	Streamwise coefficient
SI	Spark ignition
SD	Standard deviation
SMR	Steam methane reforming
TC	Turbo compound
TCT	Technology cycle time
TEG	Thermoelectric generator
WGS	Water Gas Shift
WHR	Waste heat recovery

Subscripts

avg	Average
f	Fluid
h	Hydraulic
i	P or N-type semiconductor, Gas species, Channel number
in	Inlet

max	Maximum
min	Minimum
out	Outlet
p	Pore
s	Superficial, solid
s	Strut

Superscripts

a and b	Exponential constant for methane and water

Greek letters

λ	Thermal conductivity, stoichiometric air to fuel ratio
γ	Flow uniformity
β	Mass transfer coefficient
ε'' and ε'	Stoichiometric coefficient of reactants and products
ρ	Density
Δ	Change in

Table of contents

List of figures

List of tables

List of equations

1 Introduction

This chapter introduces the importance of fossil fuels for the transport and power industries. However, emissions produced from these sectors contribute to global warming and are hazardous to human life. These concerns emphasise the need for energy recovery and emission reduction.

1.1 Context

Fossil fuels are widely used in our day-to-day life, releasing carbon dioxide (CO_2), sulphur dioxide (SO_2) and many other greenhouse gases (GHGs). These pollutants may contribute to global warming, and frequent exposure of some species, e.g. benzene and toluene, causes severe health concerns. Carbon dioxide is the primary combustion pollutant and is regulated by the carbon cycle. Plants absorb atmospheric CO_2 during photosynthesis. Rain also brings down CO_2, which gets released into the atmosphere or ultimately reaches oceans and is absorbed by living organisms such as seashells. However, heavy dependence on fossil fuels is disturbing this flux (Pastore, 2010).

Table 1-1: Each pollutant species contribution to global emission from the transport sector (Goldemberg, 2008)

Pollutants	**Transport sector contribution to global emission**
Hydrocarbons (HCs)	50%
Carbon monoxide (CO)	70%
Carbon dioxide (CO_2)	19%
Nitrous oxides (NO_x)	40%
Benzene	80%

Table 1-1 shows the transport sector individual species contribution to global pollutants emission. For example, yearly worldwide CO_2 emissions are nearly 23 billion tonnes (Lewis *et al.*, 2005), and 19% come from the transportation industry alone (Goldemberg, 2008). In addition, CO_2 is the main contributor to global GHG emission, contributing 80% of the total

(Leung *et al.*, 2018). Over time these pollutants can cause serious health problems besides breathing problems and irritation to the eyes and nostrils.

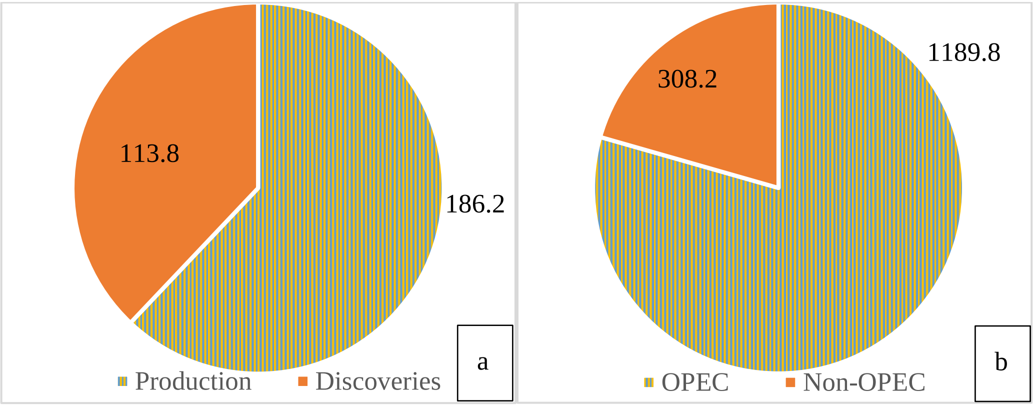

Figure 1-1: a) Oil production vs oil discoveries 2009-2018 (OPEC, 2019) b) proven global oil reserves (units are in billion barrels) (OPEC, 2018)

The second issue is the finite nature of the fuels reserves. Oil discoveries are regular, but the earth resources are limited (Figure 1-1). From 2009-2018, 113.8 billion barrels of oil was produced by OPEC (The Organization of the Petroleum Exporting Countries) nations. Meanwhile, new reserves of 186.2 billion barrels are found (OPEC, 2019). According to OPEC own estimation, the proven remaining global reserves are 1498 billion barrels (OPEC, 2018).

1.2 Transport sector emissions

About 23% of the world's emission comes from transport vehicles across the globe. The global car sale crosses a 100 million figure in 2020 (Figure 1-2). The COVID-19 pandemic has reduced this number from the previous year, but a massive sale still adds to the persistent emission problem. Annual GHGs emitted by US highway vehicles account for 1.36 billion tonnes (Brady and Fath, 2009). Similarly, in the EU (European Union), light vehicles produce 14.5% of total CO_2 emissions (European Parliament and Council of the European Union, 2020). Each litre of burnt gasoline almost creates 2 kilograms of CO_2. That is roughly 4.5 to 8 tonnes of CO_2 each year for an average vehicle usage (Pacala and Socolow, 2004).

1.3 Emission laws

Every developed country is making emissions laws stricter than ever. European Union Parliament passed a regulation 2019/631, which adds a 95 g CO_2/km target figure for 2020-2024 for all the new registered cars. The EU is looking for an additional CO_2 emission reduction of 15% from 2025 and a later 37.5% further improvement after 2030 (European Parliament and

Council of the European Union, 2020). The United States set the same emission target of 95 g, but the implementation is delayed until 2025. Overall it is a global trend, and all the governments worldwide are working to control carbon dioxide emission (Arnaud *et al.*, 2014).

Failure to meet the EU target means penalties by the respective governments. For example, until 2018, the penalty for exceeding the limit by one gram was 5 €. However, the EU modified the law and set a new limit of 95 euros for every excessive gram of CO_2 in 2019. The new rule compels the manufacturer to reduce the CO_2 emissions in one way or another, which may increase the sale price.

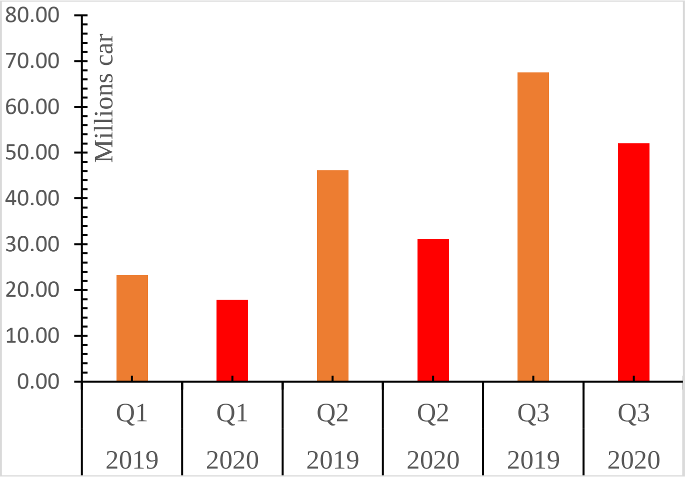

Figure 1-2: Number of vehicles produced around the world in 2019/2020 (Q1 = 1st quarter) (2020 Statistics, 2020)

1.4 Global warming

Carbon dioxide is part of the combustion product. CO_2 absorbs the large wavelength of infrared light radiated back from the earth surface, acting as a greenhouse cover in the atmosphere. This containment of heat causes global warming. Recovering waste energy by any suitable device will improve fuel consumption, resulting in lower greenhouse gas emissions such as CO_2 and sulphur dioxide. Sulphur exists as a chemical compound in fuel (gasoline, diesel) and lubricants. During engine combustion, sulphur forms SO_2, which then becomes part of the atmosphere (Hoshino *et al.*, 2015).

1.5 Clean energy options

In 2005, the annual global energy need was 13 terawatts (TW) or 4.1×10^{20} J. Every country needs power sources for its economic growth. By 2100, the world with new emerging economies and a growing population will require an energy demand of around 46 TW (Lewis *et al.*, 2005).

All the sectors in society need energy, such as industries, commercial centres and houses. However, a majority of these depend on fossil fuels to meet their energy demand. For example, road vehicles heavily depend on oil for transportation, whereas public homes and commercial centres need electricity and gas for routine operations. In addition, most power plants use fossil fuels for electricity generation. Hence, securing energy sources is a foremost challenge for every country to maintain its quality of life. Energy security is a term defined as "a reliable and adequate supply of energy at reasonable prices" (Bielecki, 2002) (IEA, 2019).

Solar radiation is the primary source of energy on Earth. It drives air and ocean currents and is essential to animal and plant life. The total value of some clean energy sources is not suitable to sustain global demand. For instance, ocean tides at any moment contain approximately a total of 2 TW of energy. Even maximum extractable wind power can only serve 1/10th of the world requirements. Similarly, according to United Nations estimates, the remaining global hydrostatic potential is negligible (0.5 TW). Hence, fossil fuels still fulfil the global power demand gap.

Annual calculated solar radiation on the earth surface is around 120 thousand TW. Just by covering 0.16% of the earth surface with 10% efficient solar cells can generate 20 TW of power. The main issue with solar cells is their cost. To replace our electricity demand, it is 5-10 times expensive than fossil fuels derived plants and can be 50 times more costly than fossil fuels as a primary energy source (Lewis *et al.*, 2005).

1.6 Fossil fuel dependence

Though the oil demand declined in 2020 due to the global COVID-19 pandemic (IEA, 2020), oil and gas will remain significant fuels for the transport sector. A 2015 Internationa Energy Agency (IEA) report, "Key World Energy Statistics 2015", shows that the transport sector's oil consumption is close to 93% (IEA, 2015).

Table 1-2: Electric power plants feed percentage for electricity generation in 2005 (Bhattacharyya, 2009)

Country	Coal	Natural gas	Oil	Nuclear	Others
UK	40.6	36.7	-	19.8	2.9
Germany	43.5	11.0	1.7	26.3	17.5
Italy	14.4	49.2	15.5	0	20.9
Spain	25.0	26.9	8.3	19.6	20.2
The Netherlands	23.5	57.7	2.3	4.0	12.5

Despite advancements in solar panels, nuclear power plants and wind turbine systems, even western countries rely heavily on fossil fuels imports for their electricity generation. These fuels include coal, oil and gas. Hence, electric vehicles would still add carbon emissions by using electricity from these power plants. Oil and gas prices are vulnerable to market and political situations, so a constant consumer price is hard to maintain. The price fluctuation also affects electricity cost. Overall, fossil fuel price affects inflation, import budget, and political security. Spain power plants (Table 1-2) have higher reliability due to their diversified resources (oil, gas, coal), but it requires a very active supply chain management (Bhattacharyya, 2009).

1.7 Emission effects on human health

A 1997 study found that truck drivers are more susceptible to lung cancer than taxi drivers (considering drivers smoking habits in the survey). The primary reason was more probable exposure to polycyclic aromatic hydrocarbons (PAHs), such as benzene. Benzene is part of fossil fuel present in diesel engine exhaust, diesel oil, lubes or any other heavy fuel such as kerosene, naphthalene, tar and so forth. These heavy hydrocarbons are also responsible for skin and bladder cancer. For example, frequent exposure to environments containing up to 1 µg of benzene per cubic meter of air is considered risky for cancer (Boffetta, Jourenkova and Gustavsson, 1997). In addition, benzene causes blood poisoning and is cancerous to both animals and humans (Lindstrom, A B., S. Waidyanatha, K. YeowellO’Connell, 1999).

Harmful hydrocarbon (HC) emissions are not only related to compression ignition (CI) engines but also to spark ignition (SI). An experimental study of an SI engine operating at stoichiometric conditions shows that commercial fuel combustion produces all hydrocarbon emissions. The engine exhaust contains methane, ethylene, acetylene, benzene, toluene and other pollutants. Toluene and benzene constitute a large proportion of exhaust in part per million of carbon percentage (ppmC). Another concern is that these pollutants share increases if their precursors in the fuel increase, such as ethylene formation from octane fuel (Zervas, Montagne and Lahaye, 2004).

Naphthalene is another pollutant that is toxic when inhaled or orally taken. It also falls in the PAHs family and is water-soluble (Judith Olsen, 1984). Heavier carbon compounds burning, e.g. coal, wood, heavy oil, tar, etc., produce naphthalene. Road transport emissions, stubble, fireworks and coal burning are the primary reasons for PAHs release in cities (Yuan *et al.*, 2010).

1.8 Motivation

Heat is a substantial source of internal combustion (IC) engine waste energy. Fuel and oxidiser are burnt in the combustion chamber, releasing combustion gases at high temperature and pressure. The engine work is done by expanding gases to drive the crankshaft that propels the wheels through the various linkages and gears.

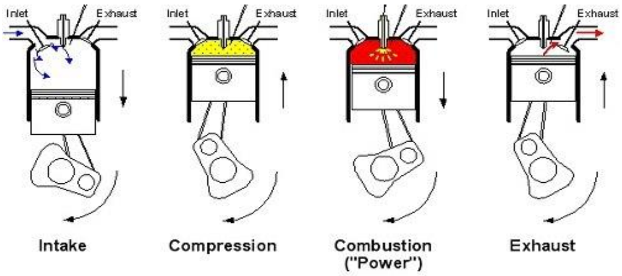

Figure 1-3: Working of 4-Stroke (the Otto cycle) diesel engine (Mechanic, 2011)

Nearly 65% to 70% of fuel energy (enthalpy) input to an IC engine is wasted (Bari, 2017) (Stobart, Wijewardane and Allen, 2017). The high inefficiency means recovering any waste energy would significantly improve the fuel economy and reduce exhaust emissions. The vehicle dissipates energy in radiation, heat and various friction losses. Some unused energy is recoverable, such as the braking energy by the regenerative braking system. Similarly, Rankine cycle (RC), turbo-compound (TC), fuel reformer (FR), thermoelectric generator (TEG), and fuel cells (FC) can recover heat energy.

Using TC, RC or TEG, up to 3-10% of the exhaust heat is recoverable (Arnaud et al., 2014). This improvement can increase the overall efficiency of the IC engine from 30 to 40%. Therefore, recovering any waste energy reduces fuel consumption, thus carbon dioxide emissions and oil imports. Still, heat recovery will not limit other harmful emissions.

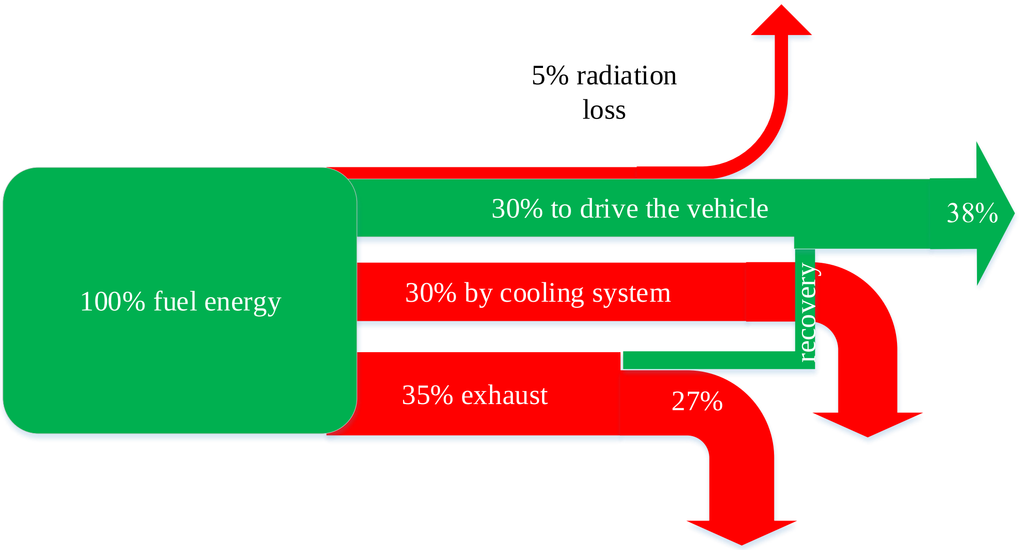

Figure 1-4: Energy flow of a gasoline engine vehicle (Bari, 2017) (Stobart, Wijewardane and Allen, 2017)

1.9 Scope of the project

Waste heat recovery is not the ultimate goal though it can reduce CO_2 emissions to meet the EU laws (see section 1.3). However, other harmful emissions (unburnt hydrocarbon, NO_x, etc.) need different treatment and strategies. Hydrogen can increase fuel heating value to increase fuel economy and oxidise harmful emissions to neutral chemical compounds. Therefore, its addition to the fuel mixture can serve both purposes (more details are in section 2.6).

1.9.1 Waste heat recovery

The slow development of clean energy technologies and the inability to give the same performance as an internal combustion engine means that the IC engine will last until the end of the 21st century (Faber and Frenken, 2009). The fuel share lost to the coolant and exhaust system is nearly the same, but the coolant temperature is not high enough to be utilised by a recovery device. So the exhaust gas is the most suitable candidate from the above owing to its higher temperature, around 775 K (Wang *et al.*, 2011) and higher share in waste energy (Figure 1-4). A typical SI engine exhaust temperature varies according to the stoichiometric air to fuel (λ) ratio. The λ varies from 1.1 to 0.9, and similarly, the exhaust temperature ranges from 825–

975 K (Leung *et al.*, 2018). A typical heavy-duty CI engine exhaust temperature varies from 775 K to 975 K (Bari, 2017).

1.9.2 Emission reduction

Replacing the IC engine with a better power unit such as a hydrogen fuel cell can be promising due to its 40-60% efficiency. This value may exceed 90% if the waste heat from the FC is utilised. A hydrogen fuel cell is also nearly pollution-free, releasing water as the main emission besides some NO_x. Though FC's NO_x emission is 1/200th of a typical diesel engine, and mainly occurs if the peak temperature is not limited (Balat, 2008).

1.9.3 Hydrogen merits

Its main advantage is that it is nearly pollution-free. In air-assisted hydrogen combustion, if the temperature exceeds 2300 K, then nitrous oxides are formed. Using it as part of fuel in IC engines increases the mixture's flammability limit and burning speed. Due to its lower density (0.09 kg/m^3), it has 2.7 times more specific energy (120 kJ/g, lower heating value LHV) than gasoline (44 kJ/g). However, hydrogen is carried in gas, so heating per unit volume is lower than liquid fuel like gasoline (720-780 kg/m^3) (Balat, 2008). For instance, 270 litres of hydrogen (15.4 kg) tank stores the same amount of energy as a 68 litres tank of gasoline fuel (41 kg) (Demirbaş, 2005). Moreover, the pumping power to transport hydrogen is 4.5 times higher than natural gas at standard conditions due to its lower density (Pastore, 2010).

There is a potential to produce 36 million tonnes of hydrogen per year by incorporating nuclear and renewable power plants performing electrolysis and fossil fuels reforming. Today, the cheapest way to produce hydrogen is through steam methane reforming (SMR) (1.5 to 3.5 $/kg), as electrolysis is only economical if electricity is more affordable. Most of the hydrogen comes from fossil fuels (96%), and the most common method is SMR (48%) (Balat, 2008).

1.9.4 Hydrogen economy

Hydrogen (H_2) is an energy carrier because it is not widely available as a free element but in a compound like water. So its extraction process consumes energy such as water electrolysis or petroleum reforming. That is why the fuel term is not sometimes associated with hydrogen (Pastore, 2010) but an energy carrier or secondary form of energy (Balat, 2008). So hydrogen economy means procuring methods of replacing fossil fuel with hydrogen.

Storing onboard hydrogen in a vehicle is another big problem. Due to its low density, a compressed hydrogen solution will reduce the vehicle range, whereas carrying it as metal hydrides will increase the weight. Therefore, mainly it is stored as a compressed gas in a transport vehicle and as a liquid at storage sites (Pastore, 2010).

1.10 Onboard hydrogen production

Replacing conventional fuel with hydrogen is not feasible due to the requirement of a massive network of production and supply plants (Singh, Singh and Gautam, 2020). Conversely, a 2005 study gives a realistic estimate that by 2040, widespread fuel cell vehicles can replace conventional cars. Moreover, considering FC efficiency to be 2.5 times more than the traditional IC engines, hydrogen-powered cars can reduce overall oil consumption. For instance, to replace 6.68 billion barrels of oil, annual production of 136 million tonnes of hydrogen is needed (Armor, 2005).

Hence, an onboard hydrogen generation device that can recover heat to produce hydrogen is the most suitable way. Further, hydrogen utilisation can curb emissions and partially increase the fuel heating value, thus improving vehicle efficiency. Similarly, a household FC can aid fuel saving by providing both heat and electricity.

In summary, a fuel cell integrated with a fuel reformer can recover heat, increase the fuel heating value and reduce harmful emissions (see section 2.6.2) from an IC engine automobile (Leung *et al.*, 2018) (Hoshino *et al.*, 2015).

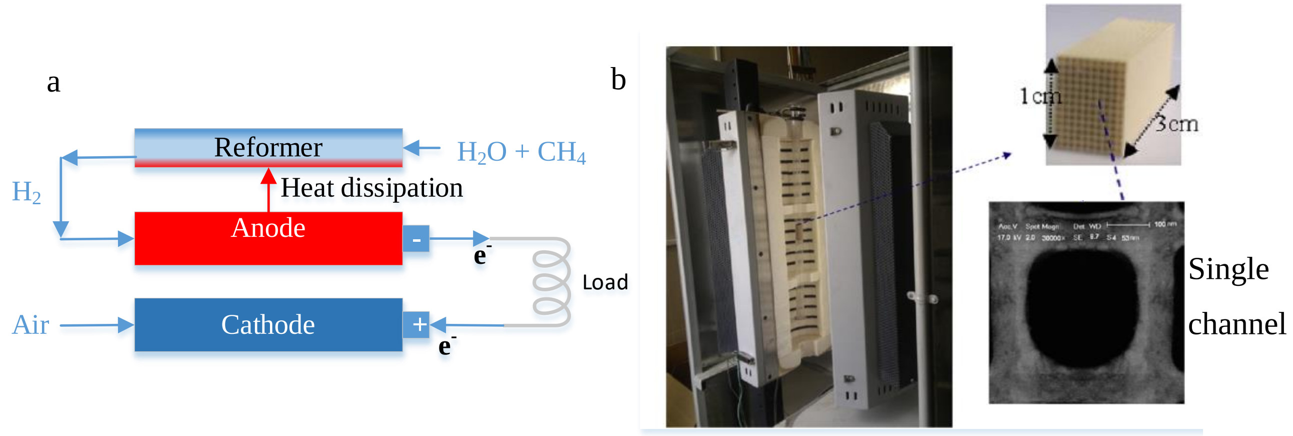

Figure 1-5: A simple description of integrated fuel reformer with solid oxide fuel cell (Settar, Lebaal and Abboudi, 2018) b) a fuel reformer monolith under test in a lab (Irani *et al.*, 2011)

1.11 Thesis organisation

The introduction chapter highlights the importance of waste heat recovery (WHR) and emission reduction. Next, this study explains stringent emission laws and associated penalties, global warming, and pollutants' effect on human health. Finally, the discussion favours onboard hydrogen power units for low emission and as WHR devices.

A short review of some of the heat recovery devices comes after that also explains the selection process. The literature review further emphasises the future of hydrogen and the importance of fuel reforming, especially in automobiles. It also highlights that catalyst structural changes like cell height, catalyst segmentation, and inter-channel mass transfer enhance FR reactor efficiency. The conclusion of this section converges on the aims and objectives of this study.

Reference design and some simplification incorporated in this study are explained in the research methodology section. It also adds the importance of parameters like flow uniformity, residence time, and light-off, which affect the reactor's efficiency. Finally, based on the literature review and research methodology, some new designs are presented.

After validating the simulations, next in line are parametric studies. These studies reveal important parameters and patterns to proceed further, such as segmentation and its possible configurations. Then comes some unique designs of this research, such as without changing the cell shape or density, the channel height is adjusted by implementing metal foam as protrusion. This modification brings high cell density monolith advantages to a standard cell shape. Overall, it improves the hydrogen yield of the reformer.

Lastly, transient simulation reveals that velocity and other parameters quickly homogenise in the catalyst volume after adding metal foam at the locations of the passive passages. These factors are responsible for higher catalytic activity. Also, metal foam can act as a flow guide to transfer heat and mass to adjacent channels as desired. A 3D model further endorses the above observations. In the end, the thesis conclusion is presented with some suggestions.

The appendix part describes some design procedures in ICEM 18.1. It shows CFX 18.1 domains settings, CEL code, some variables treatments in the software and diagrams of tested models.

1.12 Chapter 1 summary

Fossil fuels may not meet the ever-increasing energy demand in the next century. Also, emission laws can prohibit the widespread use of fossil fuels due to global warming and health concerns. Therefore, embracing clean and renewable energy resources is essential to meet future energy demand. Hydrogen can meet both the energy demand and environmental concerns for emissions; however, it requires a large generation and distribution network.

2 Literature review

This chapter describes some highly researched WHR technologies with their advantages and disadvantages. Fuel reformer catalyst is finalised as a preferred method, as its benefits in automobiles align with the IC engine efficiency and emission problems discussed in the previous chapter. Three catalyst structural modifications seem to affect the FR efficiency significantly, and the aim is to incorporate these amendments without altering the catalyst size.

2.1 The dilemma of adopting a new technology

Cutting exhaust emissions by selecting a new method does not come easy. First, there is always a doubt in the market response and technology itself. For example, manufacturing a low emission vehicle still comes with a doubt whether it can give the same performance as conventional IC cars. Then uncertainty rises from an economic perspective to environmental considerations, such as whether customers buy a low emission but expensive vehicle to protect the environment (Faber and Frenken, 2009). Government policies like a carbon tax on petroleum products or emission laws encourage cleaner energy solutions. However, strict rules may promote substandard greener options in the market as an alternative to IC engines. In the opposite direction, emissions cut by solutions like improving engine performance and catalyst efficiency hinder the industry direction towards clean energy powertrain (Barbieri, 2016).

Many forms of waste energies and recovery techniques exist, such as a regenerative braking system, heating the passenger compartment with engine heat, and many more. In the following section, only highly researched devices are studied to recover heat energy.

2.2 Selecting the heat energy recovery devices

The number of research papers on thermoelectric generators is steadily rising. In the first decade of this century, there is a sharp increase indicating researchers' interest in this technology. Strict emission policies and fuel prices can be part of this rise (Zheng, 2008).

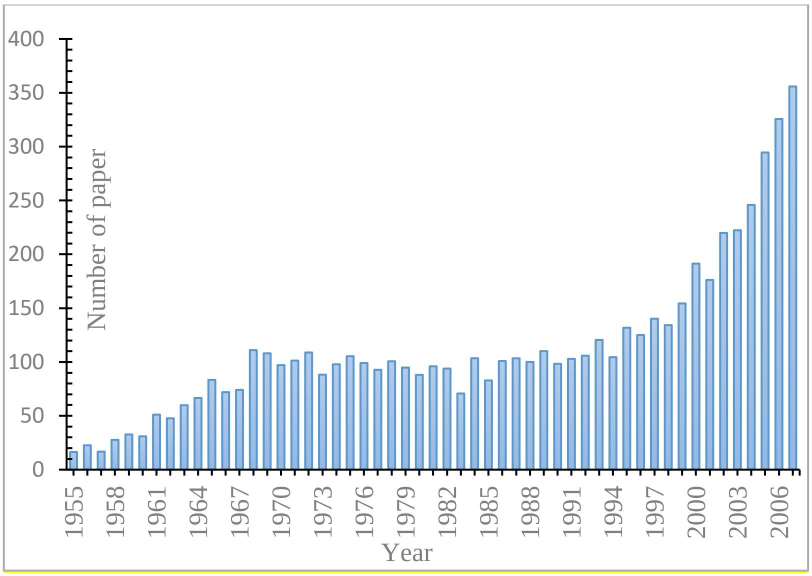

Figure 2-1: Number of research papers per year on the thermoelectric topic (Zheng, 2008)

In a patent landscape studied by Karvonen *et al*., three waste heat recovery technologies are narrowed down (Karvonen *et al.*, 2016). The authors have studied the statistics of patents published using the term “waste heat recovery using combustion engines” from 1993 to 2012. Next, a landscape study of patents origins, such as their organisation, history and country, is carried out.

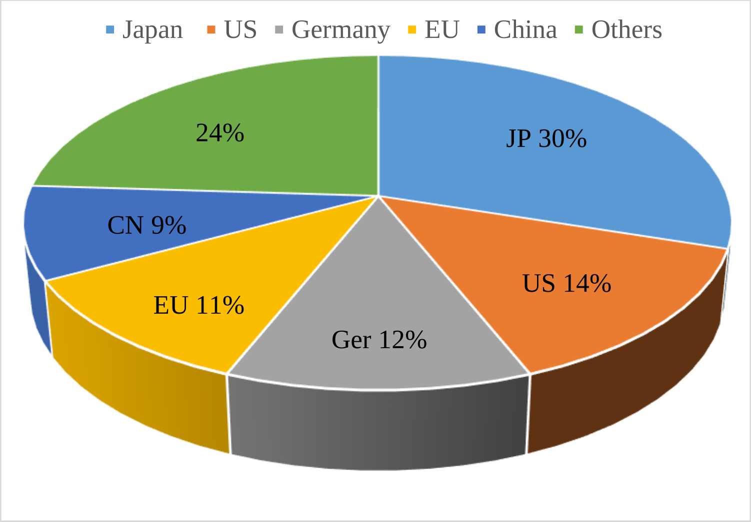

Figure 2-2: Percentage of patents filed by countries in waste heat recovery technology from 1993-2012 (15755 patents) (Karvonen *et al*., 2016)

After that, two indicators are defined to establish the most critical technologies. The first one is technology cycle time (TCT) which depends on the patent cited age. It measures the advancement pace of technology. Then comes non-patent literature (NPL) citation, which means the quality of references given in the patent. The NPL value will be higher if the references are of research papers, books, and other scientific findings. On the other hand, if the TCT value is lower, it means technology is rapidly developing.

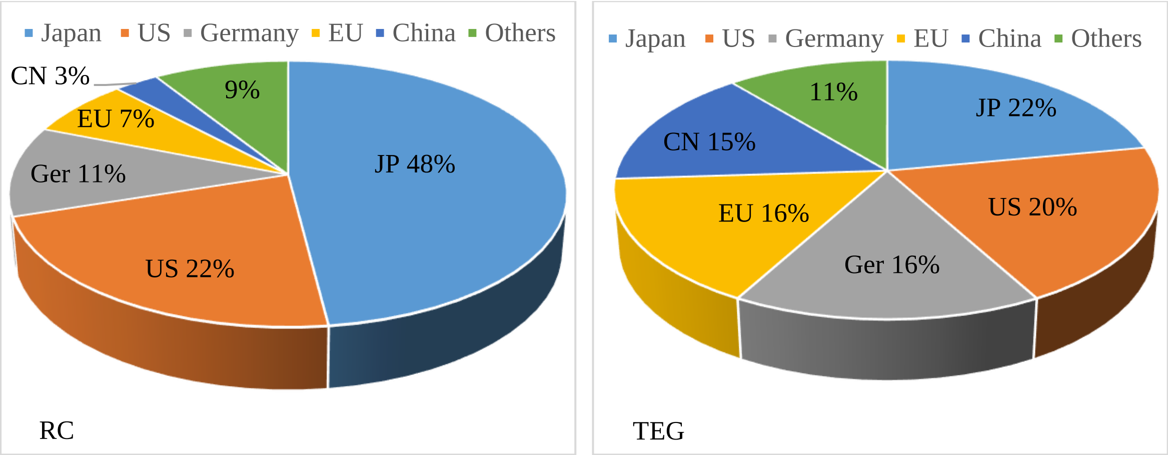

Figure 2-3: Patents files by different countries in RC and TEG system (763 patents) (Karvonen *et al*., 2016)

The landscape study shows that most patents are filed by developed countries like Japan, the US and the EU. The leading companies owning patents are Mitsubishi, Toyota, Siemens and General Electric (Figure 2-2).

In TEG patent filing, the distribution is even among the countries, whereas Japan share in RC patent is half of the other countries. Low RC shareholding means that Europe focuses on TEG induction as a WHR system, holding around 32 % of the patents in this field (Ger+EU).

Table 2-1: TCT and NPL values of patents for TEG and RC (Karvonen *et al.*, 2016)

Technology	NPL (%)	TCT
RC	16.0	9.7
TEG	6.7	4.9

Then the authors calculated the TCT and NPL values of these technologies. The data is given in Table 2-1. It shows that TEG technology is rapidly advancing as many patents appear in a short period, and the reference cited in these patents are mainly non-scientific. The reason can be that researchers have recently shown interest in it after 2000 (Figure 2-1). Overall, TEG is a highly researched technology system, but it is still immature as its NPL value is very low.

2.3 Technologies comparison

There are many methods to recover exhaust gas heat, such as turbo-compound, Rankine cycle, thermoelectric generator, fuel reformer and many more. These technologies show several advantages and disadvantages in terms of cost, size, efficiency and various other factors, which are explained following.

2.3.1 Turbo-compound

Turbo-compound consists of a turbine that is suitable to recover energy from hot exhaust gases. The gases expand in the turbine (shown in red, Figure 2-4a) and drive it. The turbine is connected mechanically to the engine via a gearbox (shown in green) and is called a turbo-compound. When the turbine is connected to a compressor, the configuration is known as a turbocharger. If a generator replaces the compressor, it is called a turbo generator.

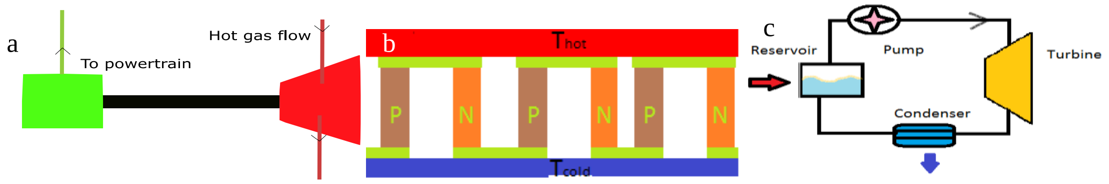

Figure 2-4: Illustrations of a) turbo-compound, b) a three units TEG modules, c) Rankine cycle engine

TC works on the principle of the kinetic energy of a fluid. So it works favourably during the acceleration (see Figure 2-7, orange dots) phase (high load). Turbo-compound is more suitable for heavy-duty vehicles.

TC can recover energy from the exhaust system. However, its high back pressure may increase fuel consumption, which reduces the work done by the exhaust stroke of the engine. Conversely, automakers exploit this back pressure when incorporating exhaust gas recirculation (EGR). Using a short route EGR system makes it easier to achieve high EGR rates to the engine inlet. In some cases, the EGR system is vital to reduce nitrous oxides emission (Greszler, 2008). As early as the 90s, some truck manufacturers installed the TC on the engine and achieved 5-10 % less fuel consumption, which means the turbo-compound is a mature technology (Arnaud *et al.*, 2014).

2.3.2 Rankine cycle

Rankine cycle engine (Figure 2-4c) is another commonly used technology in waste energy recovery. It is more like a small steam power plant. RC system consists of a heat source (e.g.

heat from car exhaust), a suitable expander (e.g. piston, scroll or turbine), a condenser (to dispose of heat) and a pump to drive the working fluid. The working fluid can be water or a mixture of organic liquids.

Same as the case of turbo-compound, large vehicles are suitable for RC systems. In one study, water is mixed with trifluoroethanol (50 % each by mole) as a working fluid for an RC. At peak condition, the system produced 26 kW of mechanical power (Patel, 1976). After 2000 many studies took place installing the RC package on a car. Endo *et al.* designed an innovative evaporation device that could extract heat from the cooling system and the engine exhaust. As a result, the working fluid quickly reached working temperature and pressure. The axial swash plate expander attained 3 kW of maximum power, improving 13% thermal efficiency (vehicle had a constant speed of 100 km/h) (Endo *et al.*, 2007).

Each working fluid affects the performance drastically. For example, the water takes a lot of time to reach its operating temperature due to its higher heat capacity. The organic Rankine cycle (ORC) utilises organic fluids to overcome high heat capacity issues. These fluids include; iso-butane, pentane, chlorofluorocarbon, perfluorocarbon mixed with water. The organic fluids have a low boiling point, but these are unstable at high temperatures, flammable and may cause damage to ozone (Karvonen *et al*., 2016).

A Rankine cycle assembly is suitable if a vehicle has a lot of space, such as trucks, buses, and ships. However, as working fluid needs some heat to become vapour, an RC system is unsuitable for a smaller engine and low loads unless it uses a low boiling point fluid mixture. So the ORC system is appropriate for small cars.

2.3.3 Thermoelectric generator

The thermoelectric generator is a device that generates electric energy when a temperature differential acts at both ends. One significant advantage of TEG is that it is a solid-state device and can produce power directly from exhaust gas through the Seebeck effect. It consists of N-type and P-type semiconductors pallets which are connected in series. Two pallets pair is called a unit or thermocouple (Figure 2-5). These units are further connected in series, up to a suitable number, to form a module (each module usually contains 30-50 units).

Each pallet is connected to the second by an electric conductor, commonly copper. A ceramic insulator encloses the conductor on both hot and cold sides for insulation. The operating temperature determines the pallet material. Such as, it can be bismuth telluride (Bi_2Te_3) for lower, and lead telluride (PbTe) for higher temperature (Figure 2-6). The pallet consists typically of a single material for a moderate temperature range (50 K). However, an optimised combination of different material pallets gives a maximum output (Figure 2-5). For example, for a temperature range of 400 to 700 K, a pallet containing bismuth and lead telluride can be used (Brownell and Hodes, 2014).

The Seebeck effect is a reversible effect which means a TEG can also act as a cooler or heater if a current passes through the thermocouple (Peltier effect). The hot side repels the free electrical charges (electron for N-type and holes for P-type) towards the cold side because it can bear excess electrical carriers on its side. The free charges redistribute themselves under the temperature gradient (differential) due to thermal diffusion (Figure 2-5). At equilibrium, the electrostatic force balances this distribution which is a unique point for each material. The difference in the number of charged particles creates a potential difference between the two sides, and when these sides are electrically connected, the current flows (close circuit).

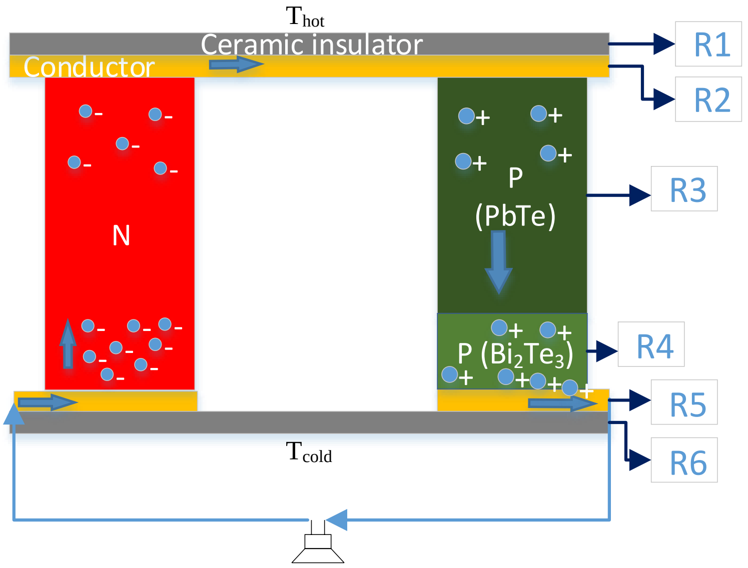

Figure 2-5: Seebeck effect illustration (Wang *et al*., 2011), R is resistance

$$\eta_{TEG} = \left(\frac{\sqrt{1+ZT}-1}{\sqrt{1+ZT}+\frac{T_{cold}}{T_{hot}}} \right) \left(1 - \frac{T_{cold}}{T_{hot}} \right)$$

Equation 2-1: Efficiency of the TEG unit (Pastore, 2010)

Mathematically these effects are described as $dV = a_i dT$ where a is temperature-dependent Seebeck coefficient, V is voltage, i is the type (P or N), and dT is temperature differential. Most of the new research in TEG is related to its segment optimisation and improving the figure of merit (Z) either by increasing pallet electrical conductivity, reducing thermal conductivity, or developing a very high Seebeck coefficient material. For total thermal resistance, R1, R2, R3 …, are added in series and similarly for total electrical resistance.

The *Z* and *T* (*ZT*) product is often used as a criterion to compare different semiconductors. For example, Figure 2-6 shows that PbTe gives a maximum *ZT* value from 600 to 800 K. Meanwhile, Bi_2Te_3 provides its peak *ZT* value from 340 to 390 K. Therefore, Bi_2Te_3 alone is not suitable for a higher temperature region such as a gasoline engine exhaust line. Hence, a segmented pallet is preferable. For instance, if the hot side temperature is 800 K and the cold side is 375 K (Zheng, 2008).

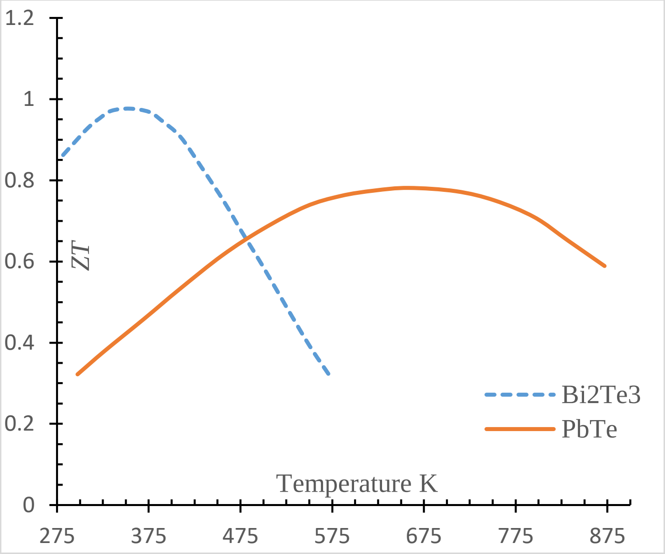

Figure 2-6: The *ZT* graph of two materials vs temperature (Zheng, 2008)

TEG is not that efficient but has a longer operational life (30 years) (Lewis *et al.*, 2005). Its efficiency is around 5-7% with current commercially available materials (Zhang and Zhao, 2015). Commercially available materials have a *ZT* value of 1 or less, but a *ZT* value of 2-3 is required for a cost-effective TEG.

Besides materials properties, a TEG assembly causes many irreversibilities to arise for heat and electrical conductance. TEG pallets have electrical losses ($Power = I^2\mathrm{R}$) due to the current flowing through a conductor. It is called the Thomson effect, where *I* is an electrical current, and R is conductor resistance. Moreover, ceramic insulator coverings increase the thermal resistance of the pallets. Adding a thermal paste between the conductor and insulator will further increase thermal resistance (Stobart, Wijewardane and Allen, 2017). Hence, a lot of research focuses on optimising pallet size, height, thermal resistance, materials and pallets quantity in each module (Brownell and Hodes, 2014).

Thermoelectric generators are suitable for all types of cars due to their modular design. Several studies show that it is installed on small vehicles to large trucks, producing 200 W to 1 kW of power (Arnaud *et al.*, 2014). An eight modules TEG is installed 2 meters away from the engine in an experimental study, depicting the installation after a real car exhaust. The TEG module used in the experiment has a *ZT* value of 0.6 and can produce 13 W power for a 200 K temperature differential. The engine-TEG combination proposes a 7.4% fuel-saving for a bus with a payback time of 6 years (for this laboratory-scale TEG fabrication, 83$ are spent for 13 W output power), and for a car, the payback time would be ten years. Lastly, the authors have neglected the pumping work for coolant delivery to TEG in the fuel-saving analysis (Stobart, Wijewardane and Allen, 2017).

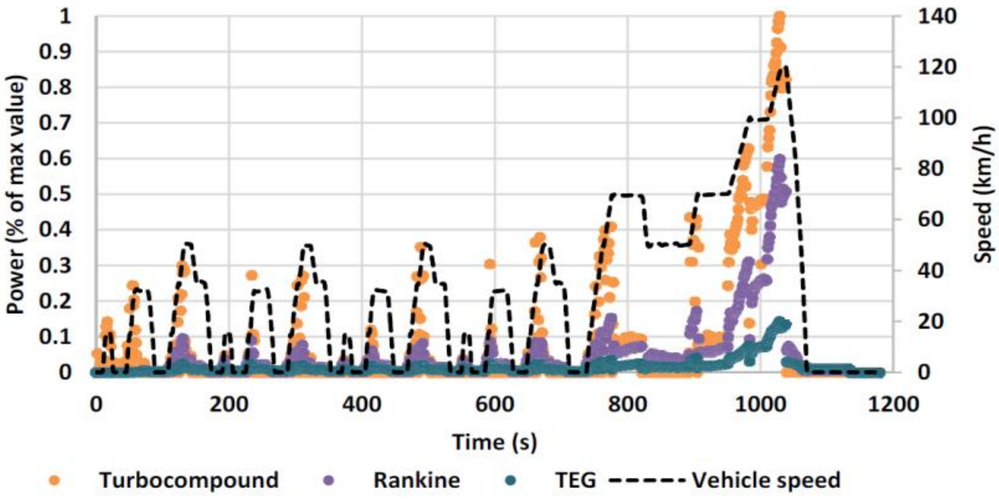

Figure 2-7: a) Different technologies working regimes with the speed profile of the New European Driving Cycle (NEDC) (Arnaud *et al*., 2014)

2.4 A short review on the studied WHR systems

Recovering energy from an automobile improves fuel-saving and CO_2 emissions, enabling a car to meet the EU regulation. Furthermore, the exhaust gases are most suitable for heat recovery due to their higher temperature (775-975 K). However, every technology has its pros and cons, shown in Table 2-2. Though TEG technology is an emerging candidate, it is still not widely adopted as RC and TC. The main reasons are its higher cost and lower efficiency.

Table 2-2: A comparison of these technologies summary from this chapter (Arnaud *et al.*, 2014) (Meda *et al.*, 2016) (Brownell and Hodes, 2014) (Stobart, Wijewardane and Allen, 2017) (Karvonen *et al.*, 2016)

Technology **Parameter**	**Rankine Cycle**	**Turbo-compound**	**TEG**
Cost $/kW	medium	low	high
Usage	Truck	Car, Truck	Truck, Car
Back Pressure	medium	high	very low
W/P kg/kW	8.75	6.25	20.4
Net fuel-saving	3-10%	5-10%	0.5-2%
Challenges	size & weight, working fluid	back pressure	module efficiency, low power, high cost
Advantages	commercialised	compact size, commercialised, high output	silent, life 100k hrs, operate in all phases of NEDC, non-toxic materials, variable array size, orientation free

A turbo-compound gives maximum fuel-saving, but it creates high back pressure. The back pressure is not included in the fuel-saving calculation (Table 2-2). Moreover, this back pressure can also add a burden on engine performance as exhaust gas would re-enter the combustion chamber at the end of the exhaust stroke. This back EGR reduces NO_x but may act as a precursor to particulate matter (PM, fuel droplets adhered to solid particles). Also, it will reduce volumetric and combustion efficiency. Overall, fuel-saving is not the ultimate goal, as emission reduction is also important. Also, the TC can only work during the acceleration phase when engine exhaust pressure is higher upstream of the turbine inlet.

For the Rankine cycle system, the major drawback is the size of the system. The evaporator needs a high heat source like a truck exhaust line. The condenser must expel heat from the working fluid, culminating in an oversized heat exchanger and more pumping load for the pump. Besides that, the expander type varies like volumetric expanders are more suitable for small RC systems. The RC system is active 64% time of the NEDC (New European Driving Cycle) run.

The most significant advantage of TEG is its durability and silent operation. Due to the lack of moving parts, it is nearly maintenance-free. It works during the entire NEDC time, but the power output is insufficient. Temperature dependence means TEG is independent of the exhaust mass flow rate. A significant disadvantage of TEG is the initial cost because of the low weight to power ratio (W/P) and efficiency. Unless there is a widely available commercial material with a *ZT* value higher than 2, TEG is only suitable for special remote applications. Due to higher reliability, its usage includes distant applications like faraway radio towers, space probes, etc. According to the size of the exhaust, a user can adjust the number of modules, so this system gives the flexibility of installation from small cars to large vehicles (Arnaud *et al.*, 2014) (Meda *et al.*, 2016) (Brownell and Hodes, 2014) (Stobart, Wijewardane and Allen, 2017) (Karvonen *et al.*, 2016).

2.5 Fuel reforming processes

The fuel reformer offers several advantages besides capturing waste heat from an automobile. Two of its products include hydrogen and carbon monoxide, known as reformer gas (RG) or syngas. The details are in the following sections, but in short, the RG increases fuel heating value and chemically reduces pollutant emissions. Hence, fuel reforming is selected as a suitable candidate for a WHR system.

2.5.1 The steam reforming

This process is widely used to obtain hydrogen from hydrocarbon fuel (Balat, 2008). The main products of this process are hydrogen, carbon monoxide, besides other products such as carbon, CO_2, and other intermediate radicals. The following equations can describe steam methane reforming and Water Gas Shift (WGS). Here methane is used as a fuel and water as the oxidising agent (Settar *et al*., 2018).

Steam methane reforming	$CH_4 + H_2O \rightarrow 3H_2 + CO$	$\Delta H\ \ 206\ \mathrm{kJ/mol}$
Water Gas Shift	$CO + H_2O \rightarrow H_2 + CO_2$	$\Delta H\ \ -41\ \mathrm{kJ/mol}$
net chemical reaction	$CH_4 + 2H_2O \rightarrow 4H_2 + CO_2$	$\Delta H\ \ 165\ \mathrm{kJ/mol}$

Table 2-3: SMR, WGS and net chemical reaction (Settar *et al.*, 2018)

There are several more sub reactions taking place. For instance, Xu (Xu and Froment, 1989) presented eleven possible reactions during SMR and concluded that the above three could fully describe SMR. In this study, for simplicity, only reaction (a) is considered. The steam to carbon ratio (S/C) is usually kept at 3 to avoid carbon formation on the catalyst site (Yun *et al.*, 2018). Carbon formation can completely cover the catalytic material (reacting material), prohibiting reactants from reaching the catalyst (fouling, Figure 2-8). In addition, carbon can act as an inhibitor and cease some processes such as water activation in the WGS reaction but does not affect CO oxidation. Nonetheless, it will reduce the overall amount of hydrogen produced (Hoshino *et al.*, 2015).

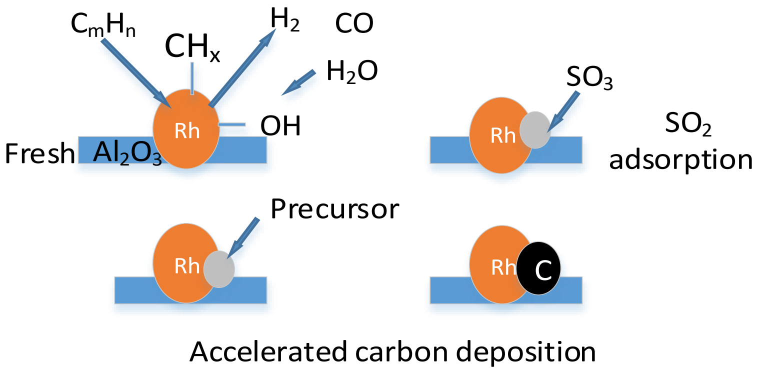

Figure 2-8: Catalyst deactivation due to SO_2 adsorption and carbon deposition (Hoshino *et al.*, 2015)

At lower temperatures, the WGS reaction is favourable as it is exothermic. However, the endothermic reaction proceeds to reactants when the operating temperature rises. Steam reforming is a highly endothermic reaction, so the emphasis is put on the heat exchanger design. On the other hand, increasing the reformer size will increase its thermal inertia and reformer activation time. One prominent advantage of steam reforming is that reactants enter the reformer in higher concentrations like fuel and steam, unlike partial oxidation, which needs air (gaseous mixture with 21% oxygen only) (Farrauto *et al.*, 2003).

An S/C value of 2 or less is good for thermodynamic study or research. Industrially up to 6.5 S/C is used to maintain efficiency. However, using higher S/C increases the reactor size for the same output and fuel consumption to generate steam. Carbon formation occurs at temperatures above 1400 K despite a steam-rich environment (Dalle Nogare *et al.*, 2007). For the SMR reaction, the product composition varies, but it is mainly hydrogen 70–75% on a dry basis, CO (7–10%), CO_2 (6–14%), and including some unconverted CH_4 (2–6%) (Balat, 2008).

2.5.2 Partial oxidation

Partial oxidation (POX) is an exothermic reaction in which fuel is burnt with air over a catalyst to produce CO and H_2. As the partial oxidation process generates heat, so internal heat exchanger is omitted. The exclusion of the heat exchanger reduces the reformer size and makes it suitable for small scale applications. The POX reaction equation is given below.

$$C_mH_n + (0.5)mO_2 = mCO + (0.5)nH_2$$

Equation 2-2: General partial oxidation reaction equation (Pastore, 2010)

The above equation shows that the POX reaction’s drawback is the low H_2 to CO ratio. For methane POX, the H_2 to CO ratio is 2:1. Besides, there is a chance of complete oxidation of the fuel (Fennell *et al.*, 2015). Using air as an oxidant dilutes the product and makes hydrogen separation harder from the mixture (Pastore, 2010).

2.5.3 Autothermal reforming

Autothermal reforming (ATR) is a combination of steam reforming and partial oxidation reforming. The following equation gives the reaction equation. (Peters *et al*., 2018)

$$C_mH_n + (0.5)mH_2O + (0.25)mO_2 = mCO + (0.5m + 0.5n)H_2$$

Equation 2-3: General autothermal reaction equation (Pastore, 2010)

Carbon can form by various methods in all kinds of fuel reforming. In an ATR study, two reactions account for carbon formation by keeping the S/C ratio at 1.9. The first one is dependent on the mutual oxidation of two carbon monoxide molecules and the second one is pyrolysis of the feed fuel (Peters *et al*., 2018).

$$\text{(a) } 2CO = CO_2 + C \text{ , (b) } C_nH_m = \frac{m}{2}H_2 + nC$$

Equation 2-4: a) Boundourad reaction b) pyrolysis (Peters *et al*., 2018)

ATR catalyst is designed so that POX reaction occurs first, which raises the reactor temperature. Down the reformer, the catalyst type changes to perform the steam reforming reaction. Though no external heat is required as POX provides the necessary heat, still preheated steam must feed the SMR reactor. POX reaction heat release (operating temperature 1025 K) can integrate with the steam generation, which otherwise may get wasted in a simple POX reaction (Pastore, 2010).

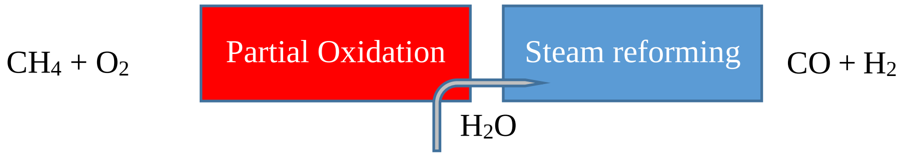

Figure 2-9: A general description of the autothermal reforming process (Pastore, 2010)

Another substantial advantage of ATR is its start-up time due to internal heat production and less thermal inertia. Theoretically, by utilising heat to make steam in a closed-loop configuration, an ATR catalyst can achieve 80% efficiency (Docter and Lamm, 1999).

2.6 Reformer gas applications

2.6.1 In fuel cell

A fuel cell has the potential to replace IC engines, especially passenger’s cars. The fuel cell’s main advantage is its higher efficiency (40-80%) than conventional combustion engines. Compared to the Otto cycle (Figure 1-3) machines, it is not limited by the Carnot efficiency $\left(1 - \frac{T_{cold}}{T_{hot}}\right)$ as it is an electrochemical device that converts chemical energy to electrical energy. Several fuels like methane can act as feed, and the generated electricity (output) may drive a pure electric or hybrid car. Other advantages of a fuel cell are:

- No or extremely low emissions of pollutants
- Silent operation
- A simple process of converting chemical energy to electrical (Agnolucci, 2007)
- Act as a stable continuous power source if it is receiving fuel and oxidiser from the tank. So it is not like a battery that stores energy and may give power fluctuation
- Fuel flexibility (Song, 2002a)

The fuel cells vary in operating temperature, structure, fuel type, and efficiency. If a heat recovery system integrates with the FC, the efficiency can reach 70 to 80 per cent. A summary of different fuel cells is given in Table 2-4.

Table 2-4: Some fuel cell types and their characteristics (Song, 2002a)

Parameter	Proton exchange membrane fuel cell (PEMFC)	Phosphoric acid fuel cell (PAFC)	Solid oxide fuel cell (SOFC)
Operating temperature	345-355 K	455 - 495 K	1075-1275 K
Fuel	H_2	H_2	H_2, CO
Charge carrier	H^+	H^+	O^{+2}
Poison	Sulphur, CO	Sulphur, CO	Sulphur
Heat generation	None	Low	High
Cell efficiency	40-50%	40-50%	50-60%
Catalysts	Platinum (Pt)	Platinum (Pt)	Nickel (Ni)

Proton-exchange membrane fuel cell (PEMFC) is 40-50% efficient, and its most significant advantage is its operating temperature (345-355 K). It can be added as a heat recovery device to an IC engine as it doesn't generate heat itself. PEMFC is susceptible to carbon monoxide (>10 parts per million (ppm)) that is poisonous for its operation. Therefore a PEMFC cannot be used alongside an FR catalyst unless some CO absorption technique is used at the FR outlet.

Solid oxide fuel cell (SOFC) can use hydrogen and CO as its fuel, but its operating temperature is very high (1075-1275 K). Hence, SOFC can provide a heat source for the WHR devices. Another advantage is its nickel catalyst which is way economical than platinum. The phosphoric acid fuel cell is another fuel cell whose features are similar to PEMFC (Song, 2002a).

The major disadvantage of adopting an FC is that there is still no widespread hydrogen distribution network. There is no suitable desulphurisation technique for the onboard hydrogen generation that can remove sulphur to a practical input level of an FC (<0.1 ppm). So sulphur removal from the fuel occurs at the refinery. Another thing is the cost of the fuel cell, which is considerably higher than IC engines. Theoretically, fuel call can achieve 70-80% efficiency if the generated heat accompanies heat recovery, like in the case of SOFC (Song, 2002a) (Song, 2002b).

2.6.2 In IC engines and exhaust pipeline

2.6.2.1 Combustion control

The HCCI (homogenous charge compression ignition) method reduces NO_x and particulate matter by operating at lean engine conditions at a lower temperature. Diesel fuel is very reactive that auto ignites during high compression pressure produced in a compression ignition engine. Mixing diesel with reformer gas changes the combustion characteristics of this mixture. Hence, the RG ratio in diesel fuel controls the HCCI regime, which is needed as HCCI parameters vary with engine speed and load. Reformate exhaust gas recirculation (REGR) is a combination of EGR and RG. A rich fuel mixture of REGR and diesel feeds the combustion chamber to prevent knock by offering smoother combustion (Figure 2-10b).

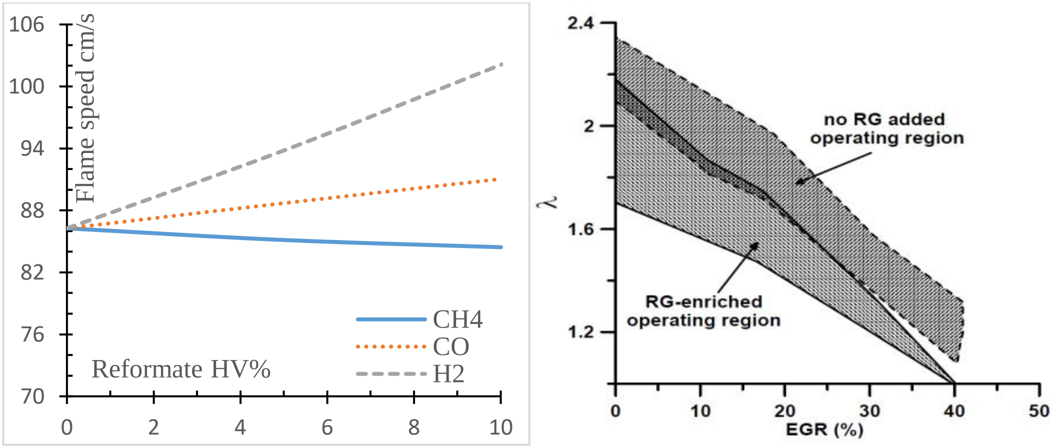

Figure 2-10: a) Flame speed of different compound (HV heating value) (Ashida *et al.*, 2015) b) Effect of RG enrichment on HCCI operating region (Hosseini and Checkel, 2007)

Similarly, only EGR is used for leaner combustion. H_2 is a stable molecule, so reformer gas slows down the heat release, which means smoother combustion for a long duration. Overall it means that the reformer gas and EGR variation (in the air-fuel mixture) can control the HCCI process effectively (Hosseini and Checkel, 2007).

Hydrogen also improves combustion speed (see Figure 2-10a), resulting in fast combustion (closer to the ideal one) (Ashida *et al.*, 2015) (Hoshino *et al.*, 2015). The fast ignition is due to hydrogen's high flammability as just 4% hydrogen by volume mixed with air creates a combustible mixture (Balat, 2008).

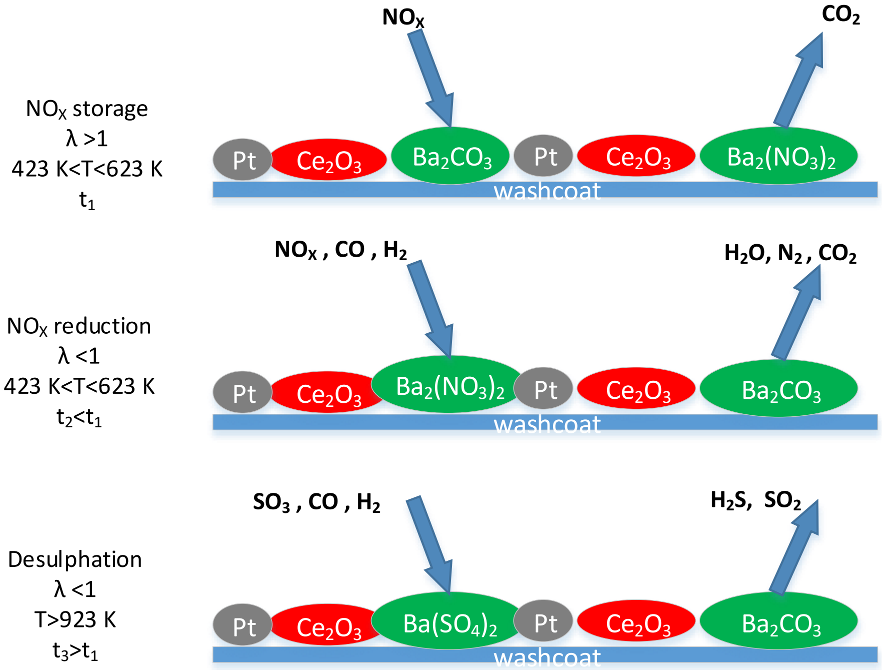

Figure 2-11: LNT catalyst regeneration and de-sulphation (Wetzel, Mccarthy and Griffin, 2010)

2.6.2.2 Catalyst regeneration

Hydrogen and carbon monoxide can de-sulphate (Figure 2-11) the Lean NO$_x$ Trap (LNT) catalyst besides oxidising unburnt hydrocarbon (Wetzel, Mccarthy and Griffin, 2010) and thus regenerate the catalyst.

Whereas CO, from the syngas, reduces combustion temperature due to higher specific heat capacity, decreasing nitrous oxide formation. CO reacts with already formed nitrous oxide to reduce NO$_x$ emissions, as depicted in Equation 2-5 (Wetzel, Mccarthy and Griffin, 2010).

$$2CO + NO_2 \rightarrow 2CO_2 + \frac{1}{2}N_2$$

Equation 2-5: Carbon monoxide attack on nitrogen dioxide (Wetzel, Mccarthy and Griffin, 2010)

Hydrogen and carbon monoxide can aid in diesel particulate filter (DPF) regeneration also. In a study performed (Hemmings, 2012), hydrogen is introduced in the exhaust stream for ignition to raise the DPF temperature. The rise in temperature makes oxidation easy for the accumulated carbon, so supporting the DPF regeneration process.

2.6.2.3 Emissions reduction

Hydrogen addition, before the diesel oxidation catalyst (DOC), limits harmful engine emissions. A study conducted on heavy HC species (carbon number varies from C_5 to C_{11}) such as isooctane, toluene, methyl-naphthalene, and so forth reveals that hydrogen addition improves three-way catalyst efficiency. It is effective for heavier and oxidation-resistant compounds like naphthalene and methyl-naphthalene. The catalyst achieves 100% efficiency for these HCs due to hydrogenation and temperature rise. The quantity of hydrogen added is 2200 ppm for 1200 ppm of these PAHs (Hasan *et al.*, 2016).

In an older study, a POX reactor was used for a gasoline engine. Reformates generated from the reformer, operating at equivalence ratio 1, reduce 75% of the HC emission than the baseline gasoline engine fuel at the cold start (Kirwan, Quader and Grieve, 2002). The equivalence ratio is the fuel-to-air ratio divided by the fuel-to-air ratio at stoichiometric conditions.

The effect of REGR on PM emission is miscellaneous. For instance, the introduction of REGR into the engine caused oxygen dilution that promotes PM production due to probable incomplete combustion. At the same time, the higher specific heat capacities of water and CO_2 reduce the PM formation. Overall, REGR reduces the PM emission more than EGR alone, especially when the soot fraction is higher. Also, REGR reacts with PM matter of all sizes, whereas EGR reduces mainly larger PM particles and is less efficient than REGR. Overall a 40% reduction in PM emission is achieved due to the physical (thermal and dilution) and chemical properties of REGR (Bogarra-Macias *et al.*, 2015).

2.6.2.4 Increasing fuel heating value

In a close loop onboard fuel reformer study by Leung *et al.*, rhodium (Rh) monolith catalyst is used with cerium and zirconium oxides. Converting half of the fuel to RG and adding it to the fuel supply, the authors show theoretically that 9.4% of fuel-saving is achievable (at 1225 K) (Figure 2-12) as both CO and H_2 have higher energy content than the parent fuel. The studies are carried out at lower engine rpm (revolution per minute) because the reformer efficiency may suffer from higher exhaust gas velocity entering the reformer at high rpm.

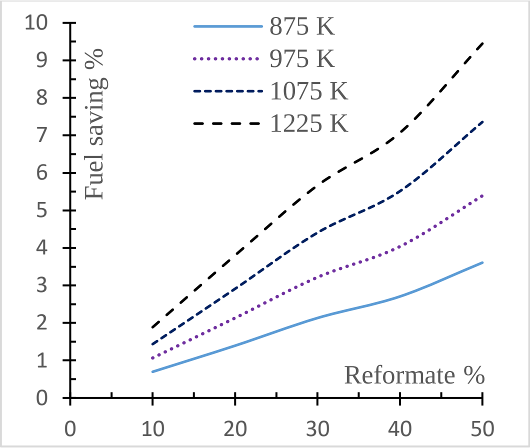

Figure 2-12: Percentage of reformate added in IC engine by converting that percentage of fuel into reformate by an onboard fuel reformer (Leung *et al.*, 2018)

Figure 2-12 shows the fuel economy improvement when a portion of gasoline fuel is replaced by reformers gas, produced at various operating temperatures in a fuel reformer. There is a higher conversion (reformate quality) to H_2 and CO with the temperature rise. However, a higher reformate quality is not necessary for the fuel-saving application. A critical part of the experiment is that the authors have used simulated reformates from gas cylinders to assess fuel savings (Leung *et al.*, 2018).

Similarly, for CI engines, a reforming catalyst uses diesel fuel and EGR containing oxygen and steam. The reformer is thermally integrated with the engine, and the authors suggested that improvement in design and fuel vaporisation will increase the reformer efficiency further. Overall the reformer achieved a 38% fumigant energy fraction, defined as the ratio of energy provided by the reformates over total diesel fuel energy (Hwang, Li and Northrop, 2017).

2.6.3 Miscellaneous usage

In summary, hydrogen is widely used in the industry besides in the automotive sector. Nearly half (49%) of the hydrogen produced worldwide is used to create ammonia to make fertilisers. For crude oil refining, almost 37% of the world hydrogen is consumed. Other hydrogen uses includes:

- Hydrogenation reaction, e.g. of mineral and edible oils
- Chemical and food industry
- Medical industry
- Gas to liquid (GTL), such as making liquid fuel from methane
- Fuel cell (Dupont, 2007)

2.7 Catalyst structure

Every chemical industry utilises catalysts such as the food industry, treatment plants, and so forth. Nearly 85-90% of the chemical products are formed through catalytic reactions (I. Chorkendorff, 2007). It assists a chemical reaction in feasible temperature and pressure conditions, thus offering a favourable energetic path. In automobiles, several catalysts are used, such as DOC, to oxidise unburnt hydrocarbon. Then come the LNT and SCR (selective catalytic reduction) catalysts to reduce nitrous oxide emissions and an optional FR catalyst to provide syngas. Last on the exhaust line is a DPF that collects and oxidises the accumulated soot. The catalyst cell shape, size, and type vary according to application. Most of the catalysts used in automobiles are heterogeneous, where the catalyst consists of solids and reactants are fluids.

Heat and mass transfer to a fuel reformer is essential for its endothermic reactions. There is no single design for an FR catalyst, and hence, the research on catalyst substrate design for reforming is very active (Tomas, 2006) (Tartakovsky and Sheintuch, 2018).

2.7.1 Basic catalyst functioning

A commercial catalyst should provide three functions: ease of reactants flow, high catalytic activity, and stability. The channel is the cell extension along the length, normal to cell face (or channel face). Its size and shape are designed according to operating conditions like fluid speed, mass flow rate, pressure drop, etc. Catalytic activity is governed by the reacting material and accessibility of the reactant to the catalyst site. Ceramic carrier pore size changes the surface area, which should be higher for higher reactivity. The stability is dependent on the catalyst resistance to; poisoning (permanent adsorption of unwanted chemical compound), sintering (large catalyst crystal formation, thus reducing surface area), and fouling (pores blockage by a neutral element like carbon or carrier) (Richardson, 1989). Stability also includes the mechanical strength of the structure (metallic or ceramic substrate).

Under the right conditions, reactants form products through the following steps (Fogler, 2020):

- Reactant(s) movement (mass transfer) from the bulk fluid to the carrier surface through the fluid boundary layer
- Some parts of the reactants diffuse from the surface to the carrier pores
- Chemisorption of reactants to the catalyst surface
- Chemical reaction

- Desorption of the products from the catalyst surface
- Diffusion of the products from pores to the carrier surface
- Diffusion of the products into the bulk gas from the boundary layer gas present at the carrier surface

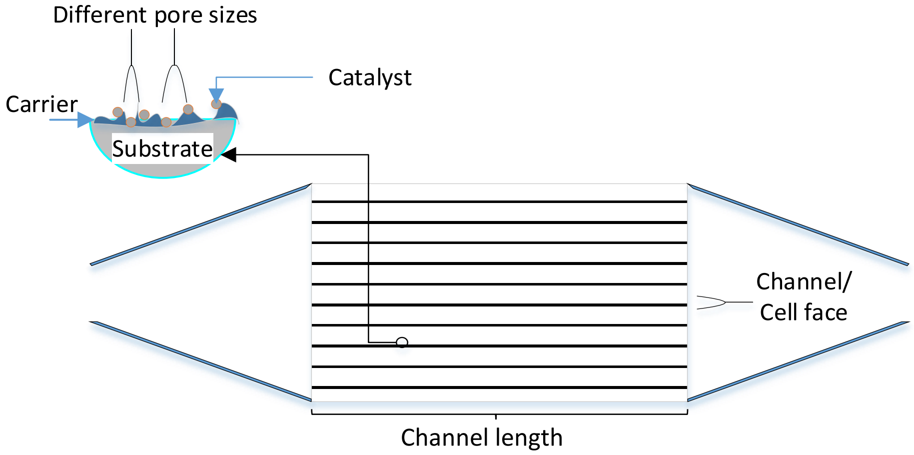

Figure 2-13: A typical monolith channel surface containing substrate (structure), carrier or washcoat, and catalyst crystals. Note: Not to scale (I. Chorkendorff, 2007)

2.7.2 Substrate and washcoat

The whole assembly is known as the catalyst, although the actual material for catalysis has a small fraction. A typical catalyst contains a substrate acting as a support structure where a washcoat (also called 'carrier') is adhered containing reacting material. Monolith, foam, tube, pallets, etc., are types of support structures. Metal oxides mainly serve as washcoat, and their primary purpose is to act as a binder between the substrate and reacting material.

The substrate can be ceramic or metal. A ceramic monolith is made from extruding ceramic slurry from a mould and then drying it. In contrast, metal monoliths are made by joining straight and corrugated metal panels. These panels are then folded and encapsulated in the cylindrical container (I. Chorkendorff, 2007) (Tomas, 2006) (Richardson, 1989).

The washcoat or binder is usually made of ceramics, e.g. alumina (Al_2O_3), ceria (CeO_2), and zirconia (ZrO_2), to name a few. It increases the specific surface area besides acting as an adhesive material. A typical monolith has a 2 m^2/g specific surface area (Tomas, 2006), while with a washcoat, it grows more than 40 m^2/g (Sanz *et al.*, 2016). The monolith wall in both cases is non-porous, so no inter-channel mass transfer occurs, but heat transfer. There are other differences between these two materials, which are explained in the following section.

2.7.3 Ceramic or metal substrate

Radial heat transfer in ceramic monolith occurs by conduction which is negligible as ceramics are bad heat conductors. The brittle nature of ceramics makes it prone to cracking under any kind of stress, like thermal stresses. However, ceramic monoliths can be of very high cell density (cpsi, cells per square inch). The metallic monoliths walls are thinner than ceramic walls due to higher mechanical strength. Also, metals are excellent heat conductors, so both radial and axial heat flow occur through conduction. Metal monoliths can also have 'passive channels' for the inter-channel mass flow, absent in ceramics monoliths formed by the extrusion method (Tomas, 2006).

Table 2-5: Properties of 400 cpsi Emitec metal and ceramic monolith catalyst (Tomas, 2006)

Properties	Ceramic	Metal
Wall thickness (mm)	0.1–0.3	0.04–0.05
Geometric surface area (m^2/m^3)	2800	3700
Thermal mass at 473 K (J/kgK)	699	490
Open area percentage	75.0	89.3

2.7.4 Dispersed precious metal

Precious metals like platinum (Pt) and rhodium (Rh) are sometimes used in fuel reforming processes to give a better yield. Adding Rh increases the catalyst resistance to sulphur adsorption (Fennell *et al.*, 2015). Lanthanum addition improves water activation for the steam reforming reaction. 'Sulphur poisoning' can also be reduced by adding a silica solution binder to prevent sulphur compounds from accessing the catalyst site (Hoshino *et al.*, 2015).

As these catalysts contain rare earth elements, they are dispersed throughout the carrier surface for cost reduction. For instance, for a REGR reformer, Fennell *et al*. use a ceramic mixture of 220 μgmm^{-3} density to paste it on 0.144 dm^3 of the plate. The mixture contained just 4% of reacting material (Pt+Rh) by weight. Similarly, in another study, 4% by weight Rh is used in the catalyst/ceramic mixture (Rh/Al_2O_3) for REGR (Hoshino *et al.*, 2015).

Another form of the dispersed catalyst is small solid particles embedded with the carrier containing reacting material. These particles fill in a cylinder forming a plug flow reactor. For example, in a shell and tube reactor for methane steam reforming, different tubes of various sizes (9-19 mm in diameter) are filled with small (3-5 mm) balls containing a blend of Rh and alumina (2% weight Rh/α-Al_2O_3) (Yun *et al.*, 2018).

2.7.5 Possibility of a pure catalyst structure

A complete reacting material can also be used for steam methane reforming, such as a thin Ni metal layer. Nickel is cheaper than precious metals (Pt, Rh) and is widely used as a catalyst in reforming reactions, especially in petroleum refining. However, compared to noble metals such as Pt, Rh, and Ru (ruthenium), nickel is less active and prone to coke formation. Still, Ni is comparatively abundant and economical. If the temperature of the reforming reaction is increased (1000-1300 K), nickel sintering occurs, especially for a dispersed catalyst (Richardson, 1989).

Sintering and coke formation are two main catalyst deactivation phenomena in reforming reactions (Abdullah, Abd Ghani and Vo, 2017). However, pure reacting material usage hasn't been found in the literature review without any carrier.

2.7.6 Metal foam substrate

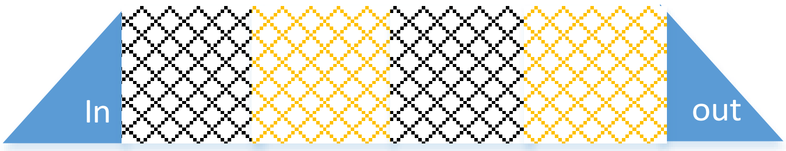

Figure 2-14: Macro patterned methane steam reformer with alternating inert (grey) and catalyst (yellow) metal foam (Pajak *et al.*, 2018)

Metal foam can also act as a substrate, like Ni/YSZ foam (nickel and yttria-stabilised zirconia). A macro-patterned catalyst is studied for methane steam reforming, where alternate steel and Ni/YSZ metal foams are used (Figure 2-14). The upper reactor wall is at constant temperature and equal to the inlet temperature of the reactants (1100 K). The lower wall is set as symmetry. The details of segmentation are given in Table 2-6.

Table 2-6: Macro-patterned catalyst with different number of catalyst and inert segments (Pajak *et al.*, 2018)

Design	**Length m**	**Radius mm**	**Catalyst seg**	**Inert seg**
Base	0.3	50	1	0
Case 2a	0.3	50	6	5
Case 3a	0.6	50	6	5

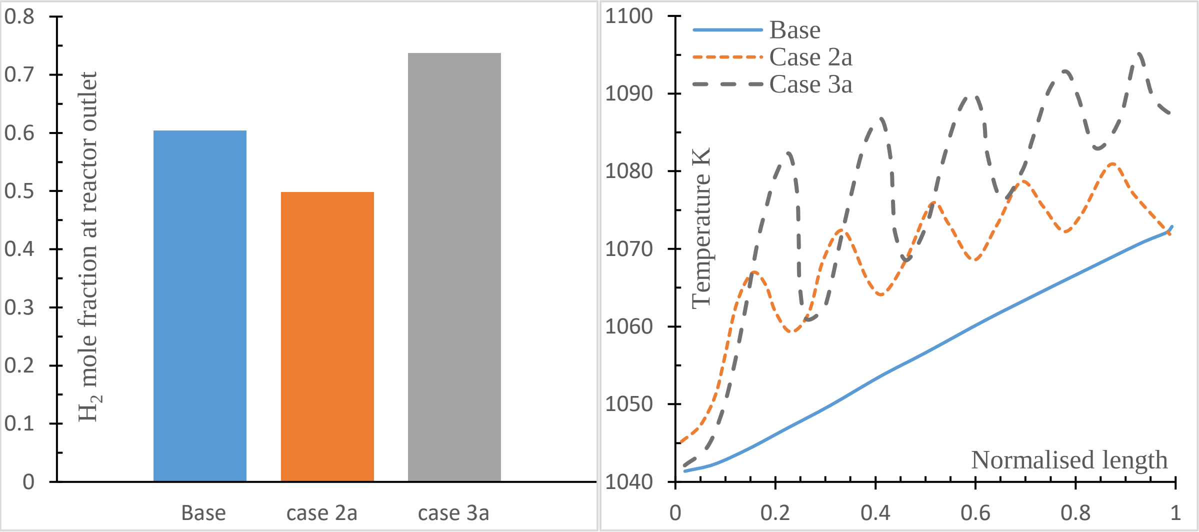

Figure 2-15: a) Hydrogen mole fraction at the outlet of the macro-patterned reactor, b) average temperature along the reactor length (Pajak *et al.*, 2018)

The authors' results show that segmentation improves the hydrogen yield. Catalyst 2a outlet mole fraction is 18.5% less than the base case even though half of the length is inert. Catalyst 3a shows a 12.3% improvement than the base case while having the same amount of catalyst.

The base case has a near-uniform temperature increment, whereas it fluctuates around 20 K for case 3a (Figure 2-15b). Variable temperature can be detrimental to the system life due to the nonuniform formation of thermal stresses. The higher efficiency is attributed to the reactants retaining heat, especially at the start of the catalyst (Pajak *et al.*, 2018).

This paper gives the importance of segmentation and heat transfer for the steam reforming reaction. Moreover, it shows that highly porous (0.85) metal foam can act as a substrate. However, the authors have used longer lengths to include the same amount of catalyst. This option is sometimes not viable for contesting space in a car.

2.8 Structural variation effect on catalyst efficiency

The size of the reformer varies according to application. Industrially, hydrogen is produced from natural gas in the shell and tube reformer. The tubes containing nickel catalyst ranges from 10-12 m (Jones *et al.*, 2008). Onboard fuel reformers can be small, such as 13 mm in length (Hoshino *et al.*, 2015). Similarly, combined heat and power (CHP) systems have an intermediate size like 420 × 90 mm^2 for household applications. A CHP unit generates electricity and heat from a fuel cell using hydrogen produced from a fuel reformer (Sigurdsson and Kær, 2012). So structural variations can be helpful but application dependent.

2.8.1 The gap between the wall and the catalyst

Steam reforming reaction is highly endothermic, so efficiency is dependent on heat transfer. Therefore, catalyst design becomes very critical.

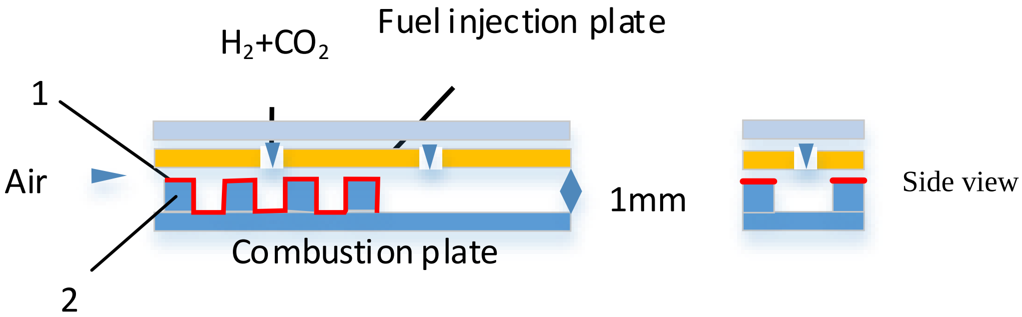

Figure 2-16: An illustration of combustion channel of an integrated FR unit with catalyst layer (1), protuberance (2) (Nagano *et al.*, 2002)

An integrated combustion and reformer unit is tested for methanol-reforming. The catalyst layer thickness is 50 microns, containing 10% Pt in the Al_2O_3 washcoat. The catalyst is pasted on the small sinusoidal square substrate to improve the thermal efficiency and provide a surface acting as a flame holder. The square is called protuberance, and this study terms this as a protrusion. After examining several heights (h) of these protrusions, h equal to 0.75 mm is found optimum for thermal efficiency. These squares also generate micro swirls for mixing the combustion mixture. Overall, protrusion changes the cell or channel height (*H*).

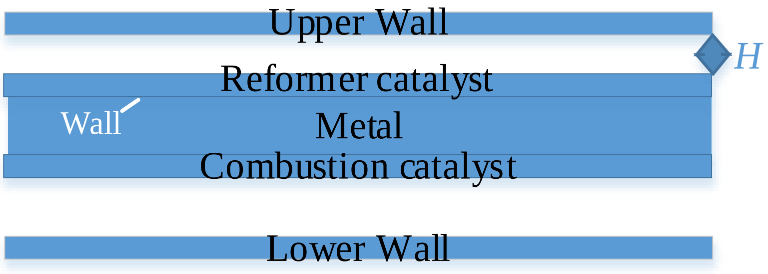

Figure 2-17: A CPR catalyst description (Zanfir and Gavriilidis, 2003)

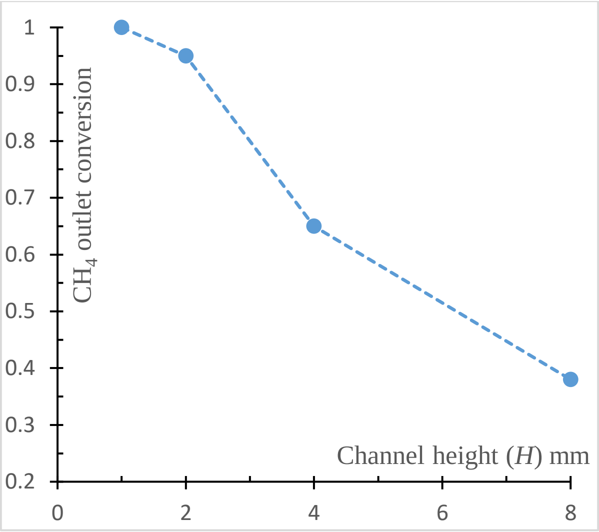

Figure 2-18: Outlet methane conversion vs channel height at constant inlet velocity (Zanfir and Gavriilidis, 2003)

The 95% combustion efficiency range improves from a 4-6 air ratio for h equals 0 mm, to a 2-10 air ratio for 75% h. Here, the air ratio is defined as the air volume flow rate to the fuel volume flow rate. Air ratio extension expands the combustion regime. The authors also suggest alternating catalyst layering to improve thermal efficiency (Nagano *et al*., 2002).

Similar observations come from another catalytic plate reactor (Figure 2-17). Methane burns in the lower channel at the combustion catalyst, and then heat travels to the reformer catalyst by conduction through the in-between metal. The channel height is changed by moving the wall away from the catalyst. Due to equivalent inlet velocity, *H* growth means that a large mixture quantity consumes the same amount of heat (Figure 2-18), turning the catalyst quantity insufficient. In addition, this decreases the bulk mass transfer from gas to catalyst position. Overall, the *H* rise reduces the methane conversion (Zanfir and Gavriilidis, 2003).

The channel height will further be studied as it seems a significant factor. However, a method would be sought, so that cell height remains unaffected. In this way, a channel height can change but does not affect the cell density. The protrusion can be a viable option for the height variation.

2.8.2 Segmentation

In a catalyst segmentation study compared to a continuous catalyst, the authors show that 66% of the combustion catalyst is saved. The metal plate separates two parallel channels of fuel reforming and combustion. The ceramic catalyst thickness is 0.02 mm with its porous material properties (Mundhwa and Thurgood, 2017).

Figure 2-19: Continuous combustion catalyst vs segmented catalyst (green) (Mundhwa and Thurgood, 2017)

A similar study by Jeon *et al*. shows that having a segmented catalyst reduces hot spots for the combustion catalyst. The continuous catalyst offers nonstop combustion, which raises the temperature at the inlet side. However, breaking it to optimum numbers offers numerous combustion spots, which in return distribute the heat. In this way, the localised temperature remains below the dangerous level (Jeon *et al.*, 2013).

Figure 2-20: a) Segmented catalyst b) continuous catalyst (green), (isothermal walls are red) (Settar, Nebbali and Madani, 2015)

Dr Settar and his team investigate the SMR performance for segmented and continuous catalysts. The walls are isothermal, having a high enough temperature for the SMR reaction. The reaction rate increases as the fluid mixture regain heat from the isothermal segments. As a result, the segmented model shows nearly 44% more methane conversion than the continuous one. The authors also investigate the performance of the FR reactor by inserting metal into the channel. Segmentation with a metal foam setting gives a slightly better yield than before. Any coupling of metal foam with the wall is not mentioned. In short, segmentation drastically improves the reformer output compared to the continuous catalyst (Settar, Nebbali and Madani, 2015).

This section has shown that catalyst segmentation overwhelmingly improves reactant conversion. So segmentation will be a must choice in this study. Moreover, Dr Settar and his team successfully defragment the catalyst without changing the channel length.

2.8.3 Inter-channel mass and heat transfer

Compared to the previous cases where flow remains exclusively in a single channel, a 1.5 mm high corrugated assembly is employed in a study for high inter-channel mass and heat flow.

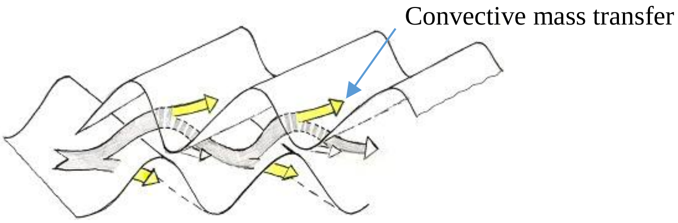

Figure 2-21: The corrugate metal panels showing fluid movement through the structure and passages (Mucha, Gaiser and Kuehnle, 2008)

Corrugated metal foam sheets are stacked together to form this catalyst. The angle between the flow and the sheets determines the orientation. If this angle is 90°, then the corrugate channels are parallel to the flow. The fluid can flow through the porous structure besides passing through the in-between passages, formed by the upper panel troughs resting on the lower panel crests (Figure 2-21).

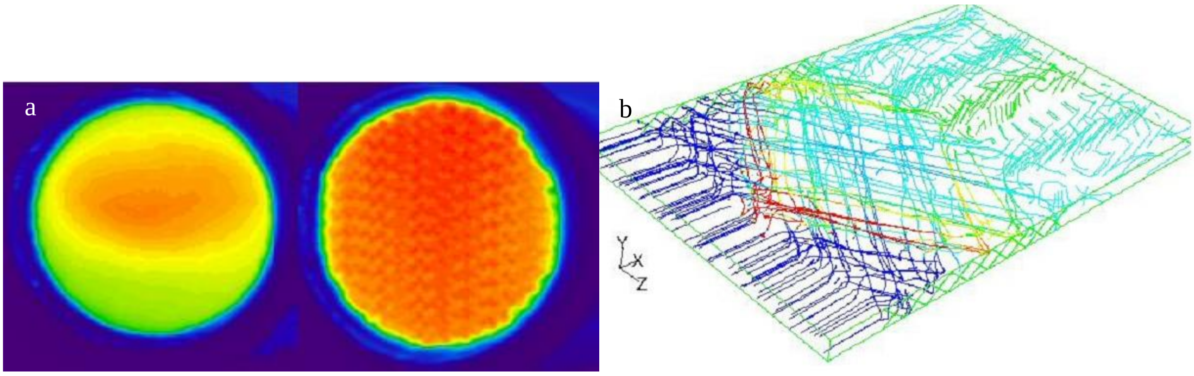

Figure 2-22: a) Outlet temperature at a defined load for ceramic monolith and metal foam corrugate b) pathlines of fluid showing mixing of flow (Mucha, Gaiser and Kuehnle, 2008)

This convective mass transfer through the metal foam corrugate improves the reaction compared to the conventional monolith catalyst, where only pore diffusion allows the fluid to reach the reacting material. Thus this construction also enables higher uniformity and residence time (Figure 2-22b). However, the tested ceramic monolith (3.6 kJ/K, 0.6 mm, 400 cpsi) and metal foam corrugate (1.7 kJ/K, 1.5 mm, 20 cpsi) have different thermal mass, cell height and density, so light-off, conversion efficiency, and pressure drop are not standardised.

Nonetheless, the metal foam corrugate attain a higher temperature than the ceramic monolith for the same operating time because of lower metal heat capacity. But the more important thing is the uniform temperature distribution across the metal foam corrugated cross-section (Figure 2-22a).

The pressure drop for the monolith rises steadily with the mass flow rate, whereas it grows slowly for the corrugate and remains lower until a higher inlet flow rate. Afterwards, it rises rapidly and crosses the monolith pressure drop line (Figure 2-23a). CO conversion of the ceramic monolith is reported in Figure 2-23b for various engine conditions. It is higher for the monolith due to higher cell density which means a higher surface area is available for the reaction. However, the conversion behaviour favours metal foam corrugate at a higher flow rate and temperature (Mucha, Gaiser and Kuehnle, 2008).

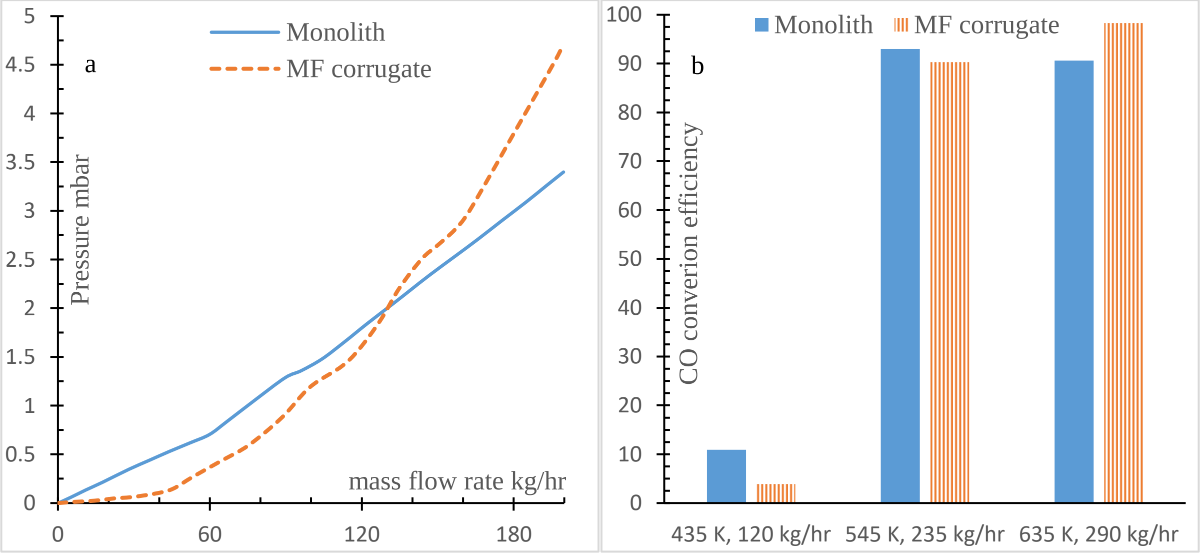

Figure 2-23: a) The pressure drop vs mass flow rate b) CO conversion efficiency of a DOC for different designs (Mucha, Gaiser and Kuehnle, 2008)

The Emitec industry has introduced several designs which improve cross-channel flow. These catalysts serve diverse applications. For instance, the LS (longitudinal structure) design is suitable for a DOC catalyst, whereas the LSPE (longitudinal-perforated) Metalit and MXPE (mixing-perforated) Metalit assist SCR catalyst better.

For the standard substrate, the flow is turbulent when it enters the channel but quickly gets streamlined due to the channel boundary. The laminar flow acts like a one-dimensional flow. Hence, the fluid going downstream interacts less and less with the catalyst at the wall.

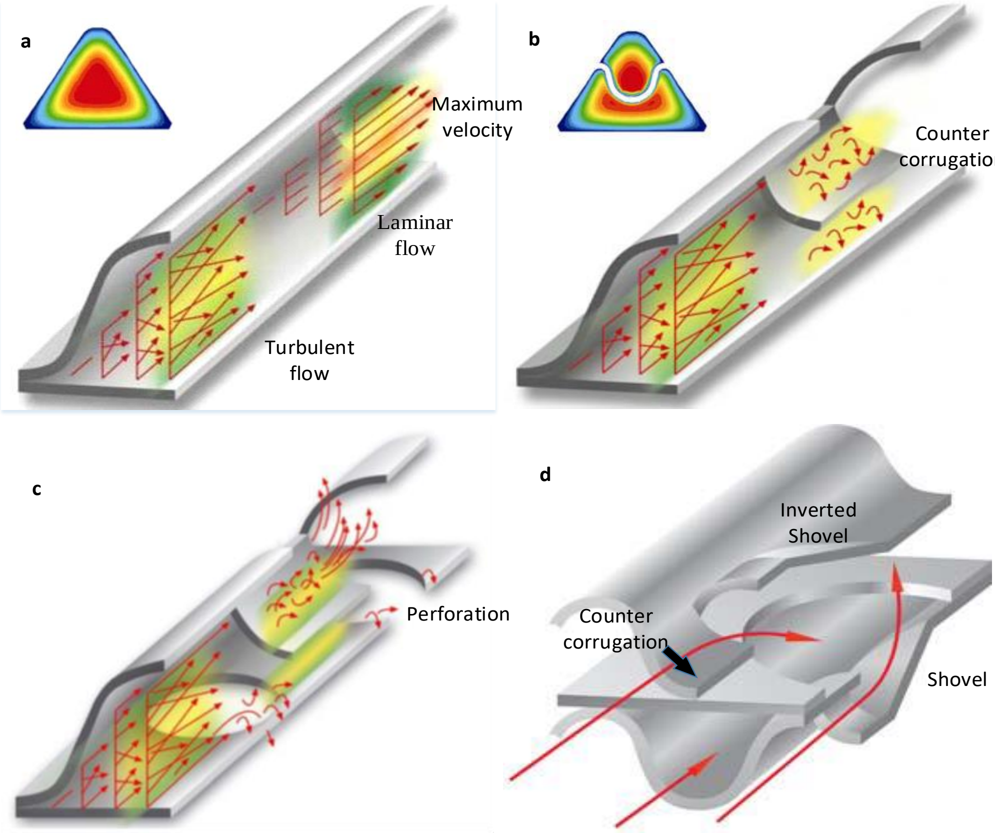

Figure 2-24: a) Standard Metalit b) LS Metalit c) LSPE Metalit d) MXPE Metalit (Rice *et al.*, 2007) (Subramaniam *et al.*, 2011)

Introducing a counter groove in the middle (LS Metalit) increases flow mixing and cross channel flow. The mass flow rate is directly proportional to the fluid velocity for the incompressible flow, which is highest at the middle of the channel. Catalysing counter corrugation surface increases efficiency as it receives the maximum reactant mass concentration at that cross-section (Figure 2-24b).

Puncturing a hole in the channel lower wall further increase the inter-channel mass and heat transfer (Figure 2-24c). Now three channels (LSPE) can interchange heat and mass at positions where counter corrugate and perforation are made.

Besides folding the corrugation, shovels like structures (MXPE Metalit) can also push the fluid upwards or downwards (Figure 2-24d). Hence, these shovels can guide the flow to regions of interest. Extending the perforation to the neighbouring channel allows the fluid to mix with the side channels. These large holes enable the fluid starting from a single channel to travel all along the catalyst cross-section.

The LSPE substrate advantage for SCR is visible in Figure 2-25a. NO_2 is a crucial compound for NO_x conversion to N_2. This substrate produces more than 24% NO_2 than standard metalit, aiding the NO_x's selective catalytic reduction. The perforations, counter corrugations and shovels are optimized according to the application. The increased efficiency means that either a smaller catalyst or less reacting material is appropriate for the same performance (Rice *et al.*, 2007; Subramaniam *et al.*, 2011).

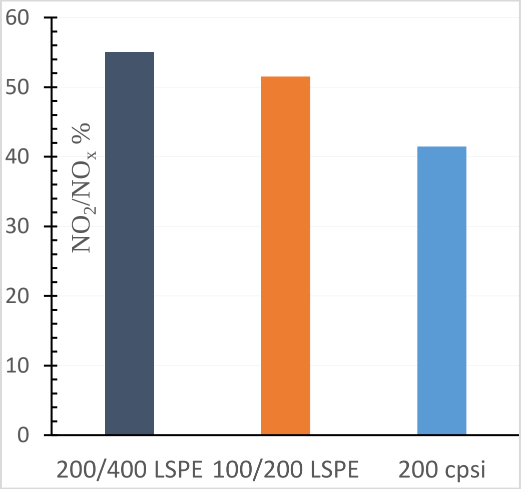

Figure 2-25: NO_2/NO_x percentage at 573 K at 100,000 1/h space velocity (Rice *et al.*, 2007)

The inter-channel mass flow gives higher conversion efficiency, uniform temperature distribution and longer fluid path. It will further be studied and included in the FR design.

2.9 Research path

Power plants and transport sectors are still heavily dependent on fossil fuels. Though electric cars do not release HCs emissions like an IC engine, yet these contribute to carbon emissions by using electricity from those power plants. A WHR system can improve the fuel economy of a car.

Some options like turbo-compound, Rankine cycle, thermoelectric generator, and fuel reformer can be viable for such systems. However, a TC mainly works when a car is accelerating, which is not always the case. An RC system requires more space, like a dedicated radiator, so it is not suitable for small cars in general. TEG offers long operational life, but its higher cost to power ratio hinders its widespread usage.

An onboard FR recovers heat besides improving combustion characteristics and reducing emissions. Furthermore, unlike a fuel cell, an FR does not need good quality syngas in large amounts, which removes any purification devices. Therefore, the FR is a preferred choice for the WHR device.

Three structural changes significantly affect catalyst efficiency. First, it is channel height which needs to be smaller for higher efficiency. The challenge would be to vary it without touching the cell design. Incorporating a protrusion in the channel can change the height.

Then comes the catalyst segmentation and its pattern. The protrusion choice has not been finalised, but the segmented catalyst should not be longer than the base design. The engine compartment is a tightly packed area with little extra room. If the new catalyst is longer than before, that may lead to compartment redesigning.

The flow guides like shovels and corrugation also allow fluid mixing and heat distribution, increasing catalyst performance. Protrusions can also act as flow guides. However, out of the three, the segmentation significantly improves catalyst efficiency.

Lastly, it is to introduce passive channels in an already existing design. Passive channels like perforations promote inter-channel flow, thus improve; temperature, mass distribution and catalyst performance. It also increases the mean fluid path in the catalyst that increases the reaction probability. Overall, cross channel flow is beneficial, and the goal is to find an innovative way to achieve this.

2.10 Aim and objectives

This study aims to increase the fuel reformer efficiency by modifying the geometry but keeping the catalyst dimensions, reacting material type and quantity unchanged.

Hence, these changes can be applied to an existing design without redesigning the overall shape of the catalyst and engine compartment. Therefore, from the industry point of view, it offers quick adaption and installation.

Every reacting material has its unique reaction rate equation. Therefore, for standardisation, it is necessary to use the same reacting material for all the tests to solely observe the effects of structural changes.

The specific objectives are as follows to address the stated aim:

I. To find a suitable reference design and experimental data to practise and validate the simulation.

II. To investigate structural variations effects on primary catalyst parameters responsible for the higher efficiency. Also, to find causes behind these parameters producing the higher yield.

III. To find methods and materials to incorporate studied structural changes like segmentation, channel height and inter-channel mass flow. This study will result in novel design suggestions for the fuel reformer.

IV. To calculate optimum values of structural features resulting in higher efficiency for the suggested designs in objective III.

V. To demonstrate that physical changes implemented in objective IV improve FR yield by conducting qualitative and quantitative analysis of methods and materials found in objective III. The improvement explanation will come from the parameters narrowed down in objective II.

VI. To carry out a transient study to analyse the evolution of the variables found in objectives II to V. It will add further reasons and importance of new FR structures proposed in this study.

VII. To carry out 2D and 3D inter-channel fluid flow simulations to observe its effects on the H_2 conversion efficiency.

2.11 Chapter 2 summary

Fossil fuels consumption has been increasing in the transportation sector, power plants and houses. There are numerous WHR technologies like Rankine cycle, fuel cell and fuel reforming to ease this fossil fuel dependence. However, adopting a clean energy solution is governed by efficiency, emissions laws, benefits, costs, and more.

The fuel reformer catalyst is the WHR choice of this study. Catalyst structural changes like channel height, segmentation and passive channels increase reformer efficiency. The task is to find methods to incorporate these changes in an already existing design. As a result, cell shape, density, catalyst quantity and length remain unaffected. Hence, no change in catalyst length or diameter occurs and thus in the engine compartment.

3 Method and materials

This section narrows down the reference design along with modelling simplifications and assumptions. Then some essential catalysts parameters and the factors affecting them are identified and discussed. Finally, based on the discussion on parameters and factors, some innovative designs are presented.

3.1 Introduction

For an accurate simulation as close to the experiment, a complete model including physics, mathematics and chemistry is needed to explain the chemical reforming reaction. For instance, a correction would be required in equations developed for low porosity medium if applied to high porosity metal foam (Bhattacharya, Calmidi and Mahajan, 2002). However, going into lengthy details is sometimes not required. For instance, a detailed SMR model was developed by Xu and Froment. The authors stated that three out of 11 reactions are dominant and direct the kinetic reaction rate (Xu and Froment, 1989).

Rate equations are developed from experiments involving various elementary reactions. The equations variables are different for each set of operating conditions and catalyst. Generating a model incorporating all the elementary reactions is possible, but it will take a lot of solver time. Moreover, it is difficult to measure the accurate surface area of the catalyst. Hence, many researchers exclude elementary reactions and use an overall rate equation deduced from an experiment (Lin *et al.*, 2013).

Fuel reforming reactions are mainly heterogeneous, where reactants react faster in the presence of catalyst than anywhere else in the system. In such a setup, reactants diffuse into catalyst sites from bulk gas. These absorb and form the products, then the products desorb and renter into the bulk fluid.

3.2 Fuel reformer design

3.2.1 Reference design

In a study supervised by Dr Kyaw Lin (LIN *et al.*, 2012), both experiment and simulation are carried out of a fuel reformer channel. For simulation, they have used experimental conditions. The reformer length is contained to save computational power and is sufficient for the variables to develop fully before the outlet. The 2D geometry depicted (Figure 3-1) is 20 mm long and is 3.1 mm high. A constant temperature is applied on the top wall, whereas the lower wall has two adiabatic boundaries from 0-5 mm and 15-20 mm. The catalyst is coated from 5-15 mm, and its thickness (0.15 mm) is neglected in simulation, so diffusion is missing within the catalyst layer.

A total of 9600 hexahedra elements are used in his study. All the reactions occur at the catalyst surface, and hence any gaseous reaction is neglected.

The two vertical lines in Figure 3-1 are interfaces between two different domains: adiabatic and catalytic regions. Overall, reactants (H_2O and CH_4) enter from the left, react at the catalyst layer to produce H_2 and CO, and leave the outlet in different proportions.

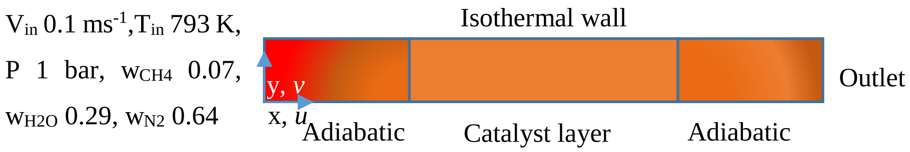

Figure 3-1: FR geometry with boundary conditions and inlet condition (left). The outlet is on the right side (LIN *et al.*, 2012)

3.2.2 Rate equation development

The authors have developed the rate equation from their experimental data. They have modelled the rate equation as if the reaction is occurring in the bulk gas. However, as the reaction occurs only at the catalyst surface, they call it the pseudo-bulk model. The following expression gives the overall rate equation:

$$\boldsymbol{rate} = A \times e^{-\frac{E}{RT}} \times CH_4P^{a} \times H_2OP^{-b}$$

Equation 3-1: Volumetric reaction rate equation for SMR (LIN *et al.*, 2012)

Where A is the pre-exponential factor, E is the activation energy of SMR reaction, R is the universal gas constant, T is temperature, a and b exponential constants, CH_4P and H_2OP are the partial pressure for methane and water. Units and values of all these variables are given in Table 3-1 for various operating pressure (LIN *et al.*, 2012).

The volumetric rate equation unit is generally in mol/m^3/s. Dr Lin does not mention the catalyst loading (g/m^2) and similarly does not specify pre-exponential (A) units but derived from the surface reaction rate units mentioned in Dr Lin paper. The same method is adopted by Dr Settar team. This study uses 0.4 g/m^2 of catalyst loading, and section 4.4 will elaborate its calculation (Settar, Lebaal and Abboudi, 2018).

Table 3-1: Rate equation variable values for different operating pressure. ‘g’ is catalyst quantity in grams (LIN *et al.*, 2012)

Pressure MPa	***a***	***b***	***A* mol/g/s/Pa$^{0.46}$**	***E* kJ/mol**
0.1	0.47	-0.01	0.392	43.2
0.2	0.32	0.16	0.131	42.1
0.3	0.37	0.15	0.148	48.2
0.4	0.4	0.18	0.062	48.7

Multiplying catalyst loading with the volumetric rate equation gives units of the rate as mol/m^2/s. It is now a surface reaction rate ($Rate$) and is appropriate to include heat and mass fluxes at the catalyst surface (ANSYS® Academic Research, 2017).

3.2.3 Boundary conditions

The boundary conditions for the channel shown in Figure 3-1 are given in Table 3-2. The variables directions are according to the axes given in the figure.

Table 3-2: Boundary conditions summary (LIN *et al.*, 2012)

	***u* [ms^{-1}]**	***v* [ms^{-1}]**	***T* [K]**	**w_i [-]**
Inlet	0.1	0	793	w_{H2O}=0.29, w_{CH4}=0.07, w_{N2}=0.64
Outlet	$\partial u/\partial x=0$	0	$\partial T/\partial x=0$	$\partial w_i/\partial x=0$
Upper wall	0	0	793	$\partial w_i/\partial y=0$
Lower wall	0	0	$\partial T/\partial y=0$	$\partial w_i/\partial y=0$
Catalyst	0	0	$\partial T/\partial y=-Rate\Delta H/\lambda$	$\partial w_i/\partial y=-Rate M_i(\varepsilon''-\varepsilon')/\rho D$

Where ε'' and ε' are the stoichiometric coefficient of reactants and products (e.g. net result is -1 for CH_4 & H_2O, 1 CO for and 3 for H_2, $Rate$ is the surface reaction rate, w is the mass fraction, ρ is density, D is diffusion and λ is the thermal conductivity

3.2.4 Adjustment factor

The authors have used an adjustment factor to match their 2D simulation results with their experimental values in the study. The stated reason is a lower catalyst temperature than the gas's bulk temperature. Hence, the reaction rate developed from the experiment may not always be appropriate for the simulation. Therefore an adjustment factor is used to scale up their A. In other words, it is like using a new pre-exponential factor of the rate equation. The authors have found some suitable factors for various operating pressure of the SMR reaction with some trials. The factors values are given in Table 3-3 (LIN *et al.*, 2012).

Table 3-3: Adjustment factors for different operating pressure (LIN *et al.*, 2012)

Pressure	**0.1 MPa**	**0.2 MPa**	**0.3 MPa**	**0.4 MPa**
Adjustment factor	3.25	2.3	2.25	2

3.3 Simplification and assumptions in this study

Flux terms are used as suggested by Irani and Pajak (Irani *et al.*, 2011) (Pajak *et al.*, 2018) (Equation 3-2).

$$mass\ flux_j = (\varepsilon'' - \varepsilon') \times Rate \times M_i\ (a)\ heat\ flux_j = Rate \times \Delta H_j\ (b)$$

Equation 3-2: a) Species generation and consumption as flux at catalyst b) heat loss or gain during the reaction as flux at the catalyst (Irani *et al.*, 2011) (Pajak *et al.*, 2018)

So heat is added at catalyst surface as heat flux, and is negative for SMR (endothermic) and is positive (exothermic) for water gas shift (WGS) reaction (j is reaction type; SMR or WGS). Meanwhile, methane and water consumption (negative flux) produces (positive flux) hydrogen and carbon monoxide. Some simplifications taken in this study are:

1. In the paper, WGS enthalpy is added as a source term in the species transport equation. The method to add WGS source in the species equation is unclear as the WGS source unit (W m^{-2}) differs from the species equation's (kg m^{-2} s^{-1}). Hence, the WGS source is subtracted directly from the overall enthalpy (206-45=165 kJ/mol). It is according to Hess's law which states, "The heat of any reaction for a specific reaction is equal to the sum of the heats of reaction for any set of reactions which in sum are equivalent to the overall reaction." (Cohen, 2020)
2. Diffusion flux is negligible as convection dominates the flow.

3. The Real Gas Combustion model is chosen.
4. The flow is steady and compressible. It is considered laminar due to the Reynolds number being less than 70.
5. Lewis number is taken as unity.
6. Radiation and body forces are neglected.
7. Catalyst thickness is negligible. Moreover, the surface-based approach is more accurate than volumetric-based modelling (Irani *et al.*, 2011).

3.4 Fuel reformer integration with power units

Numerous studies show the integration advantages of fuel reformers with a power unit like fuel cell, diesel or gasoline engine. Solid oxide fuel cell generates substantial heat during its operation where the temperature reaches more than 1000 K (see section 2.6.1). A fuel reformer can be integrated with such a high-temperature fuel cell as an internal reforming device. Dr Settar and his team have proposed this concept and conducted simulations of the reformer (Figure 1-5). The boundary conditions used are similar to a typical industrial SMR reformer (Settar, Lebaal and Abboudi, 2018; Settar *et al.*, 2019).

In an experimental study for trucks, a fuel reformer is installed after the IC engine, consuming heat and oxygen from exhaust gases. The primary reason for the leading installation is to provide syngas from the reformer to the downstream catalysts. This type of reforming is called exhaust gas reforming, where high reformate quality is not required. However, the reformer's average conversion was more than 80% for a 650 kg/hr inlet mass flow rate (Armanini and McCarthy, 2010).

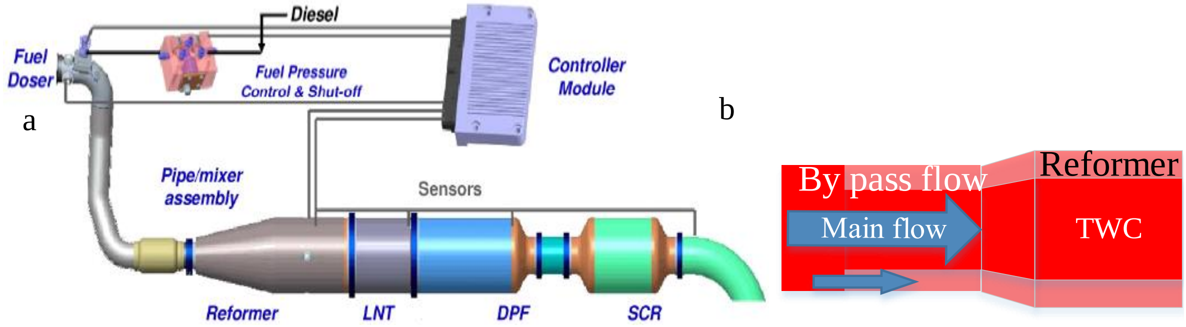

Figure 3-2: a) Exhaust treatment system for a Truck (reformer section is 760 mm long) (Wetzel, Mccarthy and Griffin, 2010) b) exhaust gas reforming (Ashur *et al.*, 2007)

For a similar study, a cylindrical (101.3 mm × ⌀300 mm) reformer is used to provide syngas for a combined catalyst package system (Figure 3-2a). The system includes FR followed by LNT, DPF and lastly, an SCR catalyst (Wetzel, Mccarthy and Griffin, 2010).

Similarly, an annular exhaust gas fuel reformer around a TWC catalyst is tested for a gasoline engine car (Figure 3-2b). The annular part receives 10-20% of the exhaust gas, containing heat and water vapour. The engine operated at a 1.1 air to fuel ratio, and the exhaust gas temperature reached 623 K. The hydrogen yield produced was more than 9 per cent by volume (Ashur *et al.*, 2007).

3.5 Primary catalyst design parameters

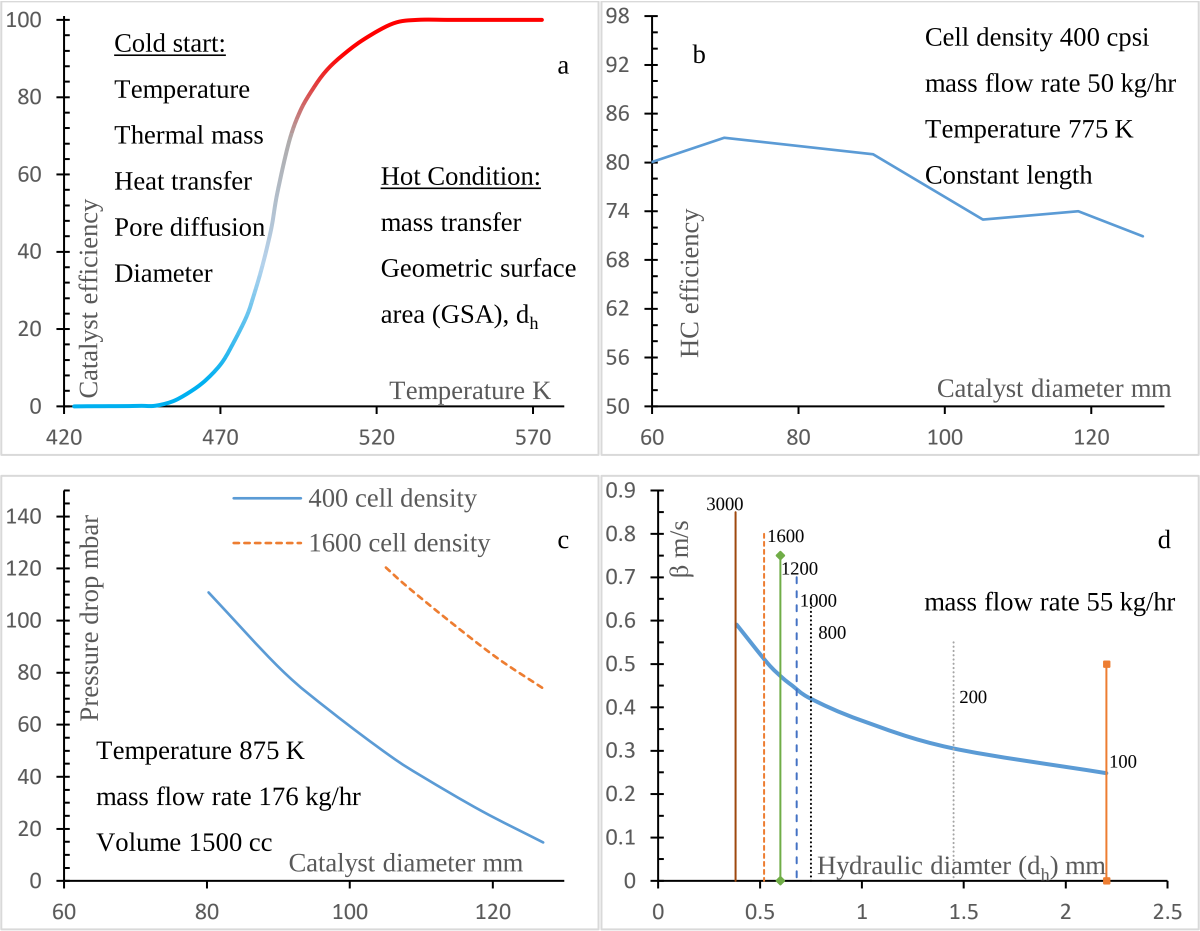

Figure 3-3: Limiting factors for catalyst efficiency for a heterogeneous catalyst a) general catalyst efficiency trend vs temperature, b) HC conversion efficiency of a catalyst vs catalyst diameter, c) pressure drop across catalyst vs catalyst diameter at constant volume, d) the mass transfer coefficient vs d_h at various cpsi (Marsh *et al.*, 2001)

Various parameters should be considered to design a catalyst. The importance of these parameters varies according to the application. For instance, it can be the light-off time for a three-way catalyst as most (80%) of the HC emission occurs at the cold start (Marsh *et al.*, 2001). Whereas for an industrial fuel reformer, efficiency overshadows the light-off performance. Overall the important parameters for a catalyst are; flow uniformity, light-off time, pressure drop, and residence time.

3.5.1 General catalyst design factors

Several factors affect these parameters, such as cell density, catalyst size, substrate thickness, hydraulic diameter, and other general parameters. (Om Ariara Guhan, Arthanareeswaren and Varadarajan, 2015) (Martin *et al.*, 1998) (Marsh *et al.*, 2001) (hydraulic diameter = cell cross-section area/cell perimeter).

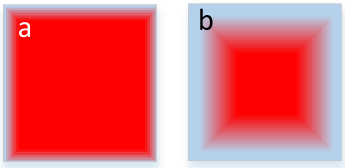

Figure 3-4: A simple illustration of reactants concentration (red) at the a) inlet and b) the outlet of a channel

3.5.1.1 Catalyst reactions regimes

At the start of the reaction, the catalyst efficiency is governed by chemical kinetics and pore diffusion (Figure 3-3a). The easier it for reactants to diffuse through washcoat layers to adsorb/desorb at the catalyst site, the higher is the cold start efficiency. Then comes heat energy which is essential for any endothermic reaction. It takes some time for a catalyst to heat up as every material has some specific heat capacity. The reactants' mass transfer rate to the catalyst controls the reaction rate at the higher end of reaction temperature.

The concentration of reactants decreases along the channel length, especially near the catalyst (placed at the wall) due to continuous product formation. Laminar flow is another reason that makes reactants reluctant to diffuse from the centre to the channel wall (Figure 3-4b).

3.5.1.2 Mass transfer coefficient

The mass transfer coefficient is $\beta = \frac{D\,Sh}{\mathrm{d_h}}$. D is the binary diffusion coefficient, Sh is the Sherwood number, and d_h is the channel hydraulic diameter. The Sherwood number depends on the Reynolds number (Re), which means the mass transfer coefficient increases with velocity. The reason for this increase can be turbulence which is dominant at high speed. Increasing the catalyst diameter will decrease β as fluid velocity slows down for a constant mass flow rate (Marsh *et al*., 2001).

3.5.1.3 Catalyst diameter

There is an optimum value after which changing the catalyst diameter decreases the efficiency. Figure 3-3b shows that catalyst has maximum efficiency at around a diameter of 70 mm. This fall in performance is due to several factors, such as β reduction with the low-speed flow for higher diameter. Decreasing it below 70 mm reduces reactants residence time in the channel, so the efficiency falls. The mass flow rate and the catalyst length are constant (Marsh *et al*., 2001).

3.5.1.4 Cell density

At constant catalyst volume, the possibility to further increase the efficiency is by modifying the geometry, such as increasing cell density which increases geometric surface area (Figure 3-3d). Increasing cell density also decreases the hydraulic diameter, and in return, β increases. The pressure drop increases with cell density and falls with the catalyst diameter. It is an essential parameter as pressure drop consumes energy from the fluid flow (Figure 3-3c). These are some general characteristics of a catalyst (Marsh *et al*., 2001).

The point to be noted is that it is a general trend. For instance, in one study, when the hydraulic diameter reduces to 361 µm from 1065 µm for the methanol-reforming, the reactor efficiency decreases by 14 %. Though the β increases, the efficiency reduces because the thermal conductivity decreases due to higher cell density (Sanz *et al*., 2016).

3.5.2 Flow uniformity effects

The flow uniformity allows more use of catalyst volume for the chemical reaction. It helps to achieve higher conversion efficiency, lower pressure drop, lesser flow losses and uniform temperature distribution (Morton, Hall and Radavich, 2013). Flow uniformity is crucial for even fuel distribution in FR catalysts. Generally, it is defined as the difference between local velocity in a single channel and the average velocity of gases in the catalyst cross-section (Wetzel, Mccarthy and Griffin, 2010). Overall flow uniformity formula is:

$$\gamma = 1 - \frac{\sum(|v_i - v_{avg}|A_i)}{2v_{avg}A_{total}}$$

Equation 3-3: Flow uniformity parameter, adopted by (Wetzel, Mccarthy and Griffin, 2010)

Here v_i velocity in cell i, v_{avg} average velocity in particular cross-section, A_i cell area, A_{total} area of that specific cross-section.

3.5.2.1 Improved mixing

When liquid hydrocarbons are used, these must be vaporised and mixed to create a uniform exhaust gas/hydrocarbon vapour mixture for the onboard fuel reforming catalyst to ensure proper operation. The temperature of exhaust gas vaporises the hydrocarbon, whereas the mass flow rate helps fluid mixing. Therefore each engine working condition has its effect on gas mixture vaporisation and mixing. In addition, mechanical mixers such as mixing tabs (Figure 3-5b) or baffles can aid in mixing gas/fuel mixture at the expense of higher back pressure.

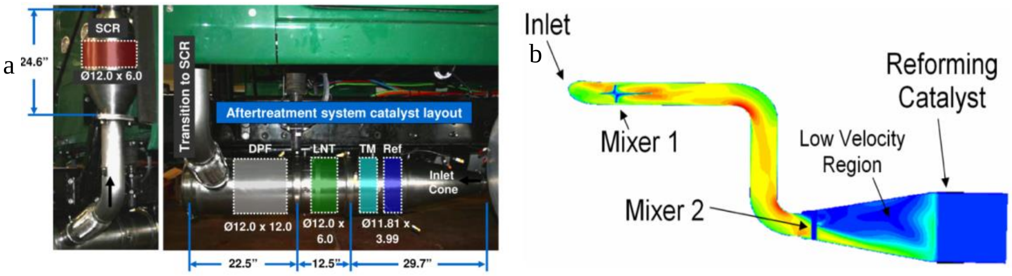

Figure 3-5: a) Eaton exhaust line with FR b) flow stall region even after installing mechanical mixers (Wetzel, Mccarthy and Griffin, 2010)

3.5.2.2 Uniform temperature distribution

Flow nonuniformity can lead to localised overheating at specific parts of the catalyst. Overheating can cause failure due to thermal stresses. It also degrades the catalyst performance by favouring unwanted reactions at a different temperature than the suitable temperature for the desired reaction. Hence, catalyst geometry is carefully designed to minimise flow nonuniformity (Sigurdsson and Kær, 2012).

Similar results are shown by Windmann *et al.* (Windmann *et al.*, 2003). A uniform flow ($\gamma \approx 1$) at the inlet causes a steady temperature rise and high conversion of pollutants for a circular three-way catalyst simulation. The test shows that uniform flow delays the light-off temperature by two seconds. However, after the light-off, uniform inlet conditions enable the catalyst to have a higher conversion efficiency.

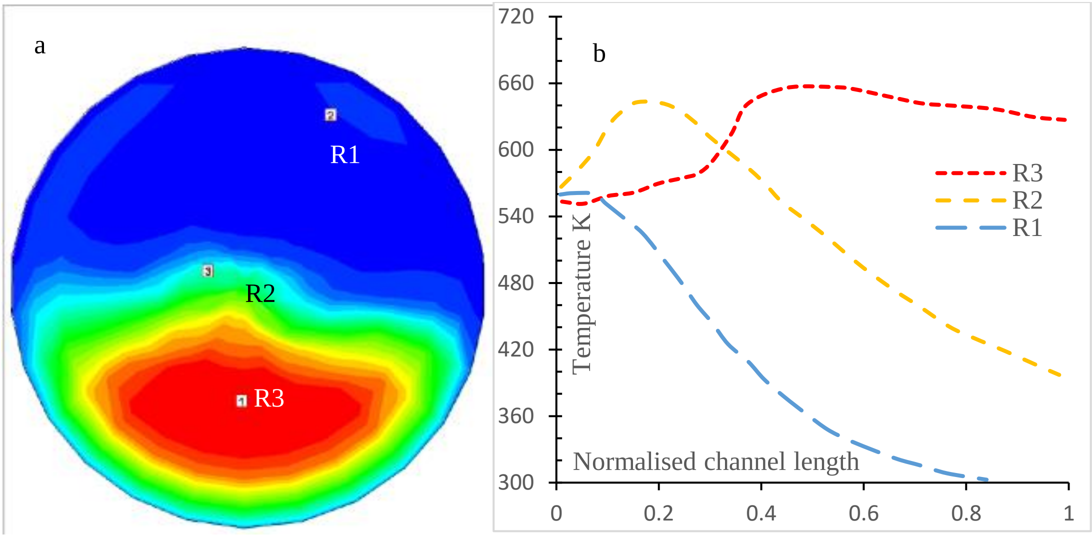

Figure 3-6: Due to non-uniform flow at the inlet, the non-uniform a) temperature contours at the outlet of the monolith 40 s after start-up b) temperature profiles along axial coordinate for the regions 1, 2 & 3 (Windmann *et al*., 2003)

The main reason for the inefficiency is the non-uniform temperature distribution inside the catalyst (Figure 3-6a and b). The non-uniform flow condition leads to early light-off, but it fails to utilise the entire catalyst volume. Hence, it cannot achieve higher efficiency. This uneven distribution also causes hotspots which compromises the catalyst durability. Moreover, if a nitrous adsorbing catalyst comes after the three-way catalyst, LNT will lose absorbed nitrous oxide due to incoming high-temperature flow (Wetzel, Mccarthy and Griffin, 2010).

3.5.2.3 High catalyst efficiency

Figure 3-7 shows flow uniformity effects for a vehicle's DOC. A 1600 cc engine is operating according to NEDC and for different uniformity indexes. Cumulative HC emissions are recorded from the car exhaust. It is visible that flow uniformity does not improve emissions at the cold start. However, the effect of uniform flow appears near 200 s. Higher HC conversion efficiency is achievable for higher γ values by the DOC (Martin *et al*., 1998).

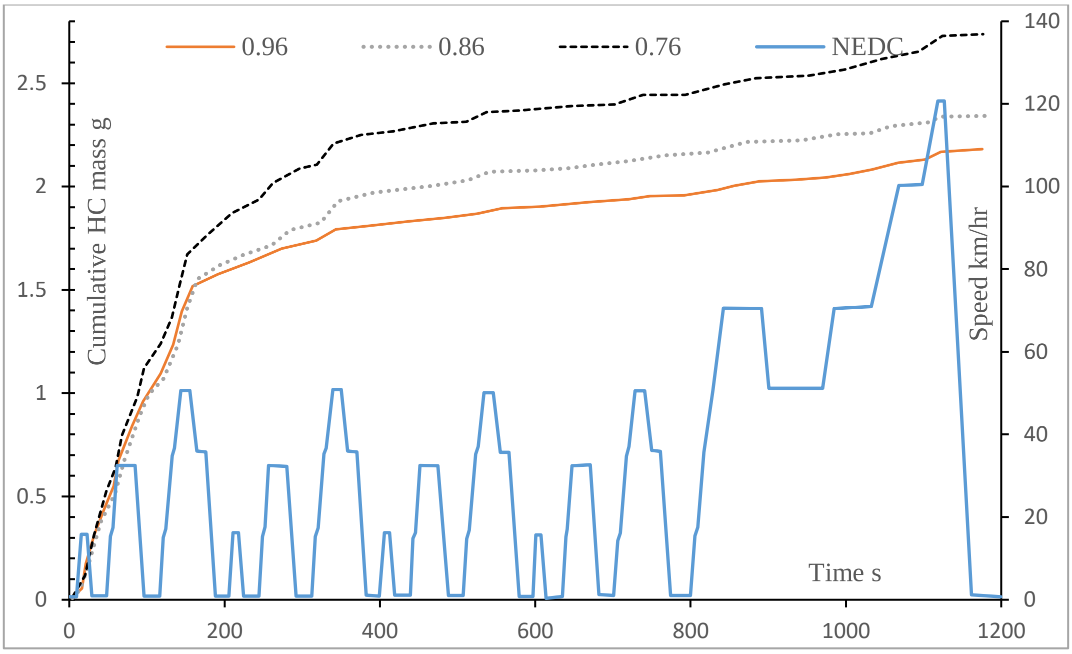

Figure 3-7: Cumulative HC emissions during NEDC (Fresh catalyst) (Martin *et al*., 1998)

3.5.3 Methods to improve flow uniformity

Overall, flow nonuniformity can lead to hot spots, hydrocarbon slip, higher pressure drop, flow reversal, and non-uniform flow distribution. This maldistribution means some channels are receiving excessive flow, and some are starving. Flow uniformity depends upon exhaust manifold inlet design, cone design, substrate dimensions & shape and configuration of the exhaust line. Modification of the monolith front shape also increases flow uniformity.

3.5.3.1 Monolith shape

In an experimental study, different frontal forms like conical and spherical are tested to evaluate this parameter. The spherical or the dome-shaped (Contura™) turns out to be most useful to increase flow uniformity and reduce pressure drop compared to the standard monolith (Figure 3-9). The flow simulation shows that from low to high Re, the uniformity index for standard substrate decreases to 51.5 from 66.9 compared to 72.1 from 81.2 (percentage) for the dome substrate (Wollin and Benjamin, 1999).

The dome monolith utilises some portion of the diffuser volume in comparison with the standard monolith, but overall volume is kept constant for comparison (Figure 3-8). The author states that the flow distributes due to the shape and not because of the elongated channel at the dome’s middle part.

However, heat loss and light-off performance are not investigated of the body, which is also important. As flow is directed outward in the dome monolith, more heat flows to the container wall and then to the surroundings, especially at the cold start (Wollin and Benjamin, 1999).

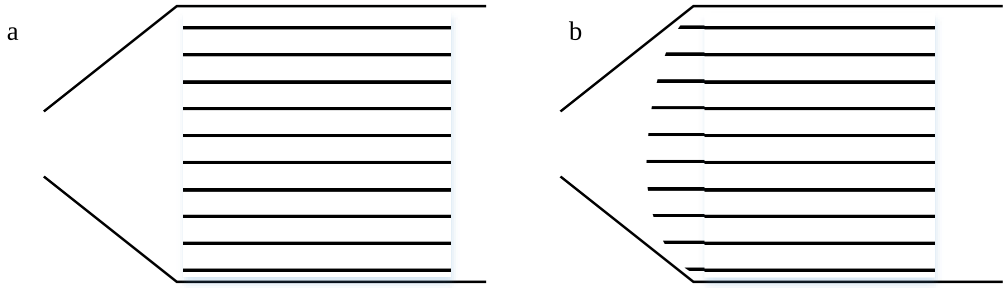

Figure 3-8: a) the standard monolith b) the dome-shaped (Contura™) monolith (Wollin and Benjamin, 1999)

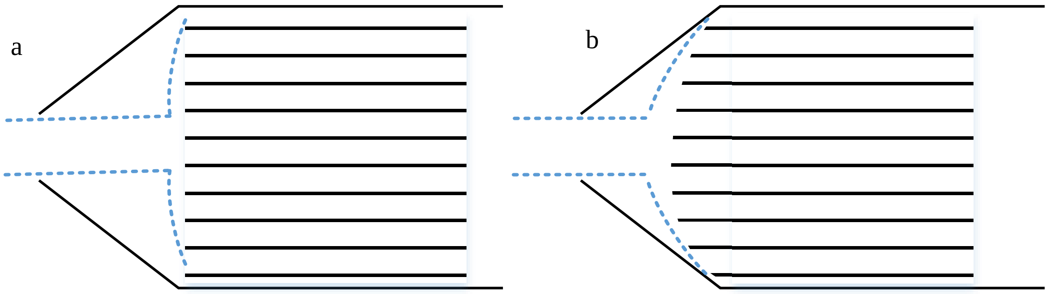

Figure 3-9: Predicted particles pathlines for a) the standard monolith and b) the dome-shaped monolith

3.5.3.2 Variable cell density

A varying cell density monolith is used to distribute the flow to the catalyst's entire cross-section uniformly. Compared to a conventional 400 cpsi monolith, a new monolith design is proposed. This new monolith has the same amount of catalyst. However, the centre region is 600 cpsi, and the surrounding structure is 400 cpsi. The surface area of the higher cell density channels is the same as the surface area of outer region channels, which determines the diameter ratio. The simulation shows that the fluid flows spread more evenly in the radial direction for the variable cell design. The small hydraulic diameter of the central region can be the reason for this uniformity as flow slows down there compared to adjacent channels.

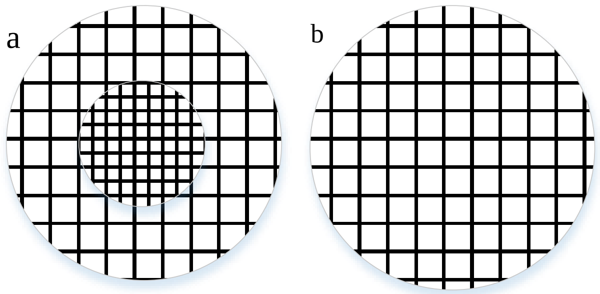

Figure 3-10: a) Variable cell density where inner monolith has 600 cpsi, and outer monolith has 400 cpsi (Volume 700 cc), b) a conventional monolith with 400 cpsi (volume 900 cc) (Yoshida *et al.*, 2017)

The new monolith is tested for DOC and LNT catalysts. The simple amendment shows that compared to the conventional catalyst, the news design can treat a higher flow rate (Figure 3-11a) and give better light-off performance by 10 K (Figure 3-11b). Thus the new monolith can be installed for a bigger engine but with a smaller volume and still perform better at the cold start. This model was adopted in actual vehicles by Toyota in 2016 (Yoshida *et al.*, 2017).

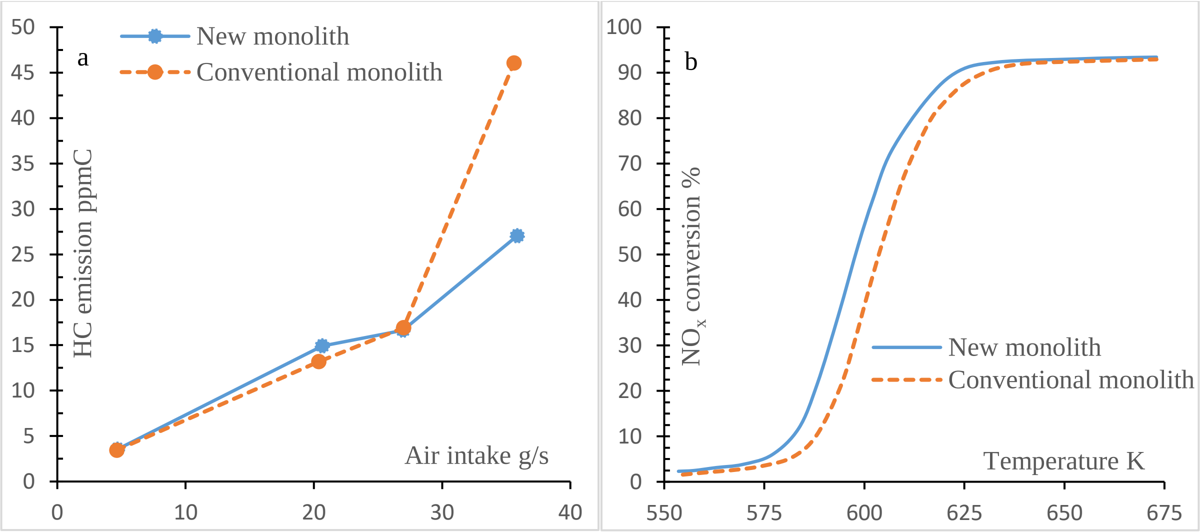

Figure 3-11: a) HC emission vs engine air intake (test) b) NO_x conversion vs catalyst temperature (test) (Yoshida *et al.*, 2017)

3.5.3.3 Changing porous material properties

A wire mesh catalyst is used as another unique design for the combined heat and power reformer unit in a catalytic plate type heat exchanger (CPHE) configuration (Figure 3-12). Flow nonuniformity is measured by the standard deviation (SD). A higher SD value stands for higher nonuniformity. The research shows that the low friction coefficient (case 1) of wire mesh shows higher nonuniformity than case 2 when the friction coefficient is higher (Table 3-4). As flow increases from 1610 to 6420 Re, the SD increases from 67 to 133% for case 1, and for the similar flow rate range of case 2, it grows from 8 to 30% (Figure 3-13b).

Higher inlet velocity causes local depression and reduces the pressure in the manifold. This pressure drop causes the flow to return to the manifold from the top channels (Figure 3-12). However, increasing the wire mesh friction in top channels (case 2) prevents this flow reversal but permits a low mass flow rate than before. The low mass flow rate is advantageous as the authors report that at full load for case 1, the last channel receives four times less average mass flow than the top one.

This trend suggests that a restriction increases the flow uniformity but at the cost of pressure drop. For example, at 4850 Re, the pressure drop for case 1 is 152 Pa, whereas 248 Pa is observed for case 2 (Figure 3-13a) (Sigurdsson and Kær, 2012).

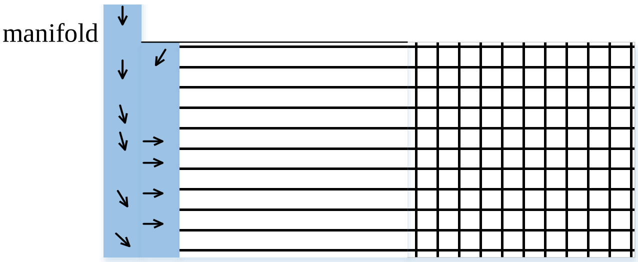

Figure 3-12: A rough side view description of a 60 channel CPHE reformer. Inlet manifold (blue), catalytic wire mesh channels (cross) (Sigurdsson and Kær, 2012)

Table 3-4: K_1 and K_2 are linear and quadratic combined constants for pressure drop, v_s is the superficial velocity, L is channel length (Sigurdsson and Kær, 2012)

	K_1	K_2	**Pressure drop per length**
Case 1	959	75.2	$\frac{\Delta P}{L} = K_1 v_s + K_2 {v_s}^2$
Case 2	6870	4730	

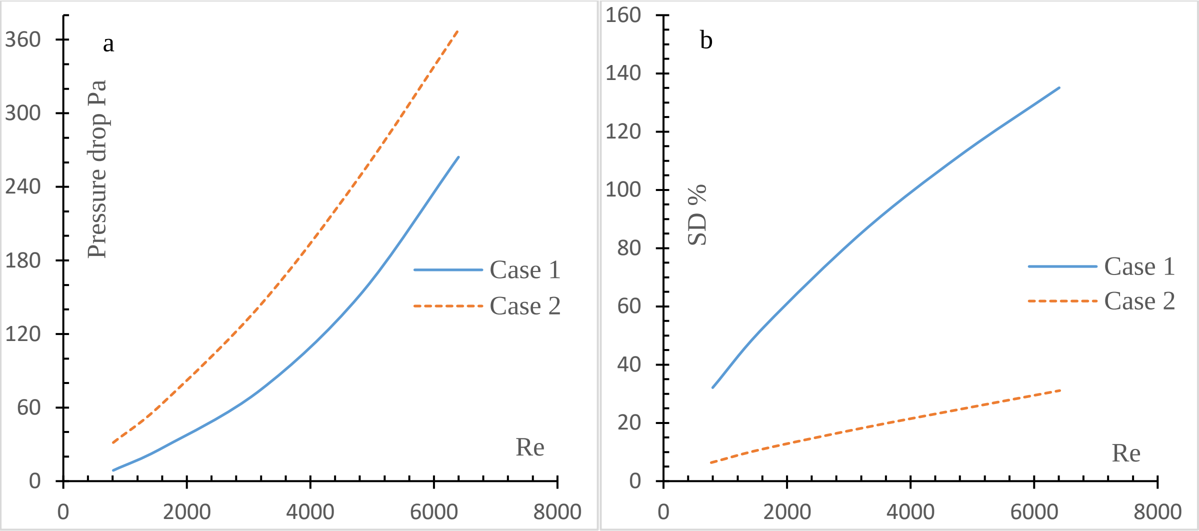

Figure 3-13: a) P_D and b) SD of case 1 and case 2 vs Re (Sigurdsson and Kær, 2012)

3.5.4 Pressure drop

Pressure drop (P_D) is the pressure loss (or energy loss) in a fluid flow. The pressure is lost in catalyst channels by substrate friction, fluid viscosity and sudden channel expansion/contraction.

3.5.4.1 Average velocity effects

Overall pressure drop in catalyst channels is given by:

$$\Delta \mathrm{P_D} = \Delta P_{inlet\ contraction} + \Delta P_{friction} + \Delta P_{exit\ expansion}$$

$$\Delta P_{inlet\ contraction} \propto f_{cont} \times v_{avg}{}^2 \text{ (a)}$$

$$\Delta P_{friction} \propto \frac{L \times v_{avg}}{\mathrm{d_h^2}} \quad \text{(b)}$$

$$\Delta P_{exit\ expansion} \propto f_{exp} \times v_{avg}{}^2 \quad \text{(c)}$$

Equation 3-4: Some correlation for pressure drop (Müller-haas and Rice, 2006), f is the expansion/contraction factor

All these equations imply that pressure drop is dependent on the local velocity of a catalyst channel. Hence, the pressure drop will be a minimum in a uniform flow distribution as even flow distribution means equal velocity in each channel. Equation 3-4a and c also depend on the area available for fluid flow. Sudden change in cross-sectional area at the monolith inlet and outlet causes pressure loss. The contraction and expansion factors are measured experimentally. Otherwise, a good approximation is 1-OFA^2. OFA depends on cell density, wall and washcoat thickness.

$$\text{OFA} = \frac{Sum\ of\ all\ cell\ area\ in\ plane}{Total\ area\ of\ cross\ section\ in\ that\ plane}$$

Equation 3-5: OFA is the open frontal area (Müller-haas and Rice, 2006)

3.5.4.2 Hydraulic diameter effects

Equation 3-4b describes the pressure drop resulting from friction between gas and substrate surface. Metallic substrates for a typical DOC have a foil thickness of 50 µm, whereas ceramic products have a wall thickness up to 220 µm. This wall thickness reduction for metal foil increases the OFA (varies from 50-80%) and hydraulic diameter. In return, the pressure drop due to friction reduces, but the mass transfer coefficient also decreases. Moreover, it is easier for the ceramic substrate to achieve higher cell density than the metallic monolith.

Due to fear of pollutants plugging the catalyst, 400 cpsi or lower cell density is usually adopted. Monolithic catalyst substrates are made of ceramics or metal. Ceramic substrates (honeycombs) usually have square cell profiles, while most metallic substrates are sinusoidal in form (Müller-haas and Rice, 2006).

3.5.4.3 Cell shape effects

Cell shapes also affect the pressure drop, such as triangular, hexagonal, trapezoidal, and so forth. The pressure loss is calculated using Darcy's friction factor for circular, triangular and square cell shapes (Equation 3-6). The catalyst is a cylinder having a diameter and length of 100 mm for all the cell shapes. The wall thickness and cell density are varied to calculate the pressure drop at different velocities. Figure 3-15 shows some of the results of this study. The study shows that a square cell outline offers a minimum pressure drop for increasing cell density. The friction factor is minimum for the triangular shape, but its hydraulic diameter is the lowest, which increase $\Delta P_{friction}$ (Enomoto, 2006).

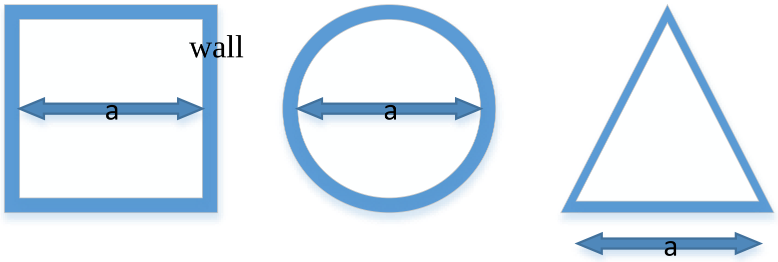

Figure 3-14: Cell shapes used for pressure drop calculation (Enomoto, 2006)

Table 3-5: Properties of cell shapes (Enomoto, 2006)

Cell shape	**d_h**	**D_c**
Circle	a	64
Square	a	57
Triangle	$(3^{0.5}/3)a$	53

$$p_{out} - p_{in} = D_c(L/\mathrm{d_h})(\rho\, v^2/2)$$

Equation 3-6: Equation used to calculate P_D. D_c is darcy friction coefficient, L is length, and v is the velocity (Enomoto, 2006)

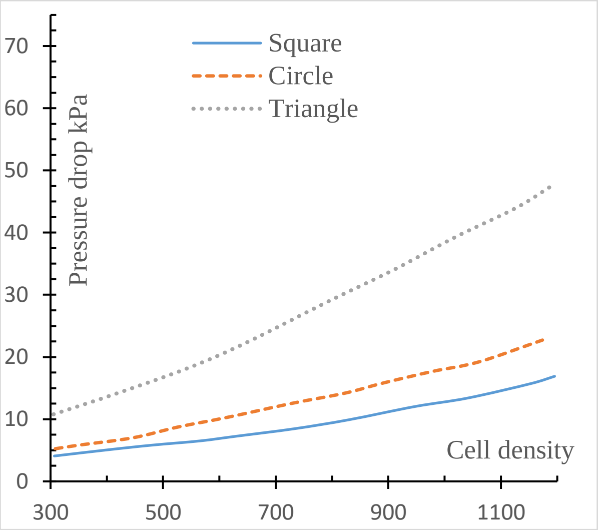

Figure 3-15: P_D vs cpsi of various cell shapes (wall thickness 0.051 mm) (Enomoto, 2006)

Since the 1940s, ICI (Imperial Chemical Industries) Billingham was using ring type pallets for its reforming catalyst until 1980 when a four-hole shaped catalyst was launched (Table 3-6). Then came the Quardralobe™ pallet (2001), which offers a 20% improved catalytic activity with better heat transfer and lower pressure drop than the four-hole. Next, the Catacel Corporation introduced $\mathrm{CATACEL_{JM}}$, another innovative design (owned by Johnson Matthey now). The fins of this model are coated with nickel catalyst for the reforming reaction. Compared to pallets, the tube filled $\mathrm{CATACEL_{JM}}$ offers way higher yield, lower pressure drop and higher heat transfer (Murkin and Brightling, 2016).

Table 3-6: Different catalyst cell/channel shape or a pallet (Murkin and Brightling, 2016)

Cross-section					
Form	Cube	Cylinder	Cylinder	Cylinder	Cylinder+foil
Shape	Square	Ring	4-hole	Quadralobe™	$\text{CATACEL}_{\text{JM}}$
Type	Cell	Pallet	Pallet	Pallet	Channel
Relative activity	1.0	1.3	1.6	2.0	3.0
Relative pressure drop	1.0	0.5	0.6	0.4	0.3

The pressure drop requires pumping work to recover the fluid kinetic energy. It can be minimised but cannot be eliminated, so optimised cell, monolith, and inlet cone design are essential factors.

3.5.5 Light-off temperature

The catalyst light-off may not be as crucial for an industrial reformer, but it does matter for onboard fuel reforming for fuel cells and HCCI combustion. It is defined as the minimum temperature necessary to initiate the catalytic reaction. The initiation temperature is the value at which 50% of reactants convert to products (Figure 3-16a).

For a close-coupled catalyst (CCC) for HC emission, light-off performance is tested for 600/4, 900/2 and 1200/2 monoliths (A, B and C, respectively). The first number represents cpsi, and the second signifies substrate thickness. Early catalyst light off means faster conversion of reactants to products and minor fuel penalty to warm it up. Manufacturing features like cell density, wall thickness and washcoat layers all affect catalyst light off. However, to evaluate the CCC light-off performance, three factors are tested independently: thermal mass, heat transfer, and mass transfer.

Under the test conditions, the mass transfer effect appears to be the most dominant factor in catalyst activation. The geometric surface area and the mass transfer coefficient increase due to higher cell density.

The study shows that thermal mass behaviour for B monolith is the best. The high performance is due to greater GSA than A monolith. On the other hand, the C monolith is better than A but equivalent to B due to its more thermal mass, which overwhelms the higher GSA advantage (Figure 3-16b). Overall, a 95% efficiency is achieved by model: C in 11 s, B in 12 s, and A in 18 s (Watling and Cox, 2014).

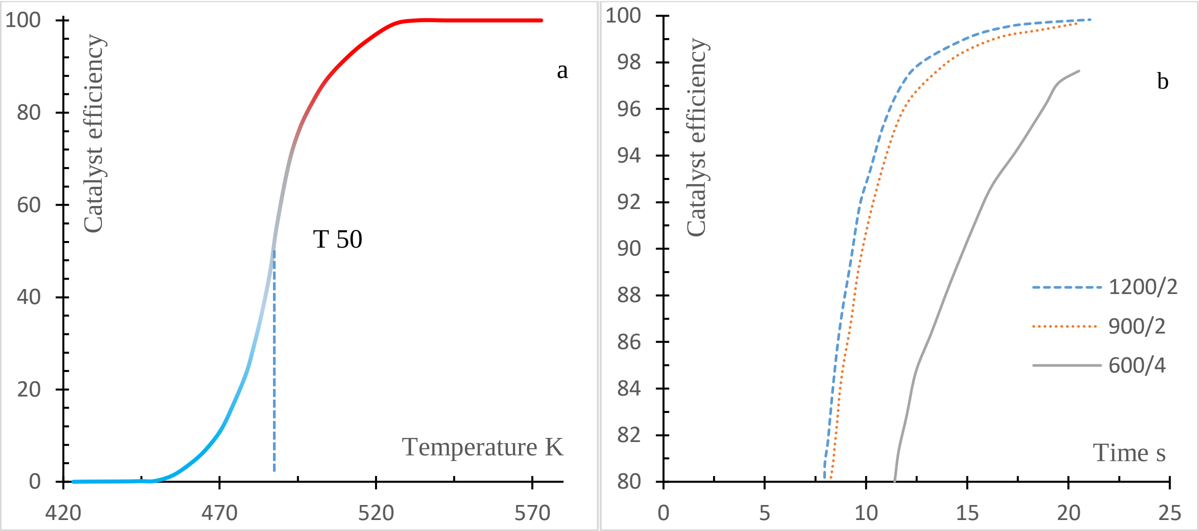

Figure 3-16: a) Catalyst light-off temperature b) Predicted overall contribution to the improvement in post-CCC HC emission with substrate 600/4, 900/2 or 1200/2 (Watling and Cox, 2014)

3.5.6 Residence time

The residence time is the time spent by the fluid in the reactor to form the products. The definition includes the time for; a chemical reaction to occur, pore diffusion of molecules, and travelling from the inlet to the outlet. A chemical reaction time varies for every reaction where bond breaking occurs in picoseconds, and reactants separation from the catalyst occurs from microseconds to minutes. The pore diffusion also has a variable time, such as from microseconds to minutes. The duration depends upon the catalyst shape, particles pathlines, carrier thickness, washcoat porosity, and so forth. So overall, the residence time varies from microseconds to minutes and can reach infinity if reactants permanently adhere to the catalyst site in the form of unwanted products (I. Chorkendorff, 2007).

3.5.6.1 Its effects on efficiency

A shell and tube configuration for a methane steam reformer shows that decreasing the reactant flow rate to 0.067 m^3/min from 0.074 m^3/min (S/C is constant) increases the efficiency. Therefore, hydrogen concentration increases by 4.6%, CO concentration increases by 0.74%, and the average temperature rises 20 K more (Yun *et al.*, 2018). Furthermore, for an autothermal reformer installed in a large vehicle, a study shows that reactants' short residence time leads to a higher unreacted fuel amount at the reformer outlet (Hoang and Chan, 2004).

3.5.6.2 Improving it by a longer flow path

In another experiment, the hot gases of EGR are passed around the catalyst in one loop instead of uni-directionally passing over it. The heat transfer from hot gases to the reformer wall thus increases. This tube reversal (Figure 3-17) saves 50% energy to operate the system during the reformer start-up. Another advantage of such configuration is that reformer operation is less affected by the pulsating engine flow. Additionally, the exhaust gas has already transferred heat to the reformer, saving work for the EGR cooler or the radiator. Therefore it maintains the volumetric efficiency due to colder EGR (Zheng and Asad, 2007).

Mechanical devices like flow guides can increase the mean path of the fluid along a length (Figure 3-18). For a methanol steam reformer, baffles are used in the shell to increase the residence time and heat transfer between oil and tubes. As a result, methanol and steam react inside the catalytic tubes by absorbing more heat from the oil (Sahlin, Andreasen and Kær, 2015).

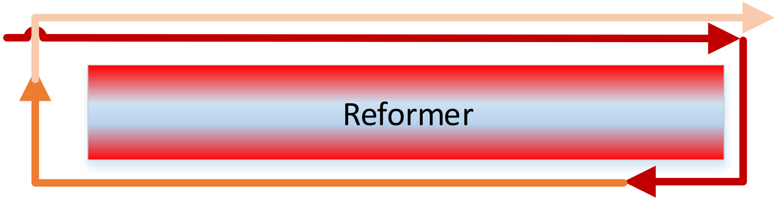

Figure 3-17: Loop of the EGR pipe around the catalyst (Zheng and Asad, 2007)

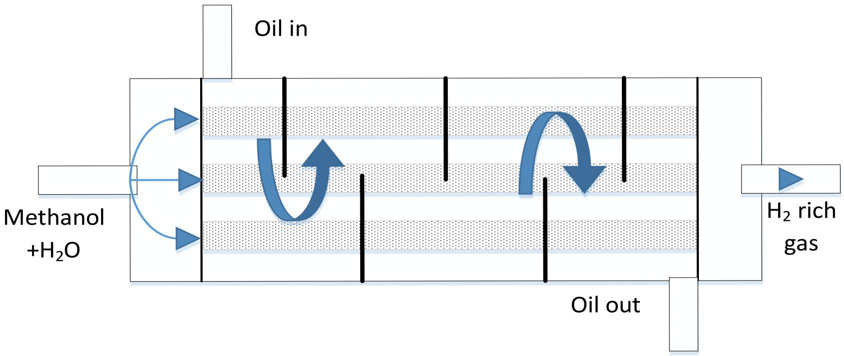

Figure 3-18: Oil heated methanol steam reformer (Sahlin, Andreasen and Kær, 2015)

3.5.7 A short review of catalyst parameters

In conclusion, a catalyst should integrate methods to embrace these main parameters such as flow uniformity, minimum pressure drop, high residence time and quick catalyst light-off. These parameters depend on several factors such as wall thickness, cell height, monolith shape, metal foam properties, to name a few. These factors, however, may oppose each other, which means an optimised solution is required.

For instance, higher cell density constitutes more thermal mass, more surface area and lower hydraulic diameter. It means catalyst light-off delays due to high thermal mass. On the contrary, lower hydraulic diameter and higher GSA result in higher heat and mass transfer from bulk gas to the catalyst, reducing the light-off time. However, both low d_h and high GSA can increase the pressure drop (section 3.5).

The objective is that neither catalyst nor cell shape would change, so catalyst diameter and cell density will remain the same. However, a protrusion can provide the same benefits to mimic a higher cell density or low cell height near the catalyst (Emitec designs in section 2.8.3). This addition will increase mainly the mass transfer coefficient or β. That is the reason why channel height has shown positive effects on efficiency in section 2.8.1.

Inserting metal foam in the channel can also act as a flow guide. Modifying its properties can control the amount and direction of flow in a particular channel to increase residence time. Moreover, metal foam can aid to attain flow uniformity in a multi-channel configuration, as shown in section 3.5.3.3. In this way, the whole catalyst volume is utilised, and reformer efficiency increases.

In summary, metal foam as a protrusion will change channel height. Moreover, it can allow fluid mixing within a single channel as a mechanical mixer. Similarly, by changing its properties, metal foam with perforations can act as a flow guide for inter-channel mass flow to attain flow uniformity and higher residence time.

3.6 Proposed designs in this study

For a heterogeneous catalyst, heat transfer and fluid mixing hold a crucial role in the catalytic reaction. Nonetheless, mass transfer from the bulk fluid to the catalyst site is the limiting factor at the high end of the reaction conditions.

3.6.1 Metal foam as heat enhancement medium (mixer)

Metal foam is a highly porous metal structure that can offer installation flexibility. In addition, its porous structure provides a large ratio of heat transfer area to volume or weight. Its fibres disturb the boundary layer and promote mixing. The same metal struts also transfer heat to the entire structure (Bianchi *et al.*, 2012). This heat enhancement of metal foam is helpful for fuel reformers working even at low operating temperatures.

3.6.1.1 Metal foam between concurrent shells

A study utilises hot reformate heat from an autothermal reaction region to form steam for the SMR stage. This steam is then fed to the steam reformer inlet with methane as reactants. For such concentric shells, water passes through the annular void between two shells (Figure 3-19a). The authors argue that a metallic structure like a wire mesh or metal foam should fill the gap to enhance the heat transfer from the reformate shell to the water. As a result, the pressure drop will be slightly higher due to the structure's high porosity, but heat transfer will be way higher than the clear configuration (Peters *et al.*, 2018).

3.6.1.2 Metal foam around tubes in a shell

For a similar shell and tube structure, Yun *et al*. suggest adding inert granules (3-5 mm) only at the inlet part of reactants (or the exit part of the hot gases) improves reformer efficiency. Adding the granules at the reformate exit of (or the inlet part of hot gases) reduces the overall efficiency, as the granules absorb unnecessary heat from the hot gases. The tubes are fitted (Figure 3-19b, blue) in a shell of hot gasses. Reactants flow in the tubes, extracting heat from the hot gasses in a counter flow configuration. The authors also suggest adding a doughnut-baffle around the tubes to enhance the heat transfer from hot gases to these pipes (Yun *et al.*, 2018). Replacing metal foam with baffles would be an interesting investigation.

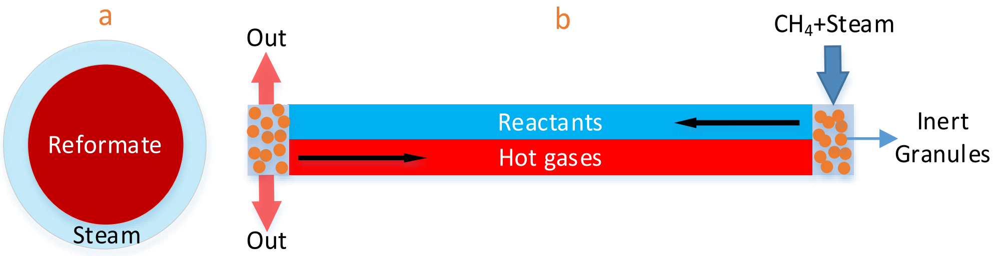

Figure 3-19: a) In concentric shells, reformate and steam are passing in a co-current direction (Peters *et al.*, 2018) b) in a shell and tube structure, reactants (steam+methane) and hot gases are running in a counter flow direction (Yun *et al.*, 2018)

3.6.1.3 Metal foam in tubes

In another experimental study, a highly porous metal foam is inserted in the catalytic channel to increase the heat transfer in a packed bed reactor between the fluid and catalyst pallets (Figure 3-20). The channel has a cylindrical shape of 28 mm in diameter. Helium (He) and nitrogen (N_2) are the fluids, whereas FeCRAlY and Al 6101 alloys metal foams are used. After inserting the metal foam (bare foam), the channel is then filled with Al_2O_3 spheres of diameter 0.3 mm (packed foam). Packing the channel with only alumina pallets is a packed bed configuration. These inert spheres will result in viscous losses and heat transfer but offer no chemical reaction. However, thermal conductivity affects the heat transfer, which is 16 W/mK for the iron alloy, whereas it is 218 W/mK for the aluminium alloy.

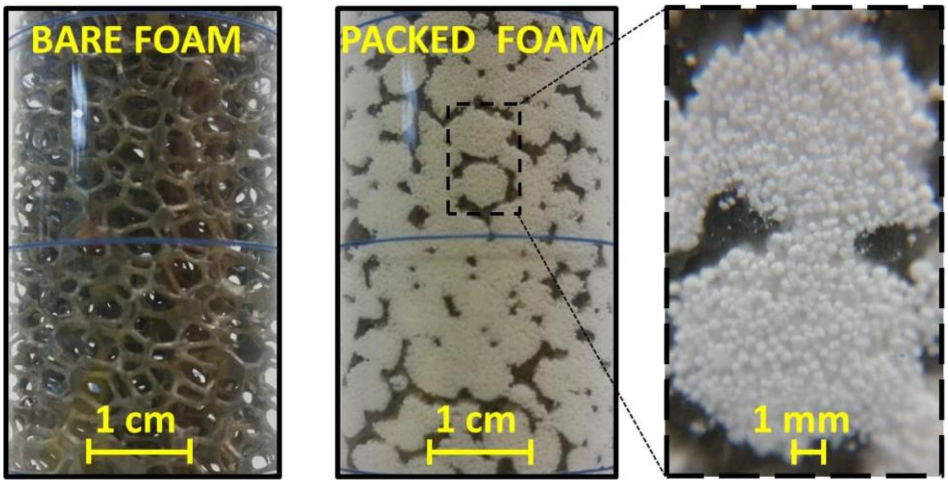

Figure 3-20: From the left, the cylinder with open metal foam, metal foam plus alumina spherical pallets, a close shot of alumina spheres (Visconti, Groppi and Tronconi, 2016)

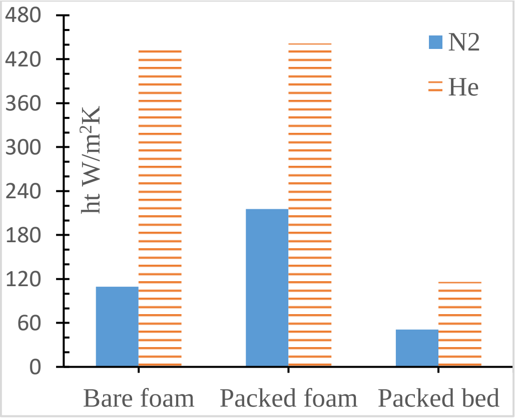

Figure 3-21: Heat transfer coefficient of open/bare foam, open foam plus alumina pallets (packed foam), and cylinder filled with only alumina pallets only (packed bed) (Visconti, Groppi and Tronconi, 2016)

The effective heat conduction occurs through pallets' boundary (sphere, cylinder, etc.) and the metal foam structure. Conduction through metal foam increases radial heat transfer and is independent of fluid flow. The former directly depends on the fluid velocity, raising the overall heat transfer coefficient with the flow rate (Figure 3-21) (Visconti, Groppi and Tronconi, 2016).

Several other approaches are compared to packed bed and honeycomb monolith (Figure 3-22) (Schwieger *et al.*, 2016). Their advantages and disadvantages are summarised in Table 3-7 (Busse, Freund and Schwieger, 2018).

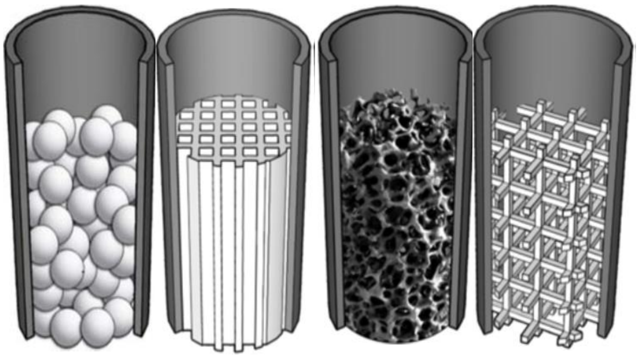

Figure 3-22: Starting from the left, packed bed reactor, honeycomb monolith, open metal foam, open cellular structure (Schwieger *et al.*, 2016) (Busse, Freund and Schwieger, 2018)

Table 3-7: A summary of catalyst technology and its pros and cons (Busse, Freund and Schwieger, 2018)

	Packed bed	**Honeycomb**	**Open foam**	**Open cellular structure**
State	mature	mature	developing	research
Radial mass transfer	high	none	high	high
Radial heat transfer	low	high	high	high
Pressure drop	high	low	low	low

3.6.2 Metal foam as protrusion and passive channel medium

Following the literature review and experimental study, this study presents a few innovative designs. These designs are not increasing the catalyst quantity and overall dimensions.

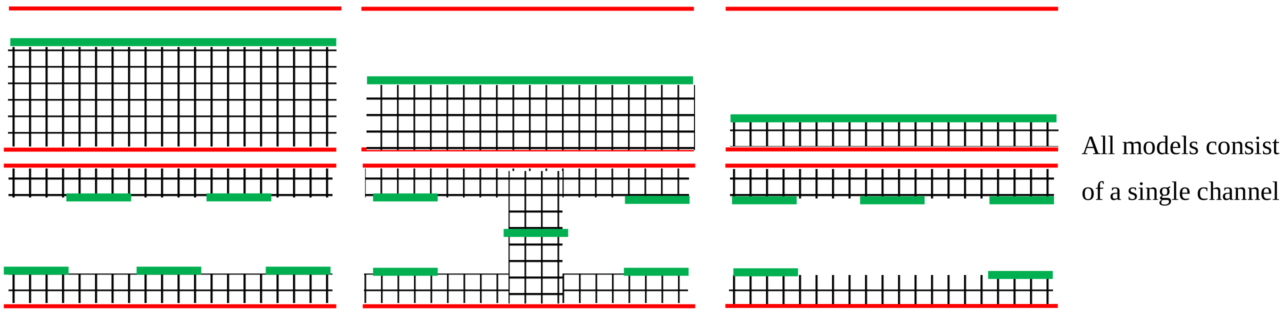

Figure 3-23: Models proposed in this study with isothermal channel walls (red), metal foam (black maze) and catalyst (green) at various positions (see Appendix D for all designs)

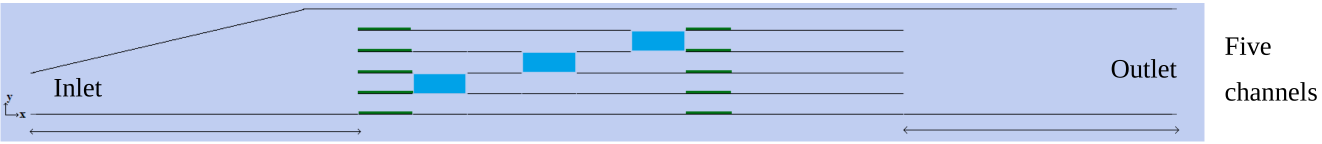

Figure 3-24: Metal foam (blue boxes) as an inter-channel mass and heat transfer medium (see Appendix D for all designs)

The first series of single-channel designs (Figure 3-23) increase productivity due to better mass and heat transfer between the catalyst and the fluid. The heat transfer occurs from the walls to the catalyst through fluid and metal foam. The metal foam protrusion should push the fluid to the clear region despite high porosity, increasing the local reactant concentrations and β. Hence, this experiment can help to narrow down an optimum protrusion height. The catalyst in these settings will be continuous. Later, its segmentation is incorporated within a fixed length by employing top and bottom protrusions.

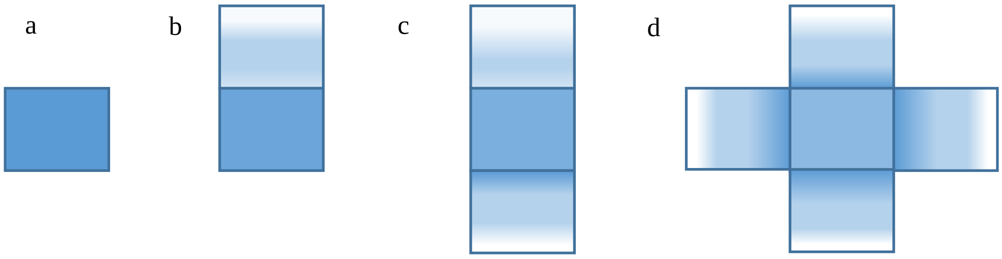

Figure 3-25: Simple description of fluid mixing between a channel b) with top channel c) with top and bottom channels d) with all adjacent channels compared to a) standard

The second suggested design (Figure 3-24) offers inter-channel (5 channels) mass and heat transfer by allowing passive flow through metal foam flow guides. Its usage as a flow guide is possible by changing the metal foam dimensions, properties and porosity direction.

The study will then compare the performance of metal foam plus perforation configuration to holes only pattern. Later, this design will be tested for transient analysis. This test can highlight the variable evolution with time. Next, this design will be extended for a 3D model to emphasise the importance of mass transfer from one channel to the entire catalyst volume (Figure 3-25d).

Hence, this study will test designs where metal foam can act as a mechanical mixer, protrusion, and medium for passive flow (flow guide).

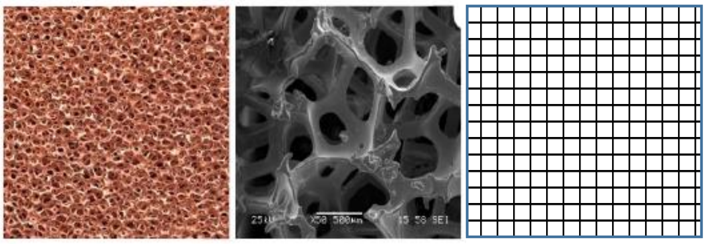

Figure 3-26: Copper (left) and nickel foams (middle) with different magnifications (Settar *et al.*, 2015), and sketch used in this study to illustrate metal foam (right)

3.7 Chapter 3 summary

A reference model of Dr Kyaw Lin is chosen for this study. It is a 2D rectangular channel for modelling methane steam reforming. In addition, some suggestions by other authors such as Pajak and Irani for boundary conditions are considered for the simulation.

Several parameters are to be taken care of in designing a catalyst, such as light-off, flow uniformity, pressure drop, residence time, etc. Moreover, factors like cell density, catalyst diameter and length, cell shape, wall thickness, and substrate thickness affect the parameters above.

Flow uniformity is necessary for uniform mass and heat distribution, increasing the catalyst efficiency and durability. Variable cell density, pressure drop, and frontal catalyst shape can control this parameter. Any catalyst will require a minimum pressure drop as it extracts energy from the fluid. Fluid velocity, cell's shape, cpsi, channel length and diameter govern the pressure drop. For a quick catalyst functioning, an early light-off is necessary. The light-off is a highly material-dependent property. After that, wall thickness, cell density, cross-section, and washcoat thickness rule it. The residence time varies from microsecond to minutes for a reactor. The goal is to raise it without extending the reactor length.

Changing the channel height without increasing the cell density is an innovative solution. Any obstruction like solid or metal foam protrusion can change it, which increase chemical activity. Thus it offers a similar solution like higher cell density but with lower pressure drop. Allowing the cross channel flow permits heat and mass transfer to neighbouring channels, promoting greater reactivity, uniformity, higher residence time and lower pressure drop (Figure 2-24).

4 Model validation

This chapter moves around the validation of the reference design. First, mesh sensitivity analysis is performed, and then some input parameters are adjusted for a good quality match. Next, A factor F1 is proposed to fill the quantitative gap. After analysing the reactor performance, the factor need arises by putting each rate equation term as an exact input boundary condition. Later, the evaluation of the rate equation terms and their non-linear contribution conclude that F1 is a net contribution value originating from each term of the rate equation.

4.1 Mesh sensitivity

By incorporating all the assumptions backed by various papers (section 3.2), the SMR reaction is simulated using the software. Firstly, geometry and mesh are generated using ICEM 18.1, and then the reaction is simulated using CFX 18.1. More details are given in Appendix A and B. Plots for reaction rate, average hydrogen mass fraction and temperature are compared with the (LIN *et al.*, 2012) paper simulation.

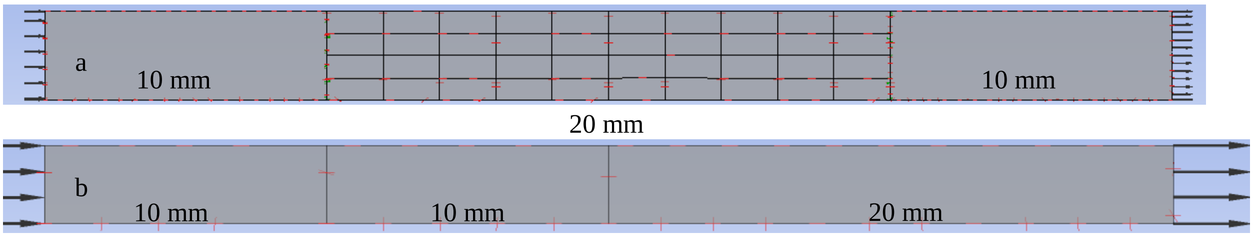

Figure 4-1: a) the ICEM geometry and interfaces bound the small domains (boxes). (B1 model, 42 total domains), b) B0 model with three domains

The geometry made is 40 x 3.1 x 1 mm^3 (length, height and width). The front and back surfaces are symmetrical to make the geometry a 2D domain. The length is sufficient so that all the variables have constant axial gradients near the outlet. The catalyst is placed from 10 to 20 mm. However, the profiles are plotted from 5 to 25 mm but dubbed as 0 to 20 mm for consistency with the paper. Some different models need more domains in the research, so a 42 domains model is made (B1).

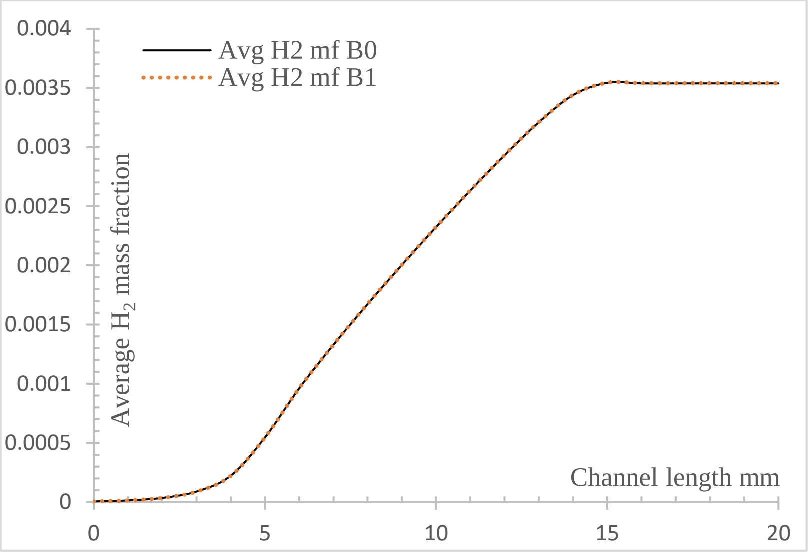

Figure 4-2: Difference between average hydrogen profile between B1 and B0 domains geometry

Every domain has a boundary, and it can exchange mass or energy with the surrounding domains depending on the interface between them. Both geometries are tested under the same conditions (B0 and B1, B means basic model). The error between the hydrogen mass fraction at the outlet is negligible. For later plots, the ‘average’ prefix before the mass fraction (mf) is removed, and all the mass fractions are average mass fractions unless they are local values at a surface. Contours values are generally local values of variables. Temperature and rate profiles are extracted at the channel's lower wall, and average values are calculated at discrete numbers of the channel's cross-section, so ‘channel length’ is used for the x-axis.

The (Figure 4-2) hydrogen profiles show that the hydrogen production for B1 and B0 models are the same throughout the length. All other profiles and contours of B1 and B0 match with the same accuracy.

4.1.1 Fine mesh

The mesh quality for the model is 1.00, and a total of 34902 hexahedra elements are used at the surface. The mesh near the wall and boundary transition is refined to the least value of 1E-5. A growth ratio of 1.2 is used, which means the next element height is 1.2 times the first element and so on. This type of mesh is called hyperbolic in the software.

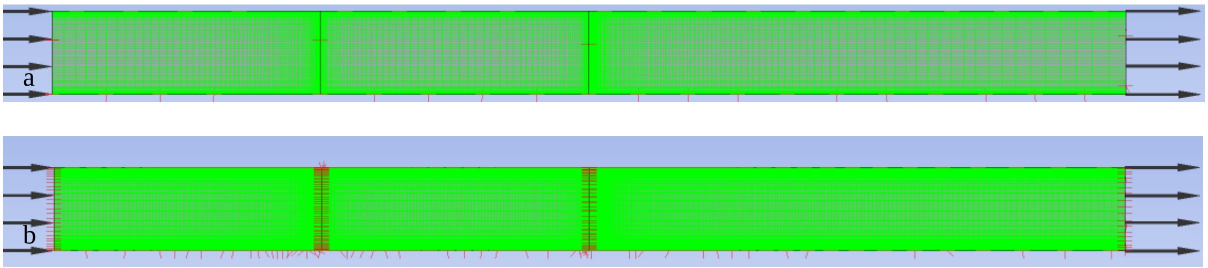

Figure 4-3: a) The hyperbolic mesh used in this study (34902 elements) b) mesh generated by setting twice edge elements for mesh sensitivity analysis (B0) (2 x 34902 elements)

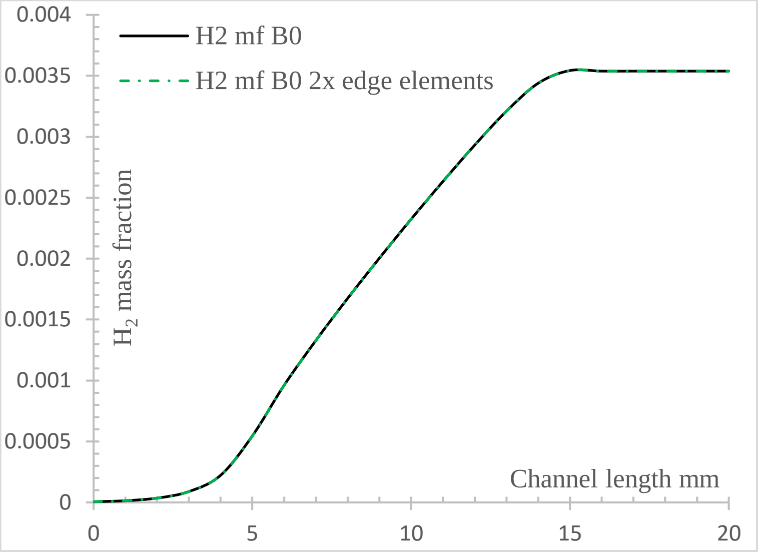

Figure 4-4: Mesh sensitivity analysis for H_2 mf profiles

Table 4-1: Difference between various quantities using different mesh sizes and number of domains

Quantity	**B1**	**B0**	**B0 2x(fine)**
T_{min}	695.35 K	695.37 K	695.36 K
$H_{2\ avg,max}$	3.539e-03	3.538e-03	3.538e-03
$CH_{4\ avg,min}$	6.061e-02	6.061e-02	6.062e-02
$H_2O_{avg,min}$	2.795e-01	2.795e-01	2.795e-01
$CO_{avg,max}$	1.639e-02	1.639e-02	1.639e-02

All the RMS (root mean squared) residuals met the convergence criteria of 1E-8. However, the energy residual remains below 1E-5 but above 1E-6, which is also sufficient. More details about mesh quality and convergence are in Appendix A and C.

The end difference between the chosen mesh size and double of it is insignificant. Overall, both profiles match well with each other.

4.1.2 Coarser mesh

Two new mesh are generated to find mesh dependency for coarser meshes, with a convergence limit set the same as before. One mesh is generated using the refinement at the boundaries (hyperbolic mesh), and the second adopted mesh contains nearly similar size cells (uniform mesh) throughout the domain. Both meshes are coarser than before. A total of 9600 elements are used for the coarse meshes.

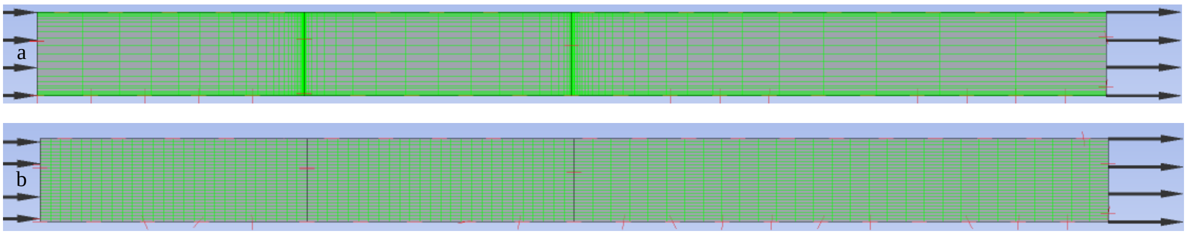

Figure 4-5: a) hyperbolic coarse b) uniform coarse mesh (B0)

After the second significant value between results, a difference shows that the mesh will not cause issues and is sufficient. So B1 model with fine hyperbolic mesh is used as a standard design for all the other models in this study unless specified.

Table 4-2: Difference between various quantities values using fine and coarser meshes (B0)

Quantity	**B0**	**B0 hyperbolic coarse**	**B0 uniform coarse**
T_{min}	695.37 K	695.27 K	695.28 K
$H_{2\ avg,max}$	3.538e-03	3.548e-03	3.556e-03
$CH_{4\ avg,min}$	6.061e-02	6.059e-02	6.057e-02
$H_2O_{avg,min}$	2.795e-01	2.794e-01	2.794e-01
$CO_{avg,max}$	1.639e-02	1.643e-02	1.647e-02

4.2 Base case

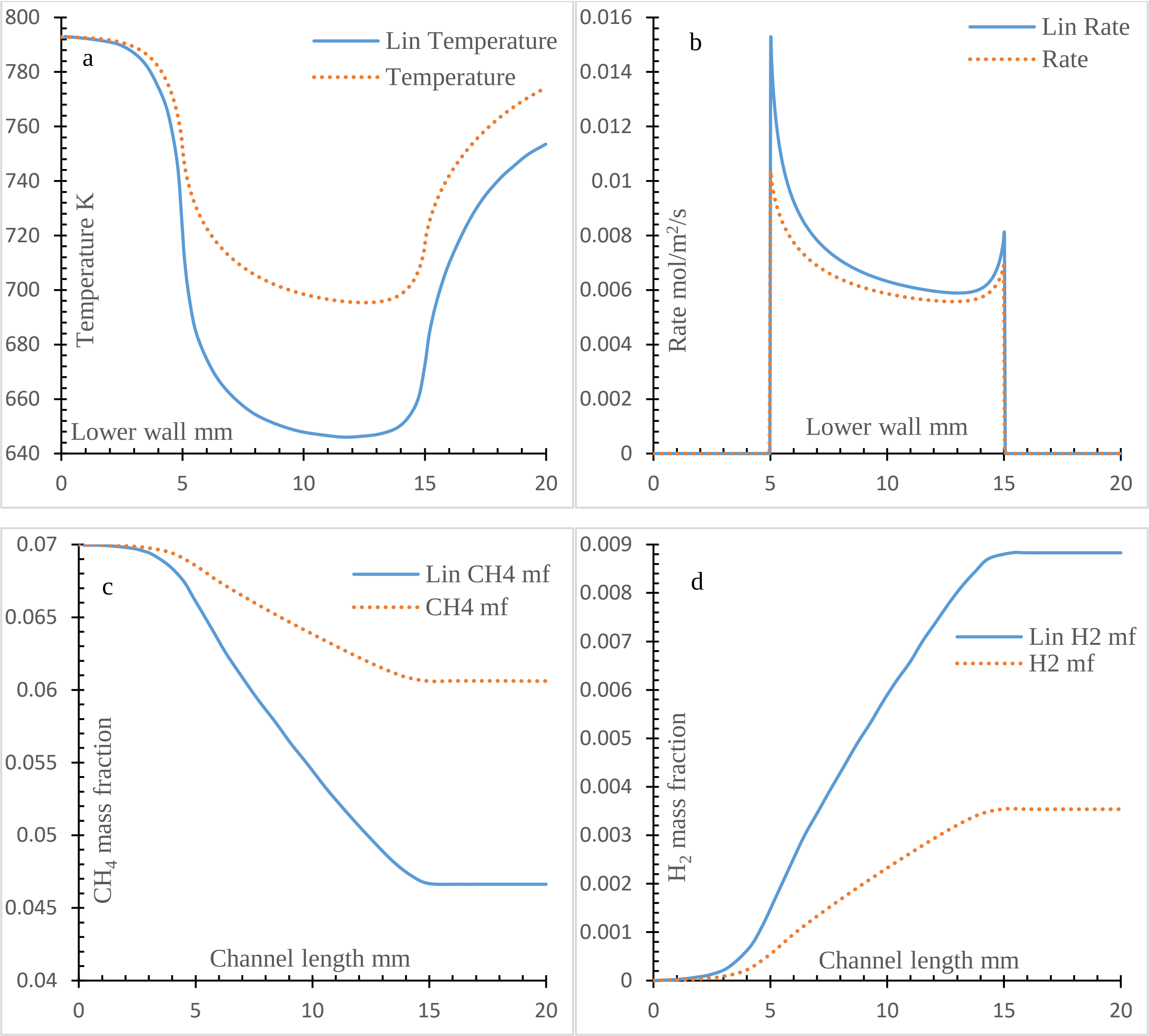

Figure 4-6 Comparison between this study and Lin’s profiles of a) temperature b) rate, c) methane, and d) hydrogen (B1 model)

The next step is to compare each parameter mentioned in Lin paper to this study results. The obtained results differ from Lin’s results in magnitude only.

The profiles for temperature, rate, and methane and hydrogen mass fractions are reported in Figure 4-6. The discrepancy between all the profiles is overwhelming, i.e. more than fifty per cent. The mf profiles for water and carbon monoxide are not stated as the reaction is conserved. So simple, one reactant (CH_4) and one product (H_2) profiles are reported.

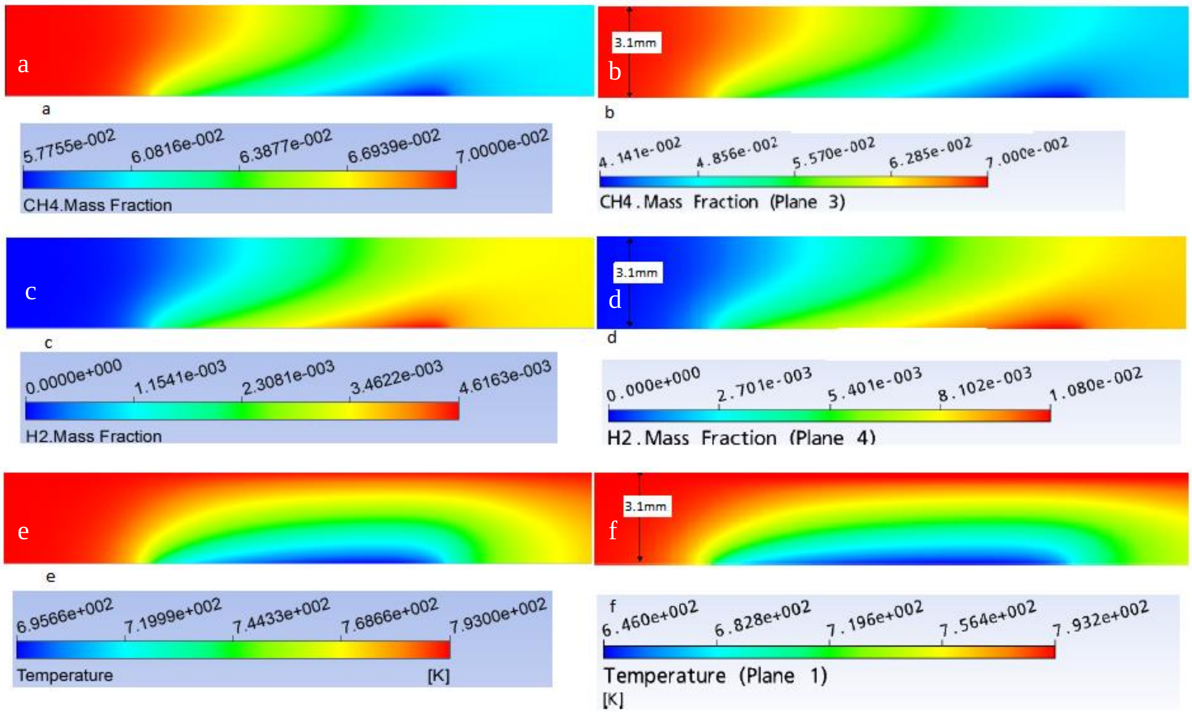

Figure 4-7: a, c, e) CH_4, H_2 and temperature contours (B1 model, default D), b, d, f) Lin *et al*. CH_4, H_2 and temperature contours

Next, contours for temperature, methane and hydrogen mass fractions are compared.

4.2.1 Diffusion coefficient

The contours show that there is a qualitative match. However, a closer look reveals that parameters in Lin's contours are more widespread. For instance, the local methane mass fraction is more prevalent from catalyst to the entire domain (blue is more dominant). This prevalence can be due to a higher value of diffusion. The same logic applies to hydrogen and temperature contours (Figure 4-7).

The diffusion coefficient (D) value is variable, and for the temperature range in Figure 4-7e, the diffusion coefficient varies from 6.8-9.2 E-5 $m^{-2}s^{-1}$. A constant value of diffusion coefficient is used until there is a suitable match between contours, qualitatively. A constant value of 10.38 E-5 for D is reasonable to give comparable contours like the paper. The results look like the following.

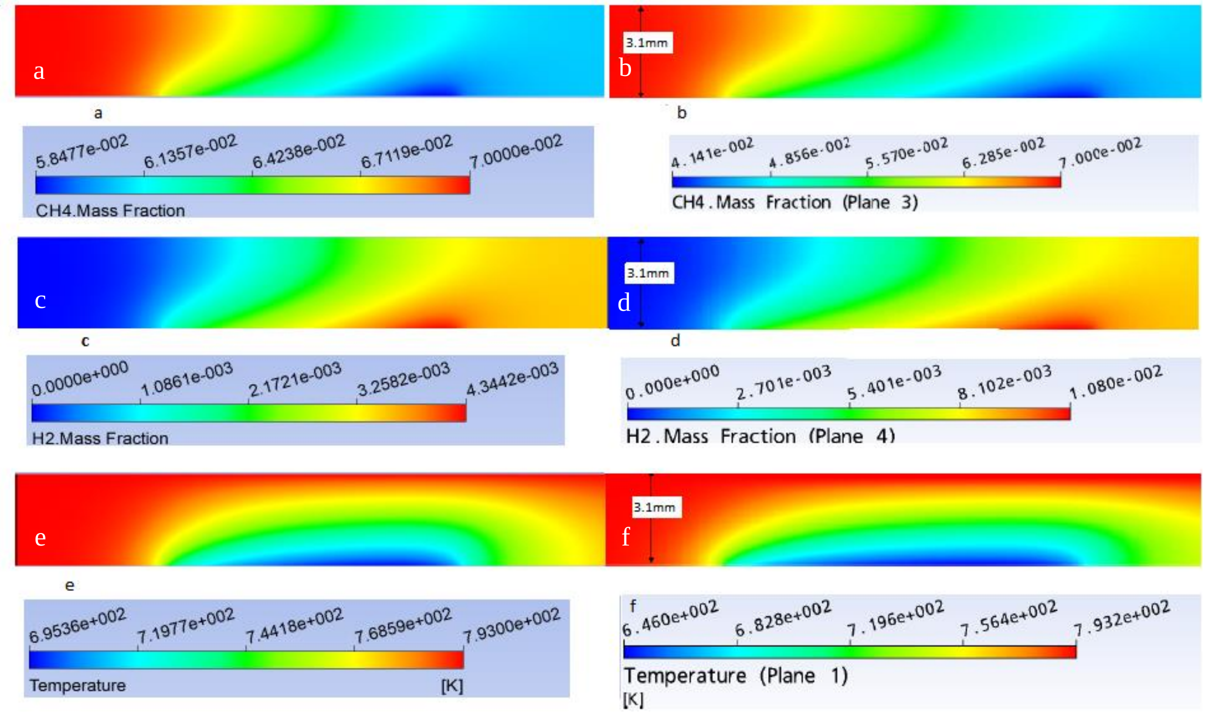

Figure 4-8: a, c, e) CH_4, H_2 and temperature contours with constant D value 10.38 E-5 (B1 model), b, d, f) Lin *et al*. CH_4, H_2 and temperature contours

The difference between variables values for default (Figure 4-7) and constant D (Figure 4-8) is evident. After setting a constant D value, the parameters diffuse more in the domain. For instance, the maximum hydrogen mass fraction for the default D is 0.00462, and constant D is 0.00434.

The temperature and other profiles (Figure 4-9) for constant (black) and default D match each other. Though mass fraction ones nearly overlap at the end of the catalyst (15 mm), it seems due to the higher diffusion value, the mass fraction profiles for constant D start a little earlier. This trend is noticeable as black lines are leading dotted lines for both mass fractions.

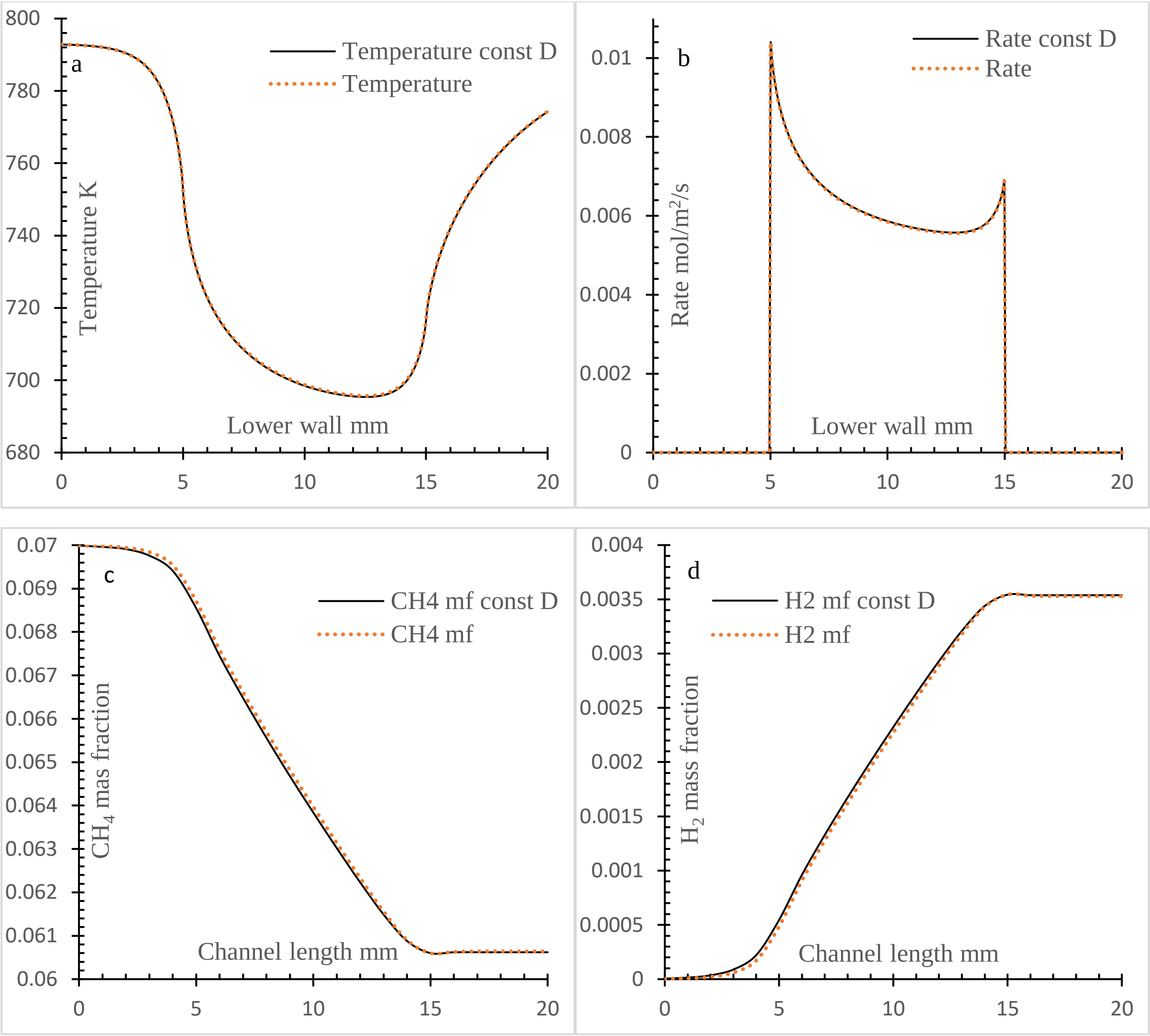

Figure 4-9 Comparison of profiles with constant and default value of D for a) temperature b) rate c) methane and d) hydrogen (B1 model)

4.2.2 Ideal Gas vs Real Gas

As a next step, the ideal gas library is selected for the SMR reaction, from materials, for the following simulation (for more details, see Appendix A). All the other conditions are the same. The ideal gas extends the local mass fractions profiles more, but the average values are nearly identical. Figure 4-10c & d compare mass fractions, and Figure 4-11 highlights the local mass fraction difference at the wall.

The temperature profile for ideal gas remains higher until the end of the catalyst near 13 mm, and the rate profile follows the temperature trend. Later, the temperature drop causes a lower rate value and reduces reactant consumption and product generation. The spread of mass fractions plots, in Figure 4-11, can be explained by different diffusion values. The diffusion expression is $D = \frac{\lambda}{\rho C_p}$ (see Appendix C). By comparing thermal conductivity λ, density and specific heat capacity at constant pressure (ρ and C_p) of Ideal Gas and Real Gas, we can determine D value.

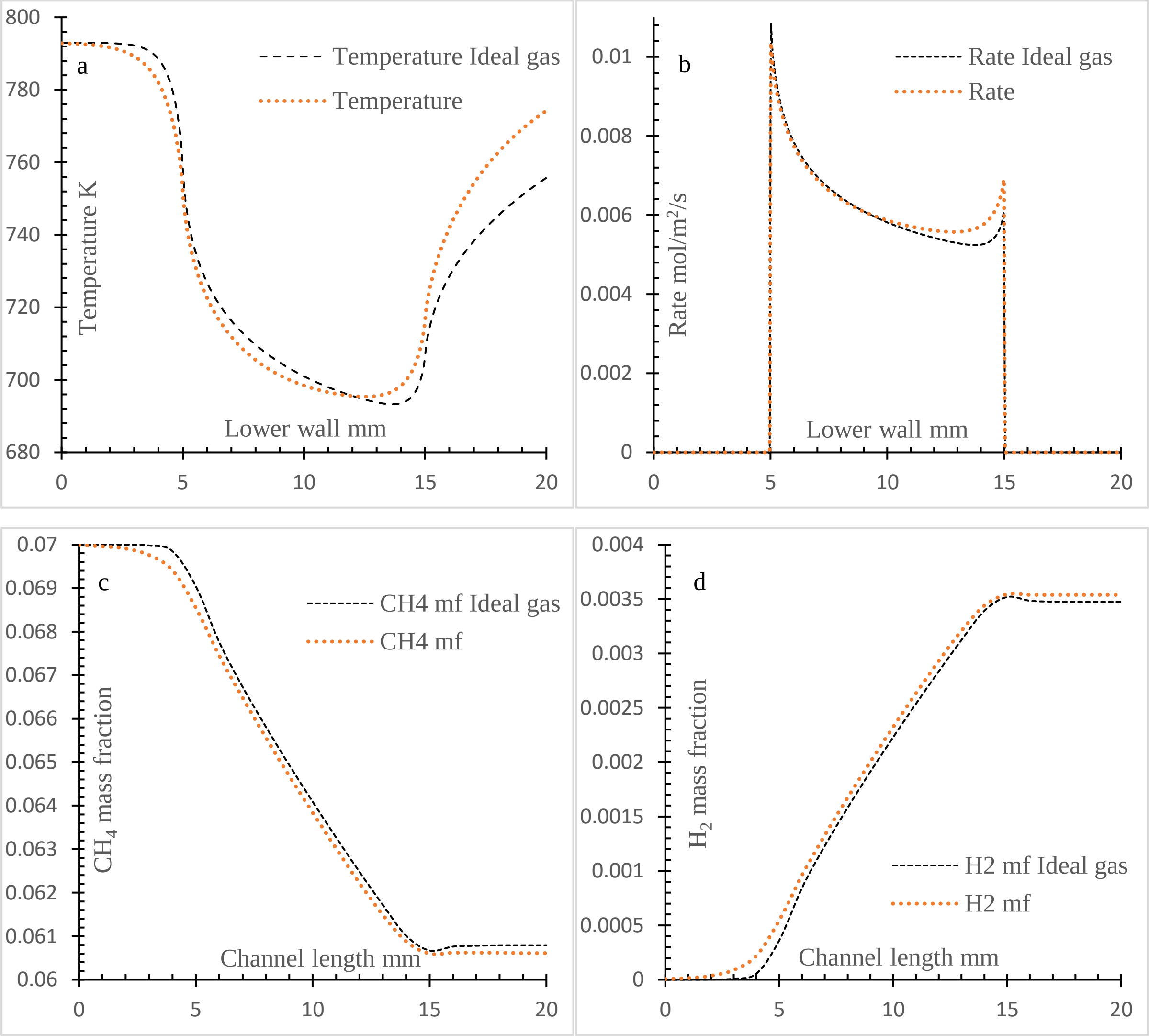

Figure 4-10 Comparison of profiles between real gas and ideal gas for a) temperature b) rate c) methane and d) hydrogen (B1 model)

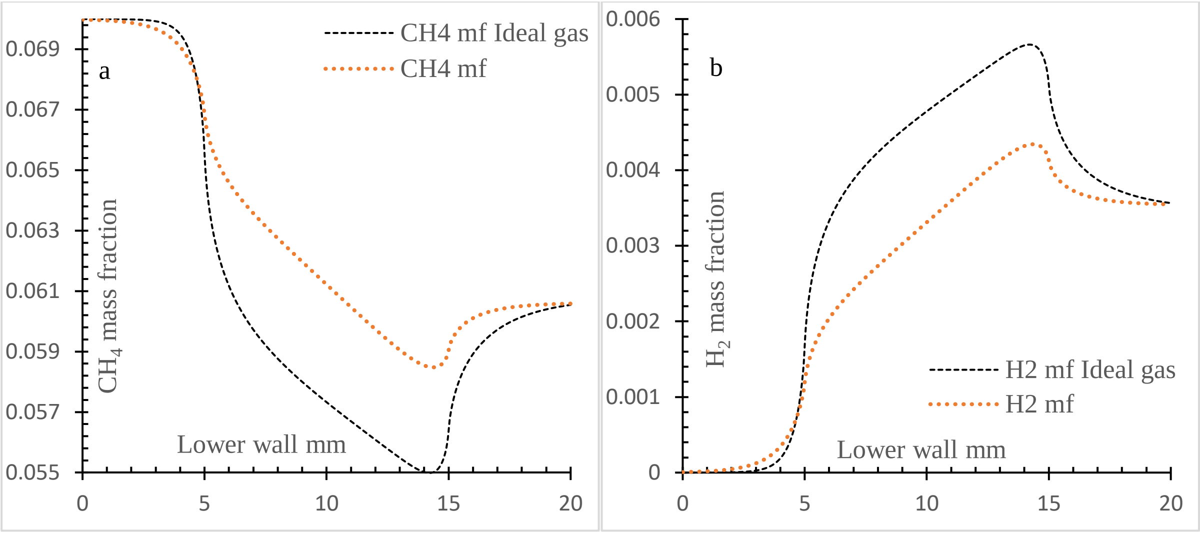

Figure 4-11 Difference between ideal local gas and real gas profiles for a) methane, b) hydrogen at the lower wall (B1 model)

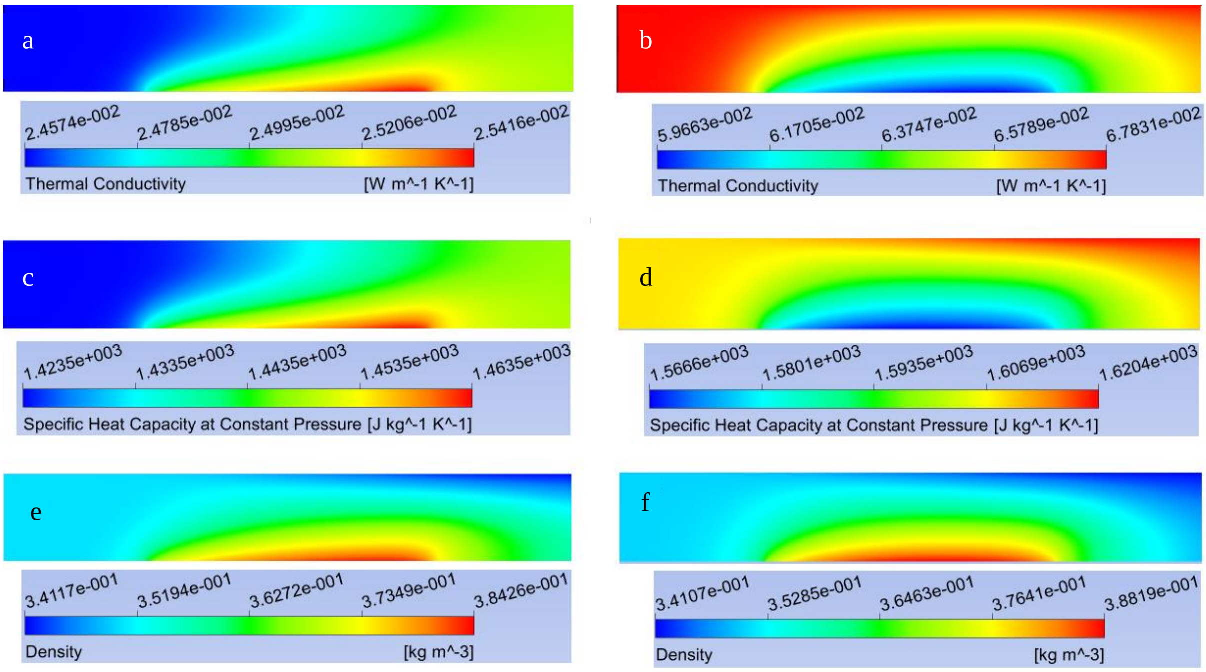

Figure 4-12 Contours for λ, C_p and ρ for a, c, e) ideal gas and b, d, f) real gas (B1 model)

The higher thermal conductivity values for real gas means that the diffusion value will be higher than the ideal gas value. This difference explains the profile shapes of Figure 4-11 for ideal gases. Therefore, the higher diffusion value makes real gas diffuse rapidly, reducing the local value of mass fraction (at the lower wall). Nonetheless, the diffusion does not significantly change the outlet's net yield (Figure 4-10c & d).

4.2.3 Velocity inlet vs mass flow inlet

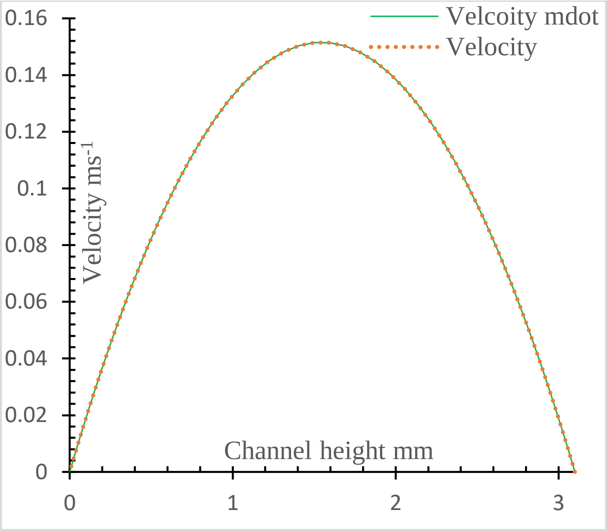

Figure 4-13: Velocity profile at 20 mm length for mass flow rate inlet (mdot) and velocity inlet condition (B1 model)

Velocity should change according to the inlet pressure. Alternatively, the mass flow rate can be evaluated at 1 bar to be used as the inlet condition for the higher pressure. Higher operating pressure constitutes higher density, so the flow speed reduces for the constant mass flow rate.

First, density is calculated using the formula given in Appendix C. The measured density value is 350.28847 gm^{-3}, and the mass flow rate is 1.08593E-7 kgs^{-1}. Both mass flow rate inlet and velocity inlet conditions give the same velocity profile at 20 mm of channel length. This equivalence ensures that the calculated mass flow rate for the velocity inlet condition is a suitable boundary condition for high operating pressure (Table 3-1).

4.3 Setting paper plots values as boundary conditions

Failure to reach the profile as in the paper, exact data points of the profiles are fed in the software in the next step. This method determines which variable is causing the error and propagates it to the others as the reaction is conserved.

The rate equation determines the reaction and both fluxes. For instance, for heat flux, only rate changes and enthalpy of the reaction is constant. Similarly, the rate portion changes for mass fluxes, and the molar mass of species is constant (Equation 4-2). Overall, if the rate profile is the same, then both heat and mass flux should produce the same results.

The rate equation weakly depends on partial pressure terms (Equation 4-1) as exponential indexes are small (*a* = 0.47, *b* = -0.01). Hence temperature is mainly governing rate profile, so the temperature profile is extracted from the paper plot through a digitizer tool. After extracting the data as CSV (comma-separated value) file, it is loaded in the simulation

4.3.1 Temperature profile as an input boundary condition

The results for putting the exact temperature profile as paper are reported in Figure 4-14. The temperature profile is now independent of reaction as the software just maps data from the spreadsheet. Now, the temperature profile values are lower than the base case, so the rate profile diminishes. As a result of reduced rate values, methane and hydrogen's average mass fraction conversions have fallen (Equation 4-2).

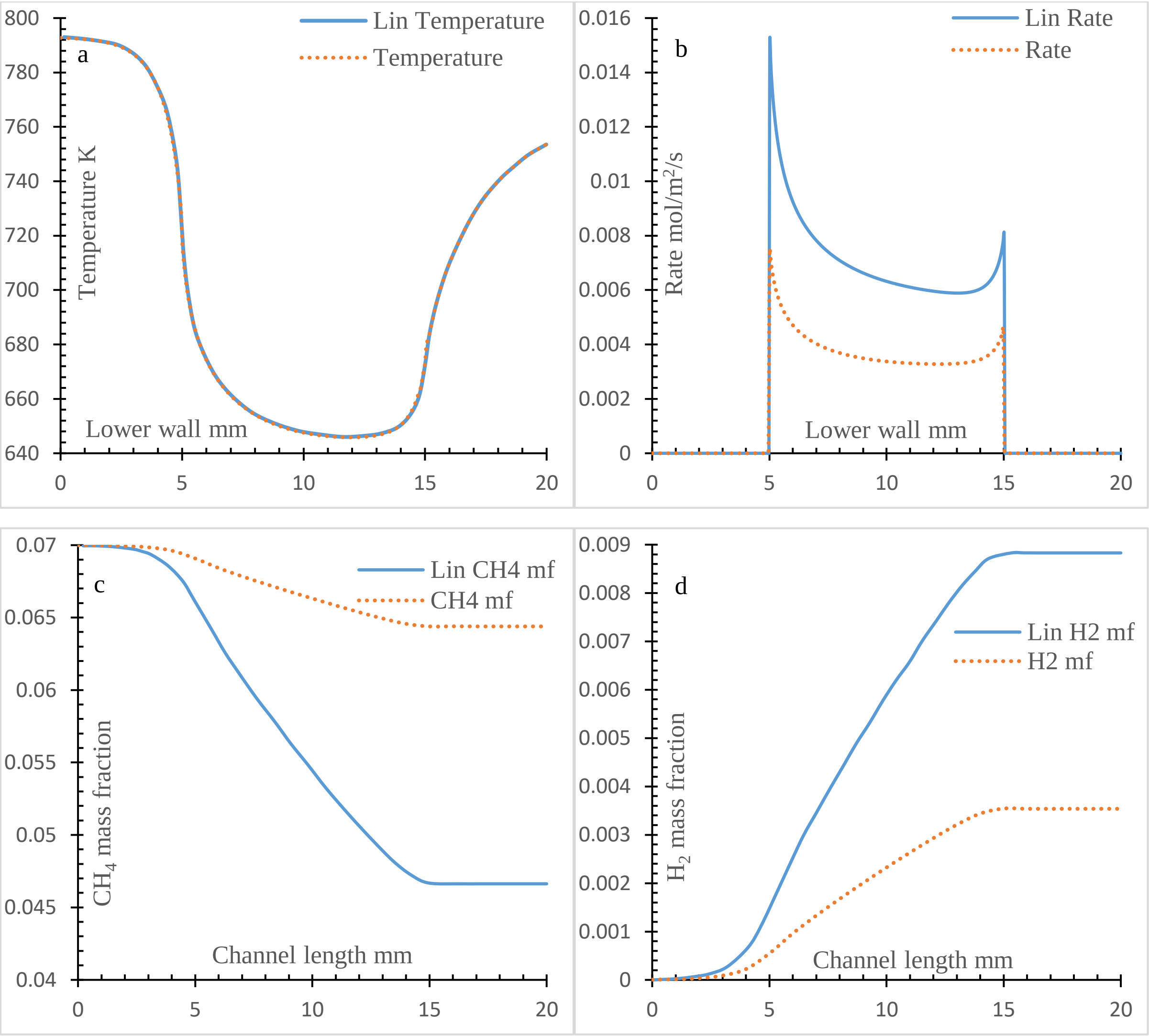

Figure 4-14: Comparison between temperature profile as input, and Lin's profiles of a) temperature b) rate c) methane and d) hydrogen (B1 model)

Overall above discussion means that the rate equation is strongly dependent on temperature. Therefore, if the temperature profile becomes accurate, the rate profile should be correct.

$$Rate = \ A \ \times e^{-\frac{E}{RT}} \times CH_4P^a \times H_2OP^{-b} \times catalyst\ loading$$

Equation 4-1: Surface reaction rate equation for steam methane reforming

$$mass\ flux_j = \ (\varepsilon" - \varepsilon') \ \times Rate \times M_i\ (a)\ heat\ flux_j = \ Rate \times \Delta H_j\ (b)$$

Equation 4-2: a) Species generation and consumption as flux b) heat loss or gain as flux at catalyst (repeated)

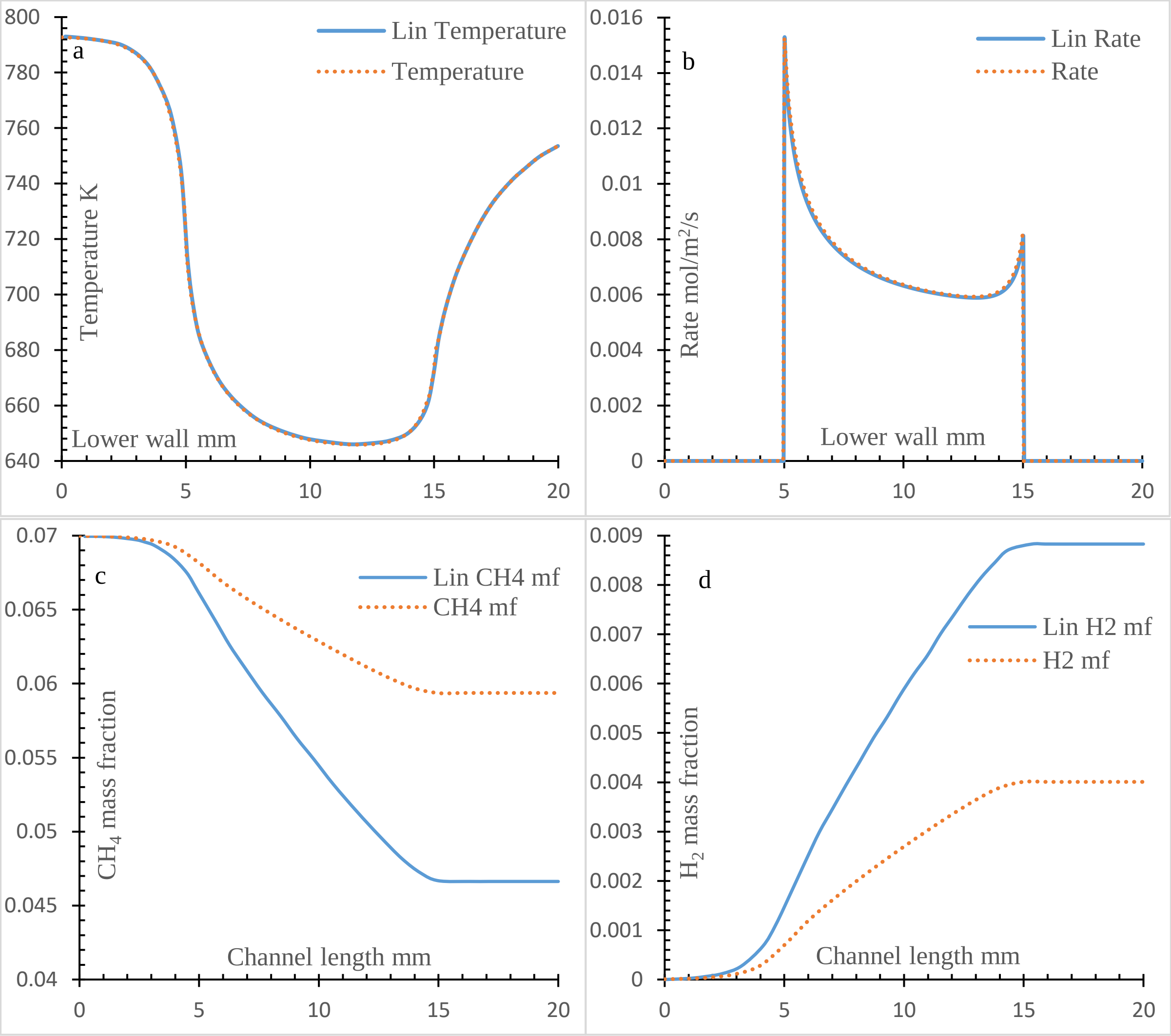

Figure 4-15: Comparison between with rate and temperature profiles as input, and Lin's profiles of a) temperature b) rate c) methane and d) hydrogen (B1 model)

The temperature profile as input does not deliver the desired results. However, having an accurate rate profile means that the reaction should produce the same amount of products and consume the same amount of reactants as the paper. The results are reported in Figure 4-14. So as a next step, both temperature and rate profiles are set as input through CSV files.

4.3.2 Temperature and rate profiles as input boundary conditions

Even setting both temperature and rate profile appears that the paper fails to give the desired mass fractions of reactant (CH_4) and product (H_2) (Figure 4-15).

4.3.3 Rate profile as an input boundary condition

The mass fractions increase for setting rate profile as input (Figure 4-16), but the temperature falls more than the base case (Figure 4-6). This trend is expected as a higher rate translates to higher fluxes (heat and mass).

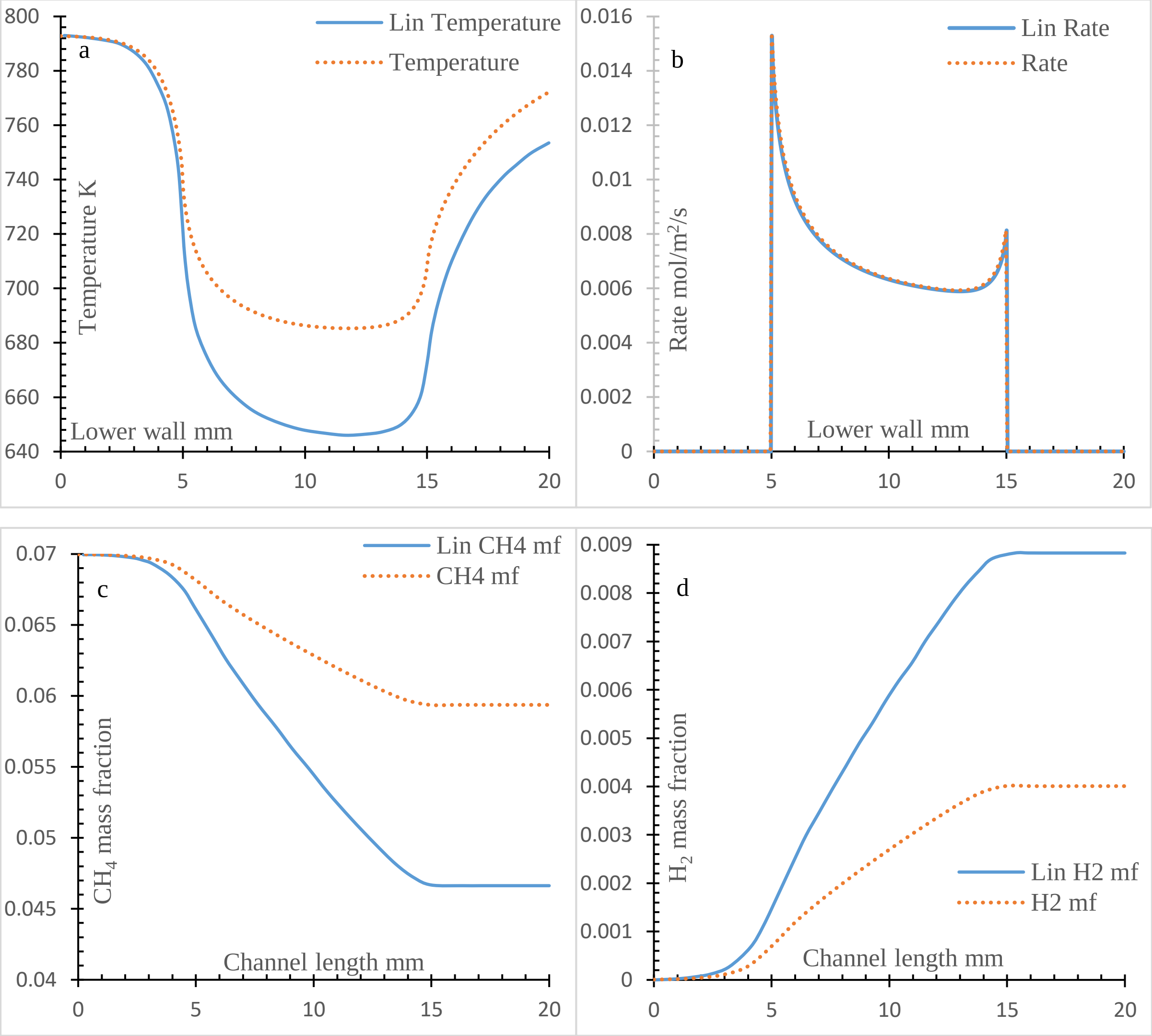

Figure 4-16: Comparison between rate profile as input, and Lin's profiles of a) temperature b) rate c) methane and d) hydrogen (B1 model)

4.3.4 Mass profiles as input boundary conditions

However, by setting mass fractions profiles as input (Figure 4-17), both rate and temperature touch lower values than the base case (Figure 4-6). The rate is directly proportional to reactants partial pressure, so lower methane concentration means lower partial pressure values. Though the rate is weakly dependent on the pressure terms, the high consumption of reactants (three times mf conversion than the base case) causes this considerable fall. Moreover, it achieves the lowest temperature, which is the primary reason why the rate profile is the lowest. The minimum temperature is due to the highest methane consumption, meaning higher is the endothermic reaction.

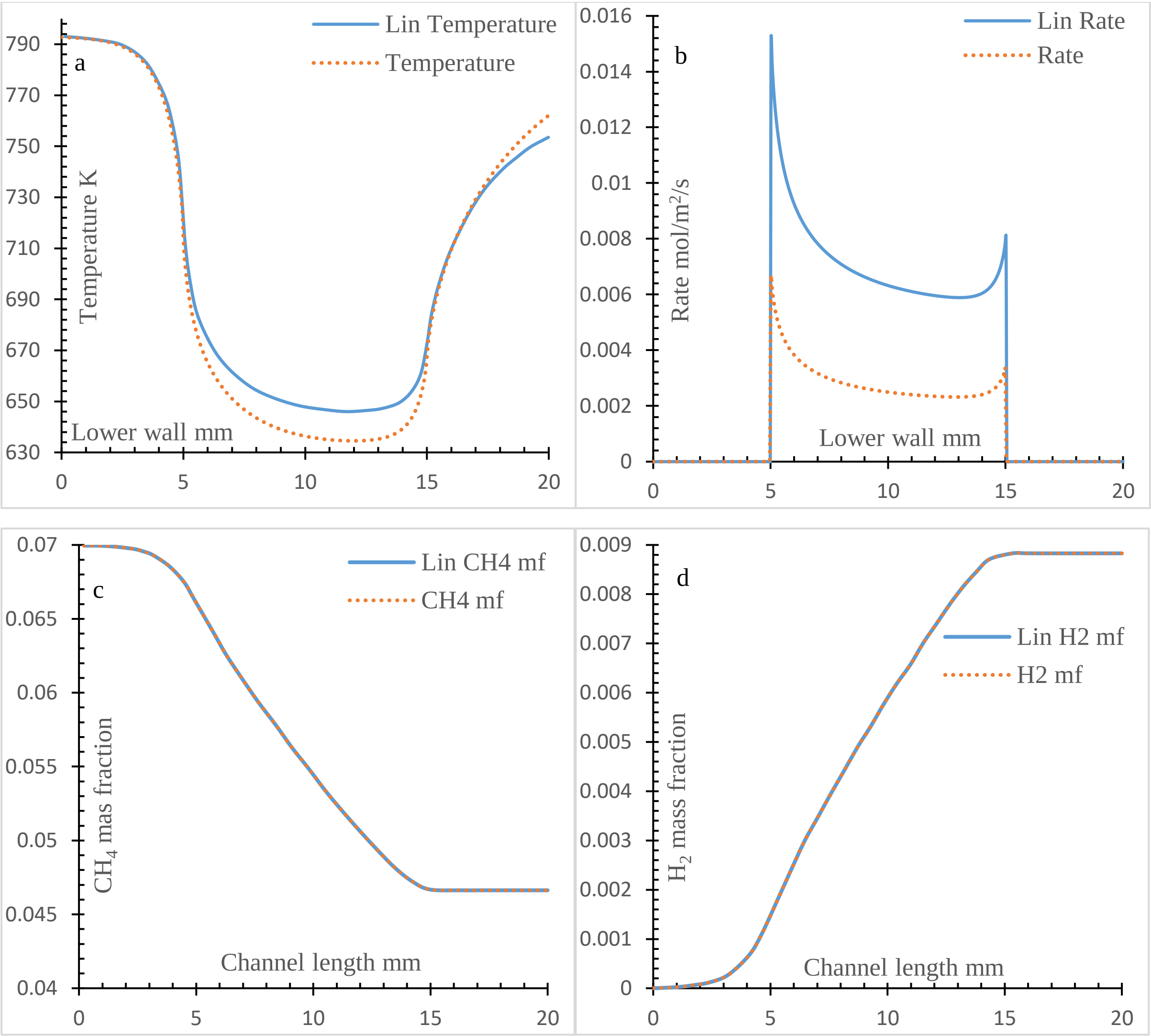

Figure 4-17: Comparison between mass profiles as input, and Lin's profiles of a) temperature b) rate c) methane and d) hydrogen (B1 model)

In general, section 4.3 shows conservation among temperature, mass fraction and rate. It also explains that each of the single terms changes the overall reaction.

4.4 Catalyst loading calculation

Catalyst loading is calculated assuming no reaction occurs but only at the catalyst surface. Thus, the mass fraction and temperature values at the catalyst start are considered the same as the inlet conditions.

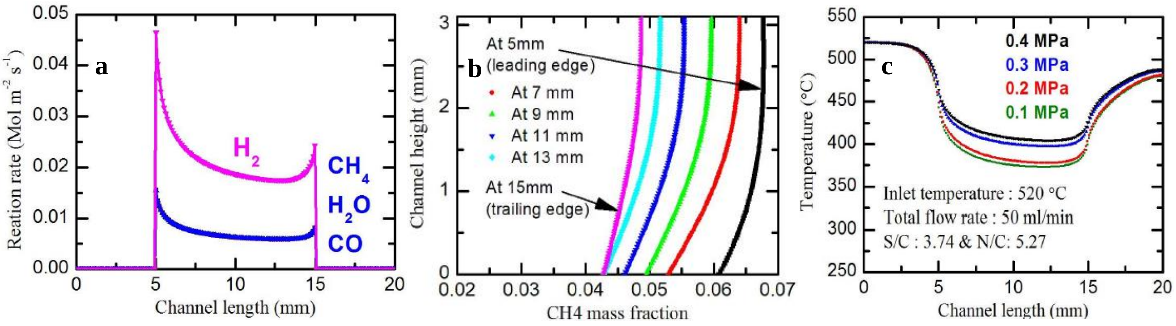

Figure 4-18: Plots for a) local surface reaction rate, b) local methane mass fraction, and c) average temperature (LIN *et al*., 2012)

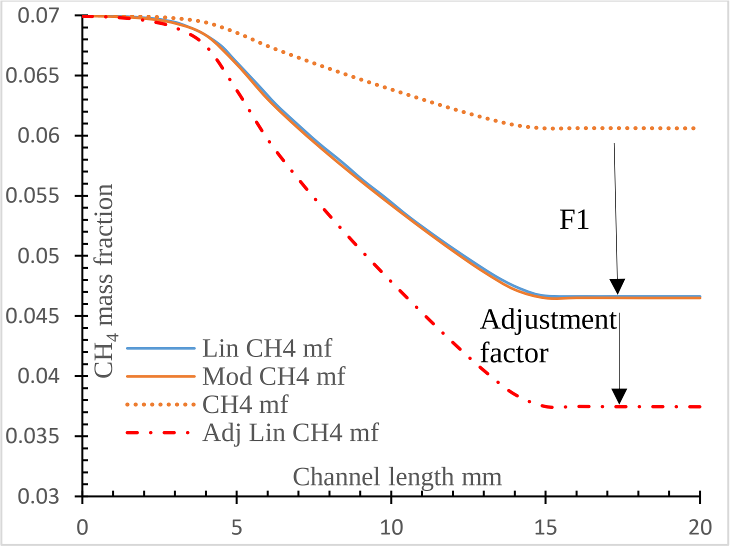

Figure 4-19: Illustration of factor ‘F1’ and adjustment factor for CH_4 at 1 bar

At 5 mm down the channel, rate, methane mass fraction and temperature values are extracted through a web digitizer tool. These values are 0.01521 molm^{-2}s^{-1}, 0.061, and 715 K, respectively, and are very different from the inlet conditions. The reasons are fluid mixing and diffusion, which reduce these temperature and mass fractions values at 5 mm. So catalyst loading is calculated from the rate equation for both conditions; the first assumes maximum mass fraction and temperature values, and the second considers local temperature and mass fractions values from the plots (at 5 mm). The rough calculations are as follows:

$$CH_4\ mass\ fraction = 0.061 = w_{CH_4},\ \sum M_{SMR} = M_{CH_4} + M_{H_2O} + M_{N_2}$$

$$\sum M_{SMR} = 16.04 + 18.02 + 28.01 = 62.07$$

$$Mass\ in\ gram_{CH_4} = 62.07 \times 0.061 = 3.772917g, \sum moles = \ 2.688022$$

$$mole\ fraction_{CH_4} = 0.235219, CH_4P^{0.47} = (0.1MPa \times 0.24)^{0.47} = 71.68786\ Pa^{0.47}$$

$$\text{Similarly } H_2OP^{-0.01} = 0.899999Pa^{-0.01}$$

$$catalyst\ loading_{local\ values} = \frac{0.01521}{0.392 \times 0.0007 \times 0.9 \times 71.7} = 0.86\ gm^{-2}$$

$$catalyst\ loading_{\max condtition} = \frac{0.01521}{0.392 \times 0.0014 \times 0.9 \times 75.8} = 0.41\ gm^{-2}$$

A more accurate values entry is given in the following Table 4-3. This upstream effect should correspond to the actual value of the rate (Figure 4-18a) at 5 mm. So, if local conditions for mass fraction and temperature are used (Figure 4-18b and c) at 5 mm, then calculated catalyst loading is 0.866858 gm^{-2}. This variance gives a scale-up value of $\frac{0.866858}{0.398563} = 2.18$. Also, local values seem more plausible as the simulation is steady-state.

Table 4-3: Catalyst loading calculated for maximum and local conditions (bold values) at 5 mm of catalyst

	Cat load	***Rate***	***CH_4P***	***H_2OP***	***T***	**$e^{-E/R/T}$**	**Pressure**	***A***	**F1**
1	0.398563	1.52E-02	75.82213	0.900069	793	0.001426684	100000	0.392	1
2	0.866858	1.52E-02	**71.24573**	**0.900117**	**715**	0.000698057	100000	0.392	2.1749

In summary, considering the inlet conditions at the catalyst start gives calculated catalyst loading to be 0.398≈0.4 gm^{-2} from the rate equation. Else, these variable values at the exact point produce 0.86 gm^{-2} of catalyst loading.

4.4.1 Variables proportionality

From Figure 4-14 to Figure 4-17 plots, it is already clear that matching only a single profile does not help to agree with the rest of the profiles. Similarly, it is safe to assume that catalyst loading cannot be solely responsible. Due to two different catalyst loadings in the rate equation, the scale-up is called “the cumulative factor of variables at local conditions” or F1.

For the sake of argument, let us assume that F1 entirely originates either from partial pressure or catalyst loading or temperature. Then its contribution from the rate equation is calculated accordingly. It is observable that each term’s contribution is not linear, though all the terms are directly proportional to the rate equation.

$$Rate \ \propto catalyst\ loading \propto \ partial\ pressure\ ^{0.46} \propto e^{-\frac{1}{T}}$$

Equation 4-3: Rate equation relation to its variables

Now suppose that from each variable, a constant C is responsible for the factor F1. So its contribution is evaluated as follows from the rate equation:

$$\mathrm{F1} \times (\ CH4P)^{.47} \times (\ H2OP)^{-0.01} = (\ C \times CH4P)^{.47} \times (\ C \times H2OP)^{-0.01}$$

$$C^{0.46} = \mathrm{F1}$$

Equation 4-4: Factor F1 is originating just from partial pressure terms

$$\mathrm{F1} \times e^{-\frac{E}{RT}} = \ e^{-\frac{E}{RT}C}$$

$$C = ln\left(\frac{1}{\mathrm{F1}}\right)\frac{RT}{E} + 1$$

Equation 4-5: Factor F1 is originating just from exponential term

$$\mathrm{F1} \times catalyst\ loading = \ C \times catalyst\ loading$$

$$C = \mathrm{F1}$$

Equation 4-6: Factor F1 is originating just from catalyst loading

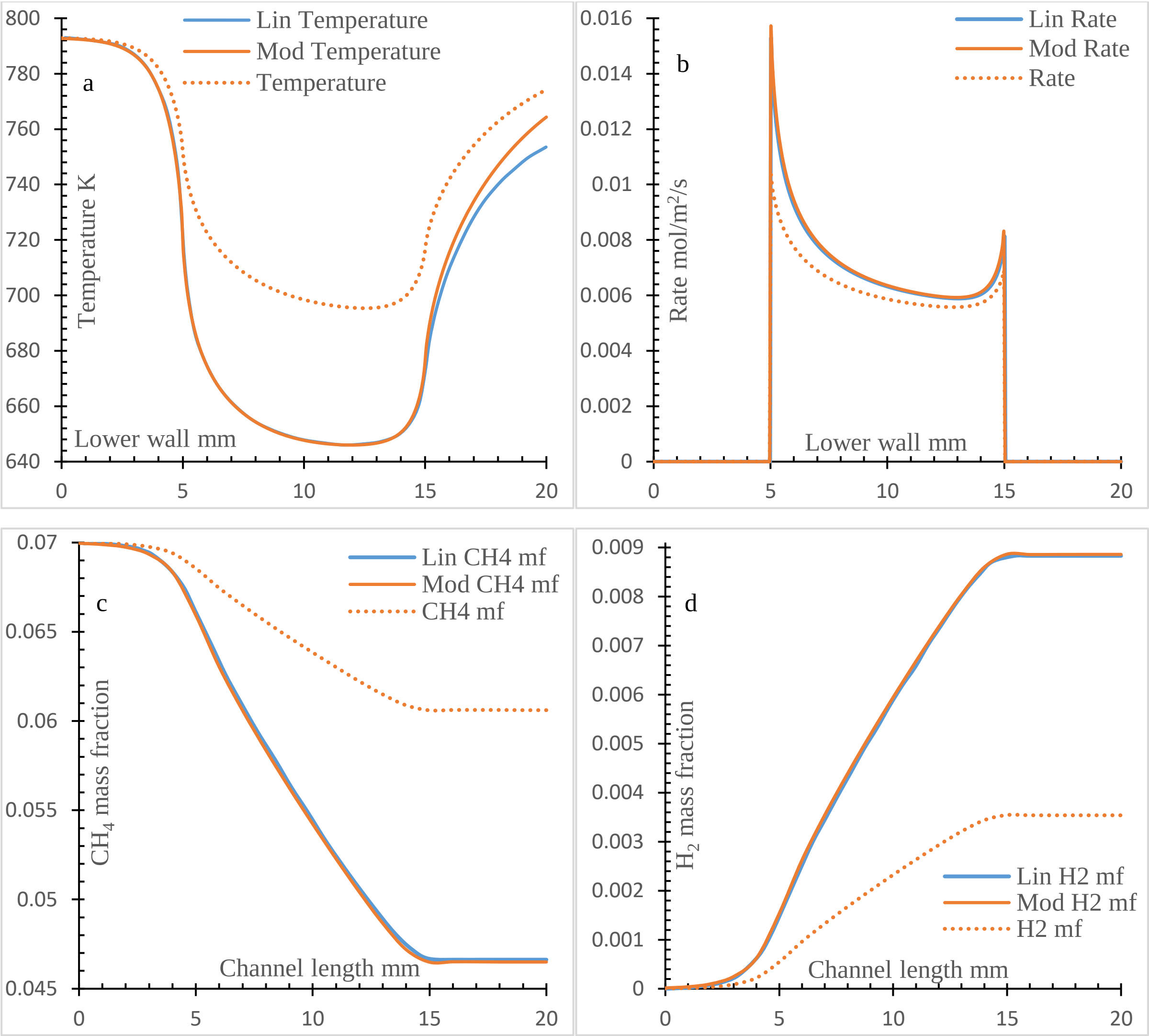

Figure 4-20: Comparison between this study, modified and Lin's profiles of a) temperature b) rate c) methane, and d) hydrogen (modified B1 model)

So F1 is introduced into mass flux, temperature flux, and pre-exponential constant in even proportion to CEL expressions (Appendix B). The assigned values for each term are such that the net value comes out to be the same as F1. There will always be discrepancies in reading slightly different temperature and mass fractions values from the plots (Figure 4-18).

$$Rate \; = \mathrm{F1} \times \; A \; \times e^{-\frac{E}{RT}} \times CH_4P^{a} \times H_2OP^{-b} \times catalyst \; loading$$

Equation 4-7: Modified (Mod) surface reaction rate equation

4.4.2 Modified rate equation and fluxes results

It can be seen that using factor F1 the values match well with Lin's results. The temperature plot for modified results deviates after 15 mm. The constant diffusion value is dominant after

F1 and allows the fluid mixture to regain heat quicker than the default D value. The reaction lasts till 15 mm, so no change in rate or mass fractions plots is observed. The modified values of the profiles match over 99% of Lin's simulation. Some maximum and minimum values are given in Table 4-4 (modified B1 model).

Table 4-4: Difference values for various quantities for the modified and Lin *et al*.

Quantity	**B1 (modified)**	**Lin *et al.***	**Margin %**
T_{min}	646.0 K	646.0 K	~0
$H_{2\ \text{avg, max}}$	0.008859	0.008829	~0.34
$CH_{4\ \text{avg, min}}$	0.04650	0.04663	~0.29
$H_2O_{\text{avg, min}}$	0.2636	0.2647	~0.42
$CO_{\text{avg, max}}$	0.04103	0.04027	~1.85

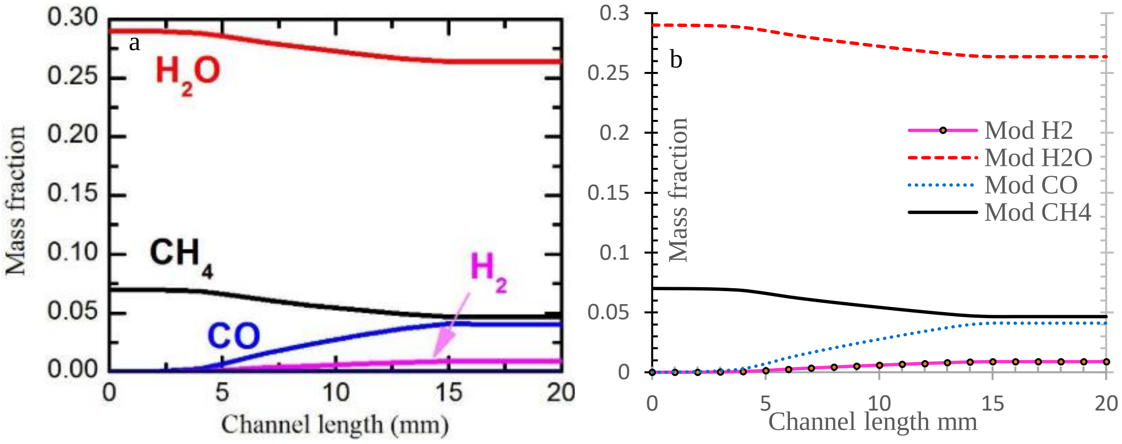

Figure 4-21: All four average mass fractions profiles a) Lin (LIN *et al*., 2012) b) this study (modified B1 model)

Average mass fractions plots are also compared with Lin's plots given in the paper. The modified rate equation plots show an agreement regarding quality and quantity (Figure 4-21). Contours for such input conditions (Figure 4-22) also match well for 0.1 MPa pressure.

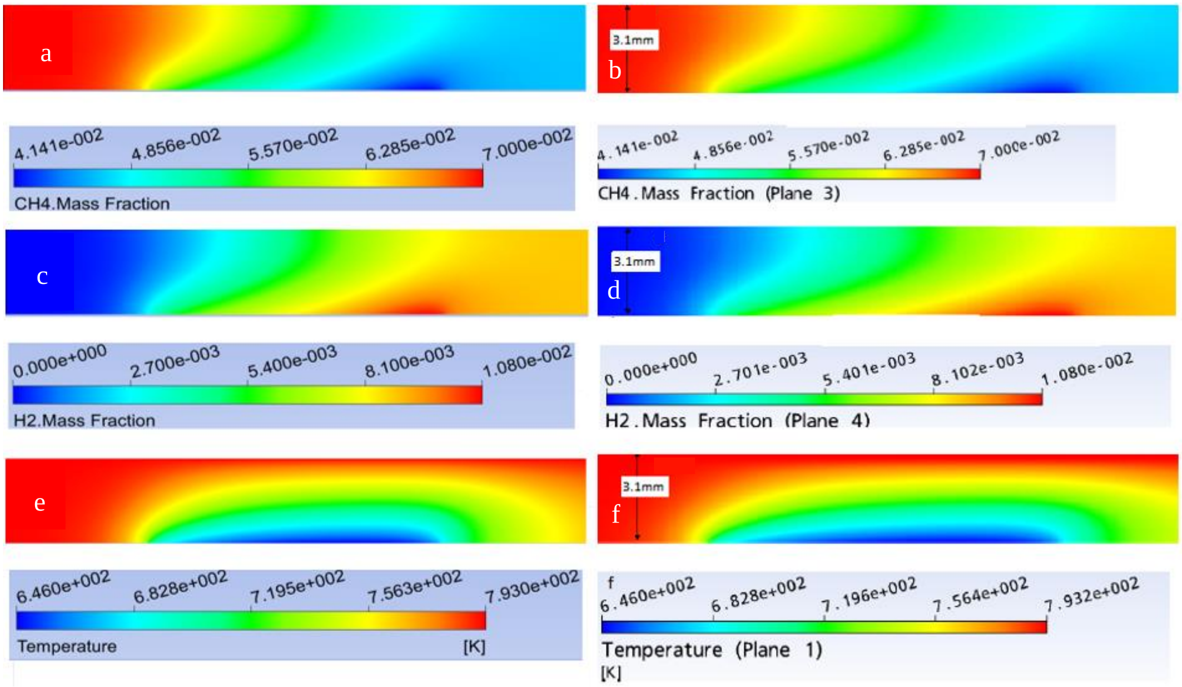

Figure 4-22: a, c, e) Modified CH_4, H_2 and temperature contours, b, d, f) Lin’s CH_4, H_2 and temperature contours (height is 3.1 mm for all, B1 model) (LIN *et al*., 2012)

The next step is to use the adjustment factor as a new pre-exponential factor to match simulation with experimental methane consumption values. Overall, there is an agreement between methane consumption results at various fuel reformers' working pressure (Figure 4-23). Furthermore, the overall confidence interval between this study and Lin’s, for various operating pressure, is more than 97 per cent.

A high factor value (of 2.2 and more) does not scale up methane consumption twice or more. It shows that the factor is a complex contribution from the rate equation. It might have behaved differently due to the higher diffusion value and Real Gas adopted in this study. High values like F1 can amplify these differences. Therefore, a difference of less than 3% is considered a validation between this study and Lin’s experimental study (Adj is after Adjustment factor, see Table 3-3).

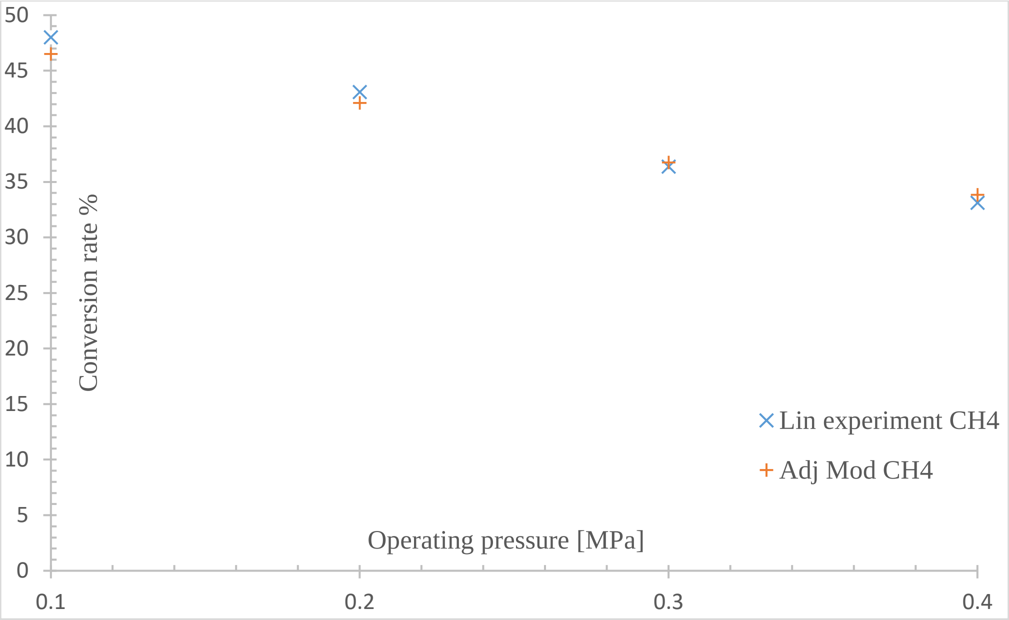

Figure 4-23: CH_4 consumption at various operating pressure (× for Lin, + is for this study) (LIN *et al*., 2012) (modified B1 model)

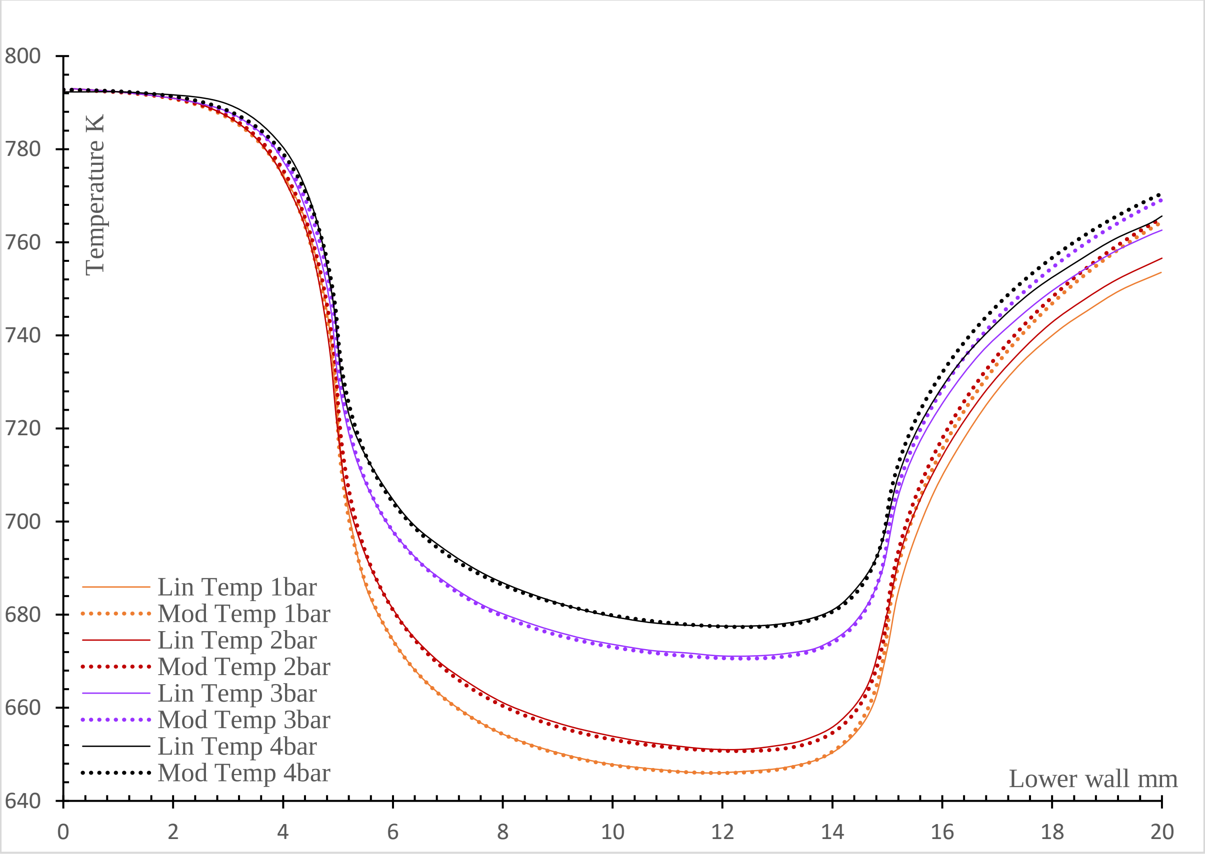

Figure 4-24: Temperature variation along the lower wall at various operating pressure for the SMR reaction (modified B1 model) (LIN *et al*., 2012)

The temperature profiles at different inlet pressure also agree with Lin's results. The 0.1 and 0.2 MPa profiles are closer. Likewise, 0.3 and 0.4 MPa profiles show a smaller gap between them. A similar trend was observed for the paper profiles.

This study's values (dotted lines) match well with the paper values (continuous lines) till the end of the catalyst (15 mm). The lowest temperature occurs at 12 mm; after that, though the reaction is still in progress, the temperature remains nearly constant due to the flat rate profile (until 15 mm). The temperature rises suddenly after the catalyst as the walls are adiabatic. So in the absence of wall conduction, the temperature rise is sharp.

As cited before, due to the higher value of diffusion coefficient D than the default value, the gas mixture regains the heat quickly, so it deviates from Lin's results after reaching the lowest temperature region. Nonetheless, at higher pressure, the difference between Lin and this study results keeps fading. This trend can be seen as black lines (0.4 MPa, continuous and dotted) have a smaller gap than orange lines after 15 mm (0.1 MPa, continuous and dotted). The smaller gap may be due to higher density at higher pressure. Similarly, in this study, gas temperature values before 5 mm are lower because it is easier for the fluid to transfer heat from the wall to its bulk (at higher pressure).

4.5 Difference between this study and Lin's model

There are few differences between Lin *et al.* and this study approach. The most noteworthy difference is that this study has not added the WGS contribution in the species transport equation. The WGS enthalpy is subtracted from the overall reaction according to Hess's Law (see section 3.3). The significant consumption of reactants has a considerable effect on rate and temperature profile, as shown in section 4.3.4. Hence, WGS omission in the species transport equation might have led to the sizeable initial discrepancy between this and Lin *et al*. results (see section 4.2).

However, after the catalyst loading calculation at local conditions, the factor F1 emerges. This factor is divided among the rate equation variables and boundary conditions so that the net value equals the same as F1 after each term's arithmetic operations (section 4.4.1). Hence, the WGS contribution in the species transport equation is compensated by the F1 variable addition in each term. The resultant boundary conditions and rate equation are therefore modified, having 'Mod' as the prefix. Therefore, this study provides an alternative method of using factor F1 instead of adding WGS contribution in the species transport equation.

The other difference is that this study has used real gas as opposed to the ideal gas used by Lin's study. However, section 4.2.2 shows that this choice causes no effect on the net yield of products.

Overall, this study model gives similar experimental values with a maximum difference of 3 per cent. The experimental values are calculated using adjustment factors proposed by Lin *et al*. Both simulations agree with each other for more than 99 per cent, as shown by temperature profiles in Figure 4-24.

The modified boundary conditions and rate equation are used for the rest of the designs and working pressure (Figure 4-20 and Table 4-4). However, the prefix 'Mod' will be dropped from the literature for the coming simulation as it is understood that all the new results include the modified rate equation and fluxes.

4.6 Chapter 4 summary

After finalising the reference designs, two models are built. The first one is B0, which is the same as Lin *et al*. but with extended length. Model B1 has 42 domains as it is needed for future designs. Incorporating all the parameters, boundary conditions and assumptions, both models agree with each other. So for further simulations, the B1 model is preferred.

After examining the contours, it appears that the diffusion value is different in the paper. Hence, a constant value of 10.38E-5 is placed as input which matches the contours with the reference. However, overall it does not affect the net reaction values at any given length.

From the paper plots, the data is extracted through a web digitiser tool in CSV files. This data is then fed as a boundary condition to the required surface. At first, the temperature boundary condition is applied in the form of exact data points. In return, the rate profile goes down, and the mass fractions profiles also diminish from the base case. When both the rate and temperature profiles are set as the boundary condition, the mass fractions profiles improves just one per cent than the base case. However, setting mass fractions profiles as input gives a closer temperature profile match but a highly deviated rate profile. It indicates that there is a high interdependency of variables.

The catalyst density is calculated using two conditions. The first assumption is no reaction before the catalyst's start, which keeps concentrations and temperature like the inlet. This assumption leads to the catalyst density being 0.4 gm^{-2}. However, due to the upstream effect at the catalyst strat, the local conditions are very different from the inlet. These local values yield a very high catalyst loading 0.87 gm^{-2} or 2.18 times than before.

However, this value is added as a resultant term of each variable contribution. The reason is that the local reduction of temperature and concentrations is not just due to the catalyst loading but originates from each of the interdependent variables. So this net value is called a cumulative factor of variables at local conditions or F1.

After putting the factor F1, the results agree well with Lin’s results. This agreement extends for higher operating pressure too. For the adjustment factor, this study simulation matches the experimental values. The overall confidence interval is more than 97%.

5 First step design

This part provides mixed results showing the effects of varying parameters on catalyst performance. The inlet and boundary conditions are the same as before unless specified. Similarly, catalyst configuration is identical except few cases which are stated before carrying out the simulation.

5.1 Parametric studies

The next step is to determine the effect of different operating conditions on fuel reformer efficiency, methane consumption, and hydrogen production. Furthermore, some parametric studies are conducted, and their results for various parameters are presented.

5.1.1 Adiabatic vs isothermal walls

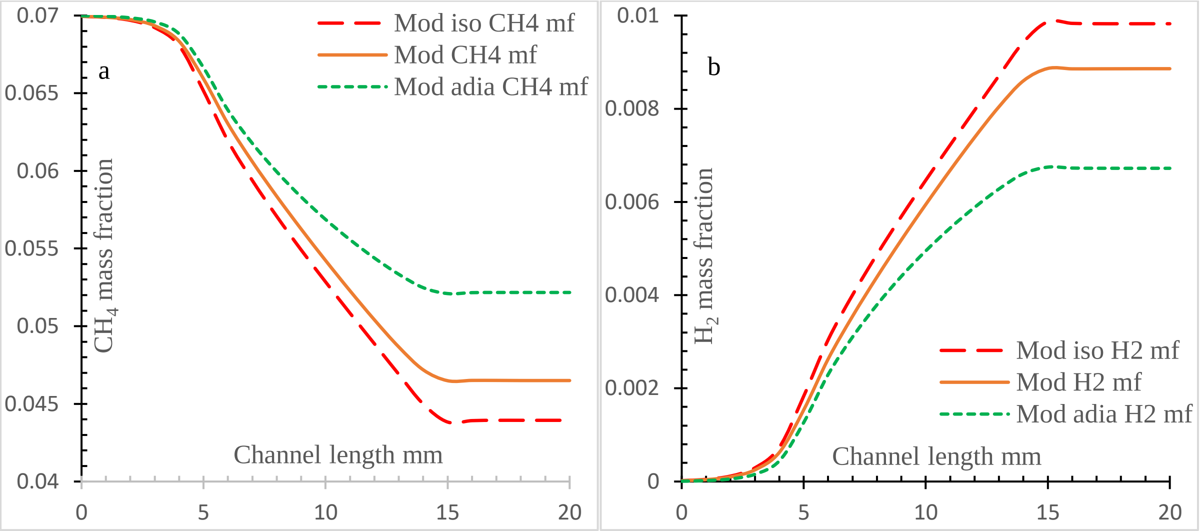

Figure 5-1: Profiles comparison of a) methane and b) hydrogen between all isothermal (Iso B1), Mod B1 model (or B1 model) and all adiabatic walls model

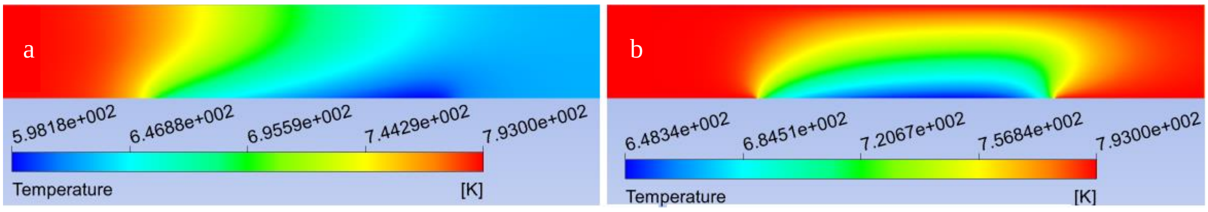

Figure 5-2: Temperature contours for all a) adiabatic and b) isothermal walls (Iso B1)

The all adiabatic walls model decreases the fuel reformer efficiency dramatically. This test emphasises the placement of heat sources near the reacting material. Hence, isothermal walls near reacting region show better results, as the surrounding temperature is higher than before.

An alternative solution can be putting a heat transfer material. For instance, a high porosity metal foam that heats the gas mixture, giving a minimum temperature gradient across the channel. Otherwise, channel height reduction can increase heat transfer from the upper isothermal wall to gases closer to the reacting material.

5.1.2 Velocity variation effects

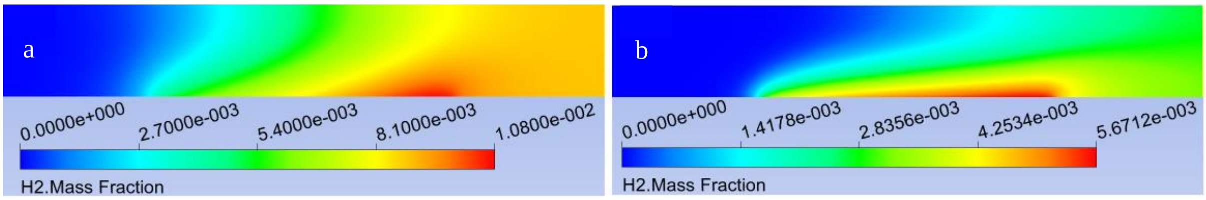

Figure 5-3: Contours for hydrogen mf for inlet velocity a) 0.1 ms^{-1} b) 0.4 ms^{-1} (B1 model)

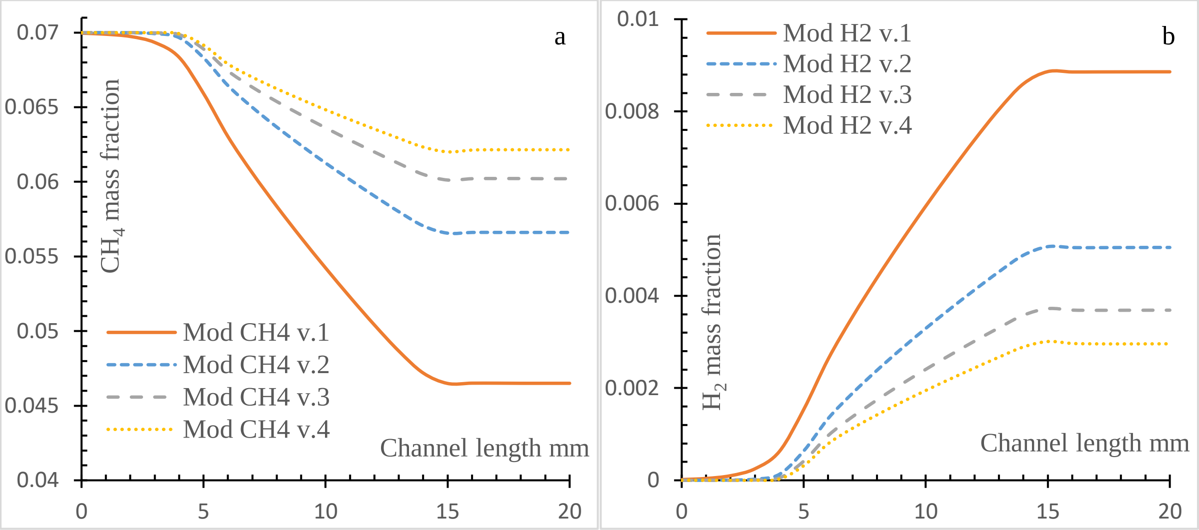

Figure 5-4: Comparison between mass fractions against various inlet velocities a) methane and b) hydrogen (B1 model)

It seems that, from the contours and plots above, increasing the velocity (0.1 to .4 ms^{-1}) reduces fuel reformer performance. Increasing the velocity at a constant mass flow rate will reduce the methane conversion because of the gas mixture's low residence time. The residence time is the time spent by fluid in the channel (section 3.5.6). Another effect of small residence time is visible by the contour for 0.4 ms^{-1}: hydrogen emerging from the catalyst (red) cannot spread in the channel but is swept by the incoming high-speed flow (Figure 5-3b).

However, as the inlet velocity increase, so does the mass flow rate. It means, at any given instant, a higher amount of reactants is present in the channel for conversion (by mass). In the table, mass fraction conversions are multiplied by the mass flow rate to give an equivalent comparison.

Table 5-1: Values for various quantities for velocities 0.1, 0.2, 0.3 and 0.4 ms^{-1} (B1 model)

Quantity	***v* 0.1 ms^{-1}**	***v* 0.2 ms^{-1}**	***v* 0.3 ms^{-1}**	***v* 0.4 ms^{-1}**
$\dot{m}_{in}$ kgs^{-1}	1.09E-07	2.17E-07	3.26E-07	4.34E-07
$H_{2\ avg,\ max}$	8.86E-03	5.05E-03	3.69E-03	2.96E-03
$CH_{4\ avg,\ min}$	4.65E-02	5.66E-02	6.02E-02	6.22E-02
$(H_{2\ avg,\ max}-H_{2,\ inlet}) \times \dot{m}_{in}$ kgs^{-1}	9.62E-10	1.10E-09	1.20E-09	1.29E-09
$(CH_{4\ avg,\ min}-CH_{4,\ inlet}) \times \dot{m}_{in}$ kgs^{-1}	-2.55E-09	-2.91E-09	-3.19E-09	-3.41E-09

It is clear from the table that a higher velocity increases the mass flow rate. Taking the difference between outlet and inlet mass fractions gives the gas species conversion fractions. Multiplying that difference with mass flow rate provides the mass conversion amount (kgs^{-1}). However, these conversions' rate decreases with speed, which means the curve is reaching a maximum value, after which increasing the velocity further will not change the conversion rate (Figure 5-5). In the case of the integrated reformer, the mass flow test gives an idea about the efficiency when the car engine is working at a high load generating higher exhaust flow rates. Note: The prefix ‘Mod’ is not used any further though the boundary conditions and the rate equation are the same as finalised in section 4.4.2.

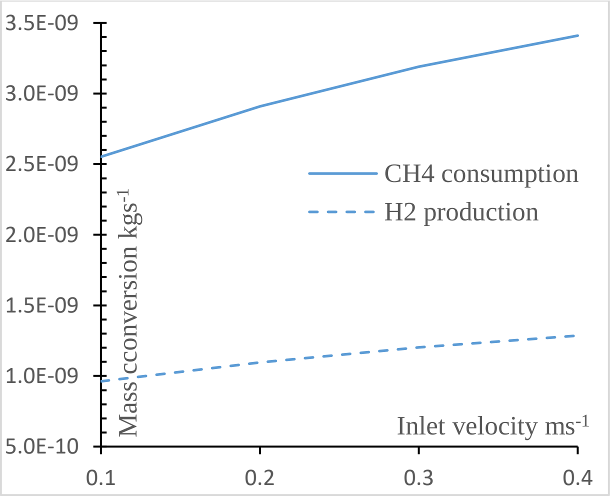

Figure 5-5: Mass conversion of SMR reaction vs different inlet velocity (B1 model)

5.1.3 Inlet methane mass fraction effects

Increasing the methane inlet mass fraction increases methane consumption due to its higher concentration. As methane is lighter than water and nitrogen, increasing its share at the inlet decreases the density for the same mass flow rate. Nonetheless, increasing twice the inlet methane mass fraction increases methane consumption by 21 per cent.

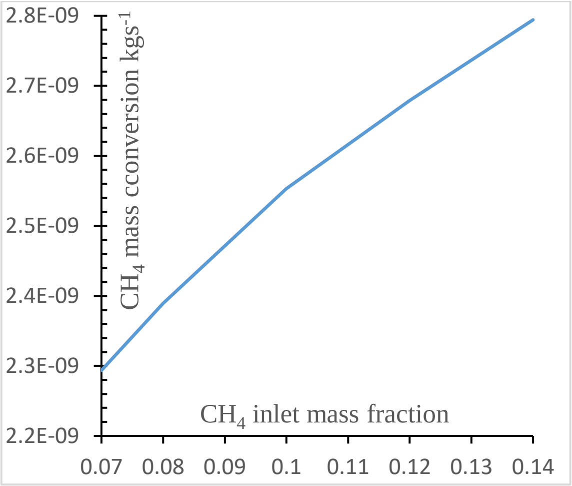

Figure 5-6: Mass conversion rate of methane at different inlet fractions of it (B1 model)

The conversion rate is slightly decreasing, as evident by the gradient of the plot. Also, for the 0.14 methane mass fraction, the remaining water mass fraction is 0.22. If methane mass fraction keeps increasing, then after a point, it will disturb the stoichiometric balance of the SMR reaction, and the conversion will decrease drastically. So, it may not reach some asymptotic value.

5.1.4 Inlet water mass fraction effects

Changing the water inlet mass fraction doesn’t cause a significant effect on the methane consumption rate. This trend validates that the rate equation shows weak dependence on the water partial pressure term. Also, the molecular weight of steam is higher than methane but lower than nitrogen, so when its share increases at the inlet, density decreases for the same mass flow rate. Overall, three times more steam is used to prevent carbon formation from choking the channel. Therefore, increasing its fraction further is energy consuming and not needed. The following plot illustrates the methane conversion rate vs inlet mf of steam.

The minimum possible inlet steam fraction must be used as water has a very high heat capacity. When the mixture's heat capacity is minimum, the gases heat up quickly to the reaction temperature.

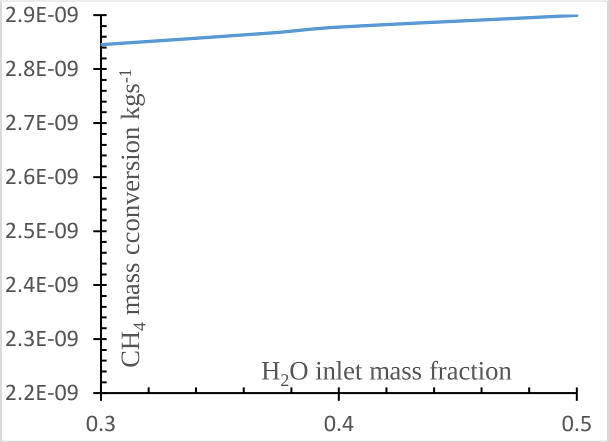

Figure 5-7: Mass conversion of methane at different inlet fractions of steam (B1 model)

5.1.5 Inlet temperature effects

For increasing the inlet temperature, methane conversion rises linearly. For each 20 K rise, there is nearly a four per cent increase in methane conversion. The gas thermal conductivity also increases at a higher temperature, which will increase the efficiency of the reformer. As the inlet mass fractions are unchanged, the temperature increases the reaction rate, increasing methane consumption. Therefore, maximum heat transfer between exhaust gases and the FR is needed as temperature decreases at lower engine loads.

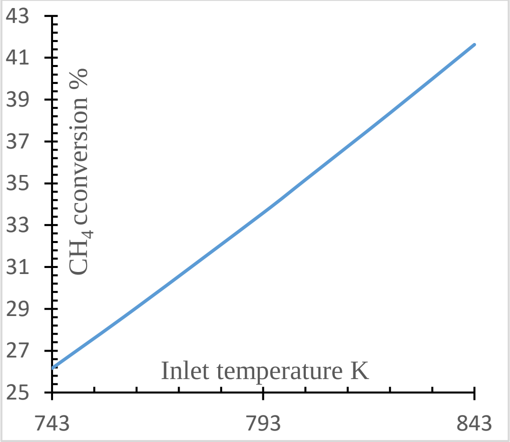

Figure 5-8: Mass conversion of methane at different operating temperatures (B1 model)

5.1.6 Segmentation and heat enhancement by metal foam

Increasing the inlet temperature is energy consuming and not the right choice for higher reformer yield. Another way is to increase the heat transfer from the wall to the fluid using high porosity metal foams. Metal foams are depicted as a sieve in figures, and it is not a proper presentation of an irregular pattern metal foam. The green bars represent reacting materials and are not drawn to actual scale.

A new catalyst configuration is tested to gauge the metal foam's most suitable position in the reformer. Instead of having a long continuous catalyst, a segmented catalyst with isothermal regions is tested. The Abdelhakim Settar team has already proposed this design, but the model does not use metal foam, and their inlet conditions are different (Settar *et al.*, 2019).

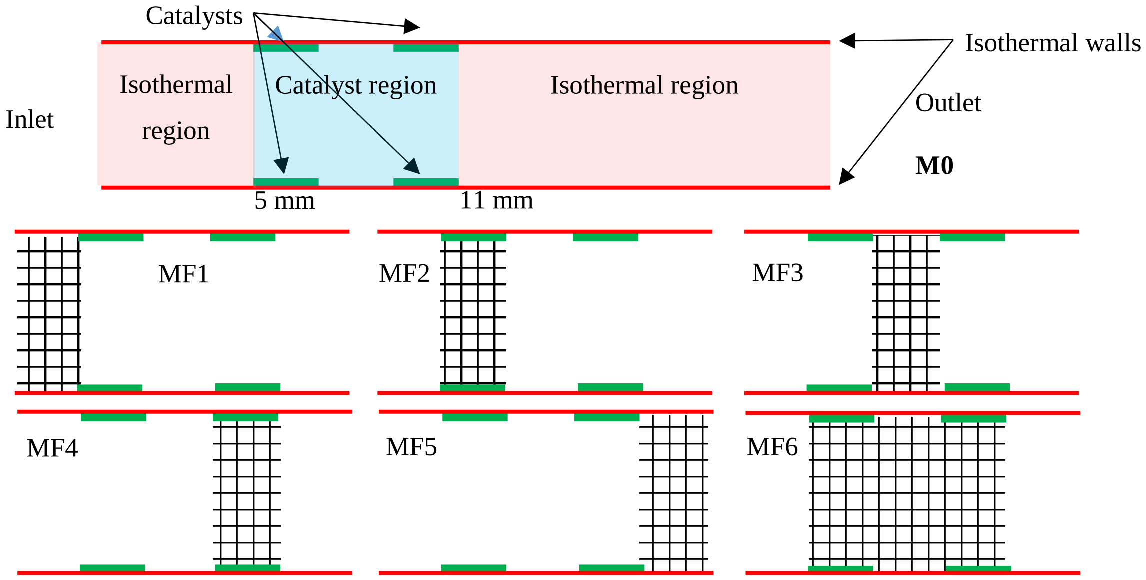

Figure 5-9: Segmented catalyst with a different configuration of high porosity metal foam (MF) as heat-conducting material (Settar *et al.*, 2019)

In this configuration, each catalyst segment is 2 mm long with a 2 mm gap between them. Thus, a total of 8 mm long catalyst is used. The catalyst region starts from 5 mm and ends at 11 mm. Metal foam is a porous material, and it occupies some space at the wall according to its porosity (metal foam properties, Table 5-4). It means metal foam positioned at the catalyst site (MF2, MF4, MF6) ceases fluid’s access to some parts of the catalyst. The source terms in such cases are multiplied by the porosity to add this deactivation phenomenon in the simulation, reducing the useful reacting material available for SMR reaction.

Continuous catalyst (MFC, Appendix D) compared to the segmented catalysts (M0) gives 35 per cent less hydrogen (Figure 5-10c). Thus, it shows segmentation is the dominating reason for the higher performance of the catalyst than the metal foam. Although metal foam reduces the available catalyst site, it is worth noticing that it slightly increases hydrogen production than the M0 model (Figure 5-10). It means metal foam enhances heat and mass transfer from walls to the bulk of the fluid, and the other reason can be lower velocity in the metal foam region (Figure 5-12). Low speed enables the gases to regain more heat after losing over the first catalyst site effectively.

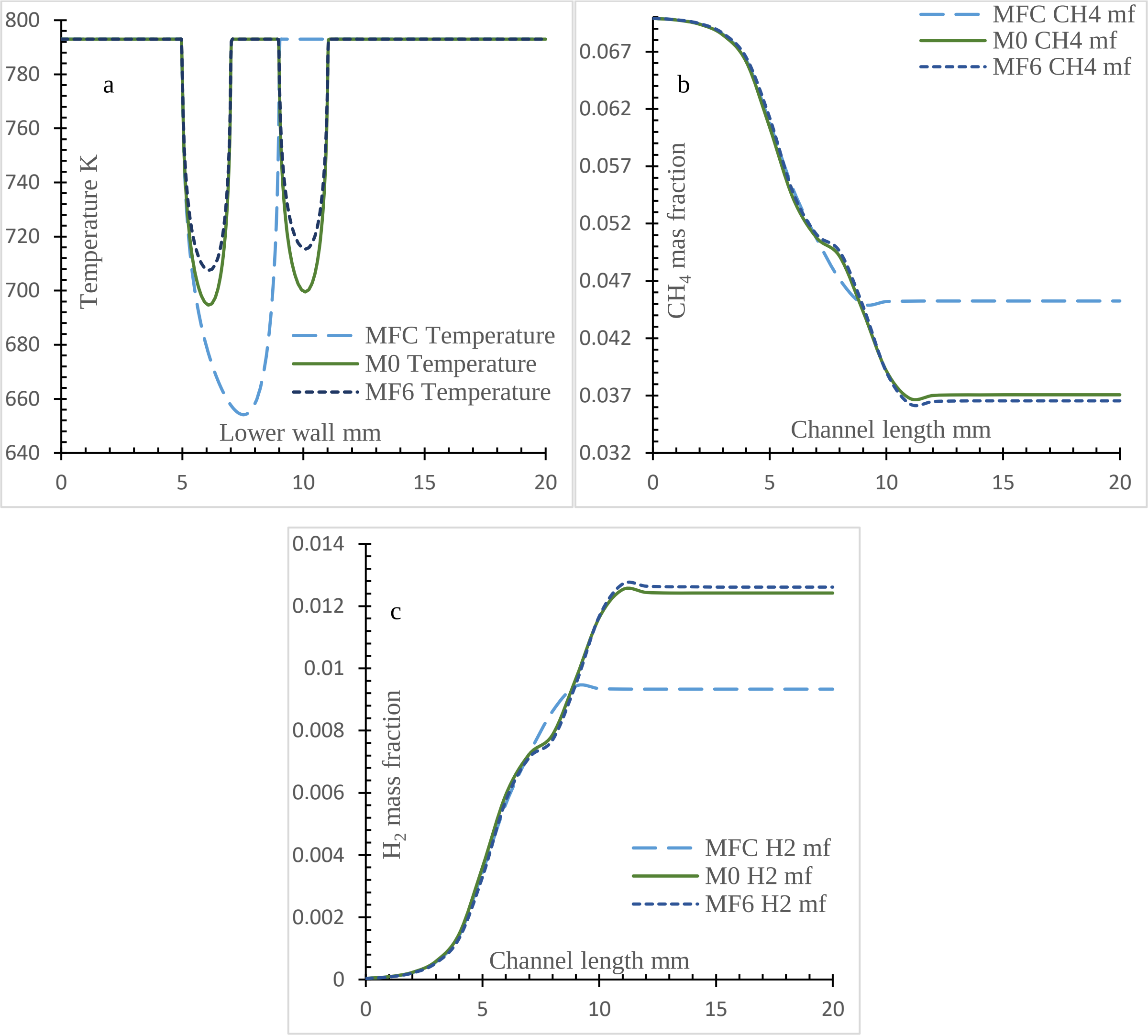

Figure 5-10: Performance of continuous catalyst, segmented catalyst and, metal foam segmented for a) temperature, b) CH_4 mf, and c) H_2 mf

The hydrogen mf rise due to metal foam is negligible, 1.6% only (Figure 5-10c). The exciting part is the temperature drop (Figure 5-10a). Firstly, the temperature gradient is the same for all the models. Next, the temperature drop for MF6 is the minimum. For the clear channel or clear configuration (M0 model), the temperature drop is 695 K compared to 707 K when the metal foam is used (MF6 model). Despite this significantly higher temperature, the hydrogen yield is not substantial, which means the deactivation portion of the catalyst (by metal foam) is cancelling the higher temperature effect.

The metal foam optimum location study investigates the metal foam's most effective position to increase SMR catalyst efficiency. In this way, either optimum directional porosity can be incorporated, meaning higher porosity is employed where needed, or metal foam is used only in the region of maximum interest. The comparison for metal foam location is given in Table 5-2.

Table 5-2: Different values of various quantities for different metal foam position

Quantity	**M0**	**MF6**	**MF1**	**MF2**	**MF3**	**MF4**	**MF5**	**MFC**
$H_{2\ \text{avg, max}}$	0.0124	0.0126	0.0124	0.0121	0.0125	0.0120	0.0124	0.0093
$CH_{4\ \text{avg, min}}$	0.0371	0.0365	0.0371	0.0378	0.0369	0.0383	0.0371	0.0453
T_{min} [K]	694	707	694	697	695	695	695	654

It suggests that having metal foam between catalysts (MF3) gives similar results as having metal foam in the entire catalyst region (MF6). The MF3 model is better than MF6 to avoid a higher pressure drop (ΔP is minuscule anyway for given inlet condition and metal foam properties, 0.3296 Pa). Metal foam is not a suitable method to increase fuel reformer efficiency for this model. Nevertheless, metal foam enhances (Figure 5-13) heat transfer from walls to fluid or vice versa (MF6, T_{min}), so it can be used in an application where the heat transfer is preferred over the chemical reaction. Moreover, these models are different from each other. Otherwise, more temperature drop means a higher endothermic reaction.

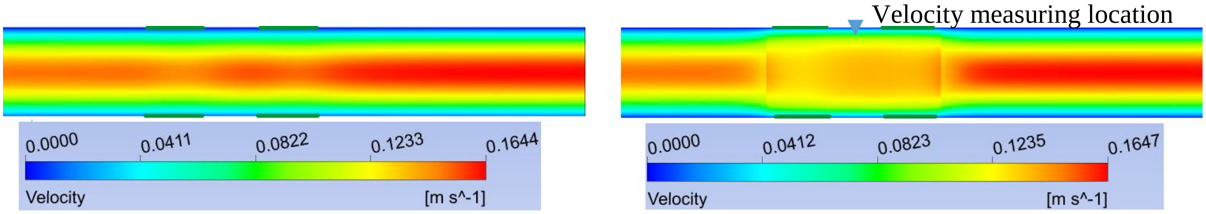

Figure 5-11: Velocity comparison between (left) M0 and (right) MF6 models

The plots also reveal other information (Figure 5-10), such as most of the reaction occurs at the first catalyst site. This considerable variation is seen in the mass fraction profile, where the hydrogen production is more after the first catalyst site (61%) than the next ones (39%). It also highlights the gap length choice to have a similar yield at the following catalyst sites. The in-between isothermal length can be increased so that the gas mixture can attain sufficient energy before reacting the second time.

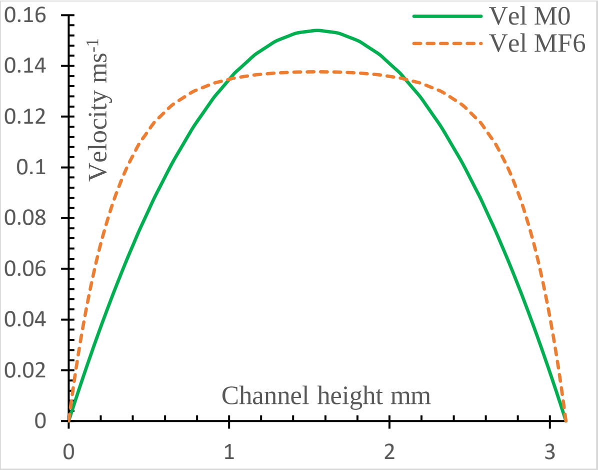

Figure 5-12: Velocity comparison between M0 and MF6 models (taken at the midway of two catalyst sites)

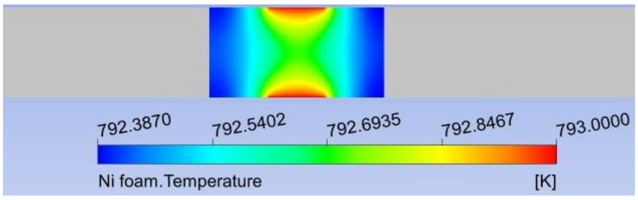

Figure 5-13: Metal foam temperature for model MF6 (Ni is nickel)

5.1.7 Metal foams as mechanical mixers

Another attempt for optimum metal foam location study is carried out to see if it can increase hydrogen yield. Dr Settar develops this pattern used but without metal foam (Settar, Nebbali and Madani, 2015).

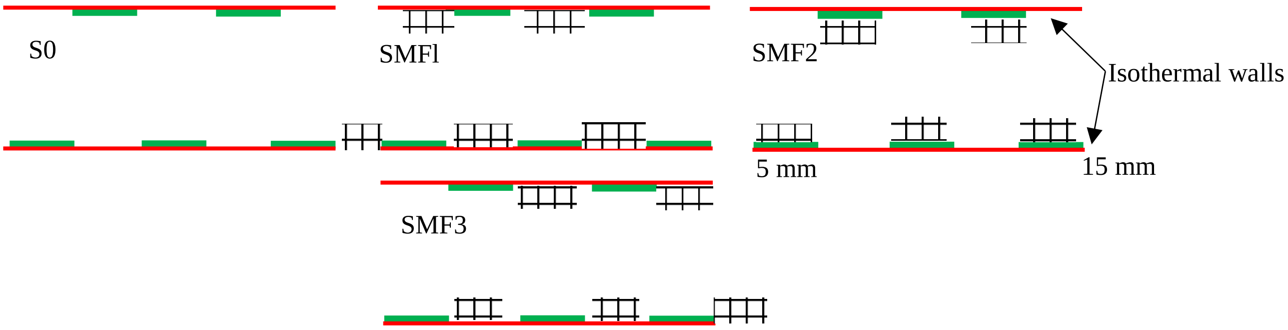

Figure 5-14: Settar segmented catalyst with a different configuration of high porosity metal foams as mechanical mixers (Settar, Nebbali and Madani, 2015)

In the previous case, the velocity slows down when there is a metal foam across the channel, increasing the residence time. So this time, the porous material (metal foam) is not put all across the channel, but the height is kept at 1.5 mm and the length to 2 mm. This arrangement should force the flow to the catalyst site using metal foam as a mechanical mixer. The flow deviation will also increase the fluid residence time as it is not going straight from inlet to outlet. The catalyst region starts from 5 mm and lasts till 15 mm. Each catalyst is 2 mm long (green), having a 2 mm gap (isothermal) between each other, and five segments are used this time. However, introducing metal foam in this case also gives no particular advantage, and the results are mentioned below. The inlet conditions are the same as the base case. Due to the low Re and loss model for metal foam, no turbulent model has been used for the simulation, which may give different results.

Table 5-3: Different values of various quantities for different metal foam position

Quantity	**S0**	**SMF1**	**SMF2**	**SMF3**
$H_{2\ \mathrm{avg,\ max}}$	0.0150	0.0150	0.0142	0.0150
$CH_{4\ \mathrm{avg,\ min}}$	0.0302	0.0303	0.0323	0.0303
T_{min} [K]	696	696	698	697

Table 5-4: Metal foam properties (Hugo, Brun and Topi, 2011)

Properties	**d_p µm**	**d_s µm**	**porosity**	**area density**	**permeability**	**loss coefficient**
Ni10	4429	409	0.92	680 m^{-1}	7.63E-8 m^2	248 m^{-1}

Where Ni10 is a nickel alloy, d_p is pore diameter, and d_s is strut diameter

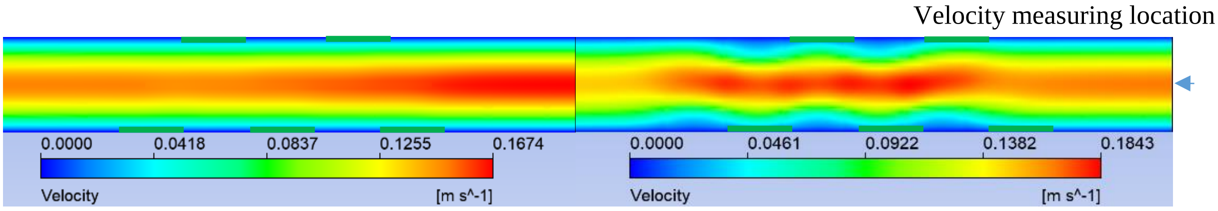

Figure 5-15: Velocity contour for S0 (left) and SMF1 (right)

The velocity contour shows that the maximum speed of the SMF1 model is higher than S0, which corresponds to a lower residence time in the channel. However, as the fluid moves in a sinusoidal fashion, it takes a longer path to exit the catalyst, increasing residence time. Overall it seems these two effects can cancel each other because of the matching hydrogen yield for most cases (Table 5-3).

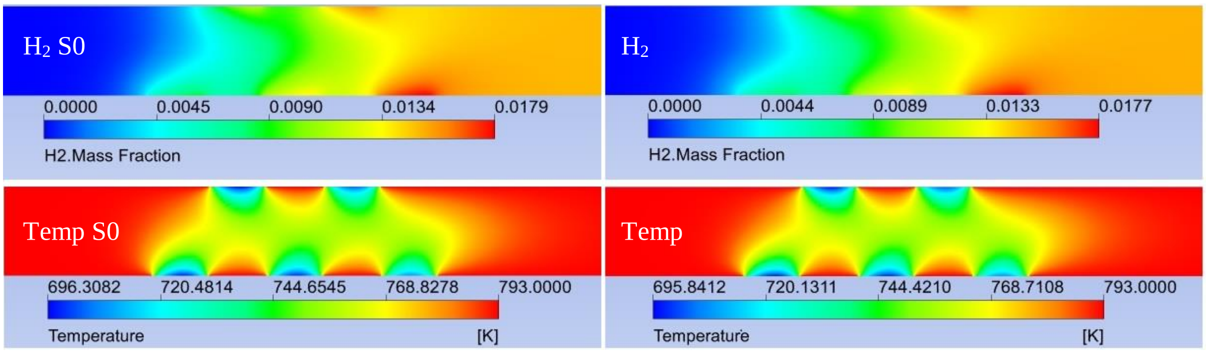

Figure 5-16: H_2 and temperature contours for S0 and SMF1 models

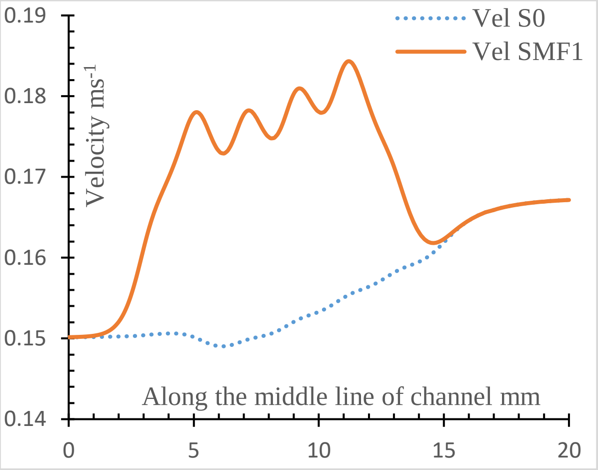

Figure 5-17: Velocity comparison between S1 and SMF1 along channel middle line

The clear channel (S0) maximum velocity occurs near the outlet, whereas the SMF1 configuration occurs inside the catalytic region (5-15 mm) (Figure 5-17).

5.1.8 Metal foam properties effects

This section signifies the effect of changing metal foam properties on mf conversion efficiencies by acting as a flow guide. These properties are porosity (eta), interfacial area density (iad), permeability (perm), resistance loss coefficient (loss), heat transfer coefficient (ht) and streamwise coefficient (SC). I-MF is an isotropic metal foam, whereas D-MF (down) means an anisotropic foam with primary flow directional vector coordinates (3,-1,0) (see Appendix D for all designs). In directional porosity, transverse directions are assigned a factor of 2 which means, the transverse losses are two times the streamwise losses. More details about SC are given in Appendix C.

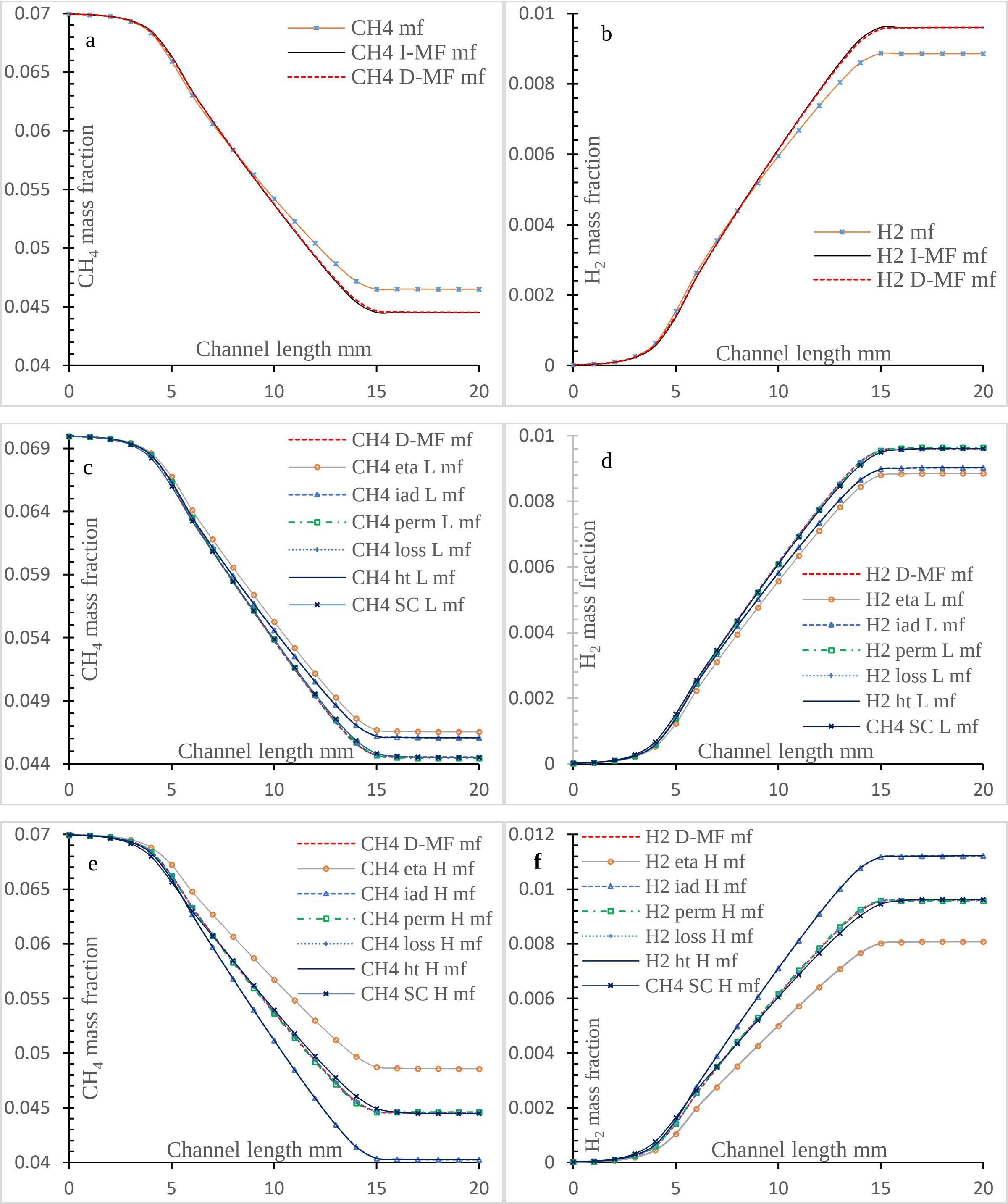

Figure 5-18: Mass fractions for clear configuration vs with metal foam inserts of a) methane and b) hydrogen. Effect of lower values of metal foam properties on mass fractions of c) methane and d) hydrogen. Similarly, the effect of higher values of metal foam properties on mass fractions of e) methane and f) hydrogen (B1 model)

5.1.8.1 Effect on catalyst efficiency

Two conditions are analysed first, by decreasing a property value (L, low condition) and the second, by increasing it (H, high condition) compared to the standard value (Table 5-5). Each parameter is separately altered while others are kept at the standard values. Thus any change that appears in the output is the result of varying just that parameter. For these changing parameters, the D-MF is used for both high and low conditions.

Although metal foam deactivates some parts of the catalyst, metal foam still improves the rector yield. Figure 5-18a and b show the improvement in mass fractions of channels with metal foam insert. This enhancement is better (Table 5-7) than previous results (MF6 design in section 5.1.6, Table 5-2) using a segmented pattern with a metal foam insert. In addition, the new simulation shows that metal foam assists in producing 8.4% more hydrogen than the clear channel (without metal foam). Thus, the continuous catalyst layer shows better performance through the metal foam insert compared to the segmented designs.

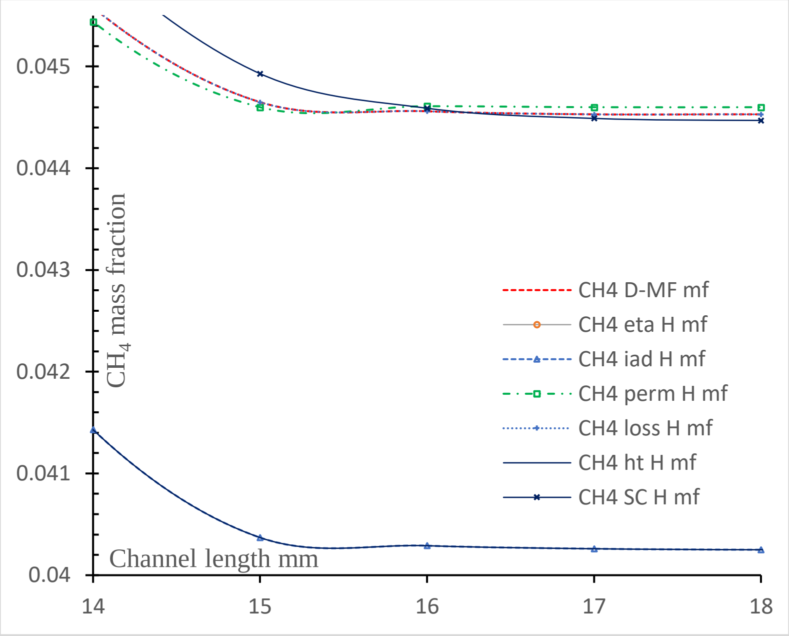

Figure 5-19: Methane mf (closer look) using high metal foam properties values (B1 model)

The low condition (Figure 5-18c and d) does not change mass fractions, although parameter values are halved or more. Except for eta and SC, where eta is set to 0.82 from 0.92, and SC is increased 2.5 times. The eta profiles show a fall in yield as lower porosity means less catalyst availability. Similarly, there is a decrease in mf conversion for iad and ht (overlapping plots). The rest of the parameters show no substantial change compared to the standard D-MF profiles. This analysis indicates that eta, iad and ht values change the reaction behaviour.

Table 5-5: D-MF properties using high and low conditions vs standard condition (Hugo, Brun and Topi, 2011)

Condition	**porosity**	**area density m^{-1}**	**permeability m^{-1}**	**loss m^{-1}**	**ht W/m^2K**	**SC**
Standard	0.92	680	7.63E-8	248	50	2
Low	0.82	340	7.63E-9	124	25	5
High	0.72	2040	7.63E-7	744	150	10

Table 5-6: Mass fractions values at the outlet using high and low values of metal foam properties (B1 model)

Variable	**eta**	**iad**	**perm**	**loss**	**ht**	**SC**
CH_4 L	4.65E-02	4.61E-02	4.46E-02	4.45E-02	4.61E-02	4.45E-02
H_2 L	8.85E-03	9.03E-03	9.58E-03	9.60E-03	9.03E-03	9.61E-03
CH_4 H	4.86E-02	4.03E-02	4.44E-02	4.45E-02	4.03E-02	4.45E-02
H_2 H	8.08E-03	1.12E-02	9.64E-03	9.60E-03	1.12E-02	9.63E-03

Table 5-7:Mass fractions at the reactor outlet with and without metal foam (B1 model)

Variable	**Clear**	**I-MF**	**D-MF**
CH_4	4.65E-02	4.45E-02	4.45E-02
H_2	8.86E-03	9.60E-03	9.60E-03

The values are increased three times or more for the higher condition except for eta (0.72 from 0.92). As before, lower porosity leads to lower H_2 output (16% reduction), and the rest of the parameters do not change the productivity except the iad and ht. Increasing ht and iad values three times give 17% more hydrogen than the comparing case of D-MF. In addition, both D-MF and I-MF give the same results (Table 5-7).

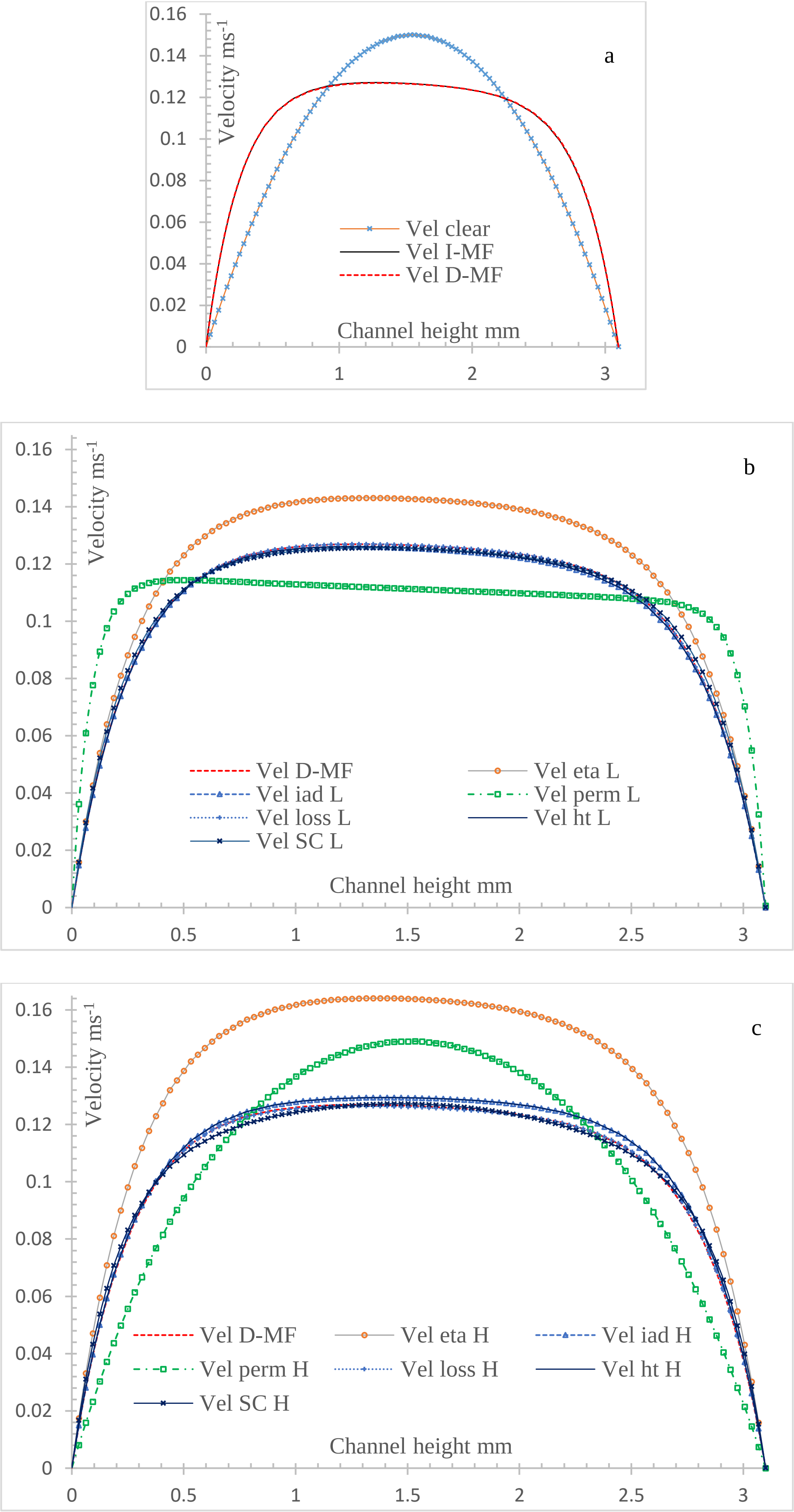

Figure 5-20: Velocity profiles for a) clear, I-MF and D-MF, b) for low condition, and c) the high condition at 10 mm (B1 model)

In summary, metal foam increases the efficiency (8.4%) compared to the clear configuration. Three metal foam variables, which are eta, iad and ht, govern the reaction output.

The heat transfer between solid and fluid is given by $Q_{fs} = ht\ iad_{fs}\ (T_s - T_f)$. The interfacial area density presents porous medium surface area per unit volume. Iad and ht profiles overlap because heat transfer (Q_{fs}) linearly depends on these parameters (ANSYS® Academic Research, 2011b). Hence, increasing any of these two by a factor causes the same heat transfer, producing similar mass fraction profiles.

5.1.8.2 Metal foam as a flow guide

The velocity profiles (Figure 5-20a) show the difference between a clear configuration and a domain filled with MF inserts. Unlike the MF6 model (Figure 5-12), the I-MF channel's velocity profile is not symmetrical. The reason can be the constant consumption of reactants due to the continuous catalyst at the single wall (the bottom one). The uninterrupted reaction changes density and concentrations near the catalyst layer, and thus velocity varies asymmetrically across the height. The I-MF and D-MF velocity profiles overlap each other because the streamwise coefficient is small (SC=2). However, changing SC to a higher value (10) does not change the central section's velocity either (Figure 5-20c). The reason is that for both the SC conditions, porosity and permeability are the same. Therefore velocity remains similar (at 10 mm) unless porosity and permeability are changed.

Figure 5-21 shows velocity contours for some of the models. It tells that though velocity variation at the middle (at 10 mm, Figure 5-20) is not high (for SC H, I-MF and D-MF), but changes rapidly at the fluid-metal foam boundary. It also reveals that the metal foam should start before the catalyst for very high directional porosity (SC H). Otherwise, it creates a low-velocity region at the start of the catalyst. Typically, the reaction rate is maximum at the catalyst strat, so any fluid void must be avoided at this location. Otherwise, it reduces both productivity and catalyst usage.

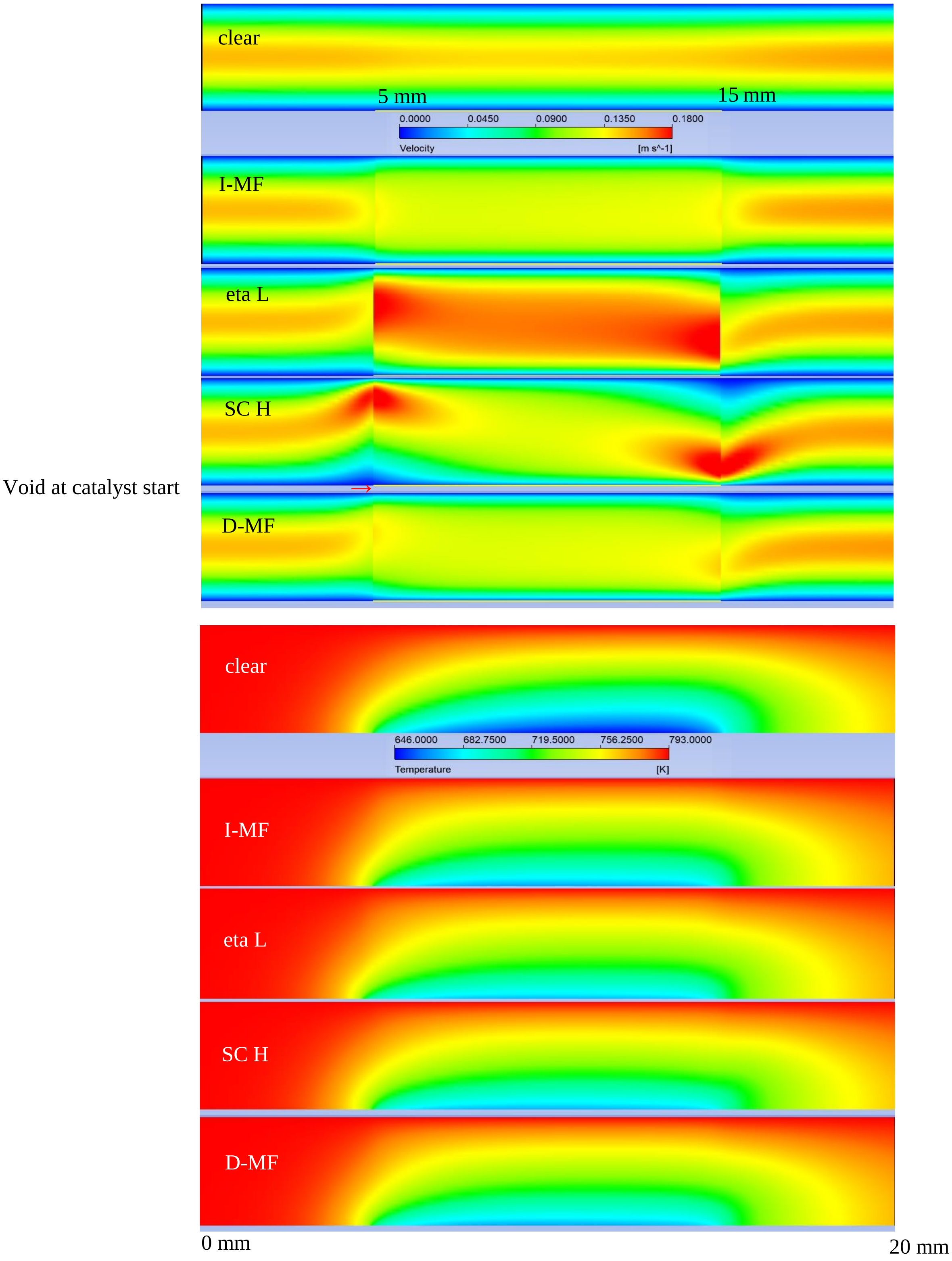

Figure 5-21: Velocity (top) and temperature (bottom) contours for some of the configuration (B1 model)

5.2 Chapter 5 summary

After finalising the design and validation, some parametric studies have shown exciting results. Isothermal walls near the catalyst improve its efficiency for the endothermic reaction. In the absence of adjacent isothermal walls, a medium that can transfer heat from a hot side towards the reaction zone can improve its performance. Increasing the inlet velocity allows more mass flow rate to enter the FR reactor, increasing the hydrogen yield. After surpassing the peak, the high-speed flow would not improve the output anymore.

Doubling the inlet methane mass fraction increases its consumption (21%) but its rate of consumption decreases. It may continue growing until the S/C ratio drops too much that methane starts encouraging coke formation. Changing the water inlet mass fraction does not significantly affect reactor production. Inlet temperature increases the reaction linearly, thus changing the reaction rate as the inlet mass fraction is constant.

Catalyst segmentation increases the conversion for the same amount of reactants and catalyst quantity. The reason is the isothermal walls which raise the gas temperature after the endothermic reaction. Increasing the distance between the two catalysts would further improve output, which is another factor besides decreasing the segment length.

Essentially, metal foams decrease the surface available for reaction, improve the residence time and increase the heat transfer from walls to the channel cross-section. Hence, the positive effects nearly balance out the negative impact, which equals some improvements. Metal foam can effectively act as a flow mixer and flow guide. However, the mechanical mixer patterns do not improve the output, though it adds a longer path but decrease the residence time. So both factors negate each other without changing the overall reactor effectiveness. Metal foam parameters affect the flow pattern, especially porosity and permeability. The rest of the parameters show no significant effect on flow behaviour despite changing their values to half or double. At the same time, interfacial area density and heat transfer coefficient affect heat transfer between fluid and metal foam.

6 Results and discussion of innovative designs

In the light of parametric studies, new designs are tested, and any improvement is presented, elaborated and discussed.

6.1 Catalyst position

In this section, metal foam is used as a catalyst support structure or protrusion because the catalyst is a very thin material. The porosity is uniform overall, but a low porous foam at the catalyst side is appropriate for providing the necessary strength. Also, the metal foam will expose both sides of the catalyst, but porosity would determine the bottom side exposure. However, only one side is activated (opposite the metal foam) to see the catalyst position's effect on the reaction. The catalyst region lasts from 5 to 15 mm for all the models starting from Iso B1 to A3 (see Appendix D for designs).

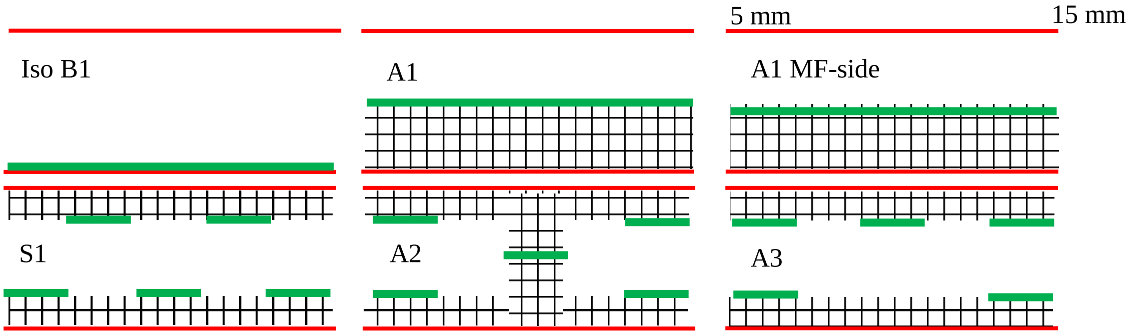

Figure 6-1: Various models tested for different catalyst positions and segmentations

In the A1 model, the catalyst is positioned in the middle of the channel. The reason is the velocity profile of the B1 model, which reveals that (Figure 4-13) maximum velocity occurs in the middle part of the channel. So to take advantage of this highest mass flow rate region, the catalyst is placed in the central location.

6.1.1 Yield increment due to fifty per cent protrusion

Compared to Iso B1, model A1 produces nearly 57 per cent more hydrogen (Figure 6-2d). It could be more if both the catalyst sides were considered active for the chemical reaction. The higher catalyst temperature (on average, 60-80 K more) is the main reason for higher conversion because of additional heat transfer from the metal foam side (Figure 6-2a). Heat conduction minimises the temperature drop along the length as the catalyst is a thin nickel/Al_2O_3 material with minimal heat capacity.

6.1.1.1 A discussion on channel height effects

Initially, the mass fraction profiles seem lagging for model A1 because of the high-speed flow at the top of the catalyst. On the other hand, rate and temperature profiles for the Iso B1 model have very high gradients. These sharp growths are there because of the isothermal walls (at 793 K) before and after the catalyst. This difference in temperature causes the profiles to reach the maximum value at the wall-catalyst transition. As rate follows temperature profile, so that is why it forms maxima at the exact locations.

Temperature, rate and mass fraction conversion values for the Iso B1 model are lower than A1. As mentioned before, a higher temperature drop means greater reactant consumption (for endothermic reaction) but for the same model and conditions.

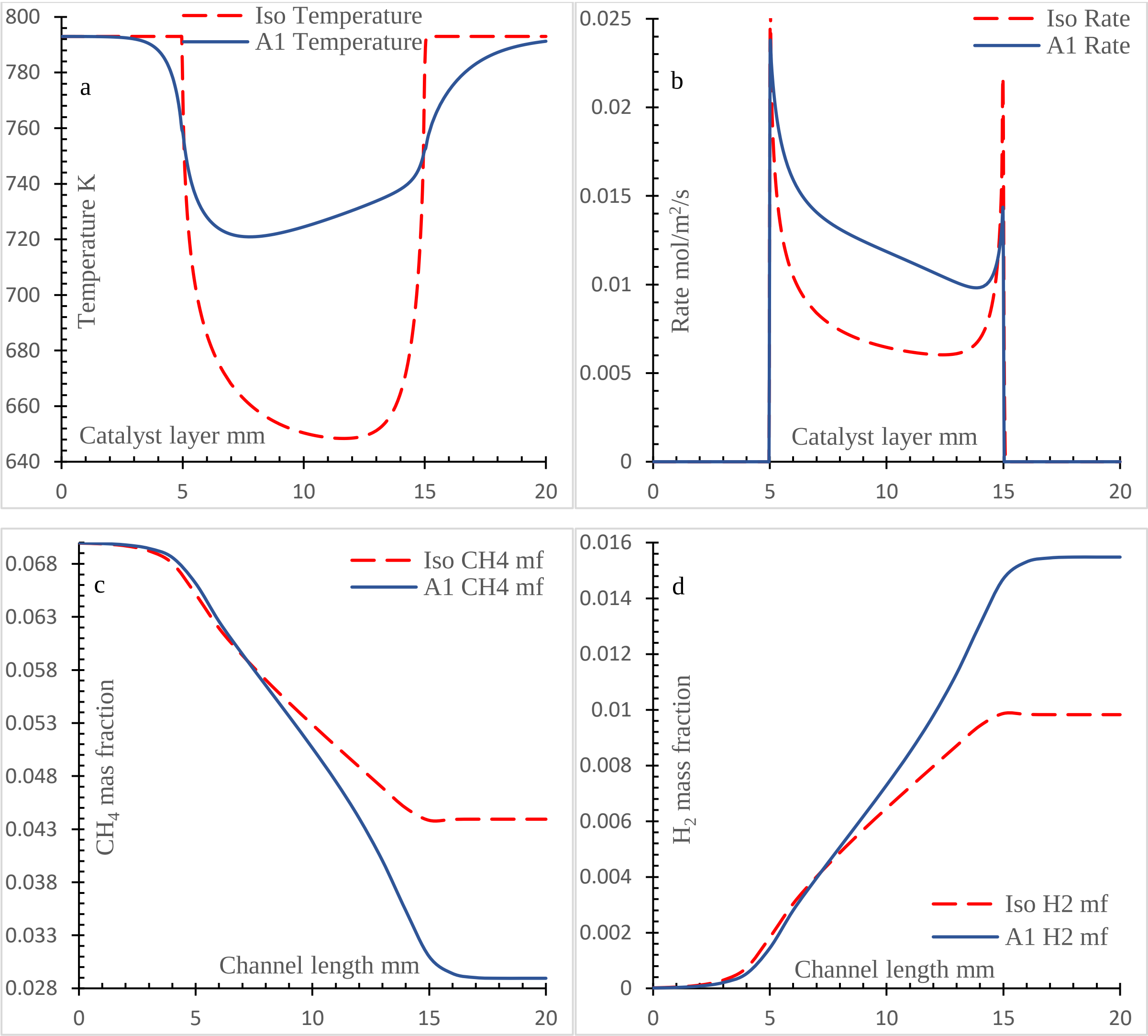

Figure 6-2: A1 and isothermal B1 comparison of profiles for a) temperature b) rate c) methane and d) hydrogen (see Appendix D for designs)

6.1.1.2 Determining catalysts layer thickness effects on efficiency

The thermal conductivity of catalyst material may affect catalyst efficiency. Hence, concrete is chosen as an interface material instead of nickel. This material selection is approximately valid for a dispersed catalyst in a ceramic washcoat. Still, to confirm the heat conduction effect of a metal catalyst, it is necessary to choose a low thermal conductivity material.

Having concrete as interface material causes no change in the reaction outcome. The primary reason is that despite having lower thermal conductivity up to 50 times (Ni 91 $Wm^{-1}K^{-1}$, Concrete 1.7 $Wm^{-1}K^{-1}$, CFX library), the catalyst thickness (0.15 mm) is insignificant to cause any change in temperature along its length in such a high-temperature environment. Therefore, the plots are not reported, but contours (Figure 6-3) as these two configuration results overlap.

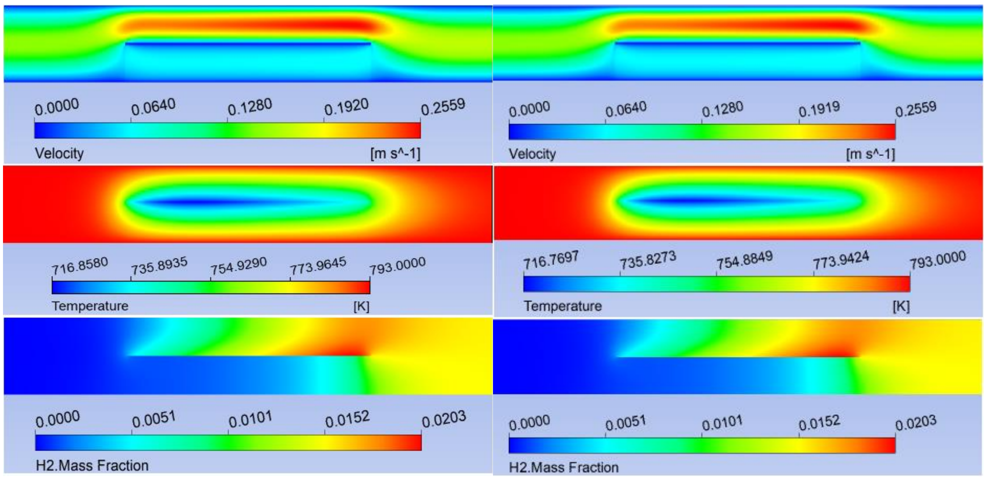

Figure 6-3: Velocity (top), temperature (middle) and H_2 mf (bottom) contours for (left) nickel (right) concrete interfaces (A1 model) (see Appendix D for designs)

6.1.2 Determining optimum protrusion height

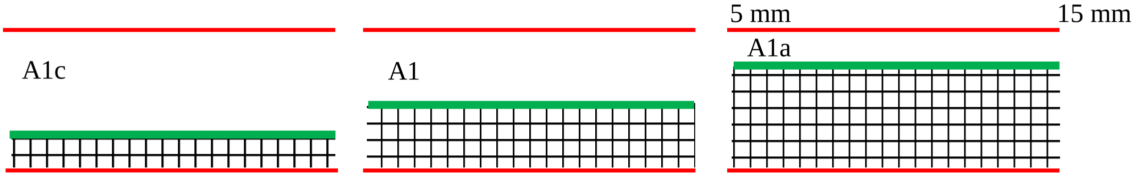

Figure 6-4: Two new models tested of A1, having catalyst at different h

Two more configurations of A1 models are tested. In one setting, the catalyst is placed at h=75% (A1a) and in the other at 25 per cent (A1c). The reason is to seek the best protrusion height for the maximum conversion of the reactants. Figure 6-3 velocity contours indicate that metal foam, even having high porosity, pushes the fluid towards the clear region, where there is no metal foam. Moreover, it will increase the fluid speed due to cross-section contraction, which will reduce the residence time and, thus, reactor performance. Hence, it is worthy of investigation which factor is dominant.

6.1.2.1 A general comparison between protrusion heights

It appears from contour (Figure 6-5 bottom) that model A1a produces the most hydrogen mass fraction owing to the minor gap between the catalyst and upper isothermal wall. A closer isothermal wall means ease of heat transfer from wall to fluid, which is highly favourable for the SMR reaction. As soon as fluid loses heat, it gains heat quickly and further down the length, the endothermic reaction overcomes, and then the temperature drops again (11-14 mm). Nonetheless, the reaction continues at the entire catalyst length (Figure 6-5 bottom).

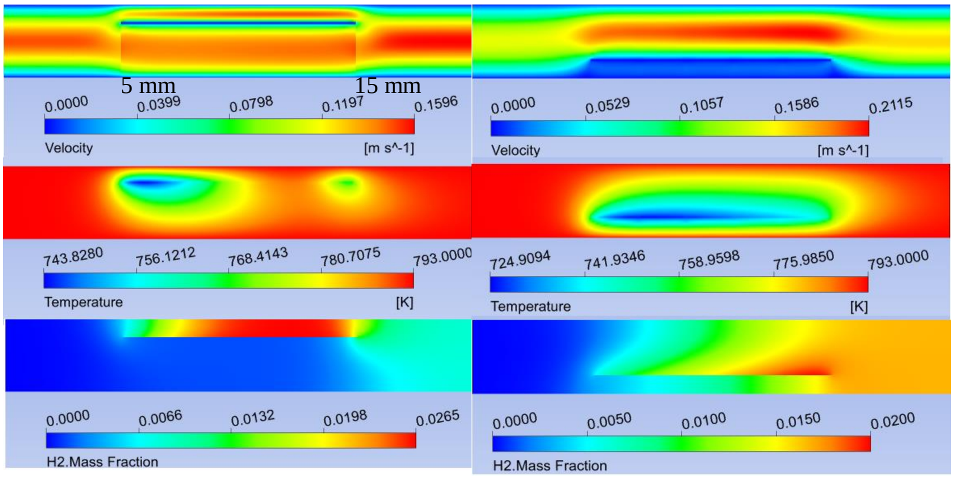

Figure 6-5: Velocity (top), temperature (middle) and hydrogen (bottom) contours for models (left) A1a (right) A1c (see Appendix D for all designs)

However, the contour (Figure 6-5 top left) shows that A1a velocity is nearly uniform and the lowest among the three in the entire cross-section. Hence, it means that most of the fluid passes through metal foam without interacting with the catalyst. Overall, this configuration obtains the highest local hydrogen mass fraction over the catalyst.

Model A1c velocity contour shows that most fluid passes over the catalyst but not through the metal foam. This share is even higher than the A1 configuration (Figure 6-5 top right). Nonetheless, the hydrogen contour shows that the hydrogen mass fraction (Figure 6-5 bottom right) is the lowest among the three. Still, its spread is the highest in the domain (orange, after the catalyst). Thus, the mass fraction contours show only maximum value and do not accurately represent reactants conversion.

6.1.2.2 A deeper look into protrusion influence on fluid behaviour

For a detailed analysis, let us see the profiles of these variables. The three models' plots are shown in Figure 6-6, confirming the contours quantitatively. Interestingly, velocity near the wall (at catalyst) is higher for the A1a model, whereas it is near zero for A1 and zero for the A1c model. However, the wall velocity seems non-zero because just 100 line points are chosen for plotting the data. Hence, these plots are not adequately registering the wall velocity.

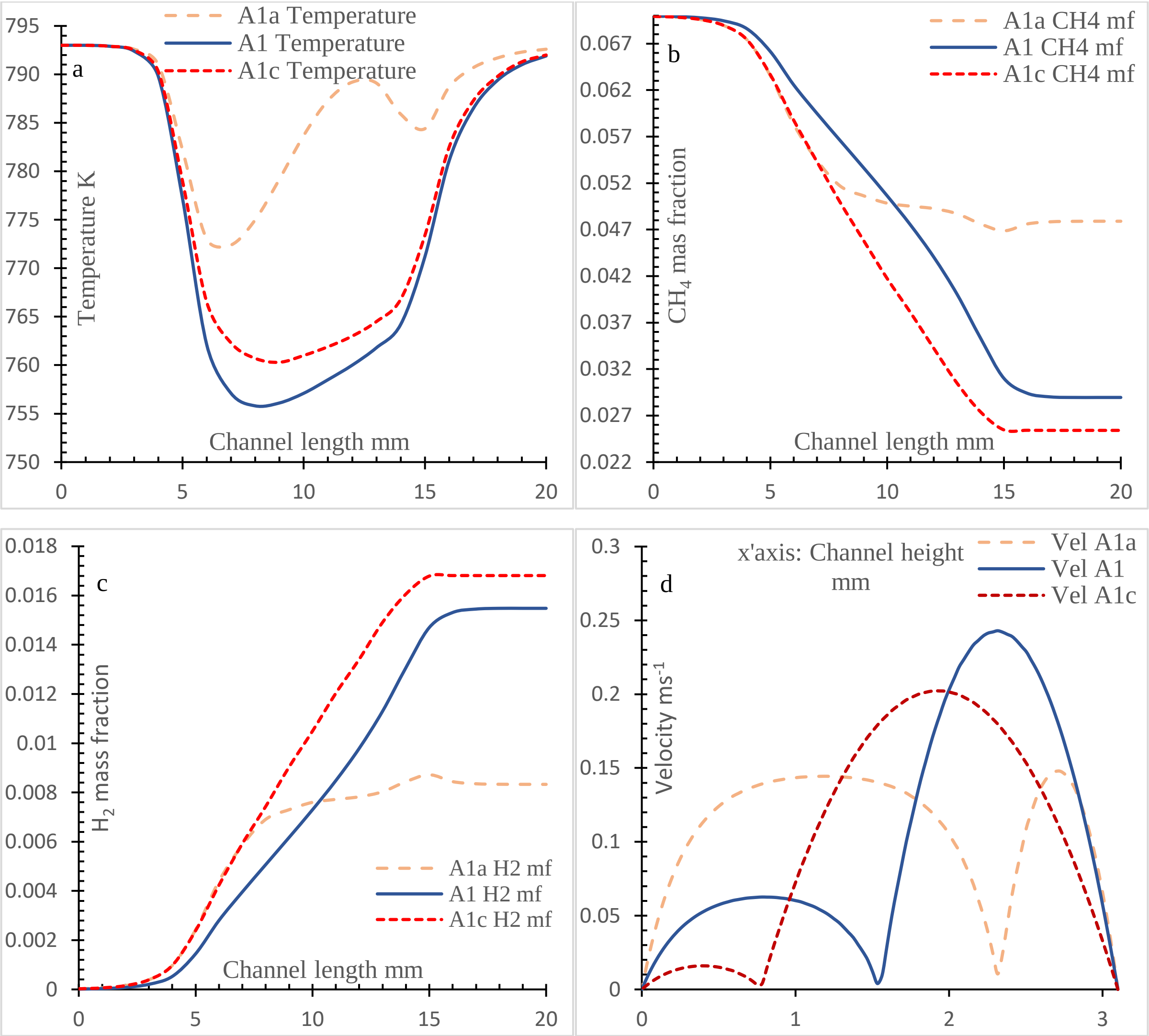

Figure 6-6: Comparison between A1a and A, and A1c models profiles of a) temperature b) methane and c) hydrogen d) velocity (see Appendix D for all designs)

The velocity profiles (extracted at 10 mm length) show why model A1c performs best. Most of the fluid (0.75 to 3.1 mm, red dashed line) passes over the catalyst (Figure 6-6d) for the A1c. The overall velocity is lower than the A1 model, meaning the fluid has more time to spend over catalyst. It has been shown previously (section 5.1.2), a higher mass flow rate means higher conversion. Henceforth, the hydrogen mass fraction of A1c is maximum because of this high mass flow rate over the catalyst (Figure 6-6c).

6.1.3 Activating catalyst on the MF-side

One last simulation of A configuration is tested to exploit the lower velocity region of the A1 model (0-1.55 mm, Figure 6-6c). So, in this case, the catalyst is placed inside the metal foam. Now the fluxes are multiplied with the porosity as metal foam covers some of the catalyst parts. So, the new configuration is called ‘A1 MF-side’. Comparing model A1 and A1 MF-side shows that activating catalyst only from beneath reduces the reactor efficiency.

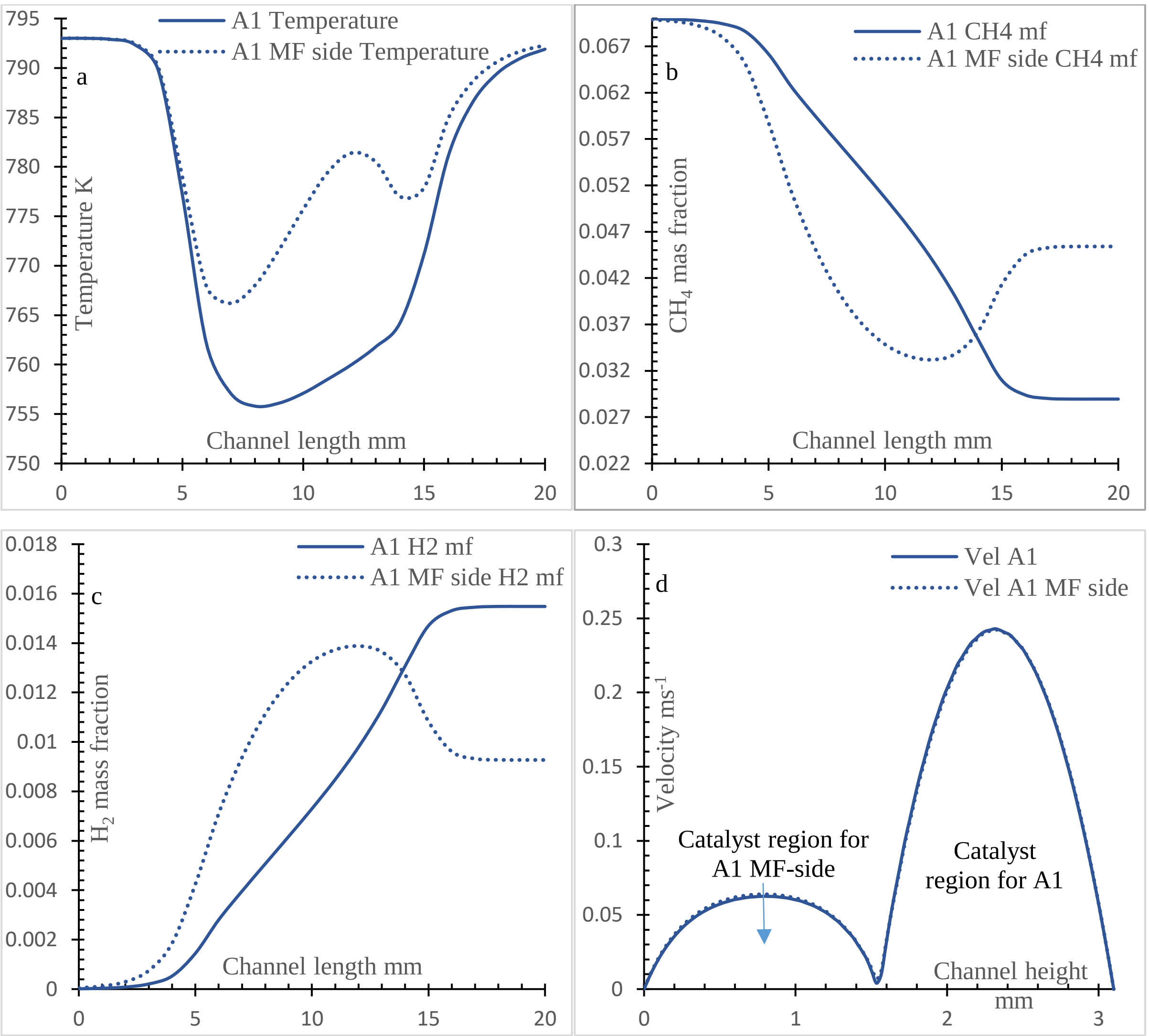

Figure 6-7: Comparison between A1 and A1 MF-side models profiles of a) temperature b) methane and c) hydrogen d) velocity (see Appendix D for all designs)

The main reasons are the lower mass flow rate passing through the metal foam region and the catalyst deactivation by metal foam placement. Otherwise, as proved in the MF6 configuration

(Figure 5-10) and section 5.1.8, metal foam increases the reactor efficiency despite deactivating some catalyst portions. Rate profiles are excluded as the rate is dependent on temperature, so the temperature profile is sufficient.

6.1.3.1 Discussing hydrogen evolution for A1 MF-side configuration

The peculiar behaviour for average mass fractions profiles (rise and fall) is that software takes average values across the cross-section (Figure 6-7b and c). In the case of the A1 MF-side, a lower mass flow rate passes through the metal foam region (0-1.55 mm, Figure 6-7d). Generally, it means the catalyst receives fewer reactants. When the catalyst ends at 15 mm, overall mass fractions suddenly change their values. For instance, the average of three values of 19, 20 and 21 will be 20, but of 19, 20 and 30 will be 23. This odd behaviour doesn't appear for models A1 or A1c as the higher mass flow rate passes over the catalyst (Figure 6-6).

Therefore, this trend is due to mass fraction summation, e.g. methane, of fluids having low concentration (from reacting region) with a higher concentration (non-reacting region) (Figure 6-7b and c).

6.1.4 Finalising optimum protrusion height

Though other designs are not taken into account, if both sides of the catalyst are considered active, then model 'A1a MF-side' may perform best due to the lowest and uniform flow speed (green dashed line, Figure 6-6d). However, assuming that low porosity metal foam is required to support catalyst from beneath, the foam side reaction is neglected for every configuration. Hence, this study adopts the A1c pattern for the following models.

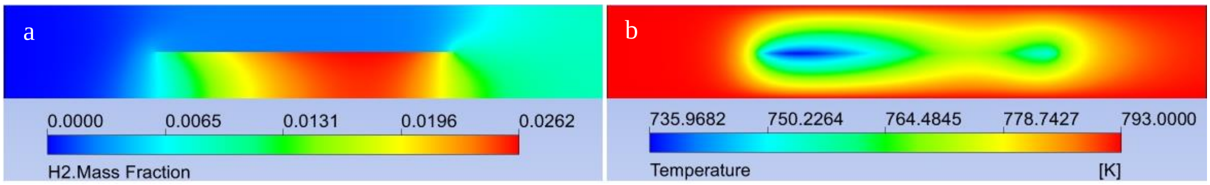

Figure 6-8: Contours for a) hydrogen mass fraction and b) temperature for A1 MF-side (see Appendix D for designs).

6.2 Segmentation

After narrowing down the favourable catalyst position (A1c), the next step is to test different segmentation of the continuous catalyst.

6.2.1 Choosing catalyst segment patterns

This placement of catalysts depends on the previous results. For instance, the A2 model utilises the A1c position of the protrusion (Figure 6-4). The middle catalyst (Figure 6-1) keeps the quantity equal. As proven by the A1 model, it utilises the maximum mass flow region, which is the middle portion of the free stream. The central catalyst is active from the bottom side only with its porosity contribution in the fluxes. Another reason to put metal foam in the middle is to attain a higher hydrogen yield (Table 5-2) by adopting the MF3 model. In addition, the highest gap observation appears after comparing the MFC and M0 model (Figure 5-10a, section 5.1.6). Hence, the top and bottom metal foams catalysts layers have the maximum possible distance between them.

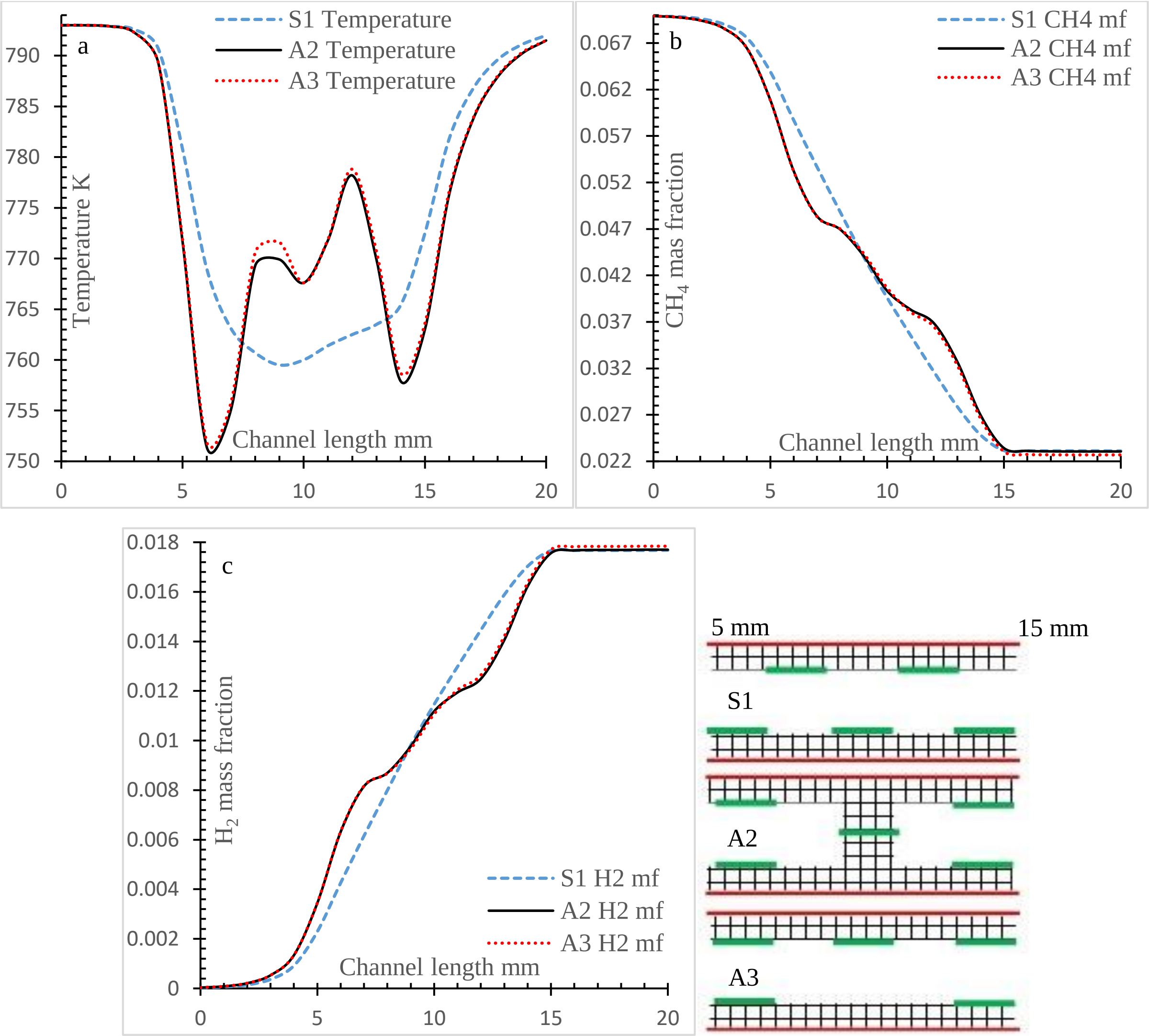

Figure 6-9: a) Temperature, b) methane, and c) hydrogen profiles for models S1, A2 and A3 along the channel length (see Appendix D for designs)

Similarly, the A3 model only offers maximum distance between the segmented catalysts at the bottom layer, so fluid regains heat loss from previous catalyst sites (Figure 6-1). On the other hand, the middle catalyst keeps the quantity similar for standardisation. Also, the central catalyst is fully available for the reaction compared to the A2 central one.

The S1 model originates from the Dr Settar model (S0), where the reactor wall incorporates the catalysts. So in this instance, catalyst layers are elevated to 25% h from each side of the reactor wall. Overall, this pattern makes S1 a new design (section 5.1.7).

6.2.2 Segmentation results

Figure 6-9 shows the average temperature and mass fractions profiles. The temperature drop for A2 and A3 is 10 K more than S1 because of the two parallel catalysts.

Between A2 and A3, A3 gains more heat after the first catalyst sites (7-9 mm). From 9-11 mm, the temperature drop of these two models is smaller. Still, mass fractions profiles variation (for the same range) suggests that the catalyst works efficiently (Figure 6-9b and c). So this minor temperature reduction is due to the single central catalyst layer. The third temperature drop (13-15 mm) corresponds to lesser conversion to products; due to reactants lower concentration than earlier and starting from a small peak temperature (779 K) just before the reaction (Figure 6-9a). Higher concentration and temperature cause a higher reactants conversion at first catalyst sites (Figure 6-9b and c) (49% of H_2 mf). For the S1 case, the minimum temperature drop is higher than in A1 and A2 cases. Its alternate pattern provides smooth profiles for the temperature and mass fractions. Despite the higher temperature, the S1 model gives the same amount of hydrogen. In fact, it is slightly less from both A1 and A2 models (Table 6-1).

6.2.2.1 Investigating local temperature and rate profiles

To investigate S1 higher temperature but similar yield, lets us compare the local temperature at the surfaces of the catalyst. Line 1 is drawn at upper catalyst layers (h = 75%), and line 3 at lower catalyst layers (h = 25%) along the x-axis. So Figure 6-10 shows that the temperature drop for the A3 and A2 models is similar to the S1 model (first catalyst position). Hence, the abovementioned average temperature values indicate a general FR performance trend. Therefore, it shows that despite S1 having a minimum average temperature drop (Figure 6-9a), it yields nearly identical mass fraction conversion (Figure 6-9b and c).

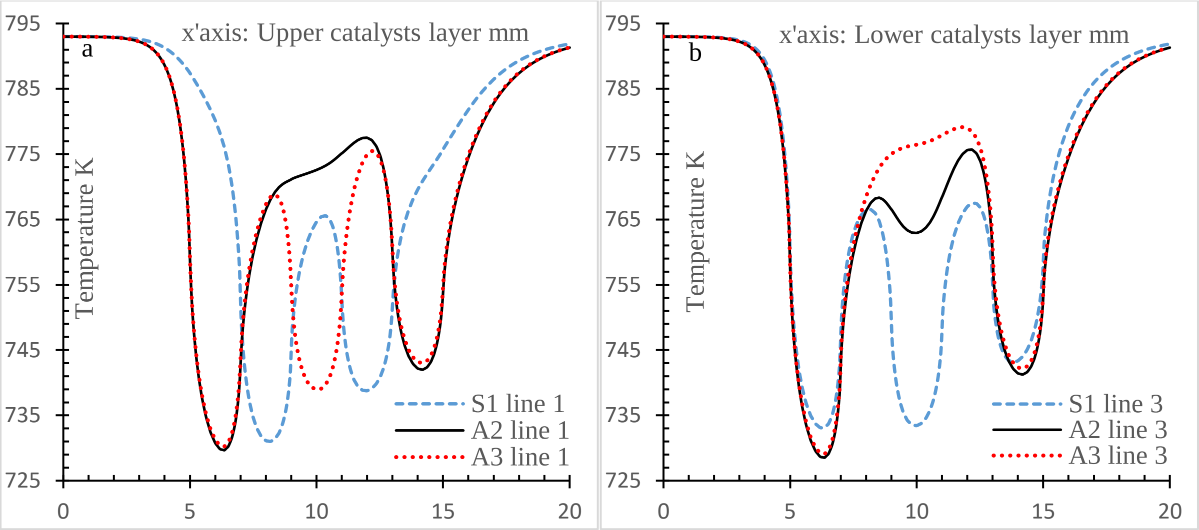

Figure 6-10: Temperature for S1, A2 and A3 at (a) upper and (b) lower catalyst layers

The overall catalyst layer temperature trend (Figure 6-10) is similar for all three models (S1, A1 and A2). It drops during the reaction and then increases to nearly 35-40 K after it. It rises 6-8 K further if there is no catalyst (A3 lower layer and A2 both layers) and falls again at the next catalyst position. The temperature drop value reduces with the length, indicating the diminishing conversion of the reactants (similar to Figure 2-15b).

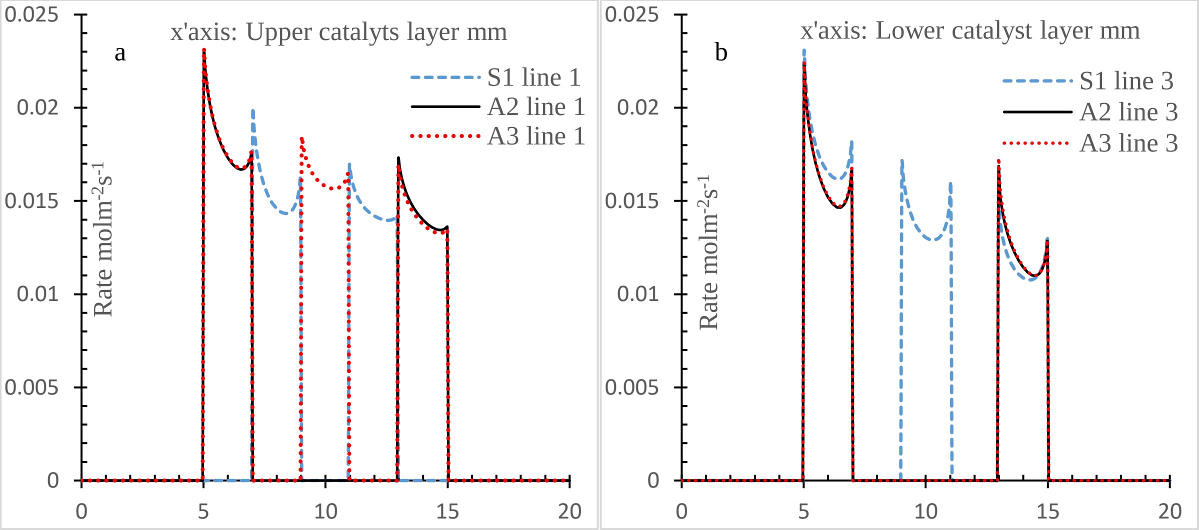

Figure 6-11: Rate for S1, A2 and A3 at (left) upper and (right) lower catalysts walls

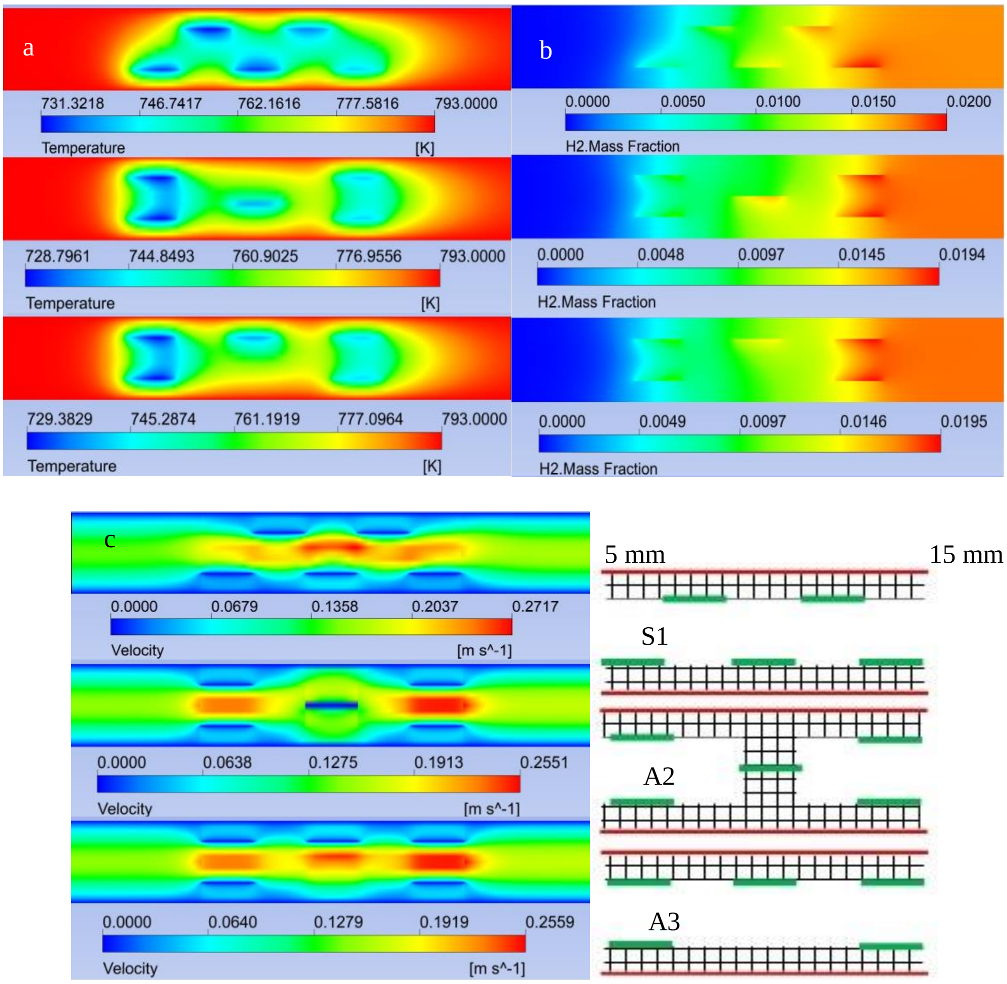

Figure 6-12: Contours of (top) temperature, (middle) hydrogen mass fraction and (bottom) velocity for model (a) S1, (b) A2, (c) A3

The rate profiles show a similar trend (Figure 6-11). Like, temperature, the reaction rate is falling along with the catalyst layer. The gradient of mass fraction profiles from 9 to 11 mm, is nearly the same for all the models (Figure 6-9b & c). Nonetheless, the third catalysts site's reactant consumption is lower than the first for both A2 and A3 models. It will be interesting to exclude the middle catalyst and then evaluate the performance of all three designs.

However, compared with the Iso B1 model, keeping a 10 mm catalyst length is necessary (Table 6-1). Another way to deal with it is to use four 2.5 mm catalysts (with 5 mm gaps) instead of five 2 mm ones, but to make everything standard, except the pattern, 2 mm catalyst length is used for all the models (see Appendix D for all designs).

6.3 Catalyst position and segmentation conclusion

A3 model produces the highest hydrogen mass fraction. As much as 81% more hydrogen is attained in this configuration than in the Iso B1 model. The average temperature variation is not severe (20 K) to cause substantial thermal stresses. Model A2 also achieves the lowest maximum velocity, which signifies separate merit. So a composite model of A2 and A3 will serve as the best possible solution.

Table 6-1: Average mass fractions at the reactor outlet (see Appendix D for all designs)

Model	$\mathbf{H_{2,avg\ mf}}$	$\mathbf{CH_{4,avg\ mf}}$	$\mathbf{H_2O_{avg\ mf}}$	$\mathbf{CO_{avg\ mf}}$	$\mathbf{H_{2,avg\ mf}}$ **↑%**
Iso B1	9.839E-03	4.390E-02	2.607E-01	4.557E-02	-
A1	1.546E-02	2.891E-02	2.441E-01	7.132E-02	57.1
A1c	1.678E-02	2.537E-02	2.406E-01	7.683E-02	70.5
S1	1.768E-02	2.311E-02	2.373E-01	8.187E-02	79.7
A2	1.771E-02	2.302E-02	2.372E-01	8.202E-02	80.0
A3	1.784E-02	2.268E-02	2.369E-01	8.261E-02	81.3

6.4 Heat and mass transfer across the channel

Metal foam can be used as a medium to transfer heat and mass across different channels. The advantage of using metal foam is that the metal foam can direct the flow according to need using a directional porous foam. Compared to the (section 5.1.7) previous study where metal foam serves as a mechanical mixture, its properties variations will make it a flow guide like shown in section 5.1.8.

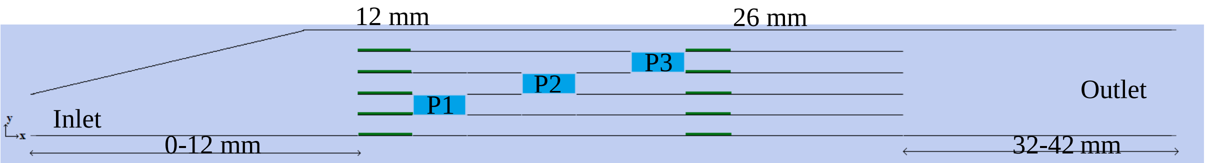

Figure 6-13: Metal foam (dark blue boxes) as inter-channel mass and heat transfer medium (green bars are reacting materials) (see Appendix D for all designs)

Metal foam location, porosity, characteristics and number are adjustable according to the mass flow rate, catalyst shape, and other parameters. In this study, however, only an initial idea is presented. Then, different configurations are tested to illustrate that metal foam is more effective for inter-channel mass and heat transfer than perforations or holes.

Such inter-channel transfer mechanisms are beneficial for different applications, as explained in section 2.8.3. In this example, each channel height is 0.775 mm, and the overall height of the cross-section is 3.875 mm, and the width is 1 mm. The channel length is 20 mm with a 10 mm diffuser section and a 2 mm straight section before channels start. At the end of the channels, there is a 10 mm straight section before the outlet. Catalysts are placed from 12-14 mm (Cat1) and 24-26 mm (Cat2). The inlet height is 1.55 mm. The topmost channel number is 1, and the bottom channel is number 5. Inlet and catalyst surface conditions are the same as the modified base case, and all the walls are adiabatic except the lower 12 and 10 mm portions, which are set as symmetry. This configuration can share mass with top and bottom channels like Figure 3-25c.

6.4.1 Steady-state analysis

Different models are tested to compare velocity, temperature and hydrogen yield at each channel. The first simulation is about when channels have straight walls (W). Next, 2 mm holes are punctured in channels number 2, 3 and 4 starting from 22 mm (P3), 18 mm (P2) and 14 mm (P1), respectively (H). P1, P2 and P3 are positions where either holes or metal foam with holes exist. Then the holes are covered with metal foam (dark blue rectangles), and different directional porosities are applied. In the first instance, porosity is kept isotropic (I), then directional porosity is applied with directional vector coordinates (3, 1, 0) (U) and with (3, -1, 0) (D). The streamwise loss coefficient is 2 (see Appendix D for all designs).

Table 6-2: Hydrogen and temperature at the end of catalysts 1 and 2, $\dot{m}$ at channel exit (W=wall)

Properties	**$H_{2,avg\ mf}$ Cat1**	**$H_{2,avg\ mf}$ Cat2**	**T_{avg} Cat1**	**T_{avg} Cat2**	**$\dot{m}$ E-8 kgs^{-1}**
Channel 1	0.00935	0.0118	591 [K]	528 [K]	1.03
Channel 2	0.00914	0.0116	588 [K]	527 [K]	1.06
Channel 3	0.00892	0.0113	585 [K]	526 [K]	1.10
Channel 4	0.00872	0.0111	583 [K]	525 [K]	1.07
Channel 5	0.00852	0.0110	579 [K]	523 [K]	0.997

Table 6-3: Hydrogen and temperature at the end of catalysts 1 and 2, $\dot{m}$ at channel exit (H=holes)

Properties	**$H_{2,avg\ mf}$ Cat1**	**$H_{2,avg\ mf}$ Cat2**	**T_{avg} Cat1**	**T_{avg} Cat2**	**$\dot{m}$ E-8 kgs^{-1}**
Channel 1	0.00944	0.0115	590 [K]	528 [K]	1.07
Channel 2	0.00917	0.0114	587 [K]	527 [K]	1.11
Channel 3	0.00879	0.0114	585 [K]	526 [K]	1.13
Channel 4	0.00872	0.0113	583 [K]	525 [K]	1.02
Channel 5	0.00866	0.0113	580 [K]	523 [K]	0.921

Table 6-4: Hydrogen and temperature at the end of catalysts 1 and 2, $\dot{m}$ at channel exit (I=isotropic foam)

Properties	**$H_{2,avg\ mf}$ Cat1**	**$H_{2,avg\ mf}$ Cat2**	**T_{avg} Cat1**	**T_{avg} Cat2**	**$\dot{m}$ E-8 kgs^{-1}**
Channel 1	0.00971	0.0129	596 [K]	550 [K]	1.06
Channel 2	0.00946	0.0129	593 [K]	548 [K]	1.07
Channel 3	0.00913	0.0128	592 [K]	546 [K]	1.12
Channel 4	0.00907	0.0126	591 [K]	544 [K]	1.05
Channel 5	0.00900	0.0125	587 [K]	542 [K]	0.956

Table 6-5: Hydrogen and temperature at the end of catalysts 1 and 2, $\dot{m}$ at channel exit (U=up (3,1,0))

Properties	**$H_{2,avg\ mf}$ Cat1**	**$H_{2,avg\ mf}$ Cat2**	**T_{avg} Cat1**	**T_{avg} Cat2**	**$\dot{m}$ E-8 kgs^{-1}**
Channel 1	0.00972	0.0129	596 [K]	550 [K]	1.07
Channel 2	0.00947	0.0129	593 [K]	548 [K]	1.07
Channel 3	0.00913	0.0128	592 [K]	546 [K]	1.12
Channel 4	0.00907	0.0126	591 [K]	544 [K]	1.04
Channel 5	0.00900	0.0125	587 [K]	542 [K]	0.955

Table 6-6: Hydrogen and temperature at the end of catalysts 1 and 2, $\dot{m}$ at channel exit (D=down, (3,-1,0))

Properties	**$H_{2,avg\ mf}$ Cat1**	**$H_{2,avg\ mf}$ Cat2**	**T_{avg} Cat1**	**T_{avg} Cat2**	**$\dot{m}$ E-8 kgs^{-1}**
Channel 1	0.00971	0.0130	596 [K]	550 [K]	1.04
Channel 2	0.00946	0.0129	593 [K]	548 [K]	1.06
Channel 3	0.00914	0.0129	592 [K]	546 [K]	1.13
Channel 4	0.00908	0.0126	591 [K]	545 [K]	1.06
Channel 5	0.00902	0.0125	587 [K]	543 [K]	0.965

6.4.1.1 Passive flow effect on hydrogen mass fraction

Metal foam as a medium of heat and mass transfer increases the reformer's efficiency by 9 to 14 per cent. This trend is visible for all three metal foam types (Table 6-2 to Table 6-6 or Table 6-7). The second column entry is the average hydrogen mass fraction at the end of the first catalyst site. For W and H, there is a significant hydrogen yield rise after the first catalyst site. However, after the second catalyst site, though net hydrogen yield is the same for both models, it is more evenly distributed for H. This uniformity indicates adequate reactants conversion in each H channel, possibly due to mass transfer between channels.

Table 6-7: Hydrogen mass fraction improvement due to metal foam in each channel

Properties	**$H_{2,avg\ mf}$ W**	**$H_{2,avg\ mf}$ H**	**$H_{2,avg\ mf}$ I**	**$H_{2,avg\ mf}$ U**	**$H_{2,avg\ mf}$ D**	**Improvement**
Channel 1	**0.0118**	**0.0115**	**0.0129**	**0.0129**	**0.0130**	**9-13%**
Channel 2	**0.0116**	**0.0114**	**0.0129**	**0.0129**	**0.0129**	**11-13%**
Channel 3	**0.0113**	**0.0114**	**0.0128**	**0.0128**	**0.0129**	**12-14%**
Channel 4	**0.0111**	**0.0113**	**0.0126**	**0.0126**	**0.0126**	**12-14%**
Channel 5	**0.0110**	**0.0113**	**0.0125**	**0.0125**	**0.0125**	**11-14%**

Figure 6-14b also reveals the same story of homogeneity (red region), where throughout the cross-section, even distribution of hydrogen is observable after the second catalyst. There is no significant temperature difference between these two configurations at each position (Figure 6-14, Table 6-2 and Table 6-3). The identical temperature growth is due to the balance between temperature, mass flow rate and reactants consumption. So the model with or without holes makes no difference for temperature distribution.

6.4.1.2 Comments on higher hydrogen production using metal foam

After each catalyst position, the average temperature and hydrogen mass fraction for I, U and D models are nearly identical. The reason for this analogous development is the same ht and iad values for these three models, as concluded by section 5.1.8.1. For instance, the metal foam has a very high porosity (0.92), affecting mass distribution slightly. As a result, even I and H models have nearly identical velocity vectors, although the H model has no metal foam (Figure 6-18). Section 5.1.8.2 shows the same result.

The lower inlet velocity (0.1 ms^{-1}) can be another reason, so the H model's full potential is not apparent. However, this study’s primary focus is to highlight the importance of metal foam as a mass and heat transfer medium. For this role, the metal foam serves the purpose because of the high hydrogen yield produced.

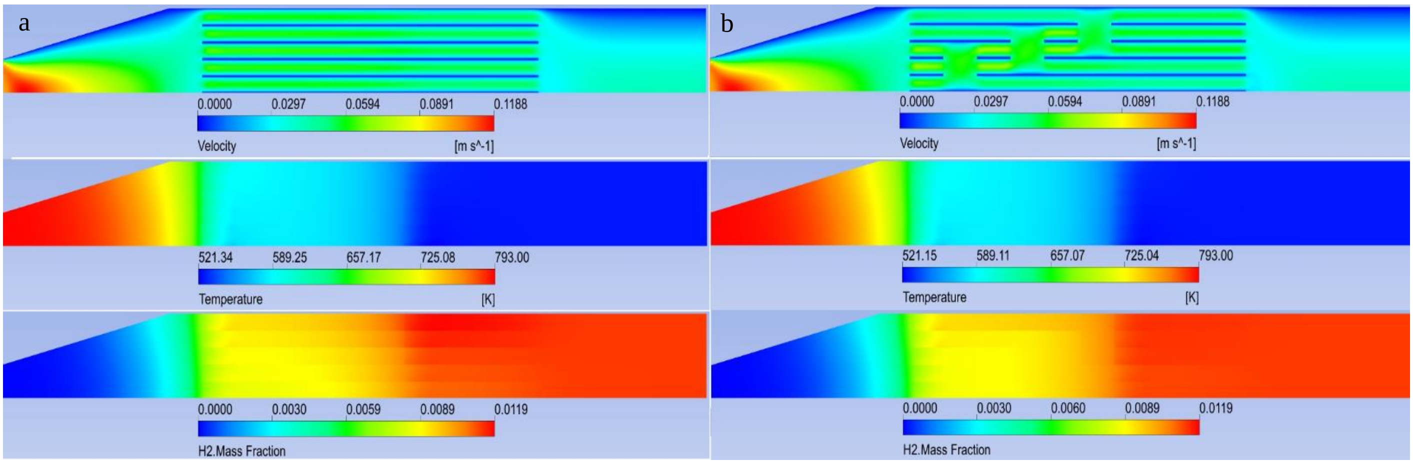

Figure 6-14: Contours for (top) Velocity, (middle) temperature and (bottom) hydrogen mf for (a) W and (b) H

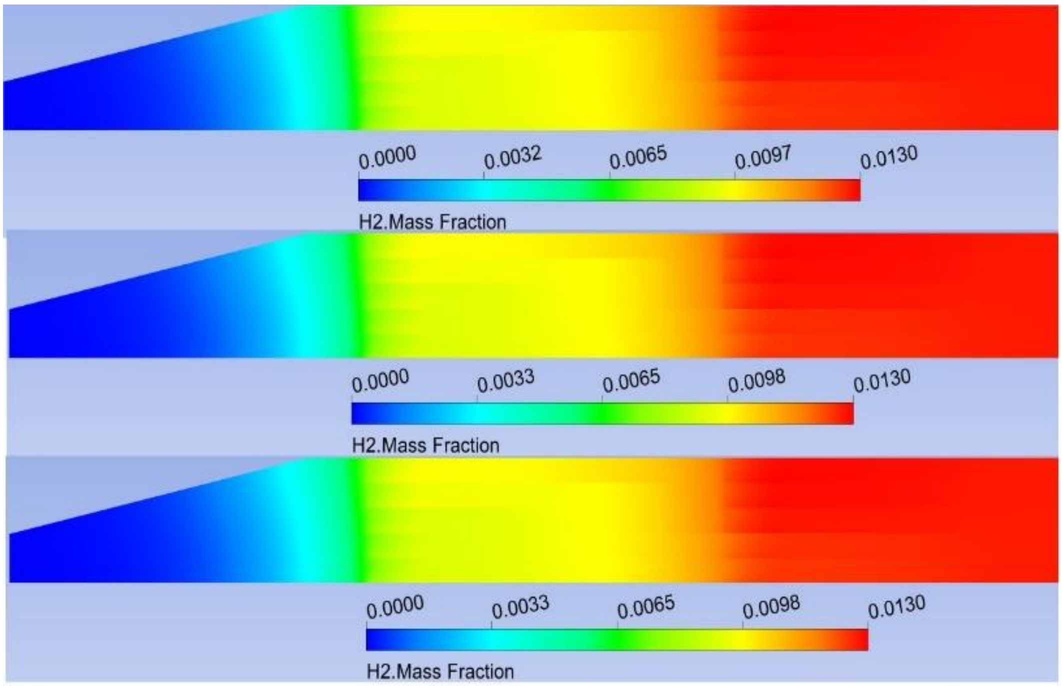

Figure 6-15: Hydrogen mf contours for (top) I, (middle) U (3,1,0) and (bottom) D (3,-1,0)

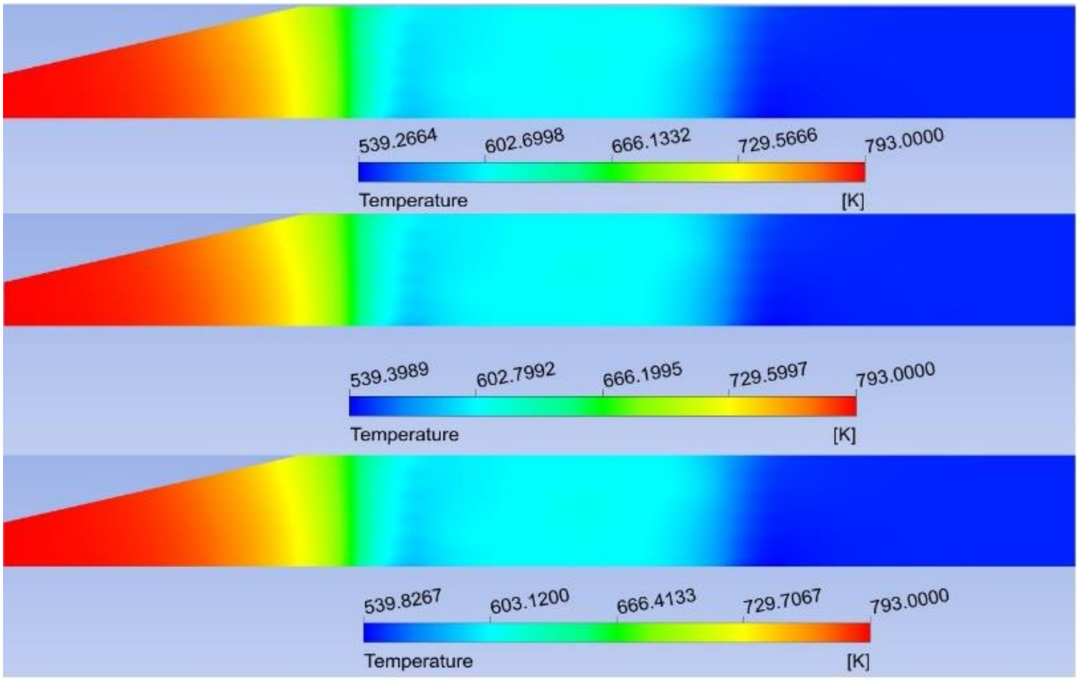

Figure 6-16: Temperatre distribution for (top) I, (middle) U (3,1,0) and (bottom) D (3,-1,0)

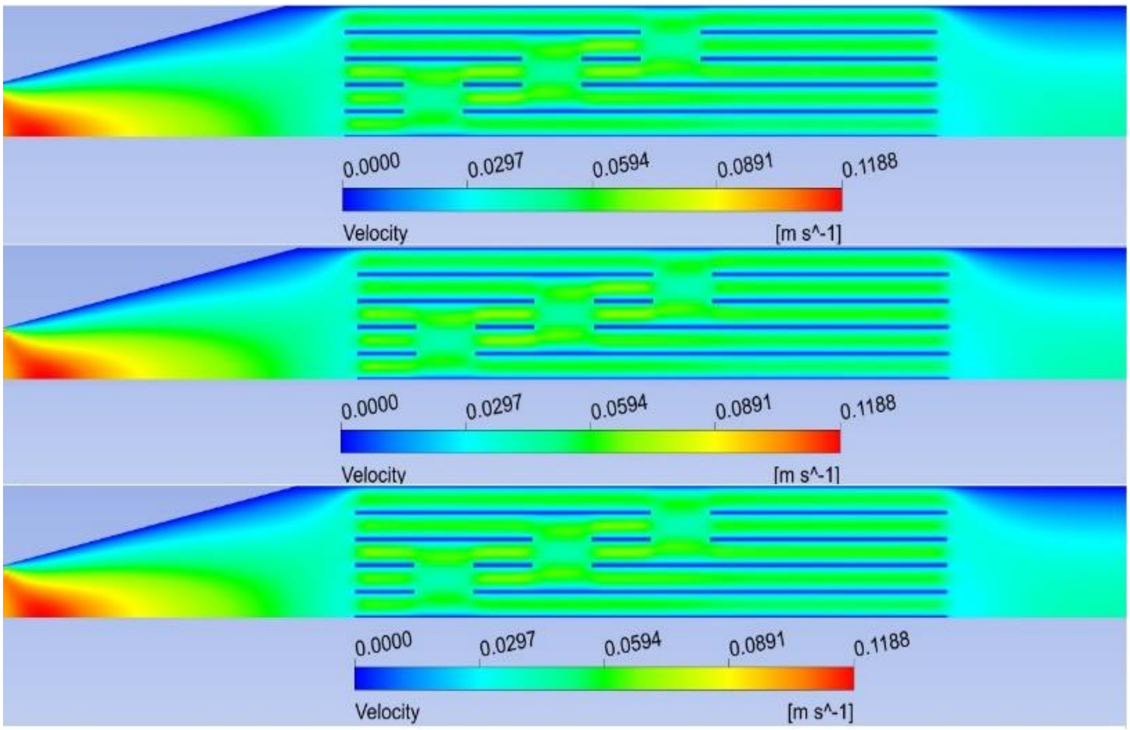

Figure 6-17: Velcoity contours for (top) I, (middle) U (3,1,0) and (bottom) D (3,-1,0)

6.4.1.3 Passive flow effects on the velocity distribution

Changing metal foam parameters, such as SC, can divert the flow to the desired channel to receive the optimum flow rate, like channel 5 of all models. Therefore, due to this minimum mass flow rate (Table 6-2 to Table 6-6), the appropriate metal foam parameters adjustment at P1 can evenly distribute flow from channel 3 to 4 and 4 to 5.

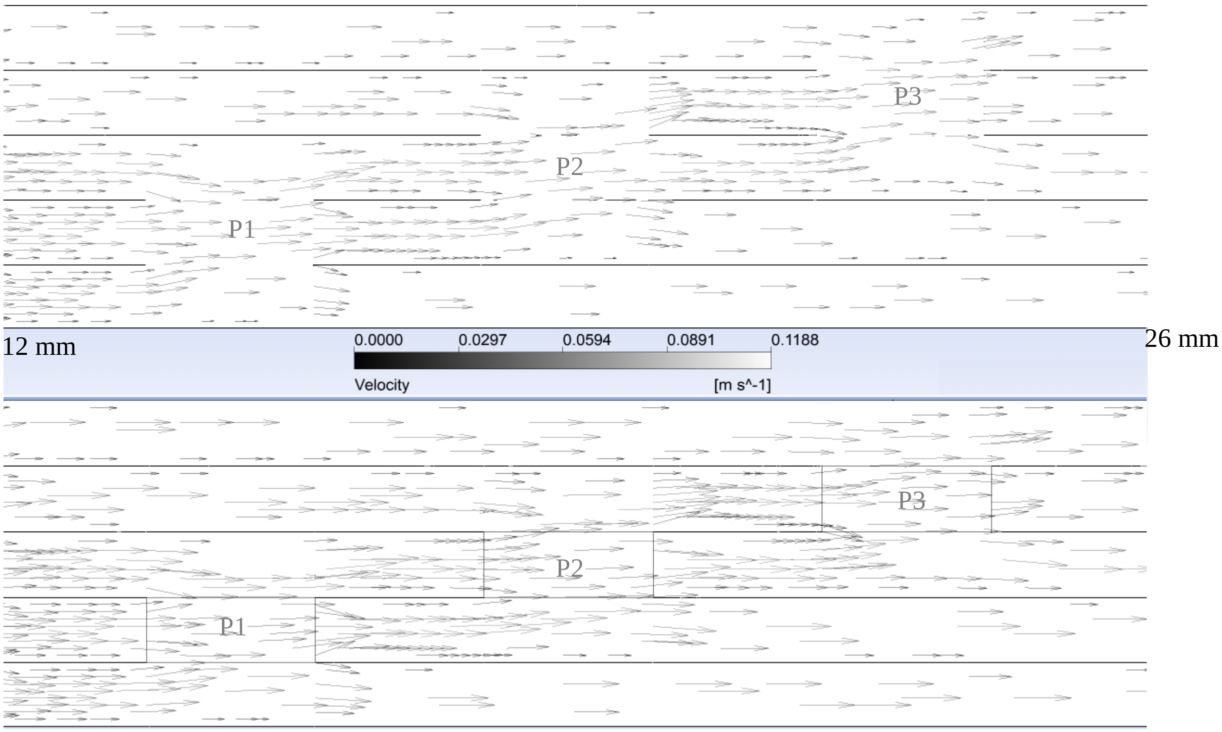

Figure 6-18: Velocity vectors for (top) H and (bottom) I models

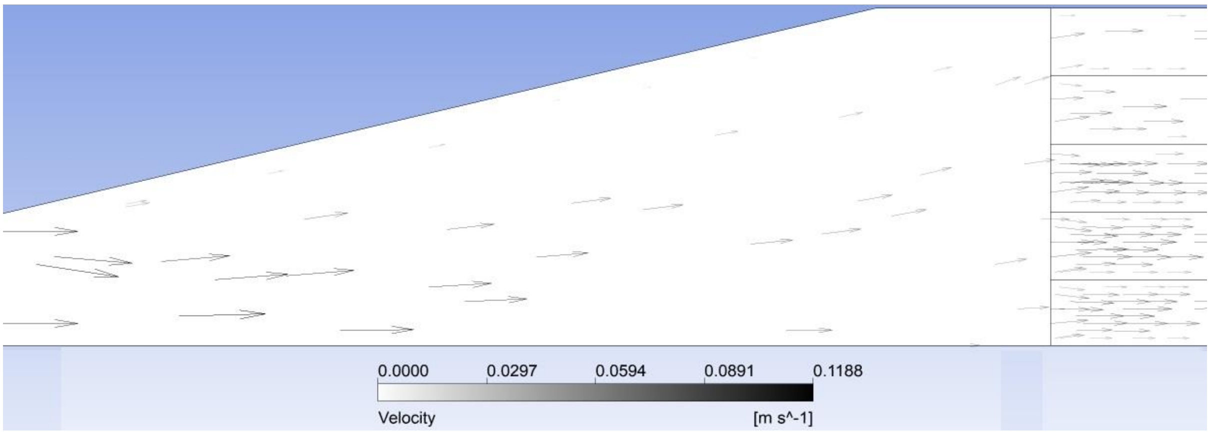

Figure 6-19: Velocity vectors in the diffuser section

Higher FR efficiency is not due to mass distribution, as shown in Figure 6-20, Figure 6-21 and Figure 6-22. At the beginning (before P1), channel 1 and 2 of model W attain the highest velocity while model H’s channel 1 and 2 gets the lowest (Figure 6-20). Similarly, channels 3, 4 and 5 of W velocity is less than model H’s channels 3, 4 and 5. However, the hydrogen yield has a variable correlation and increases or decreases with the velocity (column 3 Table 6-2 and Table 6-3). The same comparison for catalyst site 2 is not reasonable due to mass

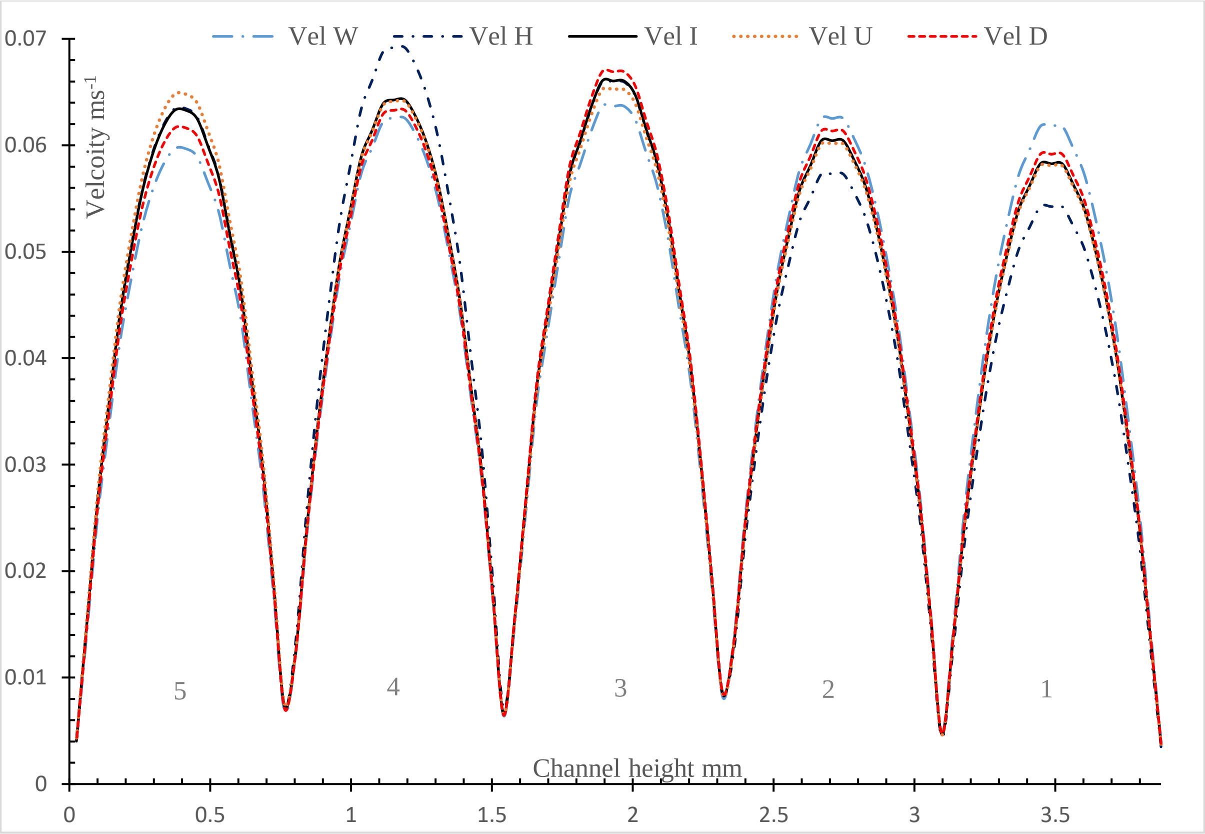

Figure 6-20: Velocity profile at 13 mm (middle of the first catalyst, before P1)

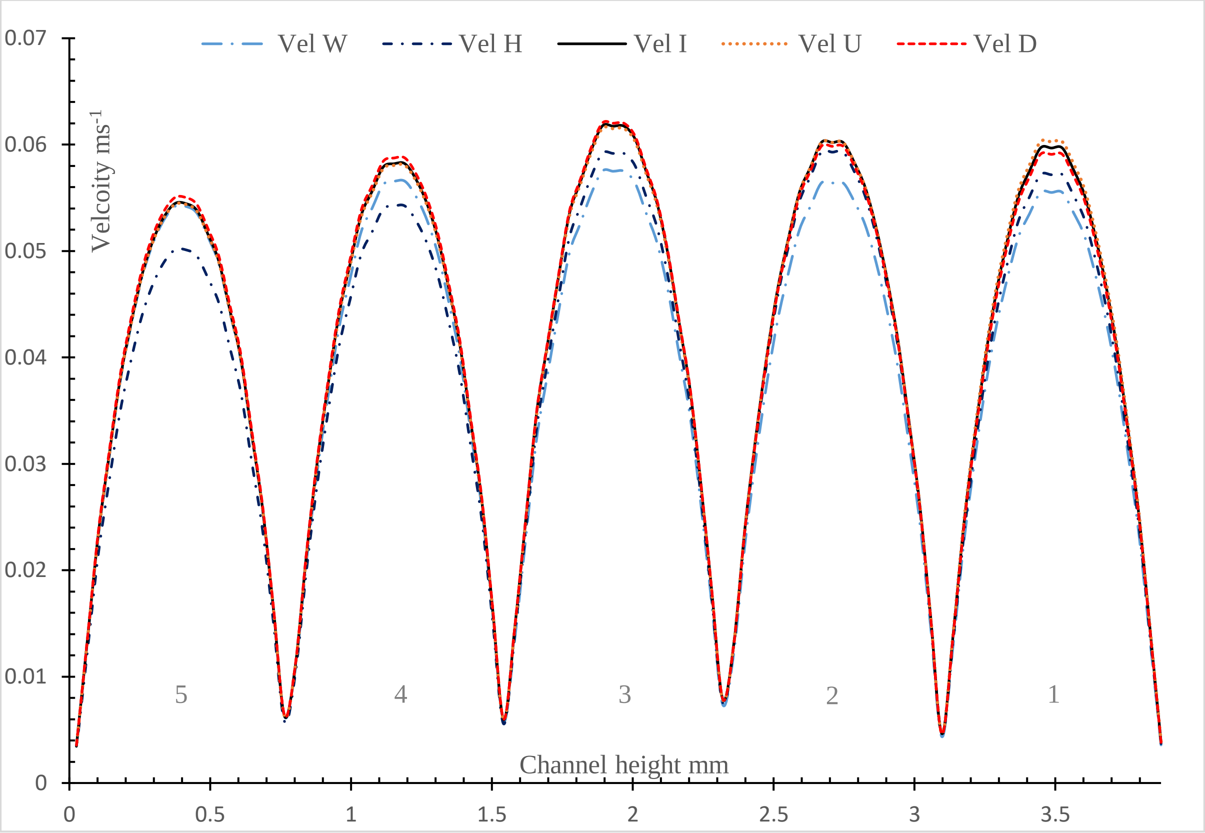

Figure 6-21: Velocity profile at 25 mm (middle of the second catalyst, after P3)

exchange. To better understand, the study will investigate the mass flow distribution effects at the channel's exit.

6.4.1.4 Temperature distribution

Next, the temperature range and values at the catalyst site are compared in column 4 (Table 6-2 to Table 6-3). The temperature range between channels varies 9-12 K after the first catalyst site and 5-8 K at the second for all the models. As all the walls are adiabatic, so there is no heat transfer between channels except through holes or metal foam. Despite this condition, both W and H have a similar temperature range and values.

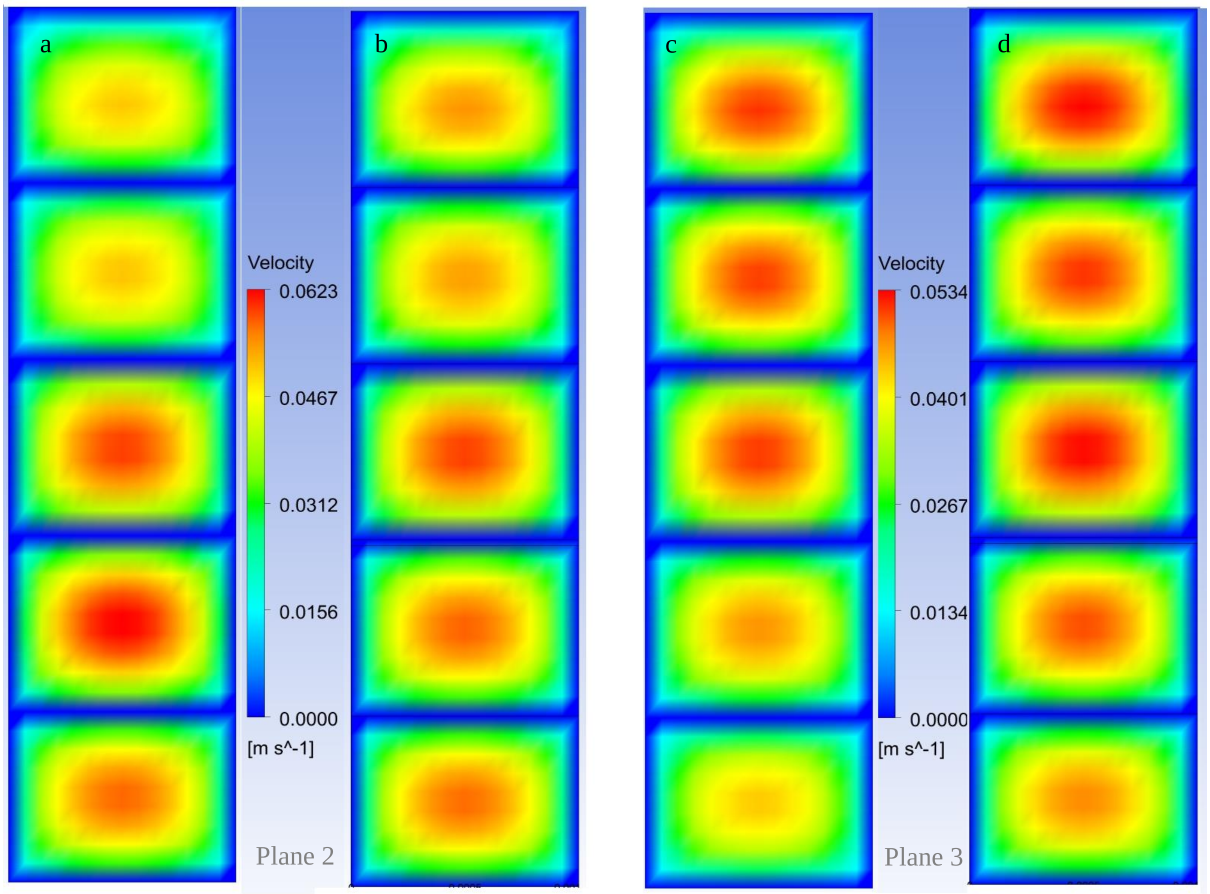

Figure 6-22: Velocity contours while entering the channels (12.1 mm, Plane 2) for a) H b) I, and exiting the channels (31.9 mm, Plane 3) for c) H d) I models

However, temperature values for models I, U and D are higher from models W and H. After the first catalyst site, it is 6 K higher, but at the end of the second, it is 20 K higher. This trend means metal foam retains the heat and distributes it to the passing fluid after losing it at the first catalyst site. The same observation appears in chapter 5.1.6 when the metal foam model (MF6) achieved the highest minimum temperature. It is 12 K more than the clear (M0) model.

It means FR's higher efficiency (9% more H_2 mf) for models I, U and D is due to the higher temperature in catalyst surroundings.

The contours (Figure 6-22) show fluid speed while entering and exiting I and H models' channels. Velocity distribution is uniform at both ends for the I model. For the H model, it somewhat reverses from the inlet to the outlet. Nonetheless, owing to the higher catalyst temperature, more hydrogen produces for all the foam configurations.

6.4.1.5 Interchannel mass distribution

The mass flow rate profiles reveal the complete picture of uniform mass conversion in the case of the H model against the W. The velocity profiles are extracted at 25 mm, whereas the mass flow rate is calculated at 32 mm. Still, it shouldn't make much difference as after 24 mm, there are only adiabatic walls without any perforation.

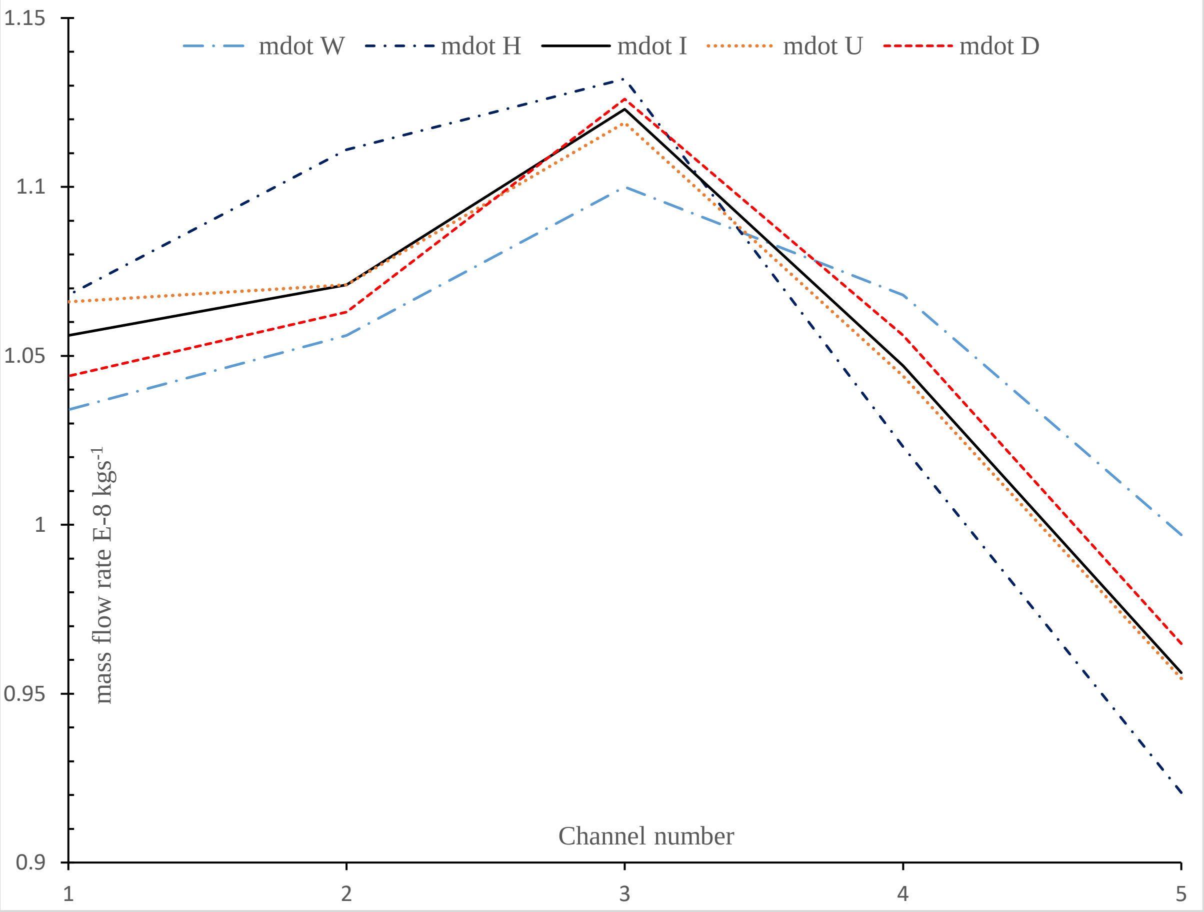

Figure 6-23: Average mass flow rate calculated at the channel exit (at 32 mm)

The velocity profiles (Figure 6-21) match the mass flow rate trends (Figure 6-23). Therefore, the velocity proportionally increases with the mass flow rate for each model. However, a direct comparison between H and metal foam models is not accurate.

Mass flow distribution explains the non-uniformity of H_2 mf in the W model. W's channel 5 has the highest mass flow rate (Figure 6-23), but velocity is similar to the H model’s channel 5 (Figure 6-21). These conditions make channel 5 of the W model convert fewer reactants to products; hence, the non-uniformity rises between channels (Figure 6-14). The D model shows a slight improvement in channel five’s mass flow rate compared to other metal foam configurations, indicating that changing metal foam properties can successfully divert the flow.

6.4.2 Transient analysis

In order to see the evolution of hydrogen mass fraction and velocity with time, transient simulations are performed. As FR catalyst is sometimes installed on a car with a pulsating incoming flow, transients simulation can help identify which channel and model can quickly adapt to these variations. It will also highlight the time to reach a steady-state solution, especially for hydrogen production.

A total simulation time of 1.4 s is selected for this simulation. This period is sufficient for the I model to reach the equilibrium state at the first catalyst site. Overall to get a total steady-state solution will require a longer time. This trend is observable from Figure 6-31, where the transient solution has not reached the steady-state for model W. So 1.4 s time is sufficient to prove that metal foam helps to achieve a fully developed solution faster.

6.4.2.1 Hydrogen mass fraction development

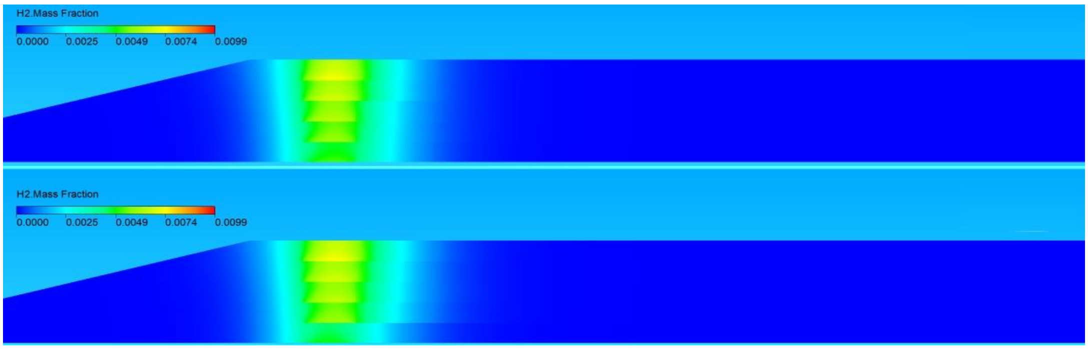

Figure 6-24: hydrogen mass fraction at 0.03 sec I (top) vs W (bottom)

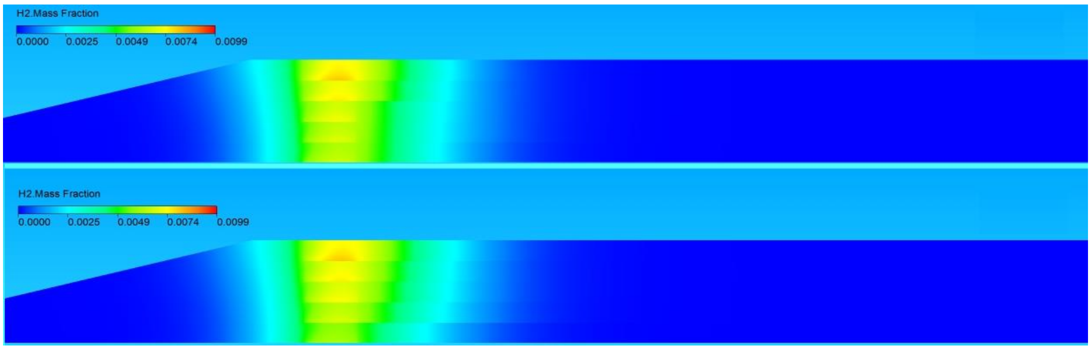

Figure 6-25: hydrogen mass fraction at 0.06 sec I (top) vs W (bottom)

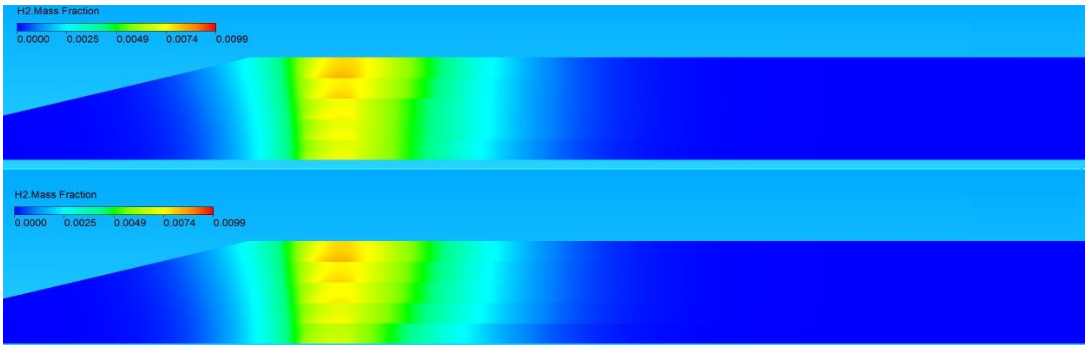

Figure 6-26: hydrogen mass fraction at 0.09 sec I (top) vs W (bottom)

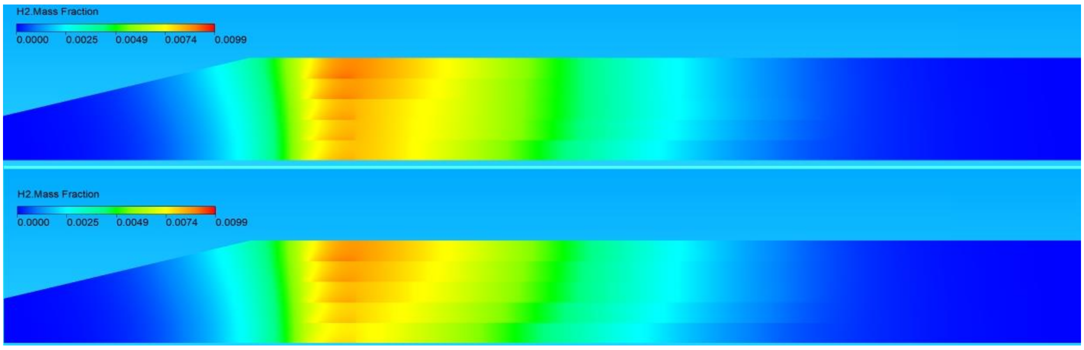

Figure 6-27: hydrogen mass fraction at 0.24 sec I (top) vs W (bottom)

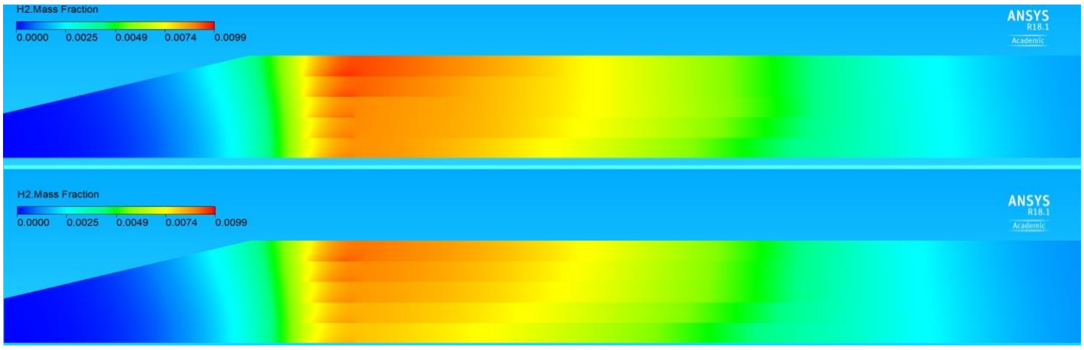

Figure 6-28: hydrogen mass fraction at 0.48 sec I (top) vs W (bottom)

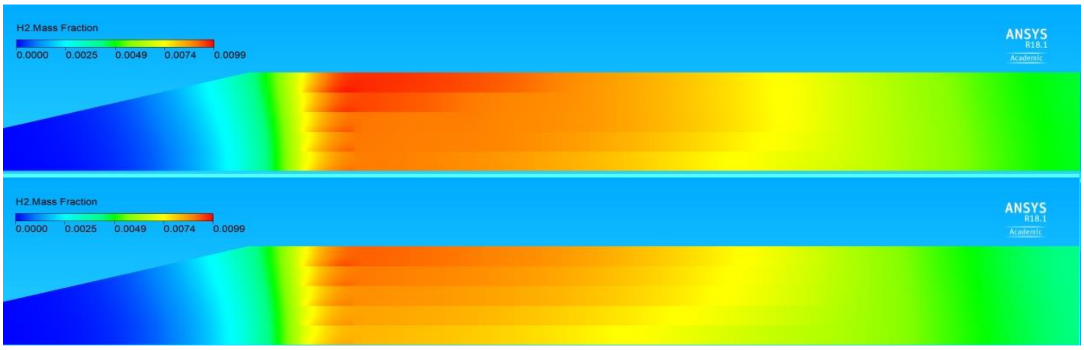

Figure 6-29: hydrogen mass fraction at 0.75 sec I (top) vs W (bottom)

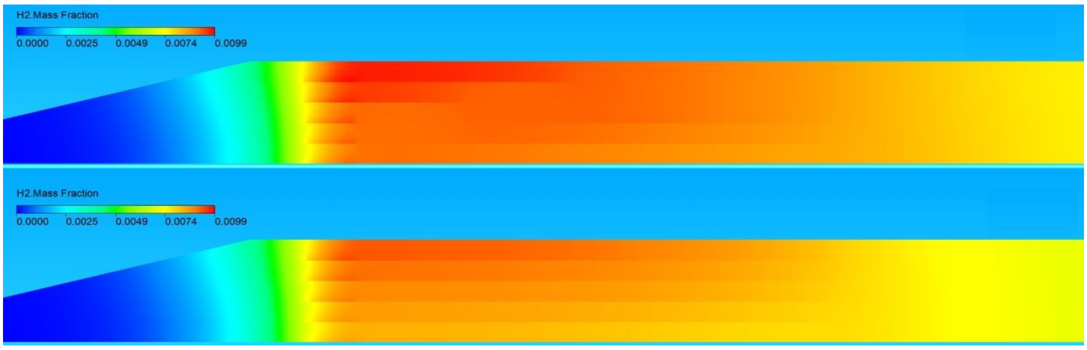

Figure 6-30: hydrogen mass fraction at 1.11 sec I (top) vs W (bottom)

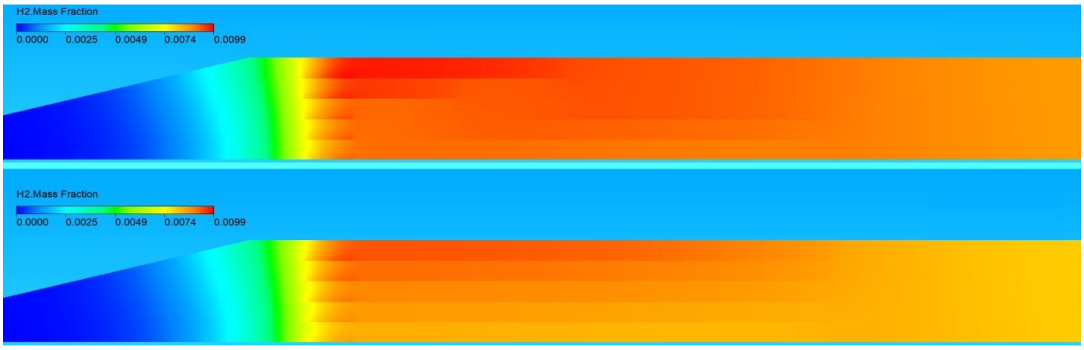

Figure 6-31: hydrogen mass fraction at 1.4 sec I (top) vs W (bottom)

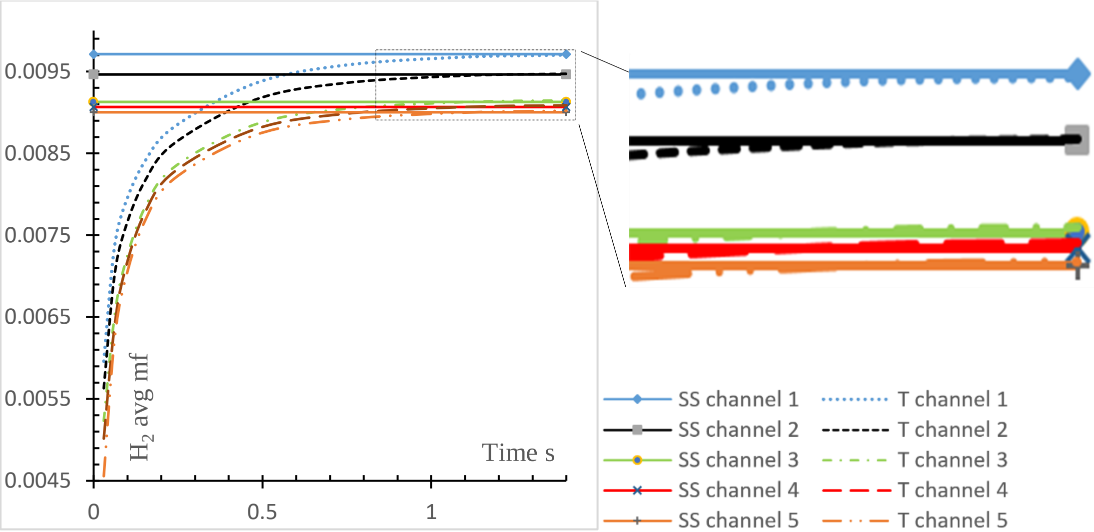

Figure 6-32: Steady-state vs transient solution for I model (SS steady-state, T transient)

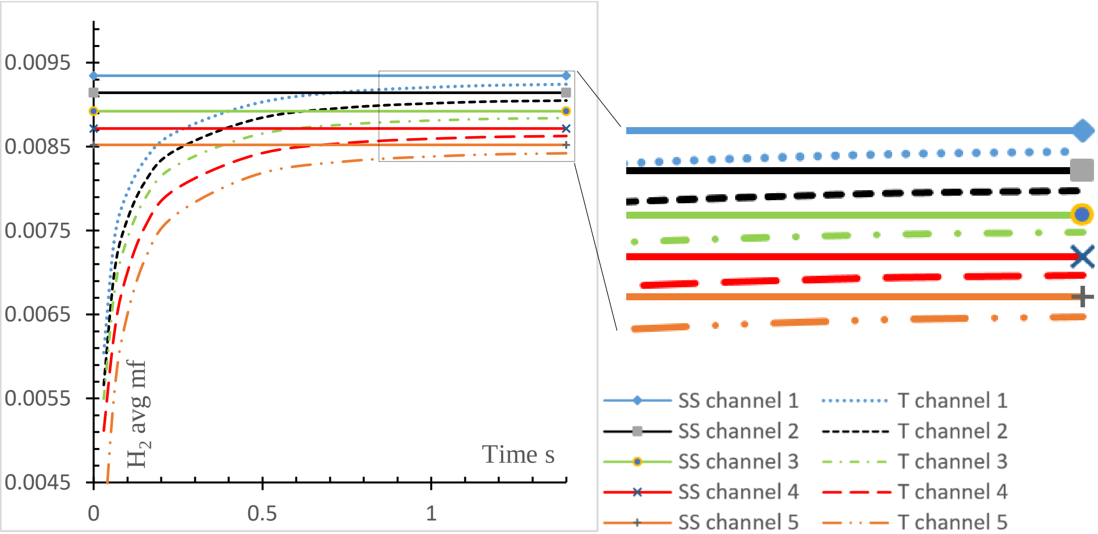

Figure 6-33: Steady-state vs transient solution for W model (SS steady-state, T transient)

The hydrogen contours (Figure 6-22 to Figure 6-32) and plots for the I model show that hydrogen is readily produced in a reactor with metal foam. On the other hand, contours and profiles for model W (Figure 6-22 to Figure 6-31 and Figure 6-33) show slow progress. At the end of 1.4 s, the hydrogen mass fraction lines (for T) are nearly flat, indicating a longer time to reach equilibrium.

So this shows that metal foam increases the fuel reformer yield and helps it achieve it quickly. It would be an interesting study to use different inlet and boundary conditions. This way, these models can fully describe the pros and cons of using metal foam in channels. It is worthy to point out that the solution fully converges but has not reached the equilibrium state as the second catalysts site (24-26 mm) does not show significant progress.

6.4.2.2 Velocity development

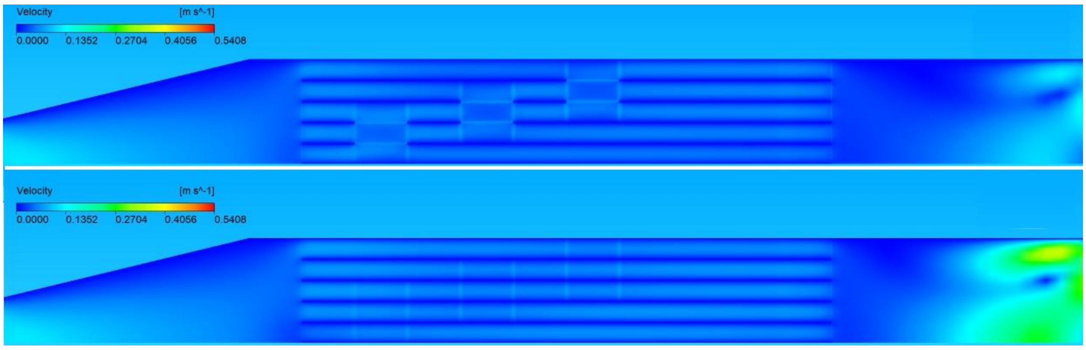

Figure 6-34: Velocity at 0.03 sec I (top) vs W (bottom)

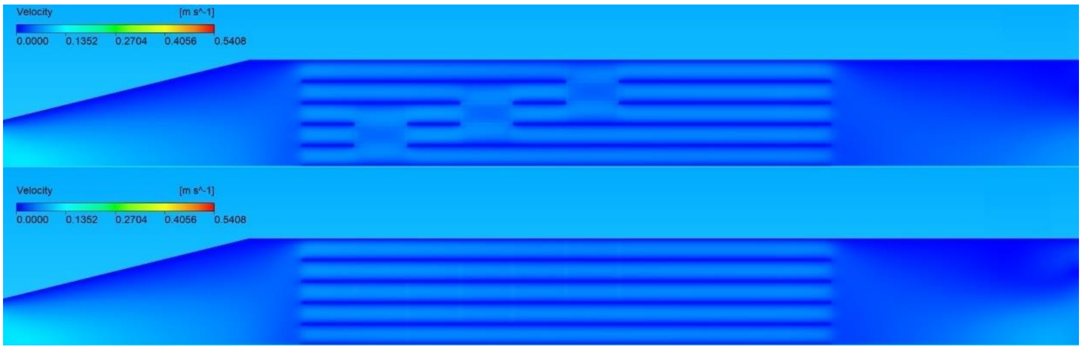

Figure 6-35: Velocity at 0.06 sec I (top) vs W (bottom)

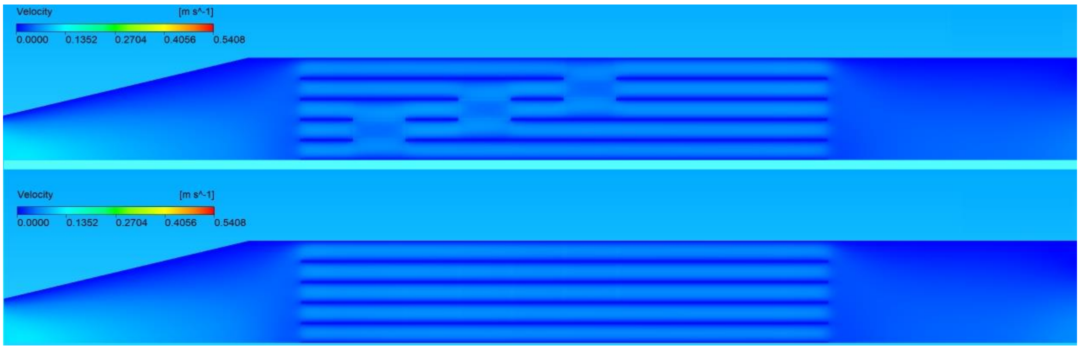

Figure 6-36: Velocity at 0.09 sec I (top) vs W (bottom)

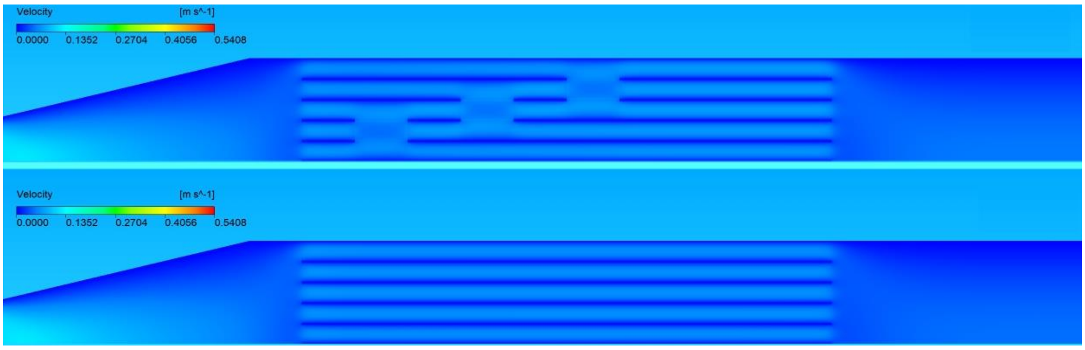

Figure 6-37: Velocity at 1.4 sec I (top) vs W (bottom)

Similar to mass fraction transients results, velocity develops faster for the I model. The vertical (white) lines at 0.03 s for the W model are interfaces. These quickly vanish after some iterations. Unlike hydrogen mass fraction, velocity quickly stabilizes itself after 0.09 s.

6.5 3D steady-state results

A 3D model is also simulated to emphasize the importance of heat and mass transfer. In the event of channel blockage by carbon formation during SMR reaction, the inter-channel mass transfer can ensure fluid mixture distribution to the adjacent channels.

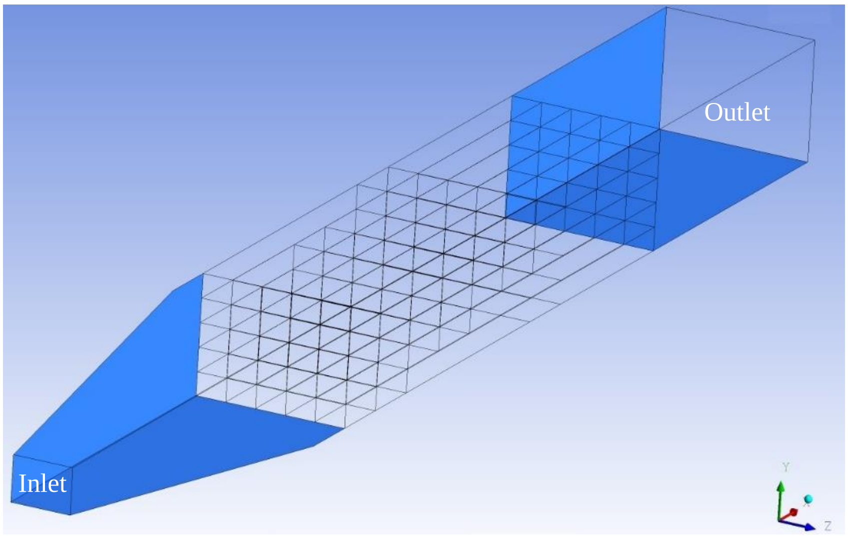

Figure 6-38: A 3D quarter model of FR catalyst

The 3D model is an extension of the previous 2D model, and a quarter model of the 3D catalyst is tested. The blue regions are symmetrical surfaces, and the rest of the surfaces are adiabatic walls. Reactor inlet size is four times the size of the channel inlet. All other dimensions are identical to the previous 2D model. Just a 5×5 channels stack is tested with the same inlet and catalyst surface conditions used before in the 2D model. This configuration can share mass with all adjacent channels like Figure 3-25d.

So in case of any blockage by foreign material or coke formation, cross channel flow can overcome this blockage. As already proven in 2D simulation, metal foam placement in the cross channel region increases the efficiency, so just Iso-porous metal foam (I3D) and channel with holes (H3D) models are tested.

6.5.1 Flow exchange during channel blockage

First of all, flow distribution from one channel to the rest is shown if all other channels inlets are closed. The distribution pattern is the same for both models. The inlet velocity is not changed, so there is a very high-speed flow at the working channel inlet. Hence, only that channel will be available for reaction in case of no passive passages, thus experiencing very high velocity and low residence time.

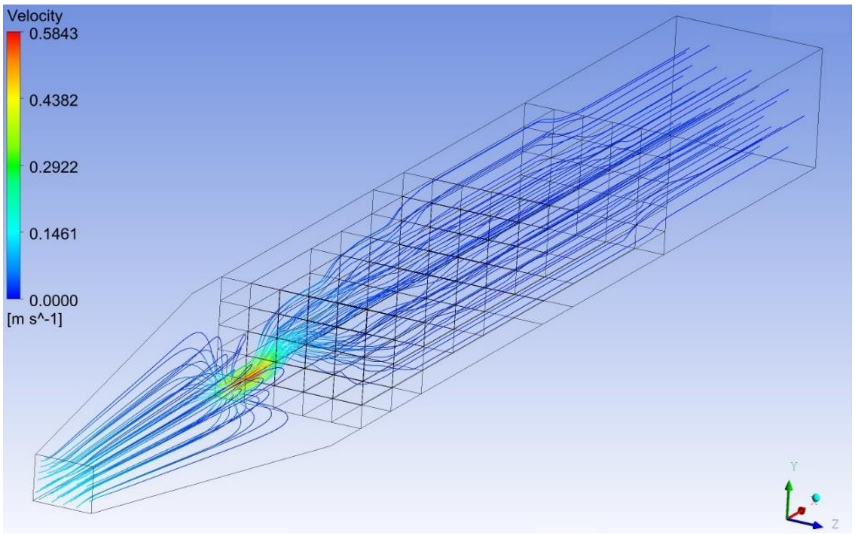

Figure 6-39: Velocity pathlines from one channel to the rest of the channels (I3D)

In such a cross channel situation (Figure 6-39), the first catalysts site, from 12-14 mm, will be inactive for the rest of the channels as the first series of catalysts end before the cross-flow passage. Then, however, the second catalysts site of all the channels, from 24-26 mm, will be available for the reaction.

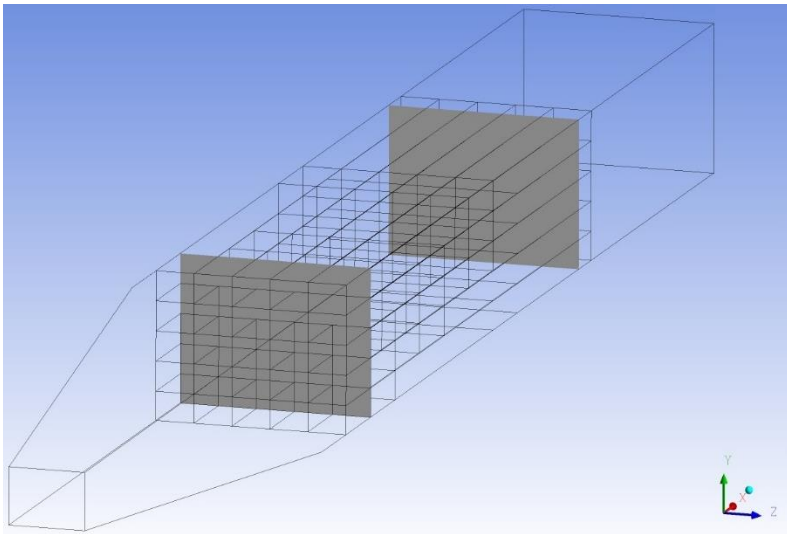

Figure 6-40: XY Plane 2 at 14 mm and Plane 3 at 31 mm

6.5.2 Hydrogen distribution

Next, simulation is performed, and all the channels inlets are open. Contours for velocity, hydrogen mass fraction, temperature and velocity are extracted at two planes (Figure 6-40), Plane 2 at 14 mm and Plane 3 at 31 mm.

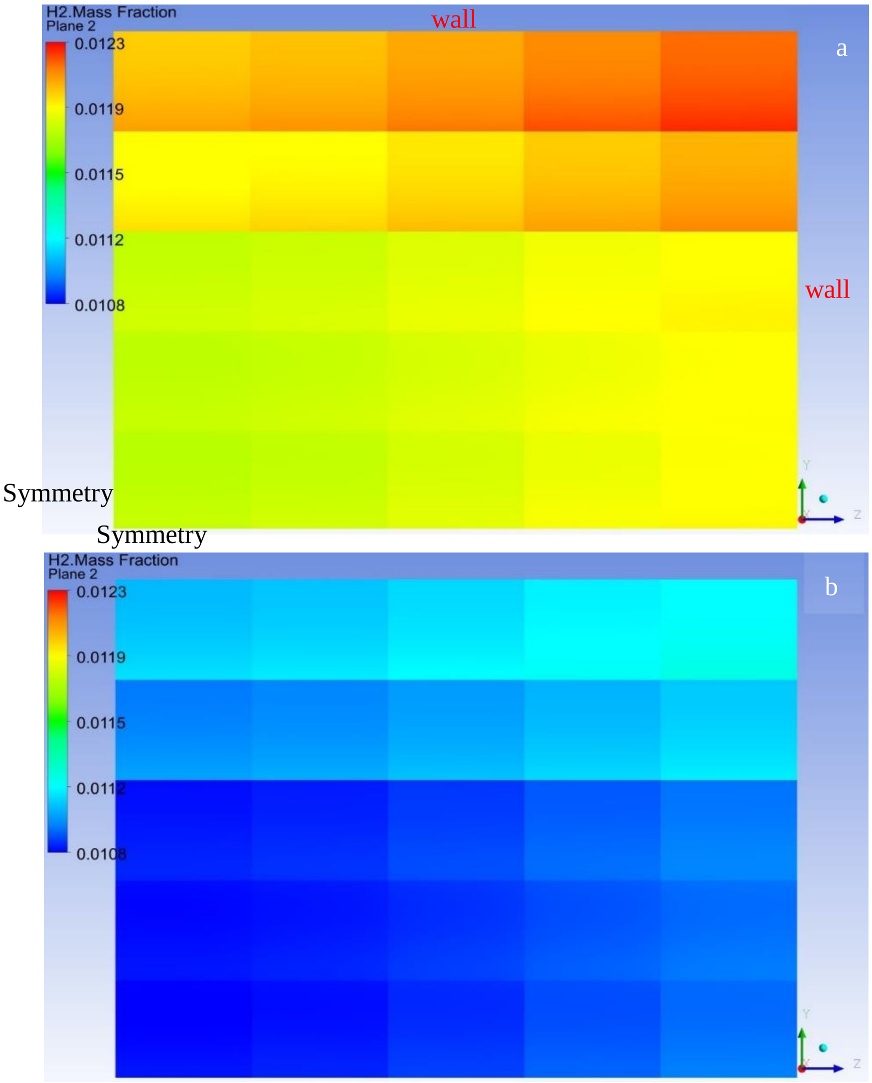

Figure 6-41: Hydrogen mf comparison at Plane 2 for (a) I3D and (b) H3D (same scale)

The maximum hydrogen mass fraction is found in the top right channel. The lower left channel has symmetry before its inlet.

Like previous 2D cases, maximum hydrogen mass fraction forms in regions surrounded by container walls. Both 2D and 3D designs show uniform hydrogen distribution after the first and second catalysts (Figure 6-41 and Figure 6-42). Nevertheless, model I3D offers a better yield than the H3D model. After the second catalyst (Figure 6-42), the I3D hydrogen mass fraction value is 0.015 compared to 0.013 of the H3D model (15% higher). Moreover, the uniformity is higher after the second catalyst, as the difference between maximum and minimum hydrogen mass fraction at Plane 2 is higher, whereas it is nonexistent at Plane 3.

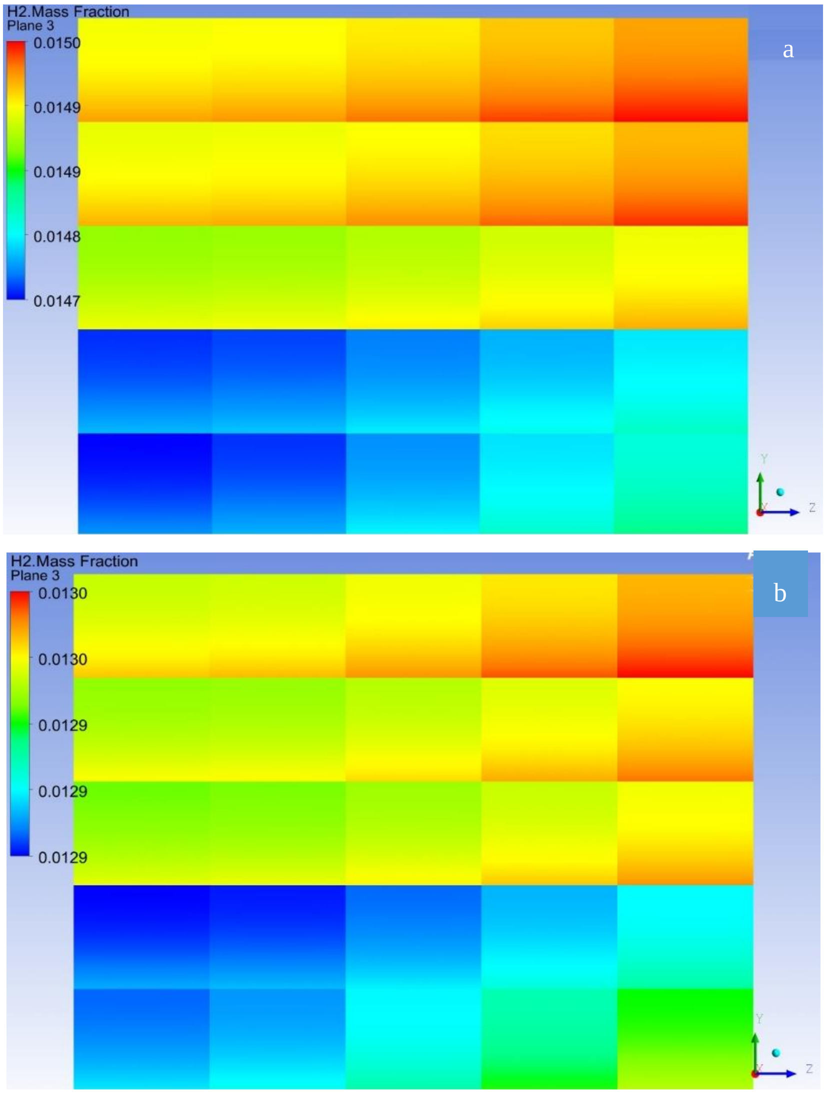

Figure 6-42: Hydrogen mf comparison at Plane 3 for (a) I3D and (b) H3D (local scale)

6.5.3 Temperature distribution

The higher hydrogen mass fraction originates from the elevated channel temperature, which is greater for the I3D.

Table 6-8: Average temperature comparison of different models in channels

#	**H**		**I**		**H3D**		**I3D**	
	$T_{avg, Cat1}$ [K]	$T_{avg, Cat2}$ [K]	$T_{avg, Cat1}$ [K]	$T_{avg, Cat2}$ [K]	$T_{avg, Cat1}$ [K]	$T_{avg, Cat2}$ [K]	$T_{avg, Cat1}$ [K]	$T_{avg, Cat2}$ [K]
1	590	528	596	550	549	491	557	511
2	587	527	593	548	547	490	556	510
3	585	526	592	546	546	489	555	509
4	583	525	591	544	545	489	554	508
5	580	523	587	542	543	488	552	507

6.5.3.1 Temperature distribution in 2D (I and H) and 3D (I3D and H3D) designs

After the first catalyst location, like 2D results (6-8 K), the temperature difference between I3D and H3D is minimal (8-9 K) (Table 6-8). Similarly, after the second catalyst, the temperature variance between I3D and H3D is around 20 K for the 3D models (identical to 2D I and H) (Figure 6-44). This similar temperature drop demonstrates that both models' simulations are reliable. However, the same temperature fall also reveals that multiple passive passages of 3D models do not improve the entire cross-section's heat homogenisation for given conditions.

Furthermore, the temperature drop between the first (Plane 2) and the second catalysts (Plane 3) position remains the same. For the H model and I, approximately 60 K and 46 K, respectively. Similarly, it remains unchanged for H3D and I3D. However, one crucial factor is that, unlike the 2D case, five times reacting material quantity is used in the 3D model while doubling the inlet mass flow rate. So, the maximum temperature drop value is different.

Individually, temperature variation (for 3D) is around 5 K across each plane. It is more evenly distributed near the end of the channel, such as a 3-4 K difference between each model's highest and lowest value (Table 6-8).

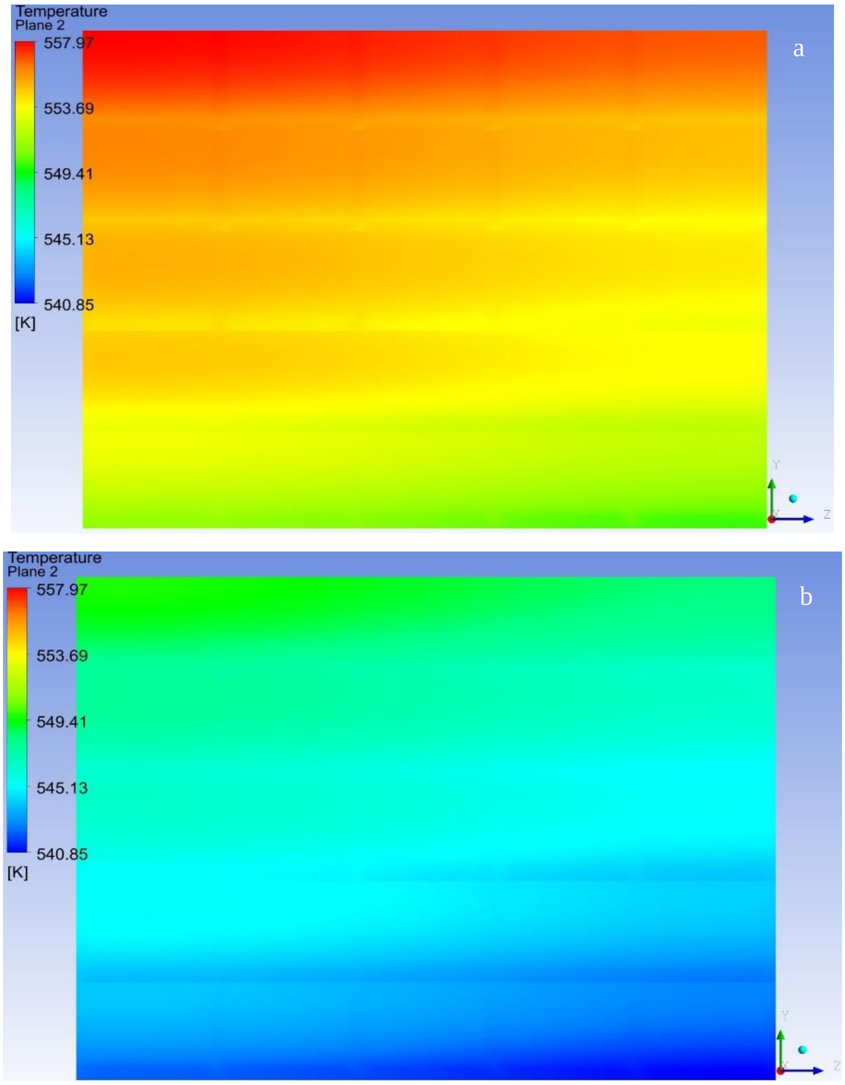

Figure 6-43: Temperature comparison at Plane 2 for (a) I3D and (b) H3D (same scale)

6.5.3.2 The overall advantage of using metal foam

The I3D temperature enhancement is advantageous as the reformer can operate even at lower inlet temperatures. Conversely, a higher temperature may cause thermal stress beyond the structural integrity of the reformer. Similarly, it may encourage unwanted reactions, which will reduce the catalyst yield.

For instance, the temperature should remain below 898 K for ethanol steam reforming. Beyond this temperature limit, ethanol can decompose to acetaldehyde and produce more CO while less H_2. An alternative solution is to increase the catalyst quantity, which in return increases the reaction rate and reduces the temperature (Uriz *et al.*, 2011).

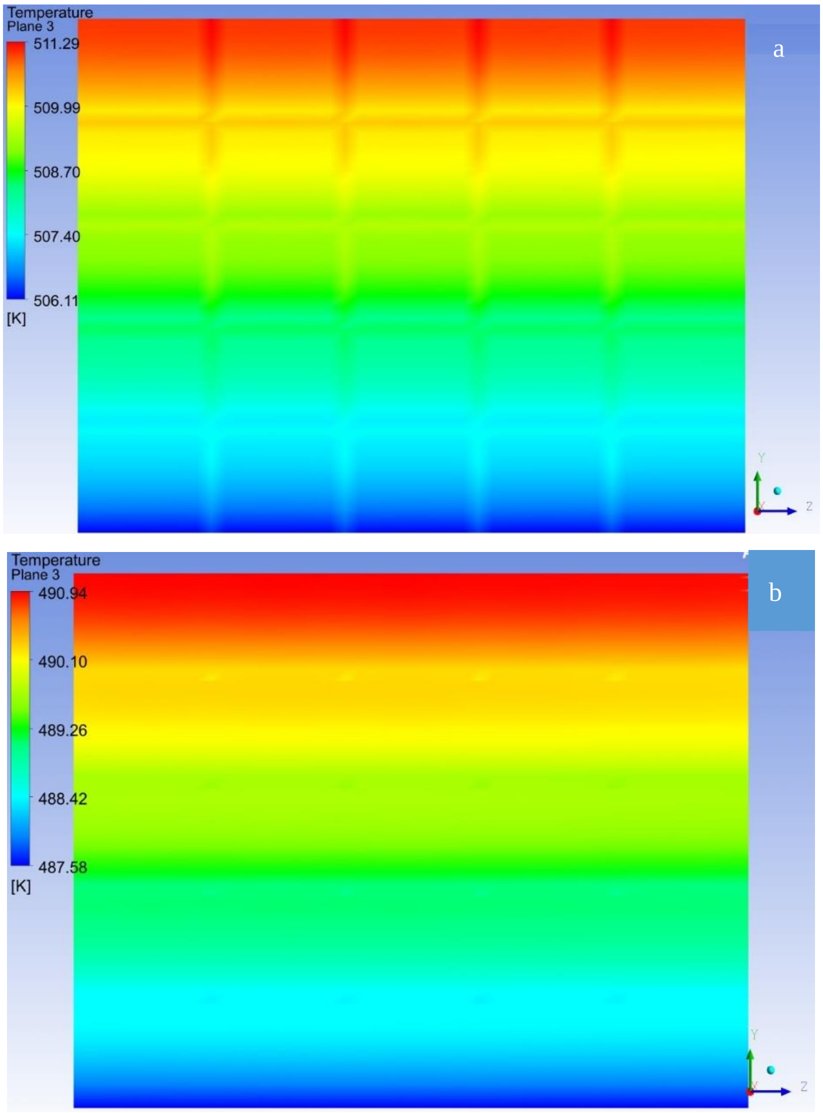

Figure 6-44: Temperature comparison at Plane 3 for (a) I3D and (b) H3D (local scale)

6.5.4 Velocity distribution

Velocity values are not that different for the two models. In the beginning, the velocity is uniform for both models, but in the end, it is better for the I3D model.

After reacting at the first catalyst site, channel 4 and its adjacent channels layers receive the highest flow speed (Figure 6-45). This distribution shows flow non-uniformity despite having passive flow passage. However, the I3D model shows better flow spreading as the channel 4 layers have the metal foam in addition to the flow passage (P1 location). The metal foam offers resistance to the upstream flow to channel 4 layers, so the flow is divided into channel 3 and 4 layers. Even channel 2 layers obtain an adequate flow rate while channel 1 layers receive the lowest.

For the H3D case, the highest flow speed region occurs in channel 4 and its neighbouring layers. Meanwhile, channel 1 and 2 layers get the lowest flow rate, which may mean catalysts in this location do not perform to their full potential as they get starved. However, velocity variation depends on several factors besides mass flow rate.

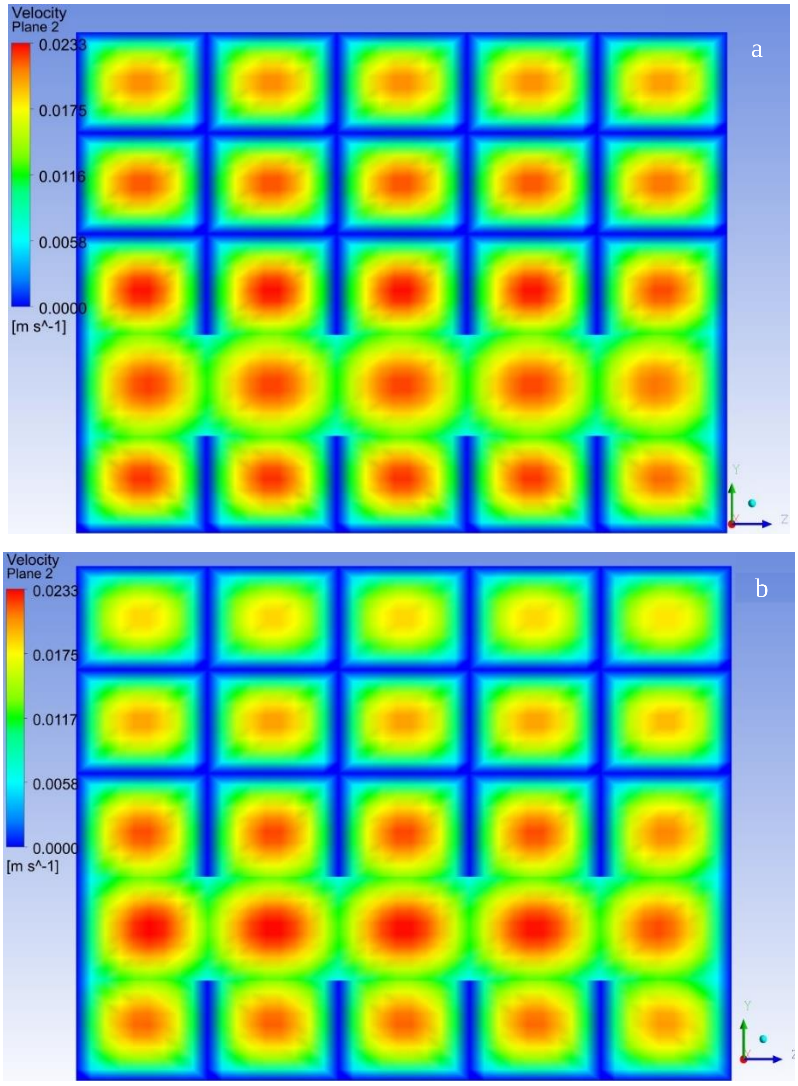

Figure 6-45: Velocity comparison at Plane 2 for (a) I3D and (b) H3D (same scale)

The flow pattern reverses for both models near the end of the channel section due to P2 and P3 passive flow locations. However, the first four layers of the I3D model show better flow uniformity, suggesting metal foam acts as a flow diverting medium. In the absence of metal foam (H3D), though the flow pattern inverts, the holes feed only their channel layers (P2 and P3 in channel 3 and 2 layers, respectively) (Figure 6-46).

In the end, the channel 5 layer shows the lowest speed values for both models but is better for the I3D. For the H3D, the flow pattern will stay the same for the given inlet conditions, but for

I3D, it can change by changing the metal foam properties. Section 5.1.8.2 indicates that permeability and porosity are the two most influencing factors affecting the flow speed. Hence, the metal foam parameters optimisation, location and numbers require more research.

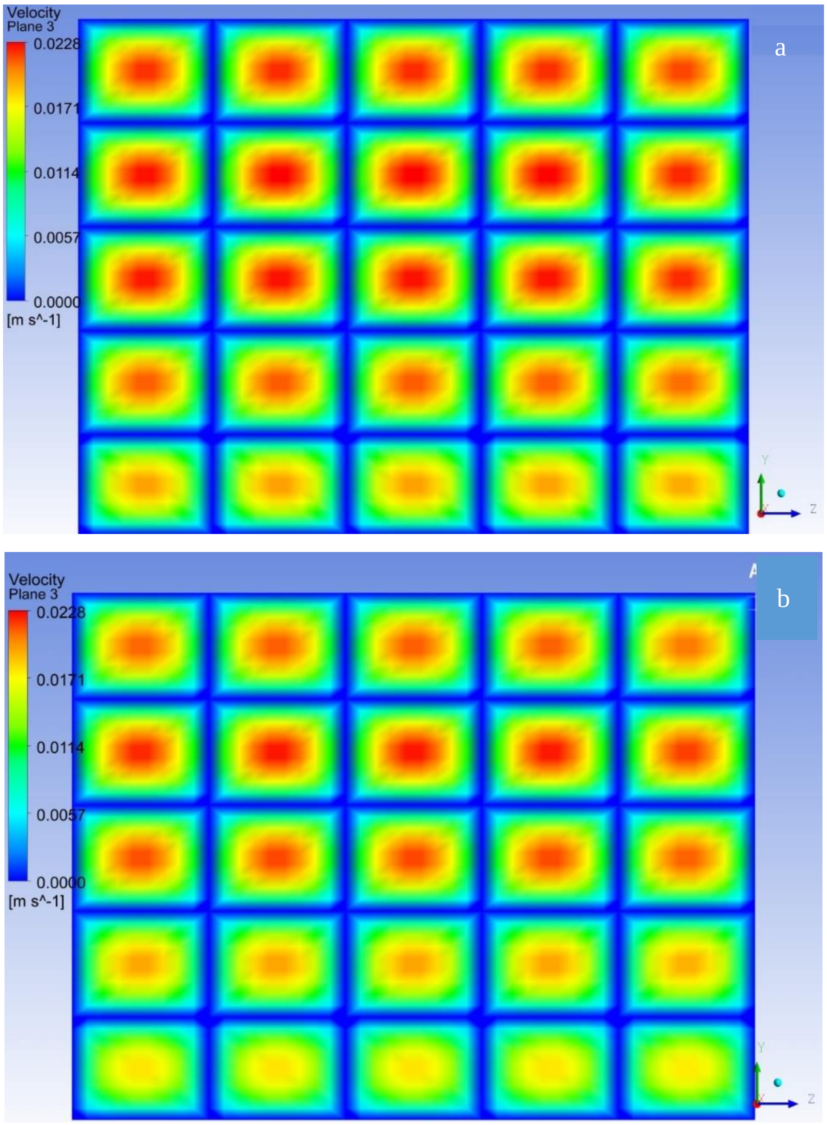

Figure 6-46: Velocity comparison at Plane 3 for (a) I3D and (b) H3D (same scale)

6.6 Chapter 6 summary

The catalytic region length is kept the same for a more standard comparison. Metal foam is now supporting the catalysts as a protrusion. Firstly, the optimum protrusion height from the wall is investigated. Catalyst at 25% h shows better flow distribution around the catalyst besides the high heat transfer from the walls. After narrowing down the h, segmented patterns are evaluated. The parallel catalysts perform better than the alternating design. Most of the reaction occurs at the first catalyst segment.

Metal foams can also transfer mass between different channels. Overall, metal foam inserts show better flow uniformity compared to empty passive passages. Altering metal foam properties, it can adjust the flow amount and direction in each channel. In this way, the flow is diverted to the starving channels offering flow uniformity, total catalyst volume usage, and higher residence time.

7 Conclusion

Automobile internal combustions engines lose nearly a third of fuel energy from the exhaust pipeline. A fuel reformer is a catalyst that can utilise this heat and reform a fuel, such as methane, to make synthetic natural gas or syngas. Redirecting the syngas to the engine increases fuel heating value, reduces emissions, and modifies combustion characteristics. In this study, catalyst structural impact on the efficiency of steam methane reforming is assessed.

The literature review establishes that cell height, catalyst segmentation, and passive channels significantly affect catalyst efficiency. Therefore, the aim is to achieve higher reformer efficiency without altering the catalyst quantity and dimensions. In this way, no modification is required in the engine compartment. Three methods are adopted to meet these objectives:

1. Metal foam as a protrusion changes the channel height without changing the cell shape.
2. The continuous catalyst is segmented at the same length by placing it on upper and lower protrusion layers.
3. Lastly, a comparison is drawn between channels with simple perforations against the metal foam as a flow guide at these cavities for passive flow.

7.1 Fuel reformer design impacts on its efficiency

A reference model of Lin (LIN *et al.*, 2012) is replicated to validate the simulations. The catalyst density is calculated from the paper plots assuming; no reaction before the catalyst and at local conditions surrounding the catalyst start position. The first method gives a catalyst density of 0.4 gm^{-2}, and the second one gives 0.87 gm^{-2} or 2.18 times than before. However, catalyst loading is fixed at 0.4 gm^{-2}, and the extra factor value is divided among each variable of the rate equation. The reasons are the analysis of the rate equation terms as an exact input boundary condition (section 4.3) and their non-linear contribution to the rate equation (4.4.1). So this net value is called a cumulative factor of variables at local conditions or F1. The F1 addition gives an overall match of more than 97% with Lin's results. After the validation, the efficiency of the reformer is improved by the following methods.

7.1.1 Channel height variation

Isothermal walls (section 5.1.1) improve the hydrogen yield for the SMR reaction by 10 per cent, and adiabatic walls drop it by 24 per cent. This assessment shows that heat transfer is essential for the endothermic SMR reaction. Hence, a heat transfer medium such as metal foam should enhance the heat transfer from the isothermal wall to the catalyst site. This hypothesis is later proved and shown (Table 5-7) that metal foam improves the H_2 yield by 12.4% compared to the clear configuration.

Another way to improve heat transfer is to reduce the distance between the isothermal walls and catalysts. Besides higher heat transfer, the small channel size increases the mass transfer coefficient. The height reduction is incorporated by employing metal foam as protrusion. Despite metal foam high porosity, the flow mainly passes through the clear region, which contracts the fluid flow passage. Hence, decreasing channel height by 50%, hydrogen production improves by 57.1% compared to the catalyst at the wall (Table 6-1, A1 model vs Iso B1).

The optimum h value is 25% from each side of the upper and lower walls, whereas the solid protrusions optimum h was 75% (2.8.1). The highly porous metal foam (eta 0.92) allows fluid flow through both clear and metal foam regions. This double passage makes the optimum h value for metal foam opposite the solid protrusion and advantageous for the pressure drop factor. As a result, the Alc model gives 70.5% more hydrogen mf than the Iso B1 (6.1.2).

7.1.2 Catalyst segmentation

Both literature review (2.8.2) and parametric study (5.1.6) show that catalyst segmentation significantly increases the conversion of the reactants using the same amount of catalyst quantity. However, section 6.2 shows that after protrusion, segmentation only improves the H_2 production by 10-11 per cent (S1, A1 and A2). Overall, segmentation and 25% h increase the H_2 output by 80-81% from the Iso B1.

The main reason for the higher reformer's output is the higher temperature. The isothermal segments raise the gas temperature after the endothermic reaction. As a result of this heat transfer, the A1 average temperature gets 60-80 K higher than the Iso B1.

7.1.3 Mechanical flow mixers

Metal foams as mixer devices raise residence time for two reasons. First, it provides a longer sinusoidal fluid path but increases its velocity (5.1.7). The second is fluid velocity reduction when it passes through the metal foam (5.1.8.2). Overall, the metal foam mixer role does not improve the H_2 yield as both factors cancel each other.

In addition, the porosity, interfacial area density, and heat transfer coefficient significantly affect the reformer's output. Decreasing the eta value by 11 and 22 per cent reduces H_2

production by 8 and 16 per cent, respectively. Increasing the iad or ht two times improves heat transfer between fluid and metal foam, generating only 17% more H_2. Therefore, one should consider these effects before using metal foam for the mixer role.

7.1.4 Passive passages

The flow guide role of metal foam is served by changing metal foam properties, especially porosity and permeability (5.1.8.2). However, porosity should stay the same to preserve the efficiency, and the target should be permeability so as not to affect the FR performance (5.1.8.1).

The metal foam can promote mass and heat transfer between different channels, as shown in Figure 3-25. Compared to straight channels (W), the perforations (H) allow better flow mixing and uniformity. However, both configurations give an identical amount of hydrogen in the end.

Perforations simultaneously hosting metal foam offers an overall 9 per cent higher yield (I, U, D) (see Figure 6-14 and Figure 6-15). However, individual channel mass fraction improvement varies from 9-14% (Table 6-7). In addition, these metal foam models temperature is higher than the W and H models (Table 7-1). After the first catalyst site, it is 6 K higher, and at the end of the second, it is 20 K higher. This temperature retention by metal foam is the main reason for the higher reaction rate, which increases hydrogen production.

Table 7-1: Temperature comparison between different 2D models

Model	Temperature K
W	523-528
H	523-528
I	542-550
U	543-550
D	543-550

The mass flow rate should be similar for 2D and 3D simulations so that a one to one comparison is justifiable. For instance, compared to the 2D simulation, five times more reacting material is employed while doubling the inlet area for 3D geometry. These settings mean the mass flow rate is twice as before but reacting material is five times. Moreover, Section 5.1.2 also reveals that the mass fraction does not accurately represent the efficiency when the mass flow rate is not similar.

The I3D model shows better H_2 yield and uniformity than the H3D model. The temperature is again the main reason for the higher hydrogen production. The I3D temperature is approximately 9 K higher than the H3D model after the first and 20 K higher after the second. Despite having 40 K less temperature (Table 6-8) and three times low velocity than 2D, the I3D gives 15% more hydrogen mf than H3D (Figure 6-17, Figure 6-46 and section 6.5). This difference was 9 per cent for the 2D case. Thus, it appears that the 3D models produce more hydrogen, but the inlet mass flow rate is different from the 2D models. Hence direct comparison between both is not accurate due to dissimilar inlet conditions. Otherwise, both models are reliable, as shown in section 6.5.3.1.

Nonetheless, the primary objective is to highlight the positive effects of metal foam placement at the passive flow sites, which has been established. Such as to show that passive passages help flow exchange to the neighbouring channels in a single channel blockage situation. The temperature drop similarity between the two models show

7.1.5 Flow guides

Model D also transfers flow from channel four to the last channel due to its downward directional porosity. This diversion establishes that metal foam properties can effectively act like a flow guide (section 6.4.1.5).

7.2 Transient analysis

The transient analysis of models I and W shows that the I model quickly achieves the equilibrium state. The velocity fully develops under 0.09 s. However, the H_2 mf reaches the steady-state value in 1.4 s for the I model, whereas it nearly touches the SS value of the W model. This fast development ensures that the duration of 1.4 s is sufficient for the analysis (6.4.2). The upper channels start quickly producing hydrogen compared to the last channels. For instance, the first channels achieve a 90% hydrogen mf yield in 0.2 s and 0.16 s for models I and W. Similarly, the last channels of models I and W achieve the same level in 0.4 and 0.25 seconds.

However, after 0.5 s for the first channel, I attains a 96.7% production level, whereas W touches 95.6%. After that, model W shows no significant progress and model I reaches the steady-state level.

7.3 Recommendations

So far, this study has assumed that a highly porous metal can act as a protrusion (Figure 7-1a). However, section 2.7.6 shows that metal foam can act as a substrate. So to mimic the catalyst and washcoat layer resting on the metal foam protrusion, a highly dense or low porosity top metal foam substrate layer is another option (Figure 7-1b). Overall, an intermediate solution between a continuous catalyst layer and catalyst embedded on the entire metal foam is achievable through this method.

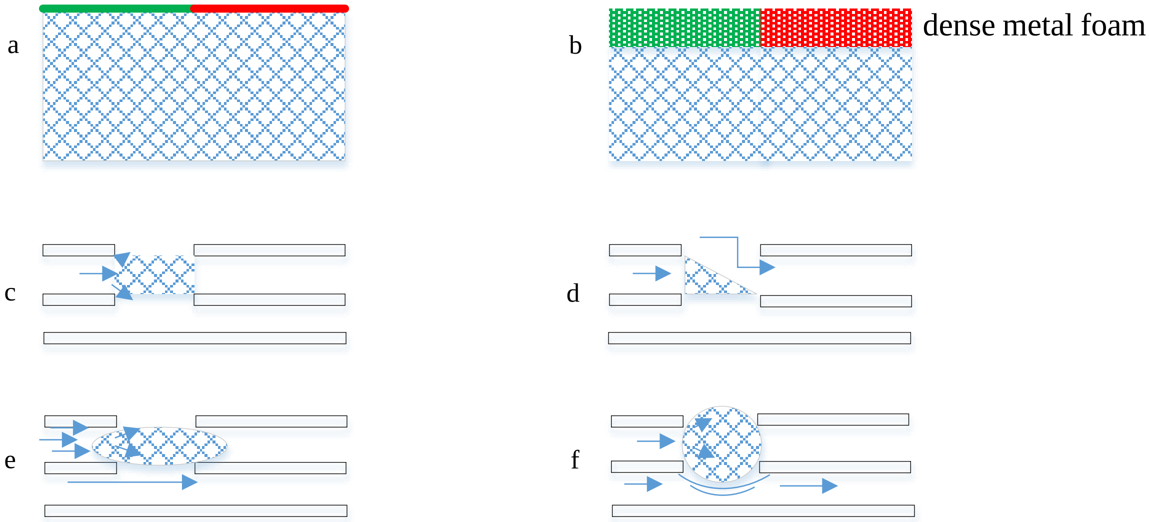

Figure 7-1: a) Catalyst on metal foam protrusion, b) variable porosity metal foam as substrate, c) metal foam + perforation in this study, d, e, f) metal foam + perforation suggestions (green is a catalytic region, red is an inert region, the maze is metal foam and black boxes are channel walls)

Similarly, this study uses a simple box-type metal foam for passive flow passages at the perforation sites. The shape and size are variable for specific applications. Such as to allow more flow from the top to the middle channel, a triangular shape metal foam is more appropriate (Figure 7-1d). An elongated shape metal foam will hinder the flow entry in that channel to limit the flow in a channel, as perhaps it receives more than neighbouring channels (Figure 7-1e). On the other hand, a large size metal foam can contract the fluid passage area of the neighbouring channels and affect the fluid path (Figure 7-1f). Moreover, foam properties (like porosity) can vary from edge to the centre to modify flow within itself.

So far, this study has tested designs of metal foam acting as protrusion, passive flow medium, and flow guide. In addition, metal foams are also tested as a mechanical mixer role to encourage gas mixing in a channel. The steady-state model shows no improvement by employing metal foams as baffles for mass transfer (5.1.7). However, metal foam enhances heat transfer significantly (5.1.6) compared to mass transfer.

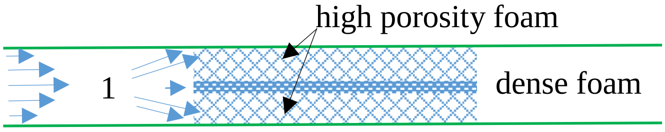

Figure 7-2: Metal foam mixer 1) disturbing the boundary layer towards the wall catalyst

The metal foam was uniform in the previous cases. However, a variable porosity metal foam mechanical mixer can disturb the laminar boundary layer in a conventional catalyst design and force the flow towards the catalyst at walls (Figure 7-2). Hence, an actual metal foam model with turbulence simulation would be a fascinating investigation. Later the optimisation study about the ratio of high to low porosity foam, the number and width of mixers can add more value to the research.

8 References

2020 Statistics (2020). Available at: https://www.oica.net/2020-statistics/ (Accessed: 29 December 2020).

Abdullah, B., Abd Ghani, N. A. and Vo, D. V. N. (2017) 'Recent advances in dry reforming of methane over Ni-based catalysts', *Journal of Cleaner Production*, 162, pp. 170–185. doi: 10.1016/j.jclepro.2017.05.176.

Agnolucci, P. (2007) 'Economics and market prospects of portable fuel cells', *International Journal of Hydrogen Energy*, 32(17), pp. 4319–4328. doi: 10.1016/j.ijhydene.2007.03.042.

ANSYS® Academic Research (2011a) *Release 14.0, ANSYS CFX: Solver Modeling Guide, ANSYS inc.*

ANSYS® Academic Research (2011b) *Release 14.0, ANSYS CFX: Solver Theory Guide, ANSYS inc.*

ANSYS® Academic Research (2011c) *Release1 4.0, ANSYS CFX: Reference Guide, ANSYS Inc.*

ANSYS® Academic Research (2012) *Release 14.5, ANSYS ICEM CFD: User Manual, ANSYS Inc.*

ANSYS® Academic Research (2017) *Release 18.2, ANSYS CFX: Solver Manager User's Guide, ANSYS inc.*

Armanini, B. R. and McCarthy, J. E. (2010) 'Fuel Vaporizer Catalyst Enables Compact Aftertreatment System Packaging by Reducing Mixing Length', *SAE International*. doi: 10.4271/2010-01-1070.

Armor, J. N. (2005) 'Catalysis and the hydrogen economy', *Catalysis Letters*, 101(3–4), pp. 131–135. doi: 10.1007/s10562-005-4877-3.

Arnaud, L. *et al.* (2014) 'Comparison and impact of waste heat recovery technologies on passenger car fuel Zconsumption in a normalized driving cycle', *Energies,* 7(8), pp. 5273–5290. doi: 10.3390/en7085273.

Ashida, K. *et al.* (2015) 'Study of Reformate Hydrogen-Added Combustion in a Gasoline Engine', *2015 JSAE/SAE Powertrains, Fuels & Lubricants International Meeting*, p. JSAE20159299 SAE2015-01-1952. doi: 10.4271/2015-01-0902.

Ashur, M. *et al.* (2007) ‘On board Exhaust Gas Reforming of Gasoline Using Integrated Reformer & TWC’, *SAE Technical Papers*, 2007–Septe. doi: 10.4271/2007-24-0078.

Balat, M. (2008) ‘Potential importance of hydrogen as a future solution to environmental and transportation problems’, *International Journal of Hydrogen Energy*, 33(15), pp. 4013–4029. doi: 10.1016/j.ijhydene.2008.05.047.

Barbieri, N. (2016) ‘Fuel prices and the invention crowding out effect: Releasing the automotive industry from its dependence on fossil fuel’, *Technological Forecasting and Social Change*, 111, pp. 222–234. doi: 10.1016/j.techfore.2016.07.002.

Bari, S. (2017) ‘An Experimental Study of a Waste Heat Recovery System Connected to a Diesel-Gen-Set’, in. doi: 10.4271/2017-01-0123.

Bhattacharya, A., Calmidi, V. V. and Mahajan, R. L. (2002) ‘Thermophysical properties of high porosity metal foams’, *International Journal of Heat and Mass Transfer*, 45(5), pp. 1017–1031. doi: 10.1016/S0017-9310(01)00220-4.

Bhattacharyya, S. C. (2009) ‘Fossil-fuel dependence and vulnerability of electricity generation: Case of selected European countries’, *Energy Policy*, 37(6), pp. 2411–2420. doi: 10.1016/j.enpol.2009.02.031.

Bianchi, E. *et al.* (2012) ‘An appraisal of the heat transfer properties of metallic open-cell foams for strongly exo- / endo-thermic catalytic processes in tubular reactors’, *Chemical Engineering Journal*, 198–199, pp. 512–528. doi: 10.1016/j.cej.2012.05.045.

Bielecki, J. (2002) ‘Energy security: Is the wolf at the door?’, *Quarterly Review of Economics and Finance*, 42(2), pp. 235–250. doi: 10.1016/S1062-9769(02)00137-0.

Boffetta, P., Jourenkova, N. and Gustavsson, P. (1997) ‘Cancer risk from occupational and environmental exposure to polycyclic aromatic hydrocarbons’, *Cancer Causes and Control*, 8(3), pp. 444–472. doi: 10.1023/A:1018465507029.

Bogarra-Macias, M. *et al.* (2015) ‘Reformate Exhaust Gas Recirculation (REGR) Effect on Particulate Matter (PM), Soot Oxidation and Three Way Catalyst (TWC) Performance in Gasoline Direct Injection (GDI) Engines’, *SAE Int. J. Engines*, 9(1), pp. 2015-01-2019. doi: 10.4271/2015-01-2019.

Brady, P. A. . and Fath, B. D. . (2009) ‘Greenhouse gas inventories of Baltimore County and county government’, *Air and Waste Management Association - Harmonizing Greenhouse Gas Assessment and Reporting Processes 2009*, 2(186 CP), pp. 513–543. Available at:

http://www.scopus.com/inward/record.url?eid=2-s2.0-78149351820&partnerID=40&md5=296be66245080110fff4de25d36a614d.

Brownell, E. and Hodes, M. (2014) 'Optimal design of thermoelectric generators embedded in a thermal resistance network', *IEEE Transactions on Components, Packaging and Manufacturing Technology*, 4(4), pp. 612–621. doi: 10.1109/TCPMT.2013.2295169.

Busse, C., Freund, H. and Schwieger, W. (2018) 'Intensification of heat transfer in catalytic reactors by additively manufactured periodic open cellular structures (POCS)', *Chemical Engineering and Processing: Process Intensification*, 124(September 2017), pp. 199–214. doi: 10.1016/j.cep.2018.01.023.

Cohen, S. (2020) *Hess's Law - Chemistry LibreTexts, University of California, Davis*. Available at: https://chem.libretexts.org/Bookshelves/Physical_and_Theoretical_Chemistry_Textbook_Maps/Supplemental_Modules_(Physical_and_Theoretical_Chemistry)/Thermodynamics/Thermodynamic_Cycles/Hesss_Law (Accessed: 10 March 2021).

Dalle Nogare, D. *et al.* (2007) 'A thermodynamic analysis of natural gas reforming processes for fuel cell application', *Chemical Engineering Science*, 62(18–20), pp. 5418–5424. doi: 10.1016/j.ces.2006.12.065.

Demirbaş, A. (2005) 'Hydrogen and boron as recent alternative motor fuels', *Energy Sources*, 27(8), pp. 741–748. doi: 10.1080/00908310490450836.

Docter, A. and Lamm, A. (1999) 'Gasoline fuel cell systems', *Journal of Power Sources*, 84(2), pp. 194–200. doi: 10.1016/S0378-7753(99)00317-1.

Dupont, V. (2007) 'STEAM REFORMING OF SUNFLOWER OIL FOR HYDROGEN GAS PRODUCTION', *HELIA*, 30, pp. 103–132. doi: 10.2298/HEL0746103D.

Endo, T. *et al.* (2007) 'Study on maximizing exergy in automotive engines', in *SAE Technical Papers*. SAE International. doi: 10.4271/2007-01-0257.

Enomoto, M. (2006) 'Comparison of pressure losses due to catalysts with different specifications using simple theoretical analysis', *SAE Technical Papers*, (724). doi: 10.4271/2006-01-0414.

European Parliament and Council of the European Union (2020) *CO_2 emission performance standards for cars and vans | Climate Action*. Available at: https://ec.europa.eu/clima/policies/transport/vehicles/regulation_en#tab-0-0 (Accessed: 21

April 2021).

Faber, A. and Frenken, K. (2009) ‘Models in evolutionary economics and environmental policy: Towards an evolutionary environmental economics’, *Technological Forecasting and Social Change*, 76(4), pp. 462–470. doi: 10.1016/j.techfore.2008.04.009.

Farrauto, R. *et al.* (2003) ‘New Material Needs for Hydrocarbon Fuel Processing: Generating Hydrogen for the PEM Fuel Cell’, *Annual Review of Materials Research*, 33(1), pp. 1–27. doi: 10.1146/annurev.matsci.33.022802.091348.

Fennell, D. *et al.* (2015) ‘Thermochemical recovery technology for improved modern engine fuel economy-part 1: Analysis of a prototype exhaust gas fuel reformer’, *RSC Advances*, 5(44), pp. 35252–35261. doi: 10.1039/c5ra03111g.

Fogler, H. S. (2020) *Elements of Chemical Reaction Engineering*. Sixth. Pearson. Available at: https://www.amazon.co.uk/Elements-Chemical-Reaction-Engineering-Fogler/dp/013548622X (Accessed: 8 January 2021).

Goldemberg, J. (2008) *Environmental and ecological dimensions of biofuels*, *esa.org*. Washington, DC. Available at: https://www.esa.org/biofuels/presentations/Goldemberg_BiofuelsPresentation.pdf (Accessed: 29 December 2020).

Greszler, A. (2008) ‘Diesel Turbo-compound Technology’, *Presentation to ICCT/NESCCAF Workshop*.

Hasan, A. O. *et al.* (2016) ‘Control of harmful hydrocarbon species in the exhaust of modern advanced GDI engines’, *Atmospheric Environment*, 129, pp. 210–217. doi: 10.1016/j.atmosenv.2016.01.033.

Hemmings, S. (2012) *SUPPORTING THE REGENERATION PROCESS OF A DIESEL PARTICULATE FILTER WITH THE ADDITION OF HYDROGEN AND HYDROGEN/CARBON MONOXIDE MIXTURES: DIESEL ENGINE AFTERTREATMENT SYSTEM*. Brunel University.

Hoang, D. L. and Chan, S. H. (2004) ‘Modeling of a catalytic autothermal methane reformer for fuel cell applications’, *Applied Catalysis A: General*, 268(1–2), pp. 207–216. doi: 10.1016/j.apcata.2004.03.056.

Hoshino, M. *et al.* (2015) ‘Development of an On-Board Fuel Reforming Catalyst for a Gasoline Engine’, *SAE Technical Papers*, 2015–Septe(September). doi: 10.4271/2015-01-

1955.

Hosseini, V. and Checkel, M. D. (2007) ‘Effect of reformer gas on HCCI combustion - Part II: High octane fuels’, *SAE Technical Papers*, 2007(724). doi: 10.4271/2007-01-0208.

Hugo, J.-M., Brun, E. and Topi, F. (2011) ‘Metal Foam Effective Transport Properties’, *Evaporation, Condensation and Heat transfer*. doi: 10.5772/21321.

Hwang, J., Li, X. and Northrop, W. (2017) ‘Exploration of Dual Fuel Diesel Engine Operation with On- Board Fuel Reforming’, *SAE International*. doi: 10.4271/2017-01-0757.Copyright.

I. Chorkendorff, J. W. N. (2007) ‘Introduction to Catalysis’, in *Concepts of Modern Catalysis and Kinetics*. Second. WILEY-VCH Verlag GmbH & Co. KGaA, Weinheim. doi: 10.1016/B978-0-12-814523-4.00001-0.

IEA (2015) *Key World Energy Statistics 2015*. Available at: https://www.connaissancedesenergies.org/sites/default/files/pdf-actualites/keyworld_statistics_2015.pdf (Accessed: 11 August 2021).

IEA, I. E. A. (2019) *Energy security*. Available at: https://www.iea.org/world (Accessed: 28 December 2020).

IEA, I. E. A. (2020) *Global oil demand growth, 2011-2025 – Charts – Data & Statistics - IEA*. Available at: https://www.iea.org/data-and-statistics/charts/global-oil-demand-growth-2011-2025 (Accessed: 28 December 2020).

Irani, M. *et al.* (2011) ‘CFD modeling of hydrogen production using steam reforming of methane in monolith reactors: Surface or volume-base reaction model?’, *International Journal of Hydrogen Energy*, 36(24), pp. 15602–15610. doi: 10.1016/j.ijhydene.2011.09.030.

Jeon, S. W. *et al.* (2013) ‘Minimization of hot spot in a microchannel reactor for steam reforming of methane with the stripe combustion catalyst layer’, *International Journal of Hydrogen Energy*, 38(32), pp. 13982–13990. doi: 10.1016/j.ijhydene.2013.08.074.

Jones, G. *et al.* (2008) ‘First principles calculations and experimental insight into methane steam reforming over transition metal catalysts’, *Journal of Catalysis*, 259(1), pp. 147–160. doi: 10.1016/j.jcat.2008.08.003.

Judith Olsen, E. D. (1984) *Health Effects Assessment for Naphthalene*. Available at: https://cfpub.epa.gov/si/si_public_record_report.cfm?Lab=NCEA&count=10000&dirEntryId=40598&searchall=&showcriteria=2&simplesearch=0&timstype= (Accessed: 10 December

2020).

Karvonen, M. *et al.* (2016) ‘Technology competition in the internal combustion engine waste heat recovery: a patent landscape analysis’, *Journal of Cleaner Production*, 112, pp. 3735–3743. doi: 10.1016/J.JCLEPRO.2015.06.031.

Kirwan, J. E., Quader, A. A. and Grieve, M. J. (2002) ‘Fast Start-Up On-Board Gasoline Reformer for Near Zero Emissions in Spark-Ignition Engines Reprinted From : SI Combustion and Flow Diagnostics’, *SAE Technical Paper*, (724), p. 1011--. doi: 10.4271/2002-01-1011.

Leung, P. *et al.* (2018) ‘Using Catalytic Heat Recovery to Improve Efficiency of Gasoline Spark Ignition Engines’, *Johnson Matthey Technology Review*, 62(4), pp. 407–416. doi: 10.1595/205651318x15318154729616.

Lewis, N. S. *et al.* (2005) *Basic Research Needs for Solar Energy Utilization*. doi: 10.2172/899136.

Lin, K. K. *et al.* (2013) ‘Comprehensive Method for Evaluating Reaction Rates of Steam Methane Reforming on Catalyst-Coated Channel Surface with Consideration of Limiting Steps’, *Journal of Thermal Science and Technology*, 8(1), pp. 165–177. doi: 10.1299/jtst.8.165.

LIN, K. K. *et al.* (2012) ‘Deduction of Proper Reaction Rate of Steam Methane Reforming over Catalyst Surface Validated with a Combination of One- and Two-Dimensional Simulations’, *Journal of Thermal Science and Technology*, 7(4), pp. 633–648. doi: 10.1299/jtst.7.633.

Lindstrom, A B., S. Waidyanatha, K. YeowellO’Connell, S. M. R. (1999) *BENZENE OXIDE PROTEIN ADDUCTS AS BIOMARKERS OF BENZENE EXPOSURE*. Newyork. Available at: https://cfpub.epa.gov/si/si_public_record_report.cfm?Lab=NERL&count=10000&dirEntryId=60616&searchall=&showcriteria=2&simplesearch=0&timstype= (Accessed: 10 December 2020).

Marsh, P. *et al.* (2001) ‘Application Guideline to Define a Catalyst Layout for Maximum Catalytic Efficiency’, *Society of Automotive Engineers, Inc*.

Martin, A. P. *et al.* (1998) ‘Effect of Flow Distribution on Emissions Performance of Catalytic Converters’, in *International Congress and Exposition Detroit, Michigan February 23-26, 1998 400*. doi: 10.4271/980936.

Mechanic (2011) *Mechanical World: The Working Cycle Of IC Engines*. Available at: https://mechlover.blogspot.com/2011/10/working-cycle-of-ic-engines_22.html (Accessed: 24

December 2020).

Meda, L. *et al.* (2016) ‘Development of a 1kW Exhaust Waste Heat Thermoelectric Generator’, *SAE International Journal of Commercial Vehicles* , 9(1), pp. 21–30. doi: 10.4271/2016-01-1273.

Morton, S., Hall, R. and Radavich, P. (2013) ‘Numerical and experimental investigation of catalyst flow and air/fuel control’, *SAE Technical Papers,* 2. doi: 10.4271/2013-01-1577.

Mucha, P., Gaiser, G. and Kuehnle, M. (2008) ‘Corrugated cross flow catalyst with permeable walls’, *SAE International Journal of Fuels and Lubricants*, 1(1), pp. 347–363. doi: 10.4271/2008-01-0809.

Müller-haas, K. and Rice, M. (2006) ‘Technology for CI Engines Used in Vehicles and Machinery to Meet Future Emission Requirements Reprinted From : Commercial Vehicle Emissions’, *Sae Paper 2006-01-3508,* (724). doi: 10.4271/2006-01-3508.

Mundhwa, M. and Thurgood, C. P. (2017) ‘Numerical study of methane steam reforming and methane combustion over the segmented and continuously coated layers of catalysts in a plate reactor’, *Fuel Processing Technology,* 158, pp. 57–72. doi: 10.1016/j.fuproc.2016.12.002.

Murkin, C. and Brightling, J. (2016) ‘Eighty Years of Steam Reforming’, *Johnson Matthey Technology Review,* 60(4), pp. 263–269. doi: 10.1595/205651316X692923.

Nagano, S. *et al.* (2002) ‘Plate type methanol steam reformer using new catalytic combustion for a fuel cell’, in *SAE Technical Papers*. doi: 10.4271/2002-01-0406.

Om Ariara Guhan, C. P., Arthanareeswaren, G. and Varadarajan, K. N. (2015) ‘CFD Study on Pressure Drop and Uniformity Index of Three Cylinder LCV Exhaust System’, *Procedia Engineering,* 127, pp. 1211–1218. doi: 10.1016/j.proeng.2015.11.466.

OPEC (2018) *OPEC Share of World Crude Oil Reserves*. Available at: https://www.opec.org/opec_web/en/data_graphs/330.htm (Accessed: 29 December 2020).

OPEC (2019) *World Proven Crude Oil Reserves*. Available at: https://www.opec.org/opec_web/en/data_graphs/331.htm (Accessed: 29 December 2020).

Pacala, S. and Socolow, R. (2004) ‘Stabilization wedges: solving the climate problem for the next 50 years with current technologies.’, *Science (New York, N.Y.),* 305(5686), pp. 968–72. doi: 10.1126/science.1100103.

Pajak, M. *et al.* (2018) ‘A numerical analysis of heat and mass transfer processes in a macro-patterned methane/steam reforming reactor', *International Journal of Hydrogen Energy*, 43(45), pp. 20474–20487. doi: 10.1016/j.ijhydene.2018.09.058.

Pastore, A. (2010) *Syngas production from heavy liquid fuel reforming in inert porous media*. CHALMERS UNIVERSITY OF TECHNOLOGY. Available at: http://www.dspace.cam.ac.uk/handle/1810/237704.

Patel, P. S. and E. F. D. (1976) 'Compounding the Truck Diesel Engine with an Organic Rankine-Cycle System', in *Proceedings of Automotive Engineering Congress and Exposition*. Detroit, MI, USA. Available at: https://www.amazon.com/Compounding-Diesel-Engine-Organic-Rankine-Cycle/dp/B007860LP8 (Accessed: 24 December 2020).

Peters, R. *et al.* (2018) 'Heat exchanger design for autothermal reforming of diesel', *International Journal of Hydrogen Energy*, pp. 1–17. doi: 10.1016/j.ijhydene.2018.03.085.

Rice, M. *et al.* (2007) 'Innovative substrate technology for high performance heavy duty truck SCR catalyst systems', *SAE Technical Papers*. doi: 10.4271/2007-01-1577.

Richardson, J. T. (1989) 'Structure of Catalysts', in *Principles of Catalyst Development*. Springer, Boston, MA, pp. 23–39. doi: 10.1007/978-1-4899-3725-4_2.

Sahlin, S. L., Andreasen, S. J. and Kær, S. K. (2015) 'System model development for a methanol reformed 5 kW high temperature PEM fuel cell system', *International Journal of Hydrogen Energy*, 40(38), pp. 13080–13089. doi: 10.1016/j.ijhydene.2015.07.145.

Sanz, O. *et al.* (2016) 'Effect of the thermal conductivity of metallic monoliths on methanolsteam reforming', *Catalysis Today*, 273, pp. 131–139. doi: 10.1016/j.cattod.2016.03.008.

Schwieger, W. *et al.* (2016) 'Hierarchy concepts: Classification and preparation strategies for zeolite containing materials with hierarchical porosity', *Chemical Society Reviews*. Royal Society of Chemistry, pp. 3353–3376. doi: 10.1039/c5cs00599j.

Settar, A. *et al.* (2015) 'Numerical investigation of convective heat transfer in a plane channel filled with metal foam under local thermal non-equilibrium', *Mechanics and Industry*, 16(5), pp. 1–7. doi: 10.1051/meca/2015035.

Settar, A. *et al.* (2018) 'Effect of inter-catalytic layer spacing at Wall-Coated Steam Methane Reformer surfaces on hydrogen production', in *The 9th International Renewable Energy Congress (IREC 2018)*. doi: 10.1109/IREC.2018.8362539.

Settar, A. *et al.* (2019) ‘Impact of Ni-based catalyst patterning on hydrogen production from MSR: External steam reformer modelling’, *International Journal of Hydrogen Energy*, 44(22), pp. 11346–11354. doi: 10.1016/j.ijhydene.2018.09.171.

Settar, A., Lebaal, N. and Abboudi, S. (2018) ‘Numerical analysis of catalytic-coated walls of an indirect internal reforming solid oxide fuel cell: Influence of catalyst coating distribution on the reformer efficiency’, *Energy Conversion and Management*, 176(September), pp. 357–371. doi: 10.1016/j.enconman.2018.09.038.

Settar, A., Nebbali, R. and Madani, B. (2015) ‘Numerical investigation on the wall-coated steam methane reformer improvement : Effects of catalyst layer patterns and metal foam insertion ScienceDirect Numerical investigation on the wall-coated steam methane reformer improvement : Effects of catalyst l’, *International Journal of Hydrogen Energy*, 40(May), p. 8966e8979. doi: 10.1016/j.ijhydene.2015.04.100.

Sigurdsson, H. O. and Kær, S. K. (2012) ‘Numerical simulation of effect of catalyst wire-mesh pressure drop characteristics on flow distribution in catalytic parallel plate steam reformer’, *International Journal of Hydrogen Energy*, 37(12), pp. 9485–9495. doi: 10.1016/j.ijhydene.2012.03.142.

Singh, R., Singh, M. and Gautam, S. (2020) ‘Hydrogen economy, energy, and liquid organic carriers for its mobility’, *Materials Today: Proceedings*. doi: 10.1016/j.matpr.2020.09.065.

Song, C. (2002a) ‘Fuel processing for low-temperature and high-temperature fuel cells: Challenges, and opportunities for sustainable development in the 21st century’, *Catalysis Today*, 77(1–2), pp. 17–49. doi: 10.1016/S0920-5861(02)00231-6.

Song, C. (2002b) ‘New Approaches to Deep Desulfurization for Ultra-Clean Gasoline and Diesel Fuels: An Overview Solid Deposition on Metal Surfaces from Heated Fuels and Hydrocarbons View project New Approaches to Deep Desulfurization for Ultra-Clean Gasoline and Diesel Fue’, *Fuel Chemistry*, 47(2), pp. 438–444. Available at: https://www.researchgate.net/publication/228900806 (Accessed: 29 December 2020).

Stobart, R., Wijewardane, A. and Allen, C. (2017) ‘The Potential for Thermo-Electric Devices in Passenger Vehicle Applications’, *SAE International*.

Subramaniam, M. N. *et al.* (2011) ‘Pre-Turbo Aftertreatment Position for Large Bore Diesel Engines - Compact & Cost-Effective Aftertreatment with a Fuel Consumption Advantage’, *SAE International Journal of Engines*, 4(1), pp. 106–116. doi: 10.4271/2011-01-0299.

Tartakovsky, L. and Sheintuch, M. (2018) ‘Fuel reforming in internal combustion engines’, *Progress in Energy and Combustion Science*, 67, pp. 88–114. doi: 10.1016/j.pecs.2018.02.003.

Tomas, V. (2006) ‘State-of-the-art in the monolithic catalysts / reactors ˇic’, *Applied Catalysis A: General*, 311, pp. 112–121. doi: 10.1016/j.apcata.2006.06.013.

Uriz, I. *et al.* (2011) ‘Computational fluid dynamics simulation of ethanol steam reforming in catalytic wall microchannels’, *Chemical Engineering Journal*, 167(2–3), pp. 603–609. doi: 10.1016/j.cej.2010.07.070.

Visconti, C. G., Groppi, G. and Tronconi, E. (2016) ‘Highly conductive “packed foams”: A new concept for the intensification of strongly endo- and exo-thermic catalytic processes in compact tubular reactors’, *Catalysis Today*, 273, pp. 178–186. doi: 10.1016/j.cattod.2016.02.060.

Wang, T. *et al.* (2011) ‘A review of researches on thermal exhaust heat recovery with Rankine cycle’, *Renewable and Sustainable Energy Reviews*, 15(6), pp. 2862–2871. doi: 10.1016/J.RSER.2011.03.015.

Watling, T. C. and Cox, J. P. (2014) ‘Factors Affecting Three-Way Catalyst Light-Off: A Simulation Study’, *SAE International Journal of Engines*, 7(3), pp. 2014-01-1564. doi: 10.4271/2014-01-1564.

Wetzel, P., Mccarthy, J. E. and Griffin, G. (2010) ‘Diesel Exhaust Aftertreatment System Packaging and Flow Optimization on a Heavy-Duty Diesel Engine Powered Vehicle’, 3(1), pp. 143–155. doi: 10.4271/2010-01-1944.

Windmann, J. *et al.* (2003) ‘Impact of the inlet flow distribution on the light-off behavior of a 3-way catalytic converter’, *SAE paper*, pp. 1–937. doi: 10.4271/2003-01-0937.

Wollin, J. and Benjamin, S. F. (1999) ‘A Study of the flow performance of ceramic contoured substrates for automotive exhaust catalyst systems’, in *International Fall Fuels and Lubricants Meeting and Exposition*. doi: 10.4271/1999-01-3626.

Xu, J. and Froment, G. F. (1989) ‘Methane steam reforming, methanation and water-gas shift: I. Intrinsic kinetics’, *AIChE J.*, 35(1), pp. 88–96.

Yoshida, T. *et al.* (2017) ‘Development of a New Ceramic Substrate with Gas Flow Control Functionality’, *SAE International Journal of Engines*, 10(4). doi: 10.4271/2017-01-0919.

Yuan, M. H. *et al.* (2010) ‘Destruction of naphthalene via ozone-catalytic oxidation process over Pt/Al2O3 catalyst', *Journal of Hazardous Materials*, 175(1–3), pp. 809–815. doi: 10.1016/j.jhazmat.2009.10.081.

Yun, J. *et al.* (2018) 'Four different configurations of a 5 kW class shell-and-tube methane steam reformer with a low-temperature heat source', *International Journal of Hydrogen Energy*, 43(9), pp. 4546–4562. doi: 10.1016/J.IJHYDENE.2018.01.069.

Zanfir, M. and Gavriilidis, A. (2003) 'Catalytic combustion assisted methane steam reforming in a catalytic plate reactor', *Chemical Engineering Science*, 58, pp. 3947–3960. doi: 10.1016/S0009-2509(03)00279-3.

Zervas, E., Montagne, X. and Lahaye, J. (2004) 'Influence of fuel and air/fuel equivalence ratio on the emission of hydrocarbons from a Si engine. 1. Experimental findings', *Fuel*, 83(17–18), pp. 2301–2311. doi: 10.1016/j.fuel.2004.06.029.

Zhang, X. and Zhao, L. D. (2015) 'Thermoelectric materials: Energy conversion between heat and electricity', *Journal of Materiomics*. Chinese Ceramic Society, pp. 92–105. doi: 10.1016/j.jmat.2015.01.001.

Zheng, J.-C. (2008) 'Recent advances on thermoelectric materials', *Frontiers of Physics in China*, 3(3), p. 12. doi: 10.1007/s11467-008-0028-9.

Zheng, M. and Asad, U. (2007) 'Preliminary energy efficiency analyses of diesel EGR fuel reforming with flow reversal and central fuelling', *SAE Technical Papers*, (724), pp. 776–790. doi: 10.4271/2007-01-4035.

9 Appendices

Appendix A

In this study, ICEM 18.1 is used for modelling and meshing, whereas problems setup, numerical solution and post-processing opt for CFX-Pre 18.1.

Firstly, points are made to mark the volume of interest, which is a fuel reforming channel. Regions of fluid, porous or solid materials are called *domains*. A separate surface is required to create each boundary, and for that, a single domain is needed.

Three blocks are necessary to create two adiabatic walls and one catalyst surface at the lower part of the FR channel. Each domain is set as fluid, solid or porous. Thus, the *interface* between them can be set accordingly, such as *fluid-fluid*, *fluid-porous*, and so on. An interface also needs a surface between different domains, and then the software can assign the same surface to two adjacent domains. Boundary conditions like *wall*, *inlet*, *outlet*, *symmetry* or interface can be applied on each sub-part of the domain.

After creating the required geometry and naming the different parts, meshing is done. Hexahedra mesh requires *blocking*, and for each domain, at least one block is assigned. Each *edge* of a block is divided into the desired number of elements for each direction. After dividing edges in all three directions, the user can generate the mesh.

Generally, a good mesh is where neighbouring elements grow smoothly, and edges of the same elements have conceivably large angles between them. In this study, refinement (compactness of element) is applied near walls and at boundary transition, such as from adiabatic wall to catalyst surface. In other words, refinement is necessary when gradients of a quantity change rapidly (ANSYS® Academic Research, 2012).

Problem setup

Geometry and computational mesh are loaded in CFX. In the **Outline** tree, there are two primary tabs which are **Mesh** and **Simulation**. Domains are added in the simulation tab according to user requirements. The **Analysis Type** has *Steady State* and *Transient* analysis options. After setting the analysis choice, domains are assigned to different regions, e.g., solid, fluid, or porous. Using the right-click (RC) on **Flow Analysis 1,** the required number of domains are inserted.

Some basic settings are required for each domain, such as *Fluid and Particle Definitions, Reference Pressure* and *Heat Transfer.* The reference pressure is set to 1 bar and heat transfer as *Thermal Energy.* In the *Turbulence* option, *Laminar* is selected, and other aspects such as buoyancy, radiation and combustion are neglected. *Kinematic diffusivity* is set to 1.038E-4 m^2 $s^{-1,}$ and an *Additional Variable* named *R11* is assigned for the rate expression.

Additional variables are scalar quantities that are transported in the domain. An algebraic equation is used in this study, and a CEL expression is assigned to each variable. It is generally needed for variables that are not available by default, such as the reaction rate. ANSYS CFX interprets these as concentrations within the fluid domain

The flow is laminar, so viscous dissipation is unchecked for the simulation. The thermal energy option is appropriate, whereas total energy is suitable when turbulent effects are dominant, such as the Mach number is more than 0.3 and when viscous heating is not negligible (ANSYS® Academic Research, 2011a).

For the *Fluid and Particle Definitions,* a new mixture is created under the **Materials** tab. The name is MSR (methane steam reforming, to be different), in which CO, H_2O, CH_4, H_2 and N_2 are added as *Variable Composition Mixture*. N_2 is a constraint that means that nitrogen mass fraction (*mf*) will be one minus the rest of the gasses mass fractions throughout the domains. *Real Gas Combustion* is chosen as *Material Group,* and Redlich-Kwong (*redkw*) library is selected.

To create an interface, just right-click the **Interfaces** tab and insert interfaces with a user name. If all the surfaces are very well defined and named in the ICEM model, assigning different interfaces between domains is very easy. First, select the interface type, which can be fluid-fluid, fluid-porous, and so on. Then the user has to choose the common surface between domains, such as *Surface 1,* and its other side, generally named as *Surface 1 shadow*.

Boundary conditions such as *inlet*, *outlet*, *wall* and *symmetry* are used. *No Slip* condition is applied. At the channel outlet, the average pressure is zero (ANSYS® Academic Research, 2017).

CEL expressions model the rate equation and other variables. The working pressure cannot be set at the inlet and can be incorporated into the rate equation. Values for local temperature, mole fractions and so forth are assigned to an expression either by user expression, **User Functions**, or built-in variables and constants (or a combination of all). Similarly, conditional statements and various other mathematical operators are available if necessary. Under the

Expressions, Functions and Variables tab, *Expressions* as input to the solver for viscosity, rate equation, heat and mass fluxes, etc., are defined.

Solver setup

After creating all the required expressions, under the **Solver** tab, *Solver Control* is configured. Users can choose different advection schemes for each of the Naiver-Strokes equations in the *Equation Class Settings*. In this study, *High-Resolution* scheme is selected for all the equations. *Timescale Factor* value is kept at 0.8 and sometimes to 0.02 to converge the solution. The timescale is defined as the length of the domain divided by the fluid velocity.

It takes more time to converge for the same problem having a small timescale factor, but *residuals* stabilize. Residuals are the imbalances produced by the discrete equations for each successive iteration. On average, 150 iterations are sufficient in this study, but sometimes 600 or more iterations are needed with a smaller timescale factor.

Residuals may be converging, diverging or oscillating. If the amplitude of this oscillation is negligible, then the solution can be considered converged. The best way to determine oscillations is to see the residual *Rate*, which should preferably be less than or around 1.00 value, which means solution convergence (ANSYS® Academic Research, 2017).

The overall convergence criteria are set to 1E-6 for the RMS (root mean square) residuals, which are easily met by all the equations except the energy equation. The H-energy RMS residual value falls below 1E-5 but remains above 1E-6.

Normally, a solution is considered converged if residual falls below 1E-5 for RMS value and 5E-4 for MAX value. RMS value is normally one order less than the MAX value (ANSYS® Academic Research, 2017).

In the case of a transient solution, *Initialization* is necessary, which can be the same as initial conditions. Also, in **Output Control,** a *Transient Results* case is needed where an *Output Frequency* number is required. The case helps the user examining each interval (the time step is 0.01 s, total time 1.4 s, 3 output frequency means after 0.03 s).

Post-processing

In the post-processing module, results can be visualized, plotted and extracted. Typically, we need *contours* for qualitative analysis and a *chart* for quantitative measurement. *Tables* are also available where the user can calculate the average value at the area of interest. For instance, a table is used to calculate the average value of all the mass fractions at the outlet. The results can be exported as an excel sheet for different plots from the chart tool. Any exported profile, like velocity profile, can also be set as a boundary condition for another case as input (ANSYS® Academic Research, 2017).

Appendix B

```
A = 0.392 [mol g^-1 s^-1 Pa^-.46]              # pre exponential factor (user expression)
CH4P = 1 [Pa]+ 1[bar]*my.CH4.molf              # partial pressure for CH4
Eact = 43200 [J mol^-1]                        #activation energy for SMR
Enthalpy = 165000 [J mol^-1]                   #enthalpy for SMR reaction
H2OP = 1[Pa]+1 [bar]*my.H2O.molf               # partial pressure for H2O
Rate = if (0.005[m]<=x&&x<=.015[m], Pterm* e^(-Eact/R/T)*Catloading,0[mol m^-2 s^-1])
SCH4 = -Rate*CH4.mw                            #methane consumption source
SCO = Rate*CO.mw                               #carbon monoxide generation source
SH2 = 3*Rate*H2.mw                             #hydrogen generation source
SH2O = -1*Rate*H2O.mw                          #water consumption source
SMR = -Rate*Enthalpy                           #SMR energy consumption source
WGS = 41000 [J mol^-1]* Rate*0                 #WGS energy generation source
eta = 0.92 []                                  #metal foam (metal foam) porosity
ht = 50 [W m^-2 K^-1]                          #metal foam heat transfer coefficient
iad = 680 [m^-1]                               #interfacial area density
Pterm = A*(CH4P^0.47)*(H2OP^-0.01)
loss = 248 [m^-1]                              #resistance loss coefficient
mdot = 1.08593E-7 [kg s^-1]                    #mass flow rate
perm = 7.63E-8 [m^2]                           #permeability
Catloading = .40 [g m^-2]
dif = 1.038E-4 [ m^2 s^-1]                     #diffusion coefficient
```

It is unnecessary to write seven lines for the rate equation, but the equation is expanded in sub-terms to distinguish between various terms. A 1 Pa pressure is added in both partial pressure terms, so these do not go to zero. The fluid is named '*my*' and *CH4.molf, T and R* are built-in values for variables like methane mole fraction and temperature, and constant like universal gas constant. The rest of the expressions are user declared variables and constants in the above code.

The value used for diffusion is called through a CEL expression *visckin.* To add it as input to a specific gas, a prefix of that gas is added, such as for methane, its expression will be

CH4.visckin. In this study, a constant value of *D* is used through the CEL expression ‘dif’ (ANSYS® Academic Research, 2017)

Appendix C

ICEM 18.1 uses numerical methods to solve partial differential equations related to fluid dynamics. These equations, including the balance of mass, momentum and energy, are called Naiver-Stroke's and the state equations. As a result, all the variables like density, three velocity components, temperature and pressure are calculated throughout the domain at each cell.

Thermal conductivity, specific heat capacity, density and viscosity for a gaseous mixture follow ideal gas law in CFX (ANSYS® Academic Research, 2011c). It means these properties of a gas mixture depends upon the sum of the product of individual constituent gas relevant property and its mass fraction (w).

$$property_{mixture} = \sum property_{individual} \cdot w_{individual}$$

$$density_{mix} = \sum density_i \cdot w_i$$

i = CH4, H_2O, H_2, N_2, and CO.

Diffusion

The Lewis number is assumed unity, which means all the species diffuse equally in the channel. So mass diffusivity (D) is described by the following equation.

$$D_i = D = \frac{\lambda}{\rho C_p}$$

Reference pressure

Reference Pressure is a datum point from which all other pressures are measured. In this study, it is found that reference pressure affects the density of the fluid. Its value is set according to the steam methane reforming (SMR) reaction pressure (1-4 bar). *Static Pressure* is the thermodynamic pressure, and *Absolute Pressure* is the sum of these two. *Static Temperature* depends upon the internal energy of the fluid mixture.

Porous medium

To model porous medium in CFX, a set of data is needed. First of wall porosity is provided. It is defined by:

$$\frac{V_{avail}}{V} = eta$$

V_{avail} is the available volume for fluid, and V is the total volume. Momentum sources (force/volume) are assigned to the isotropic or directional loss model. It is defined by (for x-axis):

$$S_{M,x} = -\frac{\mu}{K_{perm}} U_x - K_{loss}\frac{\rho}{2}|\mathbb{U}|U_x \text{ or } S_{M,x} = K_1 U_x + K_2|\mathbb{U}|U_x$$

Here K_{perm} is permeability, and K_{loss} is the quadratic loss coefficient. The first term represents viscous losses, and the second term inertial losses. Some parameters, like interfacial area density, heat transfer coefficient of the porous medium, are needed to describe the porous domain completely.

The permeability and quadratic loss coefficient of an anisotropic porous medium are defined according to the streamwise direction. The fluid flows mainly in the streamwise path along with the transverse direction. The transverse loss can be defined as a factor of streamwise coefficient or separately. So for permeability, putting a factor of 2 means transverse permeability is half of the streamwise permeability. The modified momentum sources for the directional model are (x-axis is streamwise, in this case):

$$S_{M,x} = -\frac{\mu}{K_{perm}^{S}} U_x - K_{loss}^{S}\frac{\rho}{2}|\mathbb{U}|U_x$$

In the case of a fluid domain with just a momentum loss model, porosity affects the governing equations through this loss model (such as S_M a source in momentum equation) and the rest of the terms are not changed. This model is called the *Superficial Velocity* formulation. In the case of *True Velocity* formulation, porosity effects are taken in the loss model, and as well as in other terms of the governing equations such as the continuity equation becomes:

$$\frac{\partial \epsilon\rho}{\partial t} + \nabla \cdot (\rho\mathbb{K} \cdot \mathbb{U}) = 0 \text{ where } \mathbb{K} \text{ is area porosity tensor}$$

This model is called a full porous model or true velocity formulation.

(ANSYS® Academic Research, 2017) (ANSYS® Academic Research, 2011c) (ANSYS® Academic Research, 2011b).

Convergence

Normally, a solution is considered converged if residual falls below 1E-5 for RMS value and 5E-4 for MAX value. RMS value is normally one order less than the MAX value (ANSYS® Academic Research, 2017).

Appendix D

This part includes different diagrams of models and their names. Green bars are reacting materials, and black lines are either interfaces or walls. Red colour bars are isothermal walls.

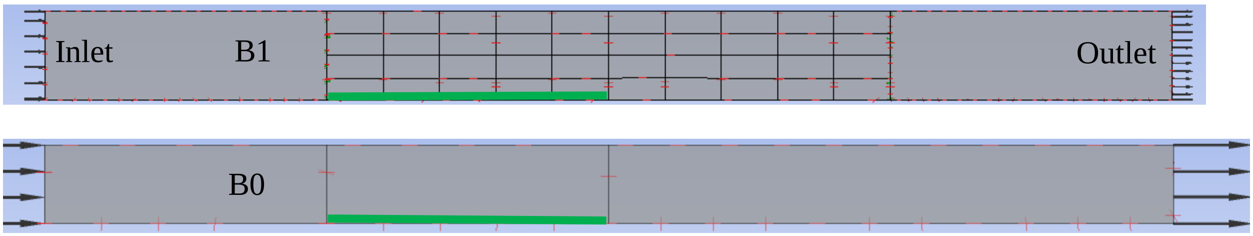

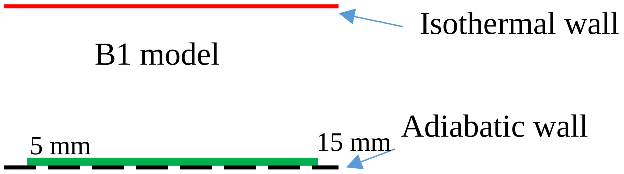

The base case has the same inlet and boundary conditions as all other models, except that its rate equation is not modified, so it excludes F1.

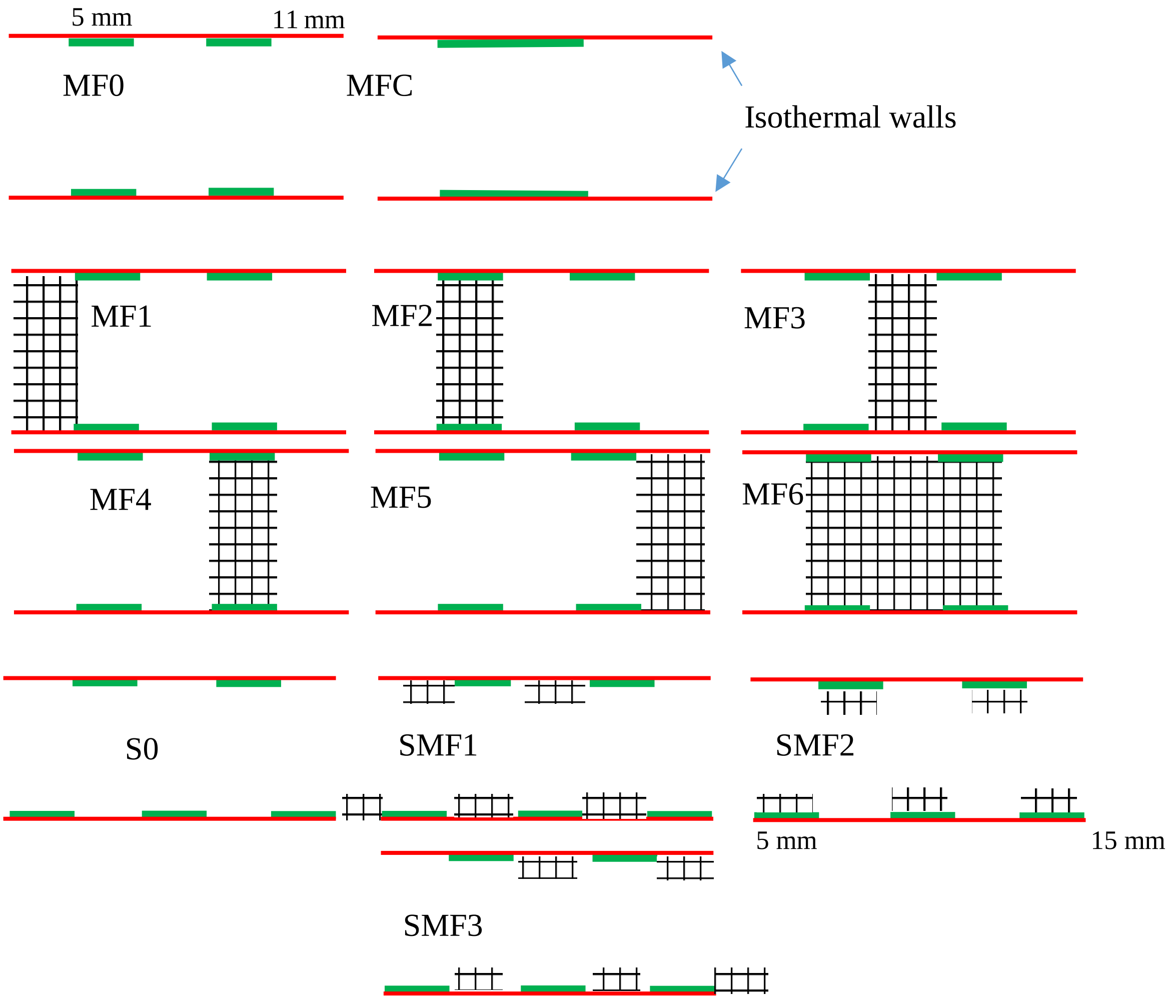

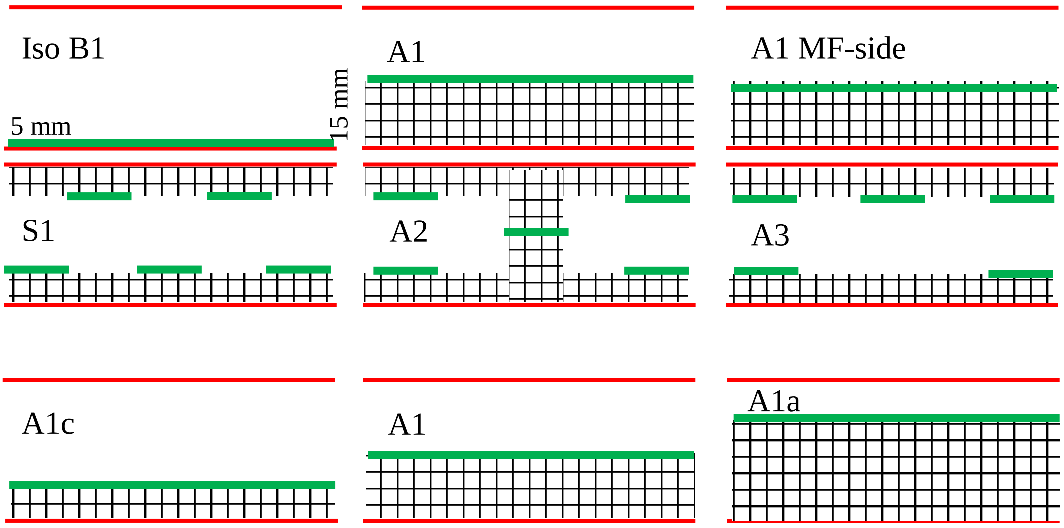

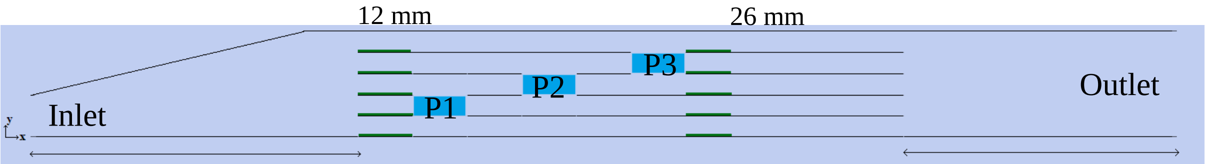

The tested 2D design for passive passages are represented. All the walls are adiabatic except the catalyst surface. The wall model (W) has continuous walls, whereas the H model has holes in it its channels. After putting metal foam at these hole locations, the model becomes either I or U or D. The 3D model is an extension of the 2D model.

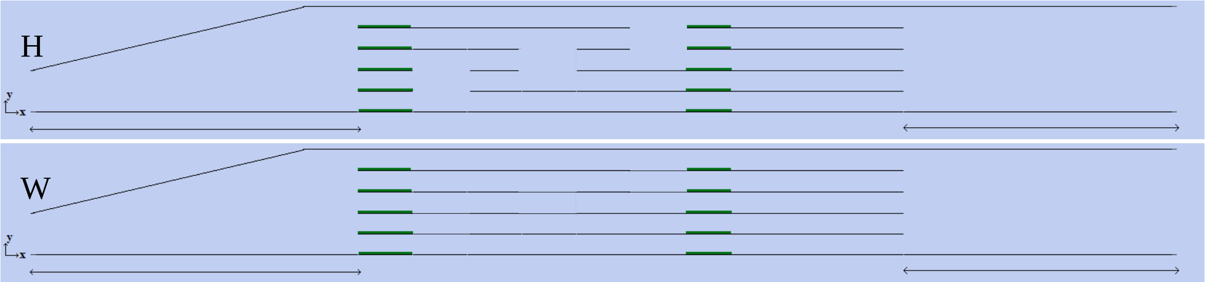

Primary flow directions inside isotropic (I), up (U) and down (D) foams in this study.